OPTICAL MICROMANIPULATION TECHNIQUES AND THEIR APPLICATIONS

By

RAKTIM DASGUPTA

Enrolment No. PHYS03200704006

Raja Ramanna Centre for Advanced Technology

Indore – 452013, India

A thesis submitted to the

Board of Studies in Physical Sciences

In partial fulfillment of requirements

For the Degree of

DOCTOR OF PHILOSOPHY

of

HOMI BHABHA NATIONAL INSTITUTE

February, 2012

Homi Bhabha National Institute

Recommendations of the Viva Voce Board

As members of the Viva Voce Board, we certify that we have read the dissertation prepared by **Raktim Dasgupta** entitled "**Optical Micromanipulation Techniques and Their Applications**" and recommend that it may be accepted as fulfilling the dissertation requirement for the Degree of Doctor of Philosophy.

P. D. Gupta 2/5/12
Date:
Chairman- Prof. P. D. Gupta

P. K. Gupta 2.8.12
Date:
Guide/Convener- Prof. P. K. Gupta

Date:
Member 1- Prof. S. Maiti

H S Rawat
Date:
Member 2- Prof. H. S. Rawat

Date:
External Examiner - Prof. D. N. Rao

Final approval and acceptance of this dissertation is contingent upon the candidate's submission of the final copies of the dissertation to HBNI.

I hereby certify that I have read this dissertation prepared under my direction and recommend that it may be accepted as fulfilling the dissertation requirement.

Date: 2.08.12

Place: Indore

Guide: P. K. Gupta
(Prof. P. K. Gupta)

STATEMENT BY AUTHOR

This dissertation has been submitted in partial fulfillment of requirements for an advanced degree at Homi Bhabha National Institute (HBNI) and is deposited in the Library to be made available to borrowers under rules of the HBNI.

Brief quotations from this dissertation are allowable without special permission, provided that accurate acknowledgement of source is made. Requests for permission for extended quotation from or reproduction of this manuscript in whole or in part may be granted by the Competent Authority of HBNI when in his or her judgment the proposed use of the material is in the interests of scholarship. In all other instances, however, permission must be obtained from the author.

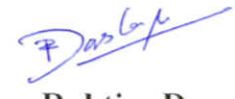

Raktim Dasgupta

DECLARATION

I, hereby declare that the investigation presented in the thesis has been carried out by me. The work is original and has not been submitted earlier as a whole or in part for a degree / diploma at this or any other Institution / University.

Raktim Dasgupta

ACKNOWLEDGEMENTS

It is my pleasure to acknowledge here the efforts of many people who have made possible the works described in this dissertation. Foremost among them is my guide Prof. P. K. Gupta, Distinguished Scientist, RRCAT, who encouraged me to pursue the research work in this area. I wish to record my deepest gratitude to him for his erudite guidance and active support at every step of this work. Two important things, which I have learnt from him in the course of this work, are the persistence and the quest for perfection in doing research.

I am extremely grateful to Prof. P. D. Gupta, Director, RRCAT, Prof. S. Maiti, TIFR, Prof S. C. Mehendale, RRCAT and Prof. H. S. Rawat, RRCAT, the members of my Ph.D. committee, for their constructive criticism, guidance and motivation.

Science is very much a team work and my heartiest thanks are to Sunita Ahlawat and Ravi Shanker Verma, who worked with me in all my experiments. They were always there with stimulating discussions and new suggestions that have helped shaping up of the work. I would also like to thank my other co-workers: Abha Uppal, Sunita Shukla, Deepa Chaturvedi and thank those who have just lifted the spirits around the lab.: Kaustuv Das, Shovan Kumar Majumder, Khageswar Sahu and Mahesh Kumar Swami, amongst others.

Last, but not the least, I want to thank, from the depth of my heart, my dearest wife Arpita, who has endured with me, through this arduous journey; our precious son Ridhaan, a constant joy to wake up to every morning and my mother and my father, who have selflessly given me all the support and encouragement. This thesis is dedicated to you.

CONTENTS

S Y N O P S I S

1. **Name of the Constituent Institution:** Laser Biomedical Applications and Instrumentation Division, Raja Ramanna Centre for Advanced Technology
2. **Name of the Student:** Raktim Dasgupta
3. **Enrolment No. :** PHYS03200704006
4. **Title of the Thesis:** Optical micromanipulation techniques and their applications
5. **Name of Supervisor:** Prof. Pradeep Kumar Gupta
6. **Board of Studies:** Physical Sciences

Optical tweezers [1] make use of optical gradient force to cause transparent particles with a higher index of refraction than their surrounding medium to get attracted towards the region of maximum light intensity. Although the optical forces are only of the order of few tens of piconewtons, such forces are often sufficient to grab and move objects - ranging in size from tens of nanometers to tens of microns.

Optical tweezers are already finding applications in diverse areas spanning from atomic physics to biological sciences [2, 3]. The range of applications may further increase if some of the problems associated with the use of optical tweezers can be taken care of. For example conventional optical tweezers make use of high numerical aperture (NA) objective lens to ensure that the gradient optical force is able to overcome the axial scattering force resulting in stable trapping. However, high NA objective lenses have short working distance and the spherical aberration effect at glass-water boundary limit the axial trapping range to about 100 μm or even less. Since typical thickness of a liquid film is larger than the available working distance in optical tweezers most of the optical tweezers applications are limited inside the bulk volume of

the liquid medium. Ability to manipulate objects at the liquid-air interface is desirable as it could prove important for studies on surface colloids, cell monolayer cultured at such interface etc. One objective of the thesis was to explore ways to overcome this limitation. First approach explored was the use of low NA objective lens having a long working distance to push the object immersed in the liquid along the direction of the beam and distort the free liquid surface [4]. It was expected that the resulting surface tension forces may help balance the scattering force and thus lead to a stable trapping of the object. The results obtained show that although the approach does succeed in trapping objects at liquid interface, the mechanisms involved in the trapping are more involved. In contrast to the expected trapping of objects at the focal point of the trap beam the objects were observed to get trapped in an annular region about the trap beam. The experimental results and their analysis reveal that apart from optical and surface tension forces, the laser induced heating of the interface and the resulting thermocapillary effect is responsible for the observed trapping of objects. Another interesting result obtained with the use of a weakly focused light beam as the trapping beam was the observation of light induced organization of microscopic particles at a glass-water boundary [5] by "optical binding" action [6] that is similar to the formation of matter by electronic interaction. More recently our studies using Laguerre-Gaussian (*LG*) beams have shown that for a given NA objective lens the use of trap beam in *LG* mode can produce larger axial trapping range compared to that available with TEM_{00} mode beam due to reduced spherical aberration effect for the former [7]. Using *LG* trap beam we could trape and transport Colo-205 cells from the bottom to the top surface of a fluid film (thickness ~ 200 μm), and monitor the changes in oxygen diffusion rate in its plasma membrane. Another interesting finding was that a change in topological charge (azimuthal index) of the *LG* mode,

which results in a change in the size of its annular intensity region, could be used for three dimensional orientation of trapped red blood cells (RBCs) with respect to the trap beam axis [8].

Another area of concern while using optical tweezers for manipulation of biological cells, is the possibility of photoinduced adverse effects on the trapped cells. Because of the much reduced absorption by cells in the near infrared (NIR) spectral range (700–1100 nm), lasers operating in this spectral range are preferred for manipulation of cells. However, due to the large intensity (a few $MW.cm^{-2}$ or higher) at the trap focus even with the use of lasers in the NIR spectral range, the possibility of adverse effects on the cells being manipulated is a matter of concern. Indeed adverse effects like a decrease in cloning efficiency and DNA damage have been reported in cells exposed to NIR optical trapping beam [9, 10]. In this respect the use of trap beam in *LG* laser mode may offer some advantage because for a given power the annular spatial intensity distribution of this mode leads to higher trapping efficiency along with a lower peak intensity compared to the usual Gaussian mode. We have therefore explored the use of *LG* beams for manipulation of spermatozoa. As expected our results confirm that for a given trap power *LG* modes can provide better trapping efficiency and significantly lower adverse effects compared to conventional TEM_{00} trapping mode [11].

Optical tweezers are also being used for spectroscopic studies on single cells, which helps account for the problem of heterogeneity present in bulk cell samples. In particular Raman spectroscopy is receiving considerable current interest for studies of the chemical composition and conformation of macromolecules in individual cells since this technique avoids the necessity of any exogenous stain. However, due to the inherent weak nature of the Raman signal, a long acquisition time, often tens of seconds to few minutes, is required to acquire spectra with a good signal to noise ratio. The cell should therefore be immobilized. But the physical or chemical

methods used for immobilization of cells in micro-Raman technique often lead to undesirable surface-induced effects on the cells or lead to strong background spectra originating from the substrate medium. The use of optical tweezers to immobilize cell without direct contact helps to avoid these problems and therefore Raman optical tweezers or a setup facilitating acquisition of Raman spectra from an optically trapped cell, are receiving much attention [12]. In particular the use of near infrared (NIR) radiation for Raman studies is gaining rapid interest due to much reduced fluorescence background that often obscures the small but important Raman bands. Raman optical tweezers have already been utilized for several interesting studies such as monitoring the real-time heat denaturation of yeast cells [13], the transition from the oxygenated to deoxygenated condition of a RBC on application of mechanical stress [14], sorting and identification of microorganisms [15] etc. Raman optical tweezers are being extensively used for studying RBCs since Raman spectroscopy is a powerful technique to monitor the oxygen carrying capacity of RBCs beacause the binding or the dissociation of oxygen with heme leads to significant conformational changes of hemoglobin that can be sensitively monitored by this technique [16]. In the last part of the thesis we describe the development of a Raman optical tweezers and its use for studies on single optically trapped RBC obtained from blood samples of healthy volunteers and malaria patients [17, 18].

The organization of the thesis is as follows.

Chapter 1 provides a brief introduction on the historical account of the invention of optical tweezers and its working principles. The optical forces responsible for trapping of microscopic objects and their dependence on the size and properties of the object are discussed. The absorption characteristics of different cell constituents and how these influence the choice of laser wavelengths for trapping biological objects is also discussed. Also apart from the

conventional TEM_{00} laser beam, the use of laser modes having different intensity patterns are also finding increasing use in this field as these laser modes have characteristics better suited for some specific applications. Therefore, properties and generation of such special laser beams are also briefly discussed with particular emphasis on *LG* beams. A brief discussion on the advantages offered by *LG* trapping beams is also presented.

The details of the optical trapping set-ups that we built to carry out the experiments reported in this thesis are presented in ***Chapter 2***. Brief discussion of the components used in the set-ups and the experimental considerations deciding their selection is also presented. Development of computer generated holograms and the use of spatial light modulator to generate *LG* beams are also discussed. Finally, characterization of the set-ups for trapping forces and trapping efficiencies is detailed.

The results of our studies on the use of long working distance objective lens for trapping objects at air-liquid interface are presented in ***Chapter 3***. The theoretical analysis carried out to comprehend the observed annular trapping around the laser beam is described and comparison of the theoretical estimates for the diameter of the annular trapping region with experimental results is also presented.

Chapter 4 describes results of our study on the use of weakly focused laser beam for creation of colloidal clusters at a glass-water boundary and trapping of other nearby particles by "optical binding" action. The theoretical analysis carried out to investigate optical binding effect produced by a simpler to model one-dimensional chain of microspheres is described and comparison of the theoretical predictions with experiments carried out on a one-dimensional chain of microspheres formed using an elliptic trap beam is presented.

The results of our study on the use of *LG* trapping beams for long axial range trapping are described in ***Chapter 5***. First, the theoretical analysis carried out by us to estimate the axial trapping range for different orders of *LG* beams and TEM_{00} beam is presented and then a comparison of the theoretical predictions with experiments performed using silica microbeads as model trapping objects is detailed. Finally, the results of our experiments on the use of LG_{01} mode to transport a human colon adenocarcinoma (Colo-205) cells from the bottom layer of a fluid medium to the top surface layer (a distance of ~200 μm) and the measurements made on the oxygen diffusivity in the plasma membrane of the cell are presented.

The results of our study on the use of *LG* modes for trapping of spermatozoa are presented in ***Chapter 6***. The experimental results obtained on the ability of *LG* trap beams with a given power but with different mode orders to trap spermatozoa swimming at different velocities are presented along with the measurements made on photodamage to spermatozoa trapped for different periods of time in these beams.

Chapter 7 presents the results of our study on the use of *LG* trap beams for orientation and rotation of trapped RBCs and describes the advantages of this method over the previously used methods for this purpose.

Details of the set-up used to simultaneously trap and record Raman spectra from single cell (Raman optical tweezers) are presented in ***Chapter 8.*** The basic concepts of Raman scattering and the spectral processing routines used by us are also discussed. Finally the results of the experiments carried out to study possible photo-induced changes in RBCs as a function of the duration of laser exposure in Raman optical tweezers employing NIR (785 nm) laser source are described.

Chapter 9 describes Raman spectroscopic studies on optically trapped RBCs collected from healthy volunteers and patients suffering from *P. vivax* infection. The spectral differences observed between the cells taken from the two classes of samples and the possible reasons thereof are discussed.

Finally in ***Chapter 10*** we present a summary of the major accomplishments. A brief outline of future investigations that may evolve from the work presented in this thesis is also provided.

Synopsis references:

1. A. Ashkin, J. M. Dziedzic, J. E. Bjorkholm, and S. Chu, "Observation of a single beam gradient force optical trap for dielectric particles," *Opt. Lett.* **11**, 288-290 (1986).

2. A. Ashkin, "Optical trapping and manipulation of neutral particles using lasers," *Proc Natl Acad Sci USA* **94**, 4853-4860 (1997).

3. S. Chu, "Laser manipulation of atoms and particles," *Science* **253**, 861-866 (1991).

4. R. Dasgupta, S. Ahlawat, and P. K. Gupta, "Trapping of micron sized objects near a free liquid surface," *J. Opt. A: Pure Appl. Opt.* **9,** S189-S195 (2007).
5. S. Ahlawat, R. Dasgupta, and P. K. Gupta, "Optical trapping near a colloidal cluster formed by a weakly focused laser beam," *J. Phys. D: Appl. Phys.* **41,** 105107 (2008).
6. M. M. Burns, J. M. Fournier, and J. A. Golovchenko, "Optical Binding," *Phys. Rev. Lett.* **63,** 1233-1236 (1989).

7. R. Dasgupta, R. S. Verma, S. Ahlawat, D. Chaturvedi, and P. K. Gupta, "Long distance axial trapping with Laguerre-Gaussian beams," *Appl. Opt.* **50**, 1469-1476 (2011).

8. R. Dasgupta, S. Ahlawat, R. S. Verma, and P. K. Gupta, "Optical orientation and rotation of trapped RBCs with Laguerre-Gaussian mode," *Opt. Exp.* **19**, 7680-7688 (2011).
9. H. Liang, K. T. Vu, P. Krishnan, T. C. Trang, D. Shin, S. Kimel, and M. W. Berns, "Wavelength dependence of cell cloning efficiency after optical trapping," *Biophys. J.* **70**, 1529-1533 (1996).
10. S. K. Mohanty, A. Rapp, S. Monajembashi, P. K. Gupta, and K. O. Greulich, "Comet assay measurements of DNA damage in cells by laser microbeams and trapping beams with wavelengths spanning a range of 308 nm to 1064 nm," *Rad. Res.* **157**, 378-385 (2002).
11. R. Dasgupta, S. Ahlawat, R. S. Verma, S. Shukla, and P. K. Gupta. "Optical trapping of spermatozoa using Laguerre-Gaussian laser modes," *J. Biomed. Opt.* **15**, 065010 (2010).
12. D. V. Petrov, "Raman spectroscopy of optically trapped particles," *J. Opt. A: Pure Appl. Opt.* **9**, S139-S156 (2007).
13. C. Xie, Y. Li, W. Tang, and R. J. Newton, "Study of dynamical process of heat denaturation in optically trapped single microorganisms by near-infrared Raman spectroscopy," *J. Appl. Phys.* **94**, 6138-6142 (2003).
14. S. Rao, S. Bálint, B. Cossins, V. Guallar, and D. Petrov, "Raman Study of Mechanically Induced Oxygenation State Transition of Red Blood Cells Using Optical Tweezers," *Biophys. J.* **96**, 209-216 (2009).
15. C. Xie, D. Chen, and Y. Q. Li, "Raman sorting and identification of single living micro-organisms with optical tweezers," *Opt. Lett.* **30**, 1800-1802 (2005).

16. B. R. Wood, B. Tait, and D. McNaughton, "Micro-Raman characterization of the R to T state transition of haemoglobin within a single living erythrocyte," *Biochem. Biophys. Acta* **1539**, 58-70 (2001).

17. R. Dasgupta, S. Ahlawat, R. S. Verma, A. Uppal, and P. K. Gupta. "Hemoglobin degradation in human erythrocytes with long duration near infrared laser exposure in Raman optical tweezers," *J. Biomed. Opt.* **15**, 055009 (2010).

18. R. Dasgupta, R. S. Verma, S. Ahlawat, A. Uppal, and P. K. Gupta. "Studies on erythrocytes in malaria infected blood sample with Raman optical tweezers," *J. Biomed. Opt.* **16**, 077009 (2011).

LIST OF FIGURES

		a new position as can be seen in frames (c-d). A new sphere (marked as 3) occupies the trapping site initially occupied by sphere 2. Scale bar, 6 μm.	
32	4.3	(a –b) Rotation of the trapped external microsphere in synchronism with the rotating trapped cluster. Interval between successive frames is ~ 15 sec.	100
33	4.4	(a) Trapping action near a linear array of three particles. The trapped particle near the microsphere chain is indicated by arrow. Scale bar, 8 μm. (b) Position histogram of the trapped particle. The positions were recorded over 200 frames taken at 40 ms intervals.	101
34	4.5	Calculated intensity pattern along the line joining the middle sphere in the 1-D array and the trapped sphere. The strongest peak is seen at a separation of 3 μm.	104
35	5.1	(a) Geometric optics representation of the refraction of a light beam focused through a refractive index interface with $n_2 < n_1$. (b) The geayscale images showing transverse focal profiles as a function of trapping distances for (i) TEM_{00} mode and (ii) LG_{01} mode. (c) The axial focal spread as a function of trapping distances for (i) TEM_{00} mode and (ii) LG_{01} mode. (d) The variation of peak intensity of the trap beam with trapping distance for different laser modes. All data shown are for laser wavelength of 532 nm. Inset in 1(d) shows the peak intensity of the trap beam with trapping distance for TEM_{00} and LG_{01} mode at laser wavelength 1064 nm.	111
36	5.2	(a) Maximum trapping depth observed for different size of silica microspheres using TEM_{00} and LG modes. (b) Manipulation of a 3 μm silica sphere from bottom of the medium upto the top free surface and back using LG_{01} mode [18]: (i) The silica sphere was trapped at the bottom layer identifiable by other untrapped spheres. (ii)-(iv) The trapped sphere being lifted from the bottom layer towards the top free surface. The untrapped spheres can be seen to be out of focus. (v) The sphere is trapped at the free top layer. As the trap focus is lifted above	118

		the top free surface the sphere can be seen to be pushed down by surface tension force. (vi-viii) The trapped sphere is manipulated back towards the bottom of the medium. Thickness of open sample film ~ 200 μm. Scale bar for 5.2(b), 5 μm.	
37	5.3	(a) The axial trapping range observed for colo cells with TEM_{00} and LG_{01} modes. The data shown are the mean over five cells. (b) Brightfield (i) and fluorescence image (ii) of a trapped colo cell. (c) The fluorescence equilibration profile of the colo cells when incubated with 30 μg/ml laurdan. The observed fluorescence seen to reach a steady state after an incubation period of ~ 25 minutes. (d) Observed mean relative fluorescence intensities of cells when trapped at the bottom (F_0) and at the top surface (F_{eq}). The data for cells althrough kept at room temperature (25 ºC) and cells heat treated for ~1 hr at an elevated temperature of ~ 55 ºC are shown. Scale bar for 5.3(b), 5 μm.	120
38	6.1	The intensity profiles of different laser modes.	125
39	6.2	Mean VSL of spermatozoa that could be just trapped by different laser modes having identical trapping power of ~ 140 mW at the specimen plane. The data presented are the mean ± standard deviation. The difference in the distribution of data was found to be statistically significant, $p < 0.05$ (one way ANOVA).	127
40	6.3	(a) $T_{paralysis}$ of the trapped spermatozoa under TEM_{00} and LG_{01} mode. (b) $T_{paralysis}$ of the trapped spermatozoa under LG_{01}, LG_{03} and LG_{05} modes each having trapping power ~ 110 mW. The data presented are the mean ± standard deviation. All distributions were found to be statistically significantly different, $p < 0.05$.	128
41	6.4	Time evolution of fluorescence spectra from AO stained spermatozoa in terms of (a) intensity ratios for red and green channels. The data are averaged over ~ ten cells and presented as mean ± standard deviation. The corresponding light dosages are also shown along the time axis. The intensity ratios are statistically significantly different with $p < 0.05$ (student's *t*-test). (b) Time lapse images of AO stained spermatozoan.	130

LIST OF TABLES

CHAPTER 1

INTRODUCTION

Since their advent in 1986, optical tweezers [1] have found many useful applications in different areas ranging from physics to biology [2-8]. In particular, the ability to exert picoNewton forces on micron-sized particles is now routinely applied to fields as diverse as the physics of colloids [4, 9], the study of biomolecular complexes at the single-molecule level [10-15] or the measurement of cellular mechanical properties [16-18]. This chapter introduces the development of the field of optical trapping, the related physical concepts and the associated applications.

In the first section I will present a brief introduction on the historical account of the invention of optical tweezers and its working principles. The optical forces responsible for trapping of microscopic objects and their dependence on the size and properties of the object are discussed next. Since the use of laser modes having a different intensity pattern to the conventional TEM_{00} laser beam are better suited for some specific applications, properties and generation of such special laser beams are also briefly discussed in section three, with particular emphasis on Laguerre-Gaussian beams. In section four different applications of optical tweezers are described in brief. Lastly an outline of the thesis is included.

1.1 OPTICAL TWEEZERS: BASICS AND BACKGROUNDS

A good example of light exerting force on an object is that of a comet whose dust particles are optically 'pushed' by radiation pressure from the Sun's light. The use of laser light to manipulate objects is a scaled down example of the same idea. Laser light has an excellent

directional property and large intensity that make it possible to use laser light to manipulate microscopic objects. In experiments performed in 1970 by Arthur Ashkin, at Bell Laboratories in USA, microscopic particles were observed to be drawn into the axis of the TEM_{00} mode laser beam from an argon ion laser and accelerated in the propagation direction [19]. The basic observation clearly pointed out the existence of two types of light forces acting on the particles, one is the light "gradient force" pulling the particles along the light intensity gradient onto the beam axis and the other one being the light "scattering force" propelling the particles along the beam. In vertical configuration, when a TEM_{00} mode laser beam was directed upwards, the upward scattering force could balance the downward gravitational force and thus microspheres could be levitated against gravity [20]. These particles were simultaneously held in the centre of the beam by the gradient force. In horizontal configuration, two opposing TEM_{00} beams could trap microscopic particles [19, 21]. The particles were drawn into the beam axis by the gradient force and trapped at a stable equilibrium point between the two counter-propagating laser beams. But the technique was not widely applicable to trap microscopic particles because of critical alignment requirements and lack of easy maneuverability of particles under microscopic observation.

It was in the year 1986 that a single laser beam was used to trap particles stably in three dimensions [1]. This trapping was due to a three dimensional gradient force field arising due to the large gradient of light intensity in all the three directions when the laser beam was focused with a high numerical aperture microscope objective. This type of single-beam gradient force trap, commonly known as optical tweezers, is now widely used in applications ranging from investigating the angular momentum of light [22-24] to measuring intracellular forces [25-27]. Unlike mechanical micro tools, the optical trap is gentle and absolutely sterile and can be used to

capture, move and position single cells or sub cellular particles without direct contact or significant damage. Further, over the past three decades, optical micromanipulation has evolved to include more complex applications like rotation [22-24, 28-34] or transportation of trapped objects [35-38], optical stretching of biological cells [39-44], recording of Raman spectra from trapped cells [45-50] and many others. With the use of diffractive optical elements such as spatial light modulators, using special laser beams like Laguerre-Gaussian beams or Bessel beams has become fairly commonplace and led to many sophisticated applications not feasible with conventional laser beam.

1.2 OPTICAL FORCES ON SPHERICAL PARTICLES

The interaction of a particle with the impinging light is defined by a momentum transfer due to scattering or absorption of photons. The Mie scattering theory can be applied to spheres of arbitrary radius and dielectric susceptibility [51, 52]. But Mie theory in strict sense is particularly applicable for interaction between a plane wave and a spherical object. It cannot be used in a straightforward manner to describe radiation force exerted by a tightly focused Gaussian beam. So modifications have been proposed to take care of practical laser beams and the modified theory is known as Generalized Lorentz Mie Theory (GLMT) [53-55]. However, a major issue in using GLMT is the difficulty of deriving all the components of the electromagnetic field at the surface of the particle, since these include contributions from the incident field as well as from the scattered and internal fields. A significant simplification of the problem can be achieved in the limit of a sphere of very large radius or very small radius compared to the wavelength. These two limiting cases are discussed in Sections 1.2.1 and 1.2.2.

1.2.1 PARTICLE SIZE >> WAVELENGTH OF LIGHT

For objects with size much greater than (i.e. size ≥ 10λ) the wavelength of the trap beam (as often is the case for biological cells), simple ray optics descriptions can be used to explain the basic idea [19]. The origin of radiation forces can be understood with a simple ray optics model as described in figure 1.1.

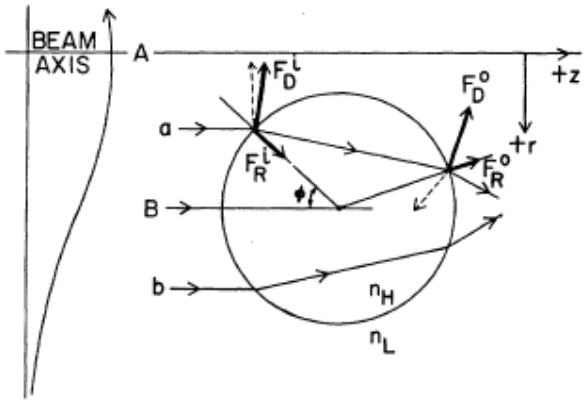

Figure 1.1 Reflection and refraction of light by a sphere illuminated by a Gaussian beam (reprinted by permission from *Physical Review Letters* [19]).

The sphere of high index n_H is situated off the beam axis inside a medium of refractive index n_L ($n_H > n_L$). The illuminating beam is assumed to be collimated having a Gaussian intensity profile. Let us consider a pair of rays symmetrically situated about the sphere axis (B). Reflection and refraction processes occurring at the refractive index interfaces cause direction changes to the two representative light rays (a and b) as shown in figure 1.1. These also lead to the change in the momentum associated with these rays. These changes in momentum are equivalent to forces acting at the interfaces and are shown for the '*a*' ray. F_R^i and F_R^o denote the force components originates from reflected light ray parts at the input and output faces respectively. Whereas F_D^i and F_D^i represent the forces occur due to refraction of the rays at the input and output faces respectively. It can be clearly seen form the figure that all forces give

acceleration in the $+z$ direction. Reflection forces cancel radially to first order. But deflection forces (due to light refraction) add radially in $-r$ direction. Thus the net radial force from the stronger ray '*a*' (considering Gaussian intensity profile of the incident laser beam) is towards the higher light intensity. The symmetrical weak ray '*b*' similarly gives a net force along $+z$ and a net outward but weaker radial force. Hence in effect the sphere is attracted onto the beam axis and driven along it. The simple picture explains the two types of radiation forces on microscopic particles: (1) a scattering force, in the direction of light propagation and (2) a gradient force, in the direction of the spatial light gradient. For most conventional situations, the scattering force dominates along the beam propagation direction. However, if there exists a steep axial intensity gradient (i.e. near the focus of a tightly focused laser beam), the second component of the optical force, the gradient force becomes stronger.

For stable trapping in all three dimensions, the axial gradient component of the force pulling the particle towards the focal region must exceed the scattering component of the force pushing it away from that region. This condition can be achieved by a very steep gradient in the light, produced by sharply focusing the trapping laser beam to a diffraction-limited spot using an objective of high numerical aperture (NA> 1). The action of this single beam optical trap or optical tweezers can be explained by simple ray diagram as shown in figure 1.2 [56]. In the figure two light rays (*a* and *b*) situated at equal radial distance from the beam axis are considered. Due to the refraction of rays *a* and *b* from the sphere, assumed to have a refractive index higher than the surroundings, there will be forces F_a and F_b respectively on it. The net force denoted as F. It can be verified from figure 1.2 that in all the cases where the sphere is positioned away from the focal point the resultant force acts to pull the sphere onto the beam focus (the equilibrium position). When at the focal point, there is no refraction and hence no

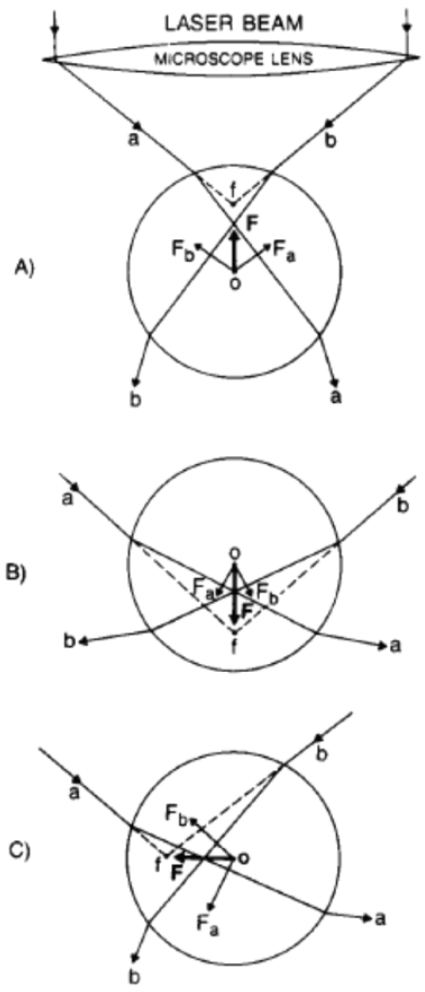

Figure 1.2 Ray diagram explanation of trapping of a spherical particle with single beam gradient force optical trap. **F** is the gradient force (reprinted by permission from *Biophysical Journal* [56]).

force on the sphere. In this ray-optics description the sphere is assumed to be weakly reflective or absorptive at the trapping wavelength so that the forces arising due to absorption or reflection of light by the sphere can be neglected.

For quantitative estimation of the trapping force using the simple ray optics concept, Roosen and co-workers [56, 57] performed computation of the optical forces on a dielectric

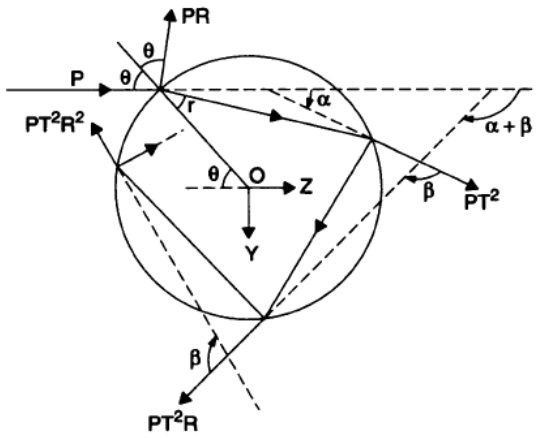

Figure 1.3 The scattering of a single incident ray of power P by a dielectric sphere. The reflected ray PR and infinite set of refracted rays PT^2R^n are shown (reprinted by permission from *Biophysical Journal* [56]).

sphere due to a light ray of power P (figure 1.3). Their analysis led to the following expression for the scattering force (please see appendix A for a detailed calculation),

$$F_Z = F_s = \frac{n_1 P}{c}\left(1 + R\cos 2\theta - T^2\,\frac{\sin(2\theta - 2r) + R\cos 2\theta}{1 + R^2 + 2R\cos 2r}\right)$$

$$\equiv \frac{n_1 P Q_s}{c} \tag{1.1}$$

where R and T are the Fresnel reflection and transmission coefficients respectively, n_1 is the index of refraction of the suspending medium, θ and r the angles of incidence and refraction of light and c is the speed of light in vacuum. The term n_1P/c is the momentum per second of the light ray. The angle r relates to θ via Snell's refraction law,

$$\frac{n_2}{n_1} = \frac{\sin\theta}{\sin r} \tag{1.2}$$

where n_2 is the refractive index of the object. Similarly, for the gradient force (please see appendix A for a detailed calculation),

$$F_Y = F_g = \frac{n_1 P}{c}\left(R\sin 2\theta - T^2 \frac{\sin(2\theta - 2r) + R\sin 2\theta}{1 + R^2 + 2R\cos 2r} \right)$$

$$\equiv \frac{n_1 P Q_g}{c} \tag{1.3}$$

Vectorial addition of these two trapping force components gives the magnitude of the force due to a single ray of power P,

$$F_{tot} = \frac{n_1 P}{c}\sqrt{Q_s^2 + Q_g^2} \equiv \frac{n_1 P}{c} Q_{tot} \tag{1.4}$$

where the parameter Q determines the fraction of power utilized in trapping. The total force on the object is found by summing over all rays passing through the trapped object [56].

It may be easily shown using similar ray optics analysis that the particle is pushed away from the beam if relative refractive index < 1. It may be noted here that for metallic objects scattering force dominates over the gradient force [58] and trapping using a Gaussian profile beam is difficult. For these and absorbing dielectric objects, where the force due to absorbed light dominates over the gradient force trapping requires low intensity regions such as that exists in Laguerre-Gaussian beams.

1.2.2 PARTICLE SIZE << WAVELENGTH OF LIGHT

The ray optics approach described above is not sufficient to calculate forces for objects with size < 0.1λ, as only a fraction of the light beam interacts and therefore has an effect on the particle [59]. In this size regime wave theory of light scattering is needed to be taken into account for explaining the trapping mechanism.

The radiation pressure force exerted on the small particles considered as point dipole can be described by two components acting on the dipole. One of these force components is the so-called scattering force, which is given by [60]

$$\vec{F}_{scatt}(\vec{r}) = \frac{C_{pr}\left\langle \vec{S}(\vec{r},t)\right\rangle_T}{c/n_1} = \vec{z}n_1 I(r)\frac{C_{sc}}{c} \tag{1.5}$$

Where $\left\langle \vec{S}(\vec{r},t)\right\rangle$ is the time averaged Poynting vector and C_{pr} the cross-section for the radiation pressure of the particle, equal to the scattering cross-section C_{sc} for Rayleigh dielectric particles that scatter light isotropically. For a Rayleigh particle of radius a,

$$C_{pr} = C_{sc} = \frac{8}{3}\pi(ka)^4 a^2\left(\frac{m^2-1}{m^2+2}\right)^2 \tag{1.6}$$

Where $$k = 2\pi/\lambda \tag{1.7}$$

λ being the laser wavelength and $m=n_2/n_1$ is the relative refractive index of the particle.

Therefore, using equations 1.6 and 1.7, equation 1.5 can be expressed as,

$$F_{scatt} = \frac{I_0}{c}\frac{128\pi^5 a^6}{3\lambda^4}\left(\frac{m^2-1}{m^2+2}\right)^2 n_1 \tag{1.8}$$

Another component is the gradient force due to the Lorentz force acting on the dipole induced by the electromagnetic field. By using the electric dipole moment as an electrostatics analogue of the electromagnetic wave, an instantaneous gradient force is defined by,

$$\vec{F}_{grad}(\vec{r},t) = [\vec{p}(\vec{r},t).\nabla]\vec{E}(\vec{r},t) \tag{1.9}$$

Where

$$\vec{p}(\vec{r},t) = 4\pi n_1^2 \varepsilon_0 a^3 \left(\frac{m^2-1}{m^2+2}\right)\vec{E}(\vec{r},t) \tag{1.10}$$

is the dipole moment of the particle acting as a point dipole under the influence of the instantaneous electric field $\vec{E}(r,t)$. ε_0 is the permittivity of the free space.

Using the vector identity that $\nabla\vec{E}^2 = 2\left(\vec{E}.\nabla\right)\vec{E} + 2\vec{E}\times\left(\nabla\times\vec{E}\right)$ and considering $\nabla\times\vec{E} = 0$, according to the Maxwell's equations, the instantaneous light gradient force can be expressed as,

$$\vec{F}_{grad}(r,t) = 4\pi\varepsilon_0 n_1^2 a^3 \left(\frac{m^2-1}{m^2+2}\right)\frac{1}{2}\nabla\vec{E}^2(\vec{r},t) \tag{1.11}$$

The gradient force which the particle experiences in a steady state is the time-average version of equation 1.11 and is given by

$$\begin{aligned}
\vec{F}_{grad}(\vec{r},t) &= \left\langle \vec{F}_{grad}(\vec{r},t)\right\rangle_T \\
&= 4\pi\varepsilon_0 n_1^2 a^3 \left(\frac{m^2-1}{m^2+2}\right)\frac{1}{2}\nabla\left\langle \vec{E}^2(\vec{r},t)\right\rangle_T \\
&= \pi\varepsilon_0 n_1^2 a^3 \left(\frac{m^2-1}{m^2+2}\right)\nabla\left|\vec{E}(\vec{r})\right|^2 \\
&= \frac{2\pi n_1 a^3}{c}\left(\frac{m^2-1}{m^2+2}\right)\nabla I(\vec{r})
\end{aligned} \tag{1.12}$$

where the relations $\left\langle \vec{E}^2(\vec{r},t)\right\rangle_T = \frac{1}{2}\left|\vec{E}(\vec{r})\right|^2$ and $\frac{n_1\varepsilon_0 c}{2}\left|\vec{E}(\vec{r})\right|^2 = I(\vec{r})$ have been used.

In terms of polarizability $\alpha = -\frac{n_1^2 a^3}{2}\left(\frac{m^2-1}{m^2-2}\right)$ of the spherical Rayleigh particle a concise expression for gradient force turns out to be,

$$F_{grad} = -\frac{n_1}{2}\alpha \nabla E^2 \tag{1.13}$$

The condition for a stable single-beam trap is that *R,* the ratio of the backward axial gradient force to the forward-scattering force, be greater than unity at the position of maximum axial intensity gradient. For a Gaussian beam of focal spot size ω_0 this occurs at an axial position,

$$z = \frac{\pi {\omega_0}^2}{\sqrt{3}\lambda} \tag{1.14}$$

The value of *R* for small value of ω_0 can be obtained as:

$$R = \frac{F_{grad}}{F_{scatt}} = \frac{3\sqrt{3}}{64\pi^5}\left(\frac{n_1^2}{\left(\frac{m^2-1}{m^2+2}\right)}\right)\frac{\lambda^5}{a^3 w_0^2} > 1 \tag{1.15}$$

From this equation it is clear that the stability condition is independent of power. But this is just a necessary condition, not sufficient condition as for stable trapping we need to account the Brownian fluctuations and ensure that the trapping potential is sufficient to overcome these.

So the additional condition for stable trapping is,

$$e^{-U/kT} << 1 \tag{1.16}$$

Where *U* is the potential of the gradient force. Expression for *U* is given as,

$$U = n_1 \alpha E^2 / 2 = n_1^3 a^3 \left(\frac{m^2-1}{m^2-2}\right)\frac{E^2}{2} \tag{1.17}$$

Equation 1.17 explains the requirement of a minimum power of the trapping beam for observable trapping action. Usually the minimum power required for trapping is few mW when the laser beam is focused down to the diffraction limit.

1.2.3 TRAPPING FORCE PROFILES IN OPTICAL TWEEZERS

In light of the above explanation of optical forces typical forces profiles along axial and transverse coordinates for a dielectric particle having refractive index higher than the surrounding medium are shown in figure 1.4. These force profiles are obtained considering the space varying light field seen by the dielectric particles as a result of the fact that the light intensity is the maximum at the focus and falls off while going away from it in all direction [56]. In transverse directions scattering force is absent and therefore the only force acting on the particle is the light gradient force (figure 1.4a). For a tightly focused beam though the scattering force is small compared to the strong axial gradient force it may still offset the total force curve towards the +z axis (figure 1.4b).

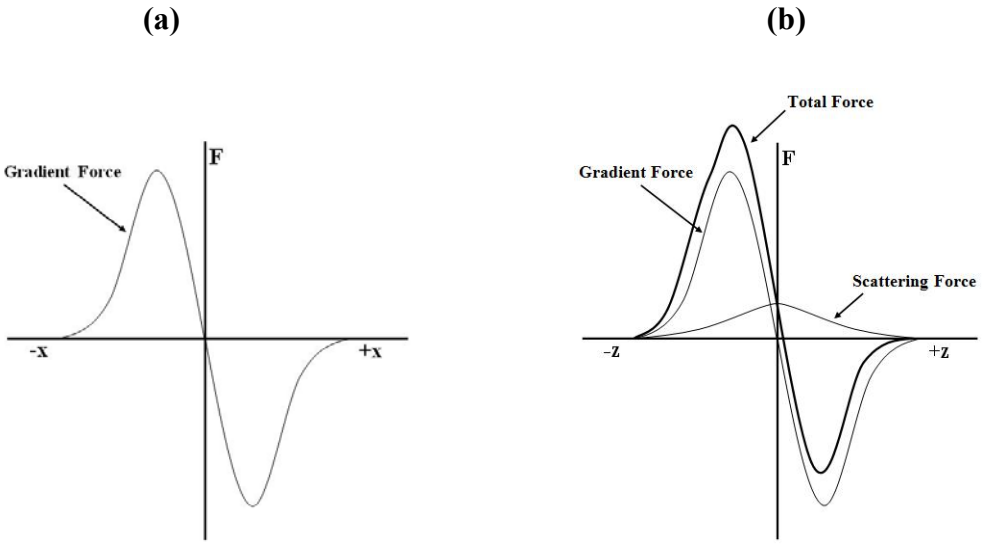

Figure 1.4 The (a) radial and (b) axial force profiles in optical tweezers.

1.2.4 ABSORPTION IN BIOLOGICAL SAMPLES

Since a significant part of the work presented in this thesis involve trapping of biological samples it is good to have a close look onto the light absorption profile of typical constituents of biological cells. Presence of absorption results in to strong axial force components and trapping of objects becomes difficult. Further, while optically manipulating biological objects one would like to minimize absorption for the reason that deposition of energy may result in irreversible changes in the sample. The absorption at a given wavelength is an average of the absorptions by several of the constituents of a biological object. In figure 1.5, the wavelength dependence of the absorption co-efficient of some important biological elements is shown [61]. The major contributors of absorption in biological samples in the ultraviolet (UV) spectral range are DNA and proteins. In the visible and near infrared (NIR) wavelength range, the absorption is dominated by hemoglobin and melanin. Water, the main constituent of all biological cells strongly absorbs beyond ~ 1.5 μm. For wavelength greater than ~ 650 nm and smaller than ~1.5 μm the overall absorption is weak and so the light causes minimum damage to biological samples. Therefore, laser emitting light in this wavelength region is preferred for making optical trap while manipulating biological objects.

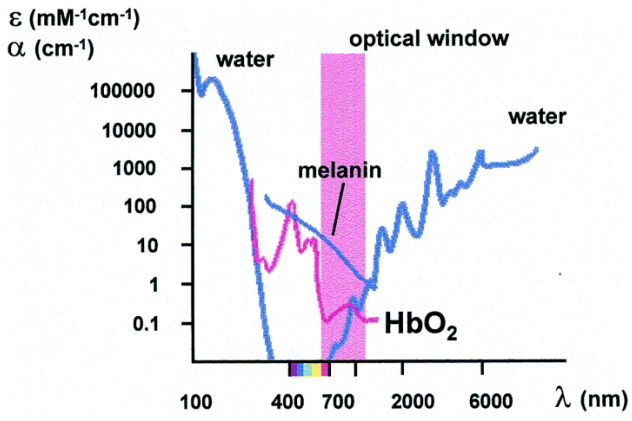

Figure 1.5 Light absorption of tissue components [61].

1.3 NOVEL LASER BEAMS IN OPTICAL TWEEZERS

The majority of optical tweezers make use of conventional TEM_{00} Gaussian beam. However, optical tweezers with more sophisticated features can be realized using a number of other beam types like the high order Hermite Gaussian beams, Laguerre-Gaussian (*LG*) beams and Bessel beams. The non-circular intensity pattern in higher order Hermite Gaussian beams have been particularly useful for rotating rod shaped or disk shaped objects like for example bacteria, red blood cells etc [30]. Optical tweezers using Bessel beams have the unique capability of trapping and rotating multiple particles that are millimeters apart and even situated in separate sample chambers [34]. *LG* beam can transfer orbital momentum to a trapped particle, inducing it to rotate around the optical axis [23, 24]. *LG* beam tweezers can also trap metallic [62] and absorptive particles [23, 62] and particles with a refractive index lower than that of the surrounding medium [63, 64]. In the following section, *LG* beams which have played an essential part in the studies presented in the thesis are discussed. The *LG* family of laser modes is introduced and their properties and generation methods using holographic techniques are described.

1.3.1 LAGUERRE-GAUSSIAN BEAM

Laguerre Gaussian beams have a spiral phase front and an integer 2π phase shift around the circumference of the beam. The phase at the centre of the beam is undefined (singularity) and results in a dark central core. Thus, the transverse intensity profile of a *LG* beam is a ring of light. These beams are usually denoted as LG_{pl} or LG_p^l, where l and p are two integer indices that describe the mode. The index l is the azimuthal index or topological charge and refers to the number of complete (2π) phase cycles around the circumference of the mode, whereas $p + 1$ gives the number of radial nodes in the mode profile. Figure 1.6 shows the wave fronts of an $l =$

0, $p = 0$ *LG* beam consisting of plane wave fronts and of an $l = 1$, $p = 0$ and $l = 3$, $p = 0$ *LG* beams with single and three intertwined helices of phase respectively.

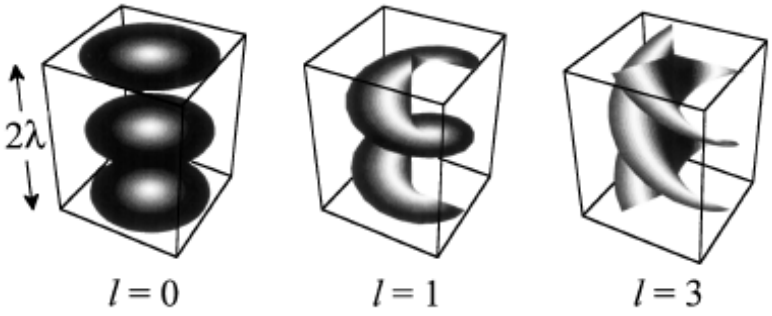

Figure 1.6 The phase fronts of *LG* modes, $l = 0$, with plane wavefronts, $l = 1$ and $l = 3$ with helical wavefronts. The phase fronts of the $l = 1$ and $l = 3$ *LG* beams are single and triple helix respectively (reprinted by permission from *Physical Review Letters* [65]).

Figure 1.7 shows intensity patterns of *LG* beams with various l and p indices. *LG* modes with $l \neq 0$ are interesting as they have an azimuthal phase variation that gives rise to the beam's spiral phase front. Since optical vortices have an inclined wavefront with respect to the optic axis and the Poynting vector, representing the energy flow, is always perpendicular to the wavefront, it has an azimuthal component, which gives rise to a well defined orbital angular momentum of $l\hbar$ per photon [66]. This is in addition to any spin angular momentum (of $\pm\hbar$ per photon) that the light may possess due to its state of polarization. These beams are also termed optical vortices [63] owing to the phase singularity present. The full mode description of a Laguerre-Gaussian beam is given by [68]

$$E(LG_p^l) \propto \exp\left[\frac{-ikr^2 z}{2(z_R^2 + z^2)}\right] \exp\left[\frac{-r^2}{w^2(z)}\right] \exp\left[-i(2p + |l| + 1)\arctan\left(\frac{z}{z_R}\right)\right] \exp[-il\phi] \times \left(\frac{r\sqrt{2}}{w(z)}\right)^{|l|} L_p^{|l|}\left(\frac{2r^2}{w^2(z)}\right) \tag{1.18}$$

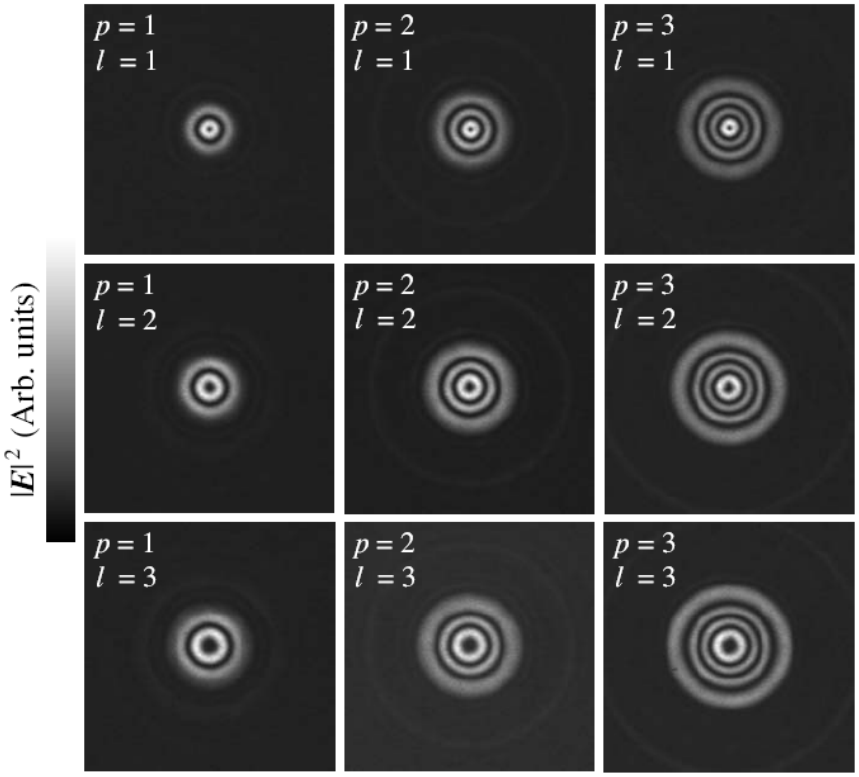

Figure 1.7 Beam profiles of *LG* beams with various *l* and *p* indices (reprinted by permission from *Journal of Optical Society of America A* [67]).

where z is the distance from the beam waist, z_R is the Rayleigh range, k is the wave number, $w(z)$ is the radius at which the Gaussian terms falls to $1/e$ of its on-axis value, r is the radial coordinate, ϕ is the azimuthal angle and $L_p^{|l|}$ is the generalized Laguerre polynomial.

1.3.2 Generation of Laguerre-Gaussian beams

Several methods exist for generating *LG* beams including the use of a spiral phase plate [69] or the direct formation of the beam inside a laser resonator [70, 71]. However, the most convenient methods are the use of a mode converter to transform a higher-order Hermite-Gaussian beam into a *LG* beam [68] and the use of holographic elements [62-64, 72-75]. The mode converter results in a pure *LG* beam but the holographic method is more versatile in a

sense that one only has to illuminate the hologram with a TEM_{00} mode and conversion efficiencies in excess of 65% are possible.

A hologram is simply a recording of a diffraction pattern between an electromagnetic field of interest and a reference field. For generation of *LG* beam we need to consider the interference pattern between a plane wave (illuminating laser beam) and the helical phase term $exp(il\phi)$ of a *LG* beam. Hence the phase modulating term defining the computer generated hologram (CGH) becomes

$$\psi(u,v) = \cos(2\pi Au - l\phi) \tag{1.19}$$

Where *u, v* are the spatial Cartesian coordinates and *1/A* is the period of the grating considering small angle of incidence between the interfering beams. The hologram pattern takes the form of a forked grating with *l* dislocations. This results in a screw phase dislocation on the beam axis that gives us the characteristic phase structure of these beams with an azimuthal index of *l*. Figure 1.8 shows the typical forked holograms used to generate *LG* beams.

It may be noted that for phase holograms discussed above, emphasis need to be made to maximize the fraction of incident laser power delivered into the useful first order. For this we note that the transmission function of a phase grating is given as [77],

$$T(u) = \exp[i2\pi MuA] \tag{1.20}$$

Where *M* is the phase stroke value and is defined as $0 \le M \le 1$. The phase shift increases linearly from a minimum value of 0 to a maximum value of $2\pi M$. The transmission function of the grating can be expanded in a Fourier series,

$$T(u) = \sum_{n=-\infty}^{\infty} T_n \exp[i2\pi MuA] \tag{1.21}$$

where

$$T_n = \exp[i(n-M)\pi]\frac{\sin[\pi(n-M)]}{\pi(n-M)} \tag{1.22}$$

We can obtain the diffraction pattern by taking Fourier transform,

$$t(x) = \sum_{n=-\infty}^{\infty} T_n \delta[x - nA] \tag{1.23}$$

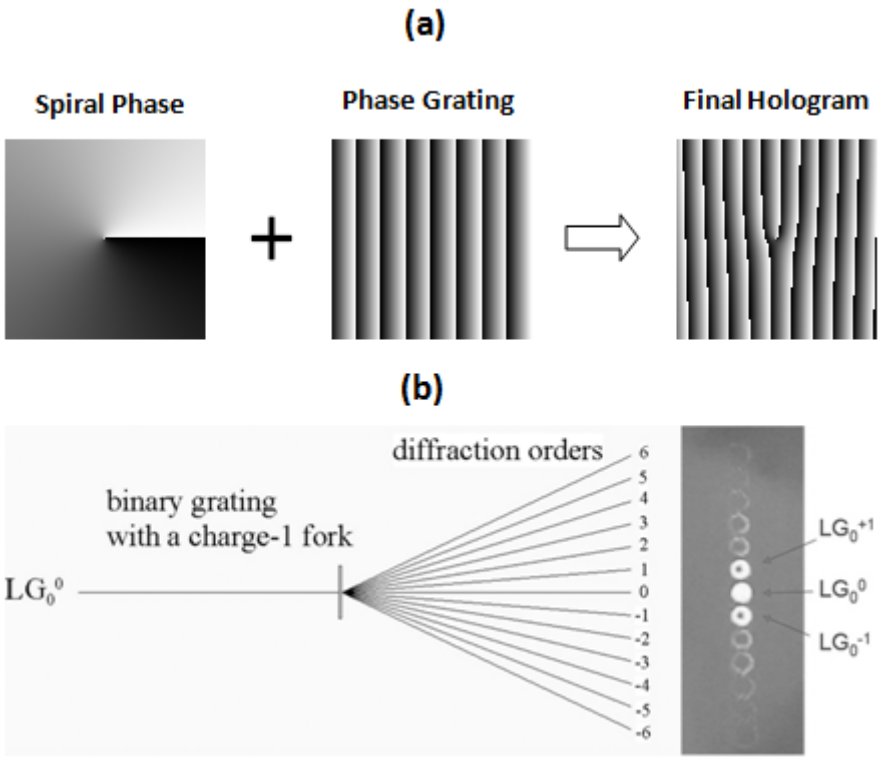

Figure 1.8 (a) Hologram used to generate optical vortices with $p = 0$ and $l = 1$ are shown. Also shown are the phase and grating holograms that are combined to give the forked hologram. Black represents a phase of zero and white represents a phase of 2π. (b) Experimental set up for generation of LG_{01} beam [76].

Therefore, the diffraction pattern consists of a series of delta functions whose amplitudes are given by the coefficients in equation 1.22. For M =1, all of the light is diffracted into the first order. This is shown schematically in figure 1.9. As the value for the parameter M decreases, the

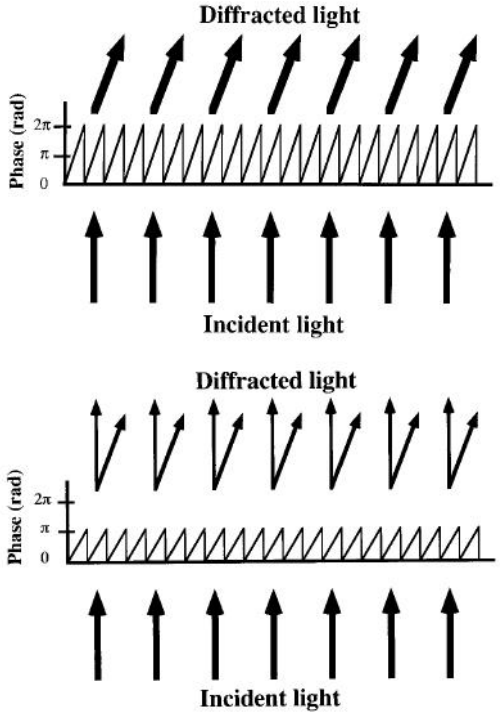

Figure 1.9 Diffraction of light by phase grating (reprinted by permission from *Applied Optics* [77]).

fraction of light diffracted into the first order decreases while the fraction of light diffracted into the zero order increases. This is shown qualitatively in figure 1.9 by the relative widths of the arrows. For holograms used in generation of *LG* beams we try to keep the modulation depth ~ 2π so that most of the optical energy can be directed into the generated *LG* beam.

Holograms can also be generated using spatial light modulators (SLMs) [78, 79]. There are various types of SLMs which act either as phase or amplitude modulators. In the following we will consider phase-only modulators as these are preferred in optical tweezers applications due to their low loss characteristics compared to their amplitude counterpart. A phase only spatial light modulator can be considered as a number of discrete pixels, each acting as a variable retarder. Each pixel consists of birefringent liquid crystals and the phase retardation value of

each pixel can be changed to sculpt any light beam which hits the SLM surface. Hence the output from the SLM can be given by:

$$A(r) = A_0(r)e^{i\psi(r)} \tag{1.24}$$

Where $A_0(r)$ is the complex amplitude of the beam incident on the SLM. The phase term, $e^{i\psi(r)}$, used to modulate the incident beam can be controlled via a computer. The generation of the hologram on the SLM is simply a matter of sending a pre-calculated image, in which the hologram phase pattern is encoded as grayscale values, from a computer to the SLM.

The SLM has a number of advantages over etched holograms. The holograms generated by the SLM do not have to be microfabricated and they can be iteratively corrected to optimize trapping. In addition, SLMs allow dynamic control on the displayed holograms so that a sequence of holograms displayed on the SLM can result in a dynamic optical trap which is not possible using an etched hologram. Current phase modulated SLMs offer zero order diffraction efficiencies (considering the unwanted diffraction effect coming from the pixellated structure of the SLM) of the order of 40 − 70%, which compares favorably with etched holograms produced lithographically.

1.4 REPRESENTATIVE APPLICATIONS OF OPTICAL TWEEZERS IN PHYSICS AND BIOLOGY

The invention of optical tweezers helped in the development of many new experimental methods in physics as well as in biology. Following the discovery of optical trapping by Arthur Ashkin and co-workers, photonic forces have been used for more than two decades to trap and manipulate non-living as well as living objects of various dimensions including atoms [80], molecules [81], organelles and cells [2, 82].

Since the laser generated forces have been found to be useful in many applications to manipulate and unravel molecular and biological processes in plant and animal systems [83, 84], optical tweezers have found the most widespread applications in biology. It has emerged as an invaluable tool in cell biological and molecular research for measuring forces exerted by molecular motors such as myosin or kinesin [84, 85], or the swimming forces of sperm [86, 87]; for studying the elastic properties of single DNA molecule [88] and cells [42], fertilization research in animal systems [89], measurement of adhesion of cell membrane [25-27] and study of chromosome movement [90] etc.

Further, the ability of optical-tweezers-based methods to orient/rotate microscopic objects can be of immense use in microfluidics as well as in biotechnology. For example, optically driven micromotors can be used for transport or mixing of fluids in microfluidic chambers or to probe viscosity of microscopic environments [91]. Novel laser beams such as *LG* beams and Bessel beams have shown to be of particular use in this area of research [33, 34]. Controlled rotation can also aid in the study of the interaction between specific regions of two different cells or even the intracellular objects or an enzyme with a substrate.

The development of holographic optical trapping [73, 79] has significantly extended the usefulness of optical tweezers. For example, affinity studies may now be performed massively in parallel, increasing throughput and improving statistics. In addition to the potential for automated construction of trapping geometries, holographic trapping has the significant capability of manipulating traps independently in three dimensions. Therefore, the technique is being effectively used to study and manipulate 2D as well as 3D colloidal crystals [92, 93]. Construction of microscopic devices using microspheres provides another example of the advantages of holographic optical trapping.

An area that has also seen rapid recent development is that of microfluidics and cell sorting. Light forces have been used to sort colloids and cells in a completely non-invasive fashion by using optical lattices [94, 95], Bessel beams [96, 97], and by light evanescent waves [98, 99]. Optical tweezers can also serve the critical purpose of driving microfluidic components [31]. The fabrication and driving of microfluidic structures, such as a peristaltic pump and a valve, microoptomechanical pumps driven by holographic optical vortex arrays [100], and optically driven micron scale tools [31] have also been demonstrated.

There also exits interests in the use of optical tweezers to investigate the fundamental properties of light such as measuring the spin and orbital angular momentum of light by the transfer of these to trapped particles [22-24], investigating coupled motion of colloids [101], testing the laws of thermodynamics [102] etc. Other uses of optical tweezers include the ability to trap and manipulate metallic and nonmetallic nanostructures [103, 104]. Further, the study of phenomena at the microscopic scale has become an important area of research since such phenomena provide an accessible testing ground for ideas about matter at the atomic scale.

1.5 THESIS OUTLINE

Optical tweezers are already finding applications in diverse areas spanning from atomic physics to biological sciences. The range of applications may further increase if some of the problems associated with the use of optical tweezers can be taken care of. For example conventional optical tweezers make use of high NA objective lens to ensure that the gradient optical force is able to overcome the axial scattering force resulting in stable trapping. However, high NA objective lenses have short working distance and the spherical aberration effect at glass-water boundary limit the axial trapping range to about 100 μm or even less. Since typical

thickness of a liquid film is larger than the available working distance in optical tweezers most of the optical tweezers applications are limited inside the bulk volume of the liquid medium. Ability to manipulate objects at the liquid-air interface is desirable as it could prove important for studies on surface colloids, cell monolayer cultured at such interface etc. One objective of the thesis was to explore ways to overcome this limitation. First approach explored was the use of low NA objective lens having a long working distance to push the object immersed in the liquid along the direction of the beam and distort the free liquid surface. It was expected that the resulting surface tension forces may help balance the scattering force and thus lead to a stable trapping of the object. The results obtained show that although the approach does succeed in trapping objects at liquid interface, the mechanisms involved in the trapping are more involved. In contrast to the expected trapping of objects at the focal point of the trap beam the objects were observed to get trapped in an annular region about the trap beam. The experimental results and their analysis reveal that apart from optical and surface tension forces, the laser induced heating of the interface and the resulting thermocapillary effect is responsible for the observed trapping of objects. Another interesting result obtained with the use of a weakly focused light beam as the trapping beam was the observation of light induced organization of microscopic particles at a glass-water boundary by "optical binding" action that is similar to the formation of matter by electronic interaction. More recently our studies using *LG* beams have shown that for a given NA objective lens the use of trap beam in *LG* mode can produce larger axial trapping range compared to that available with TEM_{00} mode beam due to reduced spherical aberration effect for the former. Using *LG* trap beam we could trape and transport Colo-205 cells from the bottom to the top surface of a fluid film (thickness ~ 200 μm), and monitor the changes in oxygen diffusion rate in its plasma membrane. Another interesting finding was that a change in topological charge

(azimuthal index) of the *LG* mode, which results in a change in the size of its annular intensity region, could be used for three dimensional orientation of trapped red blood cells (RBCs) with respect to the trap beam axis.

Another area of concern while using optical tweezers for manipulation of biological cells, is the possibility of photoinduced adverse effects on the trapped cells. Because of the much-reduced absorption by cells in the near infrared (NIR) spectral range (700–1100 nm), lasers operating in this spectral range are preferred for manipulation of cells. However, due to the large intensity (a few $MW.cm^{-2}$ or higher) at the trap focus even with the use of lasers in the NIR spectral range, the possibility of adverse effects on the cells being manipulated is a matter of concern. Indeed adverse effects like a decrease in cloning efficiency and DNA damage have been reported in cells exposed to NIR optical trapping beam. In this respect the use of trap beam in *LG* laser mode may offer some advantage because for a given power the annular spatial intensity distribution of this mode leads to higher trapping efficiency along with a lower peak intensity compared to the usual Gaussian mode. We have therefore explored the use of *LG* beams for manipulation of spermatozoa. As expected our results confirm that for a given trap power *LG* modes can provide better trapping efficiency and significantly lower adverse effects compared to conventional TEM_{00} trapping mode.

Optical tweezers are also being used for spectroscopic studies on single cells, which helps account for the problem of heterogeneity present in bulk cell samples. In particular Raman spectroscopy is receiving considerable current interest for studies of the chemical composition and conformation of macromolecules in individual cells since this technique avoids the necessity of any exogenous stain. However, due to the inherent weak nature of the Raman signal, a long acquisition time, often tens of seconds to few minutes, is required to acquire spectra with a good

signal to noise ratio. The cell should therefore be immobilized. But the physical or chemical methods used for immobilization of cells in micro-Raman technique often lead to undesirable surface-induced effects on the cells or lead to strong background spectra originating from the substrate. The use of optical tweezers to immobilize cell without direct contact helps to avoid these problems and therefore Raman optical tweezers or a setup facilitating acquisition of Raman spectra from an optically trapped cell, are receiving much attention. In particular the use of NIR radiation for Raman studies is gaining rapid interest due to much reduced fluorescence background that often obscures the small but important Raman bands. Raman optical tweezers have already been utilized for several interesting studies such as monitoring the real-time heat denaturation of yeast cells, the transition from the oxygenated to deoxygenated condition of a RBC on application of mechanical stress, sorting and identification of microorganisms etc. Raman optical tweezers are being extensively used for studying RBCs since Raman spectroscopy is a powerful technique to monitor the oxygen carrying capacity of RBCs because the binding or the dissociation of oxygen with heme leads to significant conformational changes of hemoglobin that can be sensitively monitored by this technique. In the last part of the thesis we describe the development of a Raman optical tweezers and its use for studies on single optically trapped RBC obtained from blood samples of healthy volunteers and malaria patients.

CHAPTER 2

DEVELOPMENT AND CHARACTERIZATION OF OPTICAL TRAPPING SET-UP

The construction of optical trapping set-ups and the methods used for characterization of optical traps are described in this chapter. In section 2.1, the basic optical tweezers set-up is described. Thereafter, a brief discussions on the major components used in optical tweezers set-ups are presented. Important consideration for coupling of laser beam into the microscope objective lens as well as method for measuring laser power at the focus of a high NA objective lens is also discussed. Methods for precision position detection of trapped particles either using quadrant photodiodes or analysis of image data are also described. In section 2.3 generation of Laguerre-Gaussian beam and basic details of spatial light modulators used for this purpose are presented. In section 2.4 and 2.5 the set-ups used in the experiments described in chapter three to seven of this thesis are described. Lastly, in section 2.6 methods for measurement of trapping force and characterization of optical traps are discussed.

2.1 BASIC OPTICAL TWEEZERS SET-UP

Figure 2.1 shows a schematic of the basic optical tweezers set-up developed in our laboratory. The output of a 1064 nm, 4 watt, continuous wave (cw) diode pumped solid state (DPSS) Nd: YVO_4 laser (Compass 1064-4000, Coherent Inc.) operating in fundamental Gaussian mode are expanded using a beam expander and coupled to the objective of an inverted microscope

(Axiovert 135TV, Carl Zeiss) through its bottom port via a vertically folding dichroic mirror so that the brightfield and fluorescence imaging capabilities of the microscope are retained.

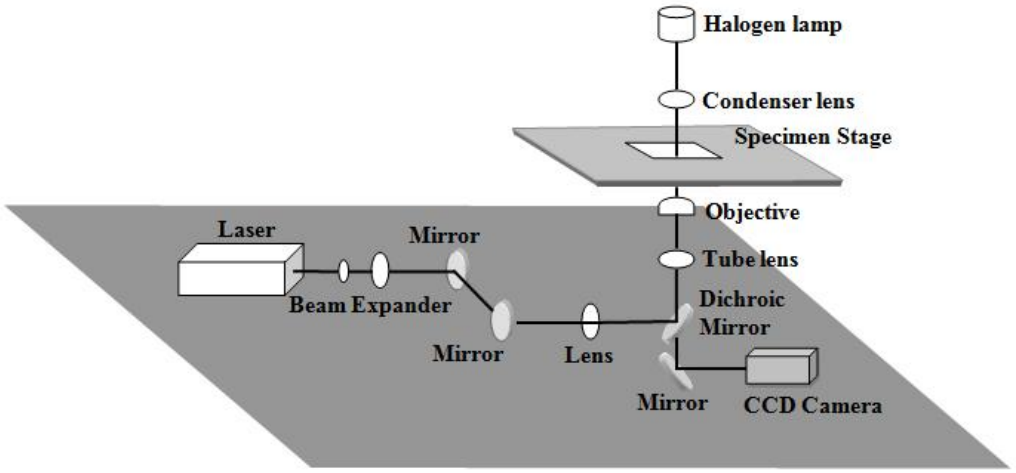

Figure 2.1 Basic optical tweezers set-up

The laser beam was expanded (3x) using two convex lenses of appropriate focal lengths resulting in beam diameter of ~ 6 mm. The beam size slightly overfills the entrance pupil of the 100X, NA 1.3 objective lens (Zeiss Plan-neofluar) used to focus the laser beam. Another convex lens (f = 150 mm) was placed into the optical path of the beam external to the microscope. This lens along with the tube lens of the microscope behaves as nearly a 1:1 telescope and thus a collimated beam is sent to the entrance pupil of the microscope objective lens.

The two beam steering mirrors placed after the beam expander are used to align the laser beam to get axially coupled onto the entrance pupil of the objective lens. The dichroic mirror shown in figure 2.1 reflects above ~ 850 nm and therefore reflects the trapping beam while transmits the visible light to the CCD camera for brightfield imaging of the sample. When required a laser line cut-off filter is placed before the CCD camera to suppress the back reflected laser light to fall on the CCD.

For some experiments a 532 nm, 5W cw DPSS Nd: YVO_4 laser (Verdi-5, Coherent, USA) beam was coupled along the same light path to the microscope. For coupling the 532 nm laser beam we used a dichroic mirror that selectively reflects the 520-540 nm spectral region and transmits rest of the light spectrum in the visible region.

2.2 DESIGN CONSIDERATIONS

The essential elements for developing an optical tweezers set-up are a laser source, beam expansion and steering optics, a high NA objective lens, a trapping chamber holder, and some means of observing the trapped specimen i.e an illumination source and a CCD camera. Optical traps are most often built by modifying an inverted microscope so that a laser beam can be introduced into the optical path before the objective, the microscope then provides the imaging, trapping chamber manipulation, and objective focus functions in a single platform. We consider each of these elements in detail.

2.2.1 TRAPPING LASER

It is important that the particle to be trapped be transparent to the laser light as absorption of the light can result in heating and therefore optical damage of the tweezed sample. For biological objects there is a window of relative transparency in the near infrared portion of the spectrum, 700–1300 nm, located in the region between the absorption of proteins in the visible and the increasing absorption of water towards the infrared. The least damaging wavelength for biological cells is believed to be 970 nm, followed closely by 830 nm [105]. Damage is significant at trapping wavelengths of 870 nm and also at 930 nm [105]. Therefore, lasers commonly used for optical tweezing include the Nd: YAG (neodymium: yttrium-aluminium-garnet) at 1064 nm, Nd: YLF (neodymium: yttrium-lithium-fluoride) at 1047 nm and Nd :YVO_4

(neodymium: yttrium-vanadate) also at 1064 nm. The Ti: Al_2O_3 (titanium sapphire) laser delivers high power ~ 1 W over a large portion of the near infrared spectrum, 750–950 nm, but these lasers are the most expensive option. Diode lasers, available at different wavelengths in the 700-1300 nm region, offer a low-cost alternative in a compact package. But these devices are typically limited to less than a few hundreds mW of power, in TEM_{00} mode, the mode required for efficient trapping. Diode lasers also suffer significantly from mode instabilities and noncircular beams, which necessitates precise temperature control instrumentation and additional corrective optics. A single focused laser beam can just trap a particle using few mW of power, but in general traps use from around 10 mW to 1 W of optical power. For optical trapping of biological particles a cw laser is preferred as pulsed lasers may damage specimens due to their high peak powers. The intensity at an one micron diameter diffraction limited spot of a typical cw trapping laser operating at around 100 mW is 10^7 W/cm^2, where as for mode locked and Q switched lasers, very high intensities in the order of GW/cm^2 are generated. Proposed mechanisms for photodamage include transient local heating [106, 107], two-photon absorption [107, 108] and photochemical processes leading to the creation of reactive chemical species [109].

Another important factor to consider when using optical tweezers is the profile of the laser beam. TEM_{00} mode Gaussian beams are the most commonly used in optical tweezers systems since the mode can be focused to the smallest diameter beam waist and will therefore produce the most efficient trap. The laser beam should have excellent pointing stability and low power fluctuations. Pointing instabilities lead to unwanted displacements of the optical trap position in the specimen plane, whereas power fluctuations lead to temporal variations in the optical trap stiffness. Pointing instability can be remedied by coupling the trapping laser to the

optical trap via an optical fiber. The solution however, results in a tradeoff between the pointing stability and amplitude fluctuations, as the fiber coupling depend on beam pointing. The choice for a suitable trapping laser therefore depends on several interdependent factors like wavelength, power, mode quality, pointing stability, power stability etc.

2.2.2 MICROSCOPE

Most optical traps are built around a conventional light microscope. This approach reduces the construction of an optical trap to that of coupling the light beam from a suitable trapping laser into the optical path before the objective without compromising the original imaging capabilities of the microscope. In practice, this is most often achieved by inserting a dichroic mirror, which reflects the trapping laser light into the optical path of the microscope but transmits the light used for microscope illumination. Inverted, rather than upright, microscopes are often preferred for optical trapping because in an upright microscope based setup the light scattering force and gravity both work against the gradient force but in an inverted optical tweezers the laser beam is focused upward onto the particles, so that the scattering force and gravity are opposed. As a result it is easier to achieve three-dimensional gradient force trapping in an inverted optical tweezers. Further, inverted microscopes are safer to use with laser tweezers because the laser beam comes in below eye level. The use of a conventional microscope also makes it easier to use a variety of available imaging modalities, such as differential interference contrast and epifluorescence.

An alternative to the redesign and retrofitting of a commercial microscope is to build the entire optical trap from individual optical components [110-112]. This approach is more involved since the imaging and trapping light paths have to be designed and built using suitable

components. The increase in complexity, however, can be offset by increased flexibility in the design and a wider choice of components, greater access to the optical paths, and reduced cost.

2.2.3 OBJECTIVE LENS

The single most important element of an optical trap is the objective lens used to focus the trapping laser. The choice of objective determines the overall efficiency of the optical trapping system (stiffness versus input power), which is a function of both the NA and the transmittance of the objective. Additionally, the working distance and the immersion medium of the objective (oil, water or glycerol) will set practical limits on the depth to which objects can be trapped. Spherical aberrations, which degrade trap performance, are proportional to the refractive index mismatch between the immersion medium and the aqueous trapping medium. The deleterious effect of these aberrations increases with trapping depth inside the aqueous medium. The working distance of most high NA oil immersion objectives is quite short (~200 μm) and the large refractive index mismatch between the immersion oil (refractive index~1.51) and the aqueous trapping medium (refractive index ~1.32) leads to significant spherical aberrations [113-115]. In practice, this limits the maximum axial range of the optical trap to less than 100 μm from the bottom cover glass surface of the trapping chamber. Trapping deeper into solution can be achieved with water immersion objectives that minimize spherical aberration. A high NA objective (typically > 1) is required to produce an intensity gradient sufficient to overcome the scattering force and produce a stable optical trap. To sharply focus the trapping beam the full NA of the objective should be effectively used and therefore the laser beam should be expanded to fill the objective rear aperture. As indicated in the figure 2.2, an expanded beam yields a larger cone angle and therefore a stronger intensity gradient at the focus. To further optimize the

trapping quality with a Gaussian profile beam, the beam should overfill the back aperture of the objective lens. This increases the intensity of the highly convergent rays coming from the edge of the aperture compared to when the aperture is just filled. These convergent rays contribute largely to axial gradient force, enabling it to overcome the axial scattering force [56].

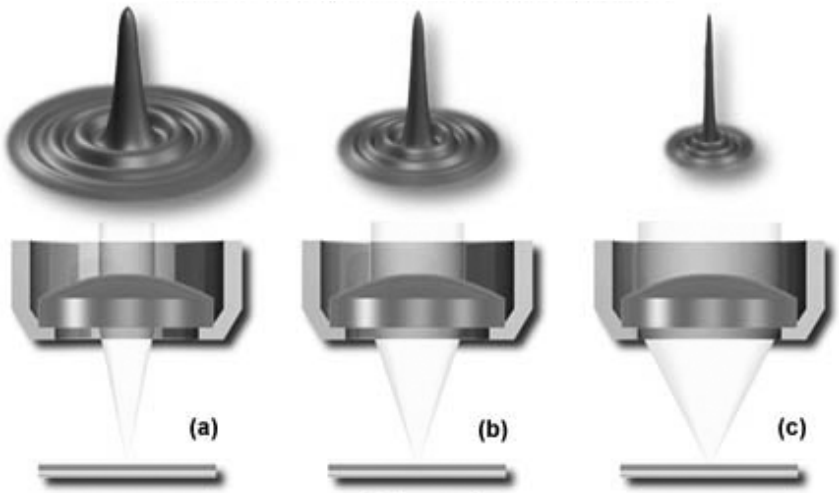

Figure 2.2 Focusing of laser beam with a high NA objective lens. (a)-(c) Tight focus spot formed with increasing input beam size. The focus spot size can be approximately estimated as $1.22\lambda f/D$, where λ is the wavelength of light, f is the focal length of the objective lens and D is the diameter of the input beam. [115]

The vast majority of high NA objectives are complex, multi-element optical assemblies specifically designed for imaging visible light, not for focusing an infrared laser beam. For this reason, the optical properties of different objectives can vary widely over the near infrared region. Therefore, given the wide variation in transmission characteristics for different objectives, an objective being considered for optical trapping should be characterized at the wavelength of the trapping light. To measure the effective transmission of a high NA objective accurately, the dual objective method is preferred [116, 117], in which two identical, matched objectives are used to focus and then recollimate the laser beam (the transmission of a single objective is the square root of the transmission for the objective pair).

2.2.3.1 MEASUREMENT OF POWER AT OBJECTIVE FOCUS

Figure 2.3 schematizes the dual objective method [116]. In this method, two identical and opposite-facing microscope objectives first focus and then recollimate the incident beam into an optical power meter. This method eliminates total internal reflection errors that are encountered in a direct objective-to-power meter measurement in air. In the dual objective method, the transmission through a single microscope objective is then the square root of the measured transmittance.

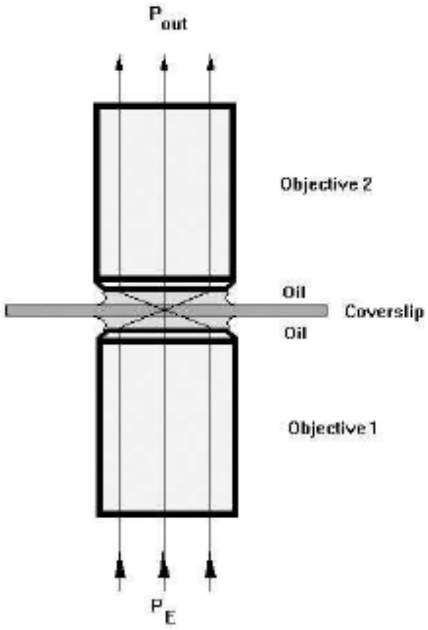

Figure 2.3 Experimental arrangements for dual objectives method (reprinted by permission from *Applied Optics* [116]).

On top of the microscope stage, with the inverted objective below, is mounted a second, identical objective, in the upright position. P_E is the power at the entrance of the inverted objective, and P_{out} is the power transmitted by the compound system. The transmittance is assumed the same for both objectives. The objectives are positioned using three axes stages and

the microscope stage in order to get a collimated beam emerging from the second objective, coaxial with the beam entering the first objective.

The transmission factor (T_{obj}) for the objective is measured as,

$$P_{out} / P_E = (T_{obj})^2 \tag{2.1}$$

It is important to note here that P_E should be measured as the power passing through the entrance pupil of the first objective lens which can be done using an aperture identical to the entrance pupil of the objective in the laser beam path.

2.2.4 POSITION DETECTION OF THE TRAPPED PARTICLE

Sensitive position detection lies at the heart of quantitative optical trapping. Although position tracking of irregularly shaped objects is feasible, precise position and force calibration are currently only practical with spherical objects. Microscopic beads are either used alone, or attached to non-spherical objects of interest as "handles," to apply calibrated forces.

2.2.4.1 PHOTODIODE ARRAY BASED POSITION DETECTION

Several photodiode array based methods have been developed that offer precise, high-bandwidth position detection of trapped objects. The most common of these is to image directly the trapped object onto a quadrant photodiode (QPD) [118, 119]. The diode quadrants are then summed pair wise, and differential signals are derived from the pairs for both x and y dimensions. If desired, the differential signals can be normalized by the sum signal from the four quadrants to reduce the dependence of the output on the total light intensity.

The detector outputs are given as,

$$V_1 = \frac{(a+b)-(c+d)}{a+b+c+d} \qquad V_2 = \frac{(a+d)-(b+c)}{a+b+c+d} \tag{2.2}$$

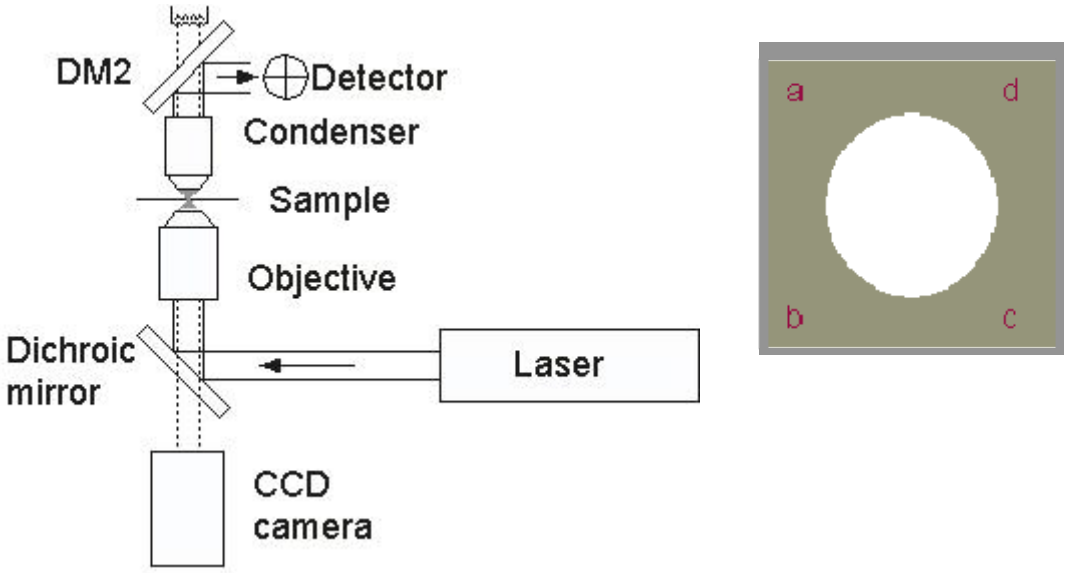

Figure 2.4 Position detection of trapped particles using quadrant photodiodes. Left: the experimental arrangement. DM2 is the dichroic mirror used to direct the forward scattered laser light onto the QPD (reprinted by permission from *Journal of Optical Society of America B* [120]). Right: Laser spot on the quadrant photodiode.

Therefore the position co ordinates can be estimated as,

$$x=\beta_1 V_1 \quad \text{and} \quad y=\beta_2 V_2 \tag{2.3}$$

where β_1 and β_2 are the position detector conversion factors (PCDF). PCDFs should be determined from known values of x and y. The technique can typically yield precision of a fraction of nm under 100x magnification.

Also the same laser beam can be used for both trapping and position detection. Laser-based detection requires the incorporation of a dichroic mirror on the condenser side of the microscope to couple out the laser light scattered by the specimen. Two different laser-based position detection schemes have been developed. The first relies on polarization interferometry [121,122]. This method is quite analogous to differential interference contrast (DIC) microscopy, and it relies on the DIC imaging components within the microscope. Incoming plane polarized

laser light is split by a Wollaston prism into two orthogonal polarizations that are physically displaced from one another. After passing through the specimen plane, the beams are recombined in a second Wollaston prism and the polarization state of the recombined light is measured. A simple polarimeter consists of a quarter wave plate (adjusted so that plane polarized light is transformed into circularly polarized light) followed by a polarizing beam splitter. The intensity in each branch of the beam splitter is recorded by a photodiode, and the normalized differential diode signal supplies the polarization state of the light. A bead centered in the trap introduces an equal phase delay in both beams, and the recombined light is therefore plane polarized. When the bead is displaced from its equilibrium position, it introduces a relative phase delay between the two beams, leading to a slight elliptical polarization after the beams are recombined. The ellipticity of the recombined light can be calibrated against physical displacement by moving a bead a known distance through the optical trap. This technique is intrinsically aligned because the trapping and detection laser beams are the same. Limitation of this technique is that it is one dimensional. It is sensitive to displacement along the Wollaston shear axis and therefore provides position detection in a single lateral direction.

A second type of laser-based position detection scheme - back focal plane detection - relies on the interference between forward-scattered light from the bead and the unscattered light [123-125]. The interference signal is monitored with a QPD positioned along the optical axis at a plane conjugate to the back focal plane of the condenser (rather than at an imaging plane conjugate to the specimen). The light pattern impinging on the QPD is then converted to a normalized differential output in both lateral dimensions as described above. By imaging the back focal plane of the condenser, the position signal becomes insensitive to absolute bead position in the specimen plane, and sensitive instead to the relative displacement of the bead

from the laser beam axis. As with the polarization interferometer, the detection beam and the optical trap are intrinsically aligned, however the QPD detection scheme has an advantage that it can provide position information in both lateral dimensions.

2.2.4.2 VIDEO BASED POSITION DETECTION

For simple imaging of a trapped particle, a video camera mounted to the camera port of the microscope (or elsewhere) often suffices. By digitally processing the signal acquired from the camera, and knowing the size subtended by a single pixel (e.g., by calibrating the video picture against a distance standard like ruled calibration glass slide), the position of a trapped object can be determined with subpixel accuracy (typically, to within 5 nm or better), using centroid-finding algorithms [126-129]. This approach is restricted to video acquisition rates (typically, 25 - 120 Hz). The discrepancy between the low video bandwidth (~100 Hz) and the much higher intrinsic bandwidth of a typical optical trap (~kHz) results in aliasing artifacts, and these preclude the implementation of some of the calibration methods.

The temporal resolution could be improved through the use of high speed video cameras [130, 131]. The sensitivity of high-speed video tracking is ultimately limited by the number of recorded photons (since shorter exposures require more illumination), so spatial resolution decreases as the frame rate increases. Generally speaking, the signal-to-noise ratio is expected to decrease as the square root of the frame rate. A brief description on the cross correlation analysis based video tracking scheme [126] is presented below.

Evaluation of cross-correlation function between image and object of interest has been utilized for high precision position measurement of the object of interest. Position resolution as low as ~ 1-2 nm has been reported earlier with this method [126]. If cross-correlation functions

are evaluated between objects of interest present in the image and the total image-field, peaks are obtained at places where the object intensity distribution matches closely to the local intensity distribution pattern. If the segment (kernel) of the complete video image (*I (x,y)*) containing the bead is denoted as *K(x,y)*, the cross-correlation function can be expressed as,

$$C(x,y) = \sum_{i=-\alpha/2}^{\alpha/2} \sum_{j=-\beta/2}^{\beta/2} \{I(x+i, y+j) - s1\} \{K(i,j) - s2\} \tag{2.4}$$

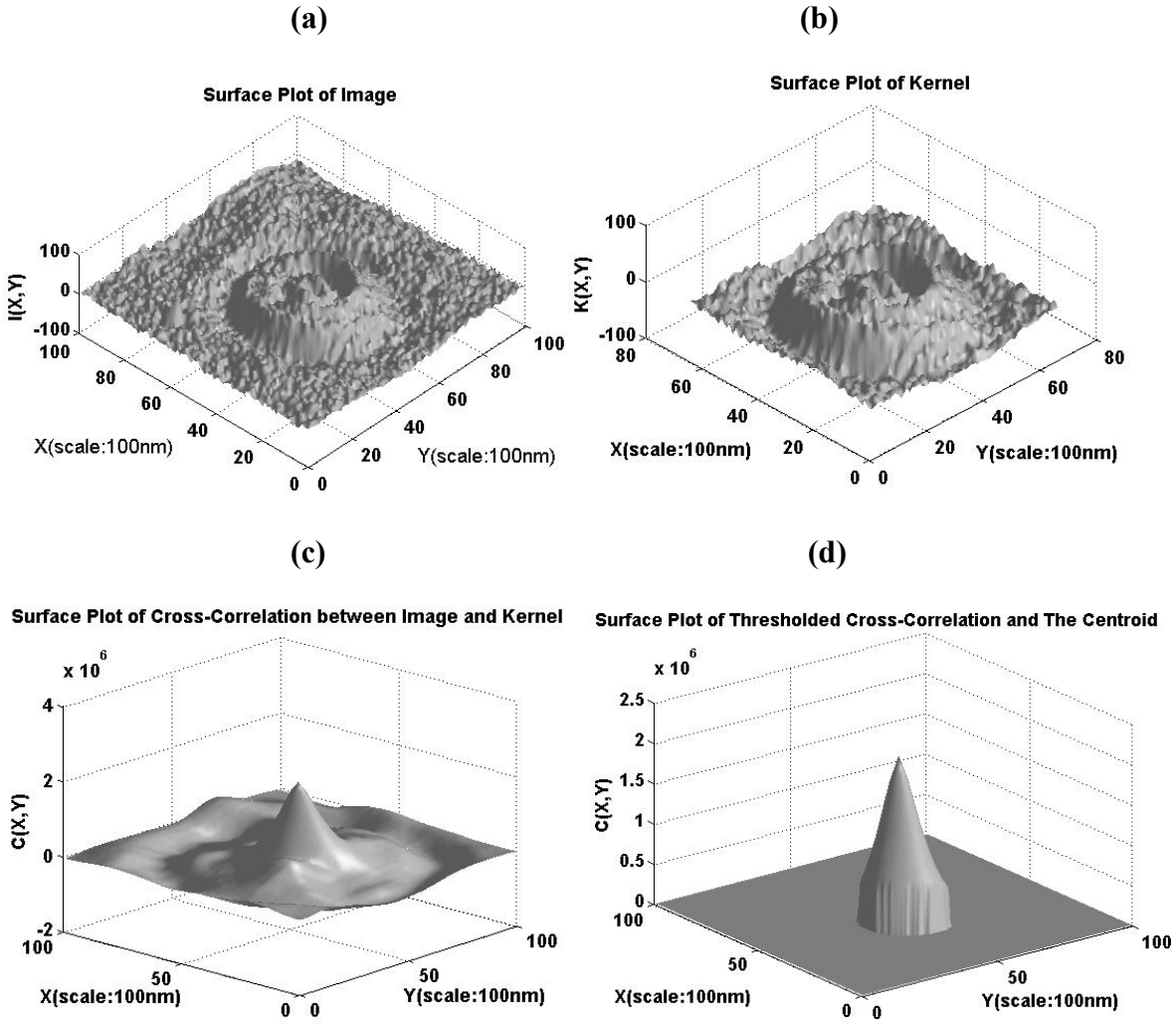

Figure 2.5 (a) Surface plot of the image of a 2 μm diameter polystyrene bead. (b) The kernel. (c) Surface plot of the cross-correlation function. (d) The single cross-correlation peak at the bead position obtained after thresholding.

The x and y dimensions of the kernel are denoted as α and β respectively and *s1* and *s2* are the average intensity values for the image and kernel respectively. *C(x,y)* contains one primary peak corresponding to the object of interest with additional peaks depending on the nature of intensity distribution present in the image. The primary peak value is well above the other peaks so that other non-significant peaks can be eliminated from *C(x,y)* by simple thresholding technique. As a result we are left with cross-correlation function containing single prominent peak giving positional information of the object of interest. The standard centroid estimation formula are given as,

$$x_c = \frac{\sum xC(x,y)}{\sum C(x,y)} \quad \text{and} \quad y_c = \frac{\sum yC(x,y)}{\sum C(x,y)} \tag{2.5}$$

where *C(x,y)* is the intensity distribution representing the images containing the segmented bead. Determination of central point of the peak gives position measurement of the object with very high (typically few nm) resolution. But it is important to note that the position information thus obtained normally indicate the central point of the intensity distribution representing the object and does not necessarily indicate the position of centroid of asymmetric objects.

2.2.4.3 AXIAL POSITION DETECTION

The position detection methods described above are to measure lateral displacement of objects within the specimen plane, a major focus of most optical trapping work. Axial motion can be determined by: measuring the intensity of scattered laser light on an overfilled photodiode [132, 133]; through two-photon fluorescence generated by the trapping laser [134]; and by evanescent-wave fluorescence at the surface of a cover glass [135, 136]. Although these various approaches all provide a signal related to axial position, they require the integration of additional detectors

and, in some cases, fluorescence capability, into the optical trapping instrument. This can be somewhat cumbersome; consequently the techniques have not been widely adopted.

Image correlation analysis can also be useful for axial position detection as the appearance of a trapped bead changes as it moves out axially from the trap focus [137, 138]. The axial position of a trapped particle can also be determined from the method based on Shannon's information entropy [139]. Information entropy of an image is a parameter, which is related to the randomness of the image intensity distribution. When bead is at different axial positions the value of the information entropy of the bead image will be different. Information entropy will be maximum for an image, which is completely random and will be zero for an image with completely even intensity distribution. Physical explanation for this observation can be stated as follows: If the bead is imaged with the same objective, which is used to focus the laser beam to create trap, when the bead is exactly at the center of the trap, image will be exactly at the focus of the objective and it is expected to get the maximum sharp image at this point. As the bead move away from focus axially, there will be a blurring of the image of the bead due to de-focusing. Bao *et al* reported that this increase in information entropy is linear to the axial displacement with minimum value at center. This linear relationship was shown to hold true for a displacement range of ~ 200 nm with a resolution of 10 nm for bead size of 2 μm [139].

Another interesting approach for estimation of axial positions of trapped objects is to apply principal components analysis (PCA) on the recorded CCD images [140]. The basic idea behind this approach is to use PCA to calculate the most meaningful *basis* (here the axial displacements of the trapped bead) to re-express the original image data set containing several other unwanted information. The approach could be successfully used to classify the position of 2 μm bead with a precision of ≤10 nm over a range of ± 300 nm from the trap focus [140].

2.2.5 PIEZOELECTRIC STAGE

A Piezoelectric stage is often used for precise position control or applying controlled motion to the sample chamber in an optical tweezers set up [141]. Stable, linear, reproducible, ultrafine positioning in three dimensions is now achievable with the current generation of piezo stages. Though a piezo drive can easily produce sample movement with sub nanometer resolution it exhibits a non linear and hysteric curve of applied voltage vs position. Therefore, stages include position sensors that provide the feedback necessary for an analog to digital servo controller to eliminate hysteresis and non linearity. For use on piezo microscope stages capacitive sensors are very popular and composed of two plates of exquisite flatness, one affixed to the moving platform and one to the stationary frame of the stage for each axis. As the platform moves it changes the gap between the plates, which changes the electrical capacitance of the cavity.

Piezo stages permit three-dimensional control of the position of the trap relative to the trapping chamber. The ability to move precisely in the axial dimension, in particular, permits characterization of the longitudinal properties of the optical trap and can be used to eliminate the creep and backlash typically associated with the mechanical (gear based) focusing mechanism of the microscope. Further, a piezoelectric stage can be incorporated into a force feedback loop, permitting constant-force records of essentially arbitrary displacement, ultimately limited by the stage travel (~100 μm) distance [142, 143]. Stage-based force-feedback permits clamping not only the transverse force, but also the axial force, and hence the polar angle through which the force is applied. But, these stages are comparatively expensive and communication with the stage controller can be slower than other methods of dynamically controlling trap position (e.g., acousto optic deflectors etc).

2.2.6 VIBRATION ISOLATION

To achieve the greatest possible sensitivity, stability, and signal-to-noise ratio in optical trapping experiments, the environment in which the optical trapping is performed must be carefully controlled. Mechanical vibrations typically arise from heavy building equipments, e.g., compressors or pumps operating nearby, or from passing trucks on a roadway. Air currents can induce low-frequency mechanical vibrations and also various optical perturbations (e.g., beam deflections from gradients in refractive index produced by density fluctuations in the convected air, or light scattering by airborne dust particles), particularly near optical planes where the laser is focused.

The amount of effort and resources dedicated to reducing ambient sources of noise should be commensurate with the desired precision of the measurements. The vast majority of optical trapping instruments have been built on top of passive air tables that offer mechanical isolation (typically, ~20 dB) at frequencies above ~ 2–10 Hz. For rejection of lower frequencies, actively controlled air tables are now commercially available. Acoustic noise isolation can be achieved by ensuring that all optical mounts are mechanically rigid, and placing these as close to the optical table as feasible, thereby reducing resonance and vibration. Use of metal or plastic enclosures for the complete set-up further improves both mechanical and optical stability by reducing ambient air currents. Both acoustical and mechanical vibration can be reduced by isolating the optical trapping instrument from noisy power supplies and heat sources.

2.3 GENERATION OF LAGUERRE-GAUSSIAN BEAMS FOR USE IN OPTICAL TRAPPING

In section 1.3.2 of chapter 1 different methods for generation of *LG* beams have been already outlined and the basic principles for the method of generation of these modes using computer generated holograms have been discussed. Here we describe the implementation of holographic methods for generation of the Laguerre Gaussian beams.

2.3.1 COMPUTER GENERATED HOLOGRAMS

Computer Generated Holography (CGH) is the method of digitally generating holographic interference patterns. An interference pattern is created by computer simulating the interference between a plane reference wave and the desired *LG* beam profile. This generated phase variation pattern is encoded in grayscale and termed as Kinoform. An interference pattern between a plane wave and optical vortex having l (=1) dislocations is shown in figure 2.6.

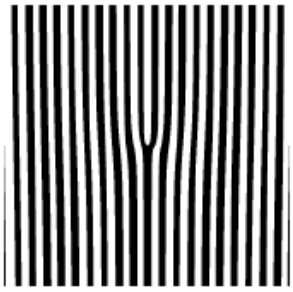

Figure 2.6 Interference pattern between a plane wave and *LG* beam.

This phase pattern is then transferred to a diffractive optical element which may often be a holographic glass plate or programmable liquid crystal spatial light modulator. When it is illuminated with the same plane wave then the optical vortex is created (please see appendix B

for conversion efficiencies measured for different orders of *LG* beams used in the experiments described in this thesis).

2.3.2 HOLOGRAPHIC GLASS PLATES

Holographic glass plate [144, 145] is a glass plate with a gelatine layer on one surface. This layer contains grains (size of order of tens of nanometer) of photosensitive silver bromide crystal which darkens when it is exposed to light. During development, the exposed crystals are chemically reduced to metallic silver to form dark fringes producing the amplitude hologram. For getting high efficiency, an amplitude hologram is converted to phase hologram by bleaching. Finally, the hologram is made permanent by fixing and drying with warm air.

2.3.3 LIQUID CRYSTAL SPATYIAL LIGHT MODULATOR (LCSLM)

A spatial light modulator can be considered as a number of discrete pixels each acting as a variable waveplate. There are various types of LCSLMs which act either as phase or amplitude modulators. In the following we will consider a phase-only modulators as these are preferred in optical trapping applications due to their low loss characteristics compared to their amplitude counterpart. The spatial light modulator (SLM) can encode an input light beam with a phase such that it produces the desired light pattern. Hence the output from the SLM can be given by:

$$A(r) = A_0(r)e^{i\psi(r)} \tag{2.6}$$

where $A_0(r)$ is the complex amplitude of the beam incident on the SLM. The phase term that we modulate the incident beam with, $e^{i\psi(r)}$ can be calculated using computer programs. Such an implementation of an SLM can be used to realize a very powerful tool for the dynamic control of complex light potentials. The generation of the hologram on the SLM is done by sending a pre-calculated image (the hologram pattern) from a computer to the SLM. Current phase modulated SLMs offer zero order diffraction efficiencies (considering the unwanted diffraction effect

coming from the pixellated structure of the SLM) of the order of 40 − 70%, which compares favorably with etched holograms produced lithographically.

There are primarily two types of liquid crystal devices (LCD) namely the neamtic LCD and ferroelectric LCD. The ferroelectric LCD can operate at frame rates exceeding ten kilohertz [146], but have poor phase modulation properties. The nematic SLM devices run at the rate of ~ 60 Hz, limited by the properties of the nematic liquid crystal material but comes with good phase modulation properties [147]. Since for optical trapping applications phase holograms are almost always preferred due to their low insertion loss characteristics, here we will discuss the nematic LCD.

2.3.3.1 BASIC PHYSICAL PROPERTIES OF PARALLEL ALIGNED NEMATIC LIQUID CRYSTAL

Nematic liquid crystals are dielectric anisotropic liquids which exhibit a low temperature phase with elongated molecules aligned in one direction with position disorder. This orientation order gives nematic liquid crystals the optical properties of a uniaxial crystal. The direction of the molecules is called the director of the liquid crystals. The positive and negative direction of the director is indistinguishable. Light propagating through such a liquid with its polarization parallel to the molecular direction encounters an extraordinary refractive index, but if its polarization is perpendicular to the molecular direction, it encounters a different refractive index called the ordinary index [148].

Due to their unusual optical properties, nematic liquid crystals can be used to make variable, controllable refractive index devices. Such a device is made by filling the gap between

two parallel glass plates with the liquid crystal material. The two glass plates are coated on the inside with transparent electrodes so that the device can be driven electrically. The inner surfaces of the liquid crystal cell are rubbed with a certain orientation so that the molecules align themselves with the surface microgrooves and parallel to each other. When an electric field of sufficient strength is applied to the electrodes of the liquid crystal device, the molecules away from the surfaces tend to realign in the direction of the applied field. If the applied field is in a normal direction to the surfaces of the device, the molecules away from the surfaces tend to tilt away from the initial orientation. This tilt angle of the molecules depends on the strength of the applied field and the distance of the molecules from the surface. When no field is applied, the equilibrium organization of the molecules is parallel to the surfaces of the cell, shown in figure 2.7 (a). When an electric field above certain strength (critical field) is applied, the molecules start to tilt away from the surface as shown in figure 2.7 (b). When the applied field becomes strong enough (usually several times stronger than the critical field) all molecules tilt to 90°, that is, normal to the surfaces, except those next to the surfaces, as shown in figure 2.7 (c).

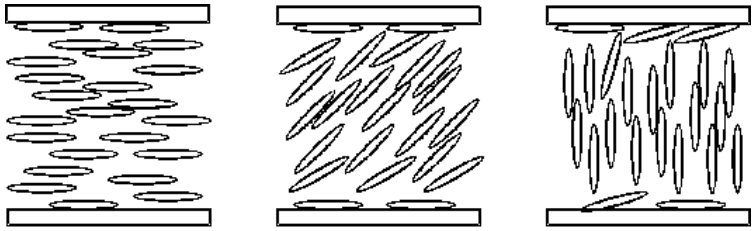

Figure 2.7 Molecule orientation in a liquid crystal device: (a) at equilibrium with no field, (b) with a field slightly larger than the critical field, (c) at equilibrium with a strong field [149].

To understand the phase modulating properties of SLM let us consider when the incoming electric field is parallel to the director, it sees an extra-ordinary refractive index all through the liquid crystal material, if the applied field is zero. But with an increasing applied

field the change of tilt of molecules changes the refractive index from extraordinary to ordinary as the tilt varies from 0° to 90°. Therefore, the phase of the propagating wave can be modulated by changing the applied voltage across the electrodes. Using a pixellated electrode structure one can effect varying phase retardation across the wavefront of the incident laser beam.

2.3.3.2 BASIC PHYSICAL PROPERTIES OF TWISTED NEMATIC LIQUID CRYSTALS

In the twisted nematic LCD the two rubbed orientations of the two inner surfaces are at different angles. The angular separation (twist angle) causes the orientations of the liquid crystal molecules to change continuously between the two plates. If a light beam propagates through such a device, the polarization of the beam will follow the direction of the director so that the device acts as a polarization rotator (see figure 2.8). Because the effective polarization rotation angle varies with the driving electric field, amplitude control of the light beam can be obtained by inserting the twisted nematic LCD between two polarizers. In figure 2.8, the twisted angle of the LCD is 90°, and the polarizer and analyzer are oriented perpendicular to each other. If no electrical field is applied to the LCD, the maximum output light beam is obtained. If an

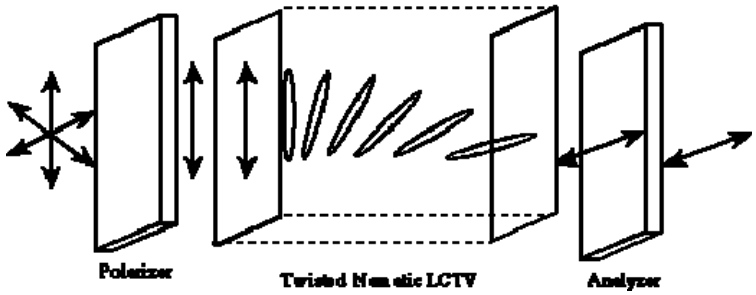

Figure 2.8 Polarization-rotation property of the twisted nematic LCD. [149]

electric field is applied to the LCD, the molecules tilt and the effective rotation angle varies so that the amplitude of the output light varies as well. If the applied field is strong enough, the molecules will all tilt to 90° (aligned with the electric field), and the input light will not rotate so

that there is minimum output light because the polarization of the analyzer is perpendicular to the input light. Thus the amplitude of the output light beam can be controlled by the driving voltage. Note that the polarization rotation and the resulting amplitude modulation occur for incoming light polarized either parallel (as shown in figure 2.8) or orthogonal to the director of the liquid crystal.

Implementation of phase-mostly and amplitude-mostly modes

For the twisted nematic LCTV illustrated in figure 2.8, when the incoming electric field is parallel to the director, the change of tilt with voltage also changes the refractive index from extraordinary to ordinary as the tilt varies from 0° to 90°, just as it did in the untwisted case shown in figure 2.7; therefore, the phase of the propagating wave is modulated significantly. If the incoming electric field is orthogonal to the director, on the other hand, the propagating wave sees a refractive index that corresponds closely to the ordinary index for all values of tilt so that very little phase modulation results. This property allows the device to be operated in phase-mostly or amplitude-mostly mode by simply orienting the polarization of the incoming light parallel or orthogonal to the director, respectively. Thus, phase modulation can be obtained with very little cross-coupled amplitude variation if the incoming electric field is parallel to the director [150]. Of course, the purest phase modulation is achieved by using an untwisted nematic liquid crystal device. Amplitude modulation with very little cross-coupled phase variation can be obtained by making the incoming electric field orthogonal to the molecules.

2.4 OPTICAL TRAPPING SET UP USING LAGUERRE-GAUSSIAN BEAMS

The basic optical tweezers set-up has been discussed in detail in section 2.1. The basic set-up employs conventional TEM_{00} laser beam focused through a high NA objective lens to form the optical trap. For experiments using Laguerre-Gaussian beams a spatial light modulator was inserted into the beam path to phase modulate the laser wavefront. The experimental set-up used for trapping objects with *LG* beam is shown below.

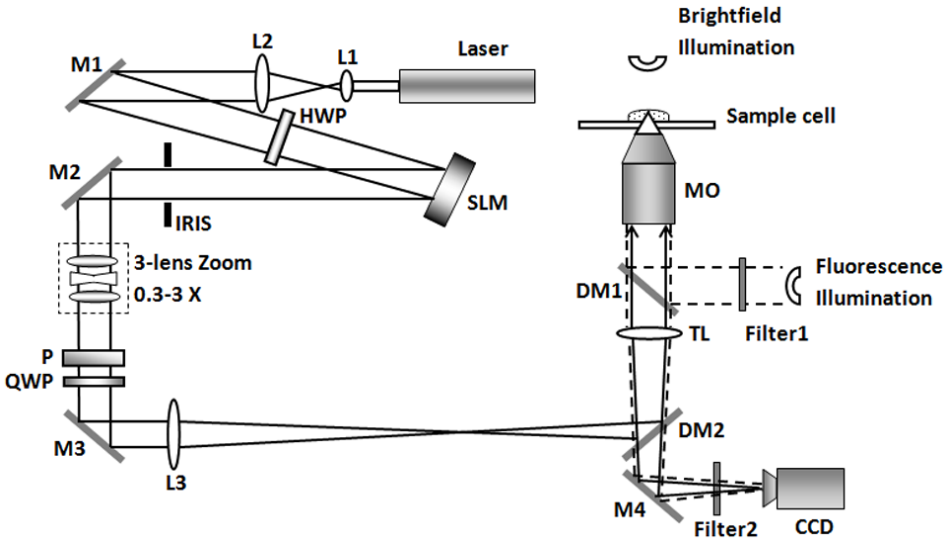

Figure 2.9 Schematic of the experimental set-up. Lenses L1-L2 expand the laser beam so that it nearly fills the SLM pixel array. Half wave plate (HWP) was used to orient the polarization of the input beam for phase only operation of the SLM. The diffracted first order was selected through the iris. A three lens zoom was used to resize the beam to suitably fill the entrance pupil of the objective lens. Polarizer (P) and quarter wave plate (QWP) were used to control the ellipticity of the laser beam. Mirrors (M1-M4) steer the laser light path. Lens L3 was used to compensate for the effect of tube lens (TL) on the trapping laser beam. The objective lens (MO) and the tube lens together form images of the trapped objects onto the CCD camera. Dichroic mirror (DM1) serves to couple the fluorescence excitation light onto the objective lens and another Dichroic mirror (DM2)

was used to selectively reflect the trap laser beam towards the objective lens and transmit the imaging broadband/fluorescence light to the CCD camera.

The experimental set-up consists of the trapping laser sources. Both the fundamental mode Nd:YVO_4 laser emitting at 1064 nm (Compass 1064-4000, Coherent Inc) and the frequency doubled Nd:YVO_4 laser emitting at 532 nm (Verdi-5, Coherent Inc) were used. The linearly polarized cw Gaussian beam from the laser was phase modulated by a spatial light modulator to generate different orders (azimuthal indices) of *LG* modes. The polarization of the incoming light to the SLM was adjusted using a half wave plate such that the SLM acts as a phase shifter. Two models of SLM, LCR-2500, Holoeye and PLUTO, Holoeye, optimized to produce a maximum of ~ 2π phase stroke at the laser wavelengths of 532 nm and 1064 nm respectively were used. The diffracted first order was directed onto a microscope objective lens, either Zeiss Plan-Neofluor 100X, 1.3 or Zeiss Acroplan 63X, 0.85, to form the optical trap. The sample cells were mounted upon a piezo-controlled x-y-z translation stage (P-517.3CL, Physik Instruments) that can be moved with a step resolution of ~ 1nm. A three lens zoom assembly was used to size the different orders of *LG* beams to fill ~80% of the objective entrance aperture. The polarization ellipticity of the trap laser beam was controlled using a polarizer and quarter wave plate combination placed after the SLM. A halogen illumination source (12 V, 100 W) and a 50 W high pressure mercury arc lamp, equipped with suitable bandpass filters, were used for brightfield imaging and fluorescence illumination of the sample respectively. The brightfield and fluorescence images of the sample were observed with either a video rate color CCD camera (Watec Inc) or a high sensitivity Peltier cooled monochrome CCD camera (DC350F, Leica). Filters were used to suppress the back scattered laser light and fluorescence excitation bands.

2.5 OPTICAL TRAPPING SET UP USING LOW NA OBJECTIVE LENS

The other set up used in the experiments presented in the thesis comprises of a long working distance low NA objective lens to weakly focus the laser beam to trap them at liquid air interface or at a glass boundary. A schematic of the set up is given below,

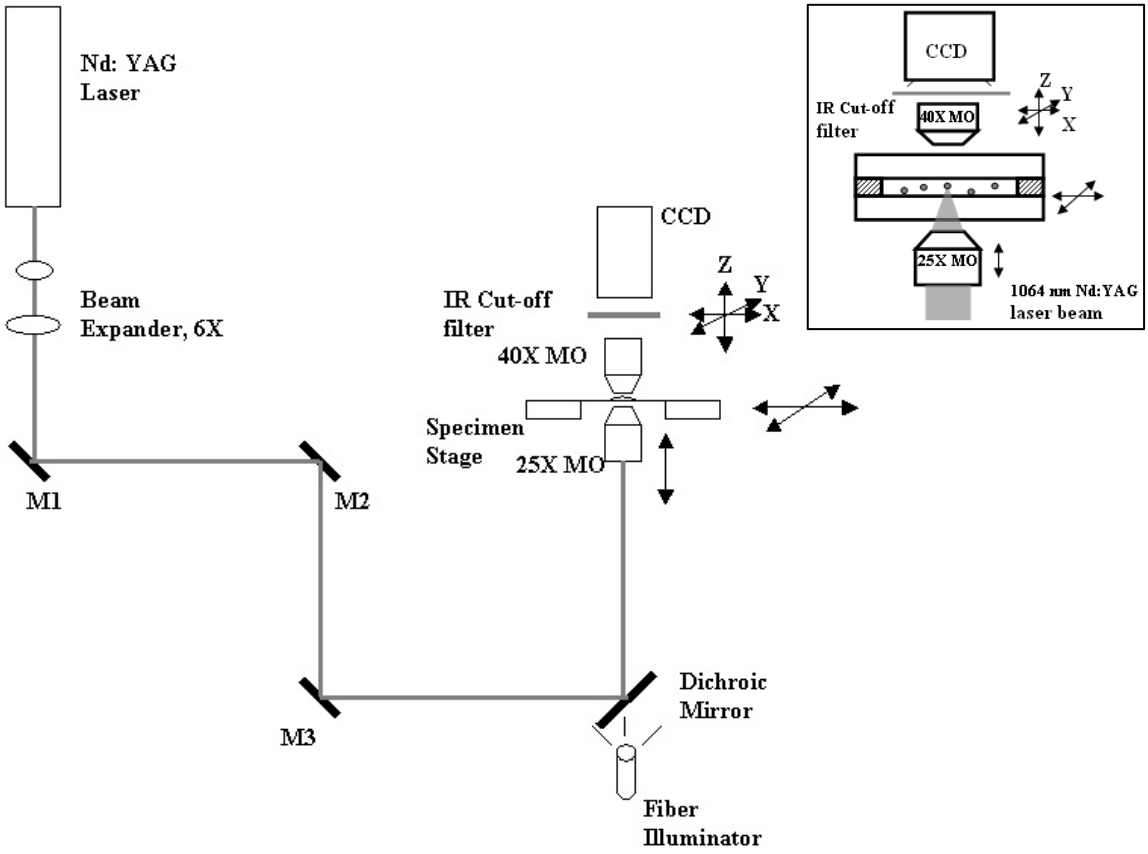

Figure 2.10 A schematic of the experimental set-up. A cw 1064 nm beam from Nd: YAG laser was expanded and coupled to a 25X microscope objective through a dichroic mirror. The beam was focused by the 25X objective at the water surface. The trapped object was viewed and imaged through a combination of 40X objective, 1064 nm cut-off filter and CCD camera. The 40X objective, 1064 nm cut-off filter and CCD camera was mounted on a XYZ stage for 3D scanning of the sample. Inset: Trapping at the upper glass boundary of the sample chamber.

The 1064 nm output from a cw, Nd:YAG laser (Home built) was coupled to a 25X, NA 0.5 microscope objective lens using alignment mirrors (M1, M2, M3) and a dichroic mirror. The light from a halogen lamp was also coupled through the same microscope objective using a fiber optic light guide. The sample was placed on a XY translation stage just above the 25X objective. The objective height could be adjusted to make the focal point coincident with the liquid surface or the upper glass boundary of the sample chamber (inset). In contrast to the arrangement described in figure 2.9 here the trapped objects were imaged using a combination of a 40X microscope objective and a CCD camera. The use of separate objective lens for imaging the sample was necessary as the trapping plane was not coincident with the imaging plane of the bottom 25X objective lens when the laser beam was focused slightly above the sample volume to have a larger laser spot size at the interface. An IR cut-off filter was used to suppress the laser beam from reaching the CCD. The 40X objective, IR cut-off filter and the CCD camera were mounted on a 3-axis translation stage to scan the whole volume of liquid sample.

2.6 MEASUREMENT OF TRAPPING FORCE

Forces exerted on trapped particles are in the piconewton range. For small displacements from the center of an optical trap, optical tweezers act like a Hookeian spring characterized by a fixed stiffness, because the restoring force is proportional to displacement. In most of the experiments, the interest lies mainly in the lateral stiffness, i.e., the stiffness in the plane of the specimen. The stiffness depends on the wavelength and power of the laser used, NA of the focusing objective used and size and refractive index of the particle and the refractive index of the surrounding medium. In combination with high-resolution position detection facility, the

optical tweezers can be used to make quantitative measurements of the forces applied to trapped objects, once the stiffness is calibrated. Here I first describe the escape force method that estimates the maximum trapping force associated with an optical trap and thereafter drag force method, equipartition method and power spectrum methods useful for estimation of stiffness of the optical trap are discussed.

2.6.1 ESCAPE FORCE METHOD

This method determines the minimal force (F_{escape}) required to pull an object entirely out of the trap or the maximum trapping force experienced by a trapped object at a given trap power. To produce the necessary force, the particle may either be pulled through the fluid (by moving the trap relative to a stationary stage), or more conventionally, the fluid can be moved past the particle (by moving the stage relative to a stationary trap) [151]. Many variations of the method exist: one of the simplest is to record a movie of a trapped particle in a fixed trap by translating the microscope stage at increasing velocities, until the particle just escapes. The particle velocity immediately after escape is measured from the recorded video. From this one can estimate the escape force, provided the viscous drag is known. The escape force can be easily derived from the Stokes law,

$$F=\beta v \tag{2.7}$$

where β represent the Stokes drag coefficient and v the stage velocity at escape. The Stokes drag coefficient for a sphere of radius a is generally calculated as

$$\beta=6\pi\eta a \tag{2.8}$$

where η is the viscosity of the liquid. However, since most of the optical tweezers experiments

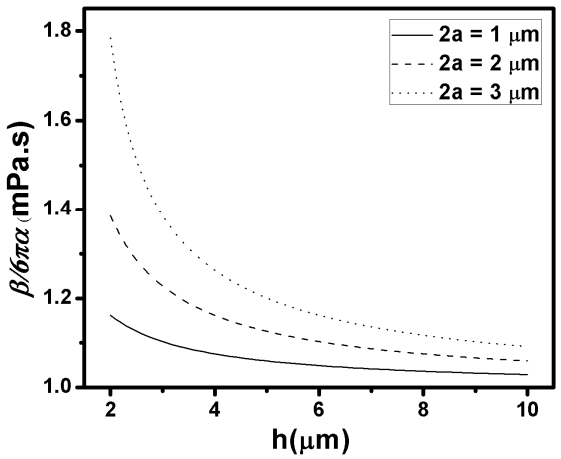

Figure 2.11 *β/6πa* for water at 25 °C plotted vs the distance of the bead from the cover-slip surface, *h*, for beads of different diameters (*2a*).

occur near the surface of the cover-slip, the interaction of a sphere with the boundary layer of water near a surface leads to an increase in the hydrodynamic drag coefficient, which is estimated by the Faxen's law (see figure 2.11) [152],

$$\beta = \frac{6\pi\eta a}{1 - \frac{9}{16}\left(\frac{a}{h}\right) + \frac{1}{8}\left(\frac{a}{h}\right)^3 - \frac{45}{256}\left(\frac{a}{h}\right)^4 - \frac{1}{16}\left(\frac{a}{h}\right)^5} \tag{2.9}$$

Whre *h* is the distance of the surface.

2.6.2 MEASUREMENT OF TRAP STIFFNESS

The optical tweezers creates a three-dimensional potential well for a trapped micron sized bead that can be approximated by three independent harmonic oscillators, one each for the *x*, *y*, and *z* direction. The potential energy of such an oscillator for one direction can be written as,

$$U(x) = \frac{1}{2} k_t (x - x_0)^2 \tag{2.10}$$

where k_t is the trap stiffness typically expressed in pN/μm, *x* the position of the trapped bead, and x_0 its center position within the trap. The force needed to displace a trapped bead by a distance *x*

(taking x_0 =0) is thus,

$$F_t = -\frac{dU}{dx} = -k_t x \tag{2.11}$$

If the optics are well aligned, the x and y spring constants will be roughly the same and the z spring constant is typically smaller by a factor of ~5 [141].

For measuring the value of k_t for an optical trap set-up, bead positions (x) have to be determined with precision of few nm. The position data of the trapped bead can be obtained either by using video analysis techniques or by position sensitive photodetectors as described in section 2.2.4. There are several methods to estimate k_t from the measured position data of the trapped bead and prominent among them are the drag force method, equipartition method and power spectrum method. These methods are discussed below.

2.6.2.1 DRAG FORCE METHOD

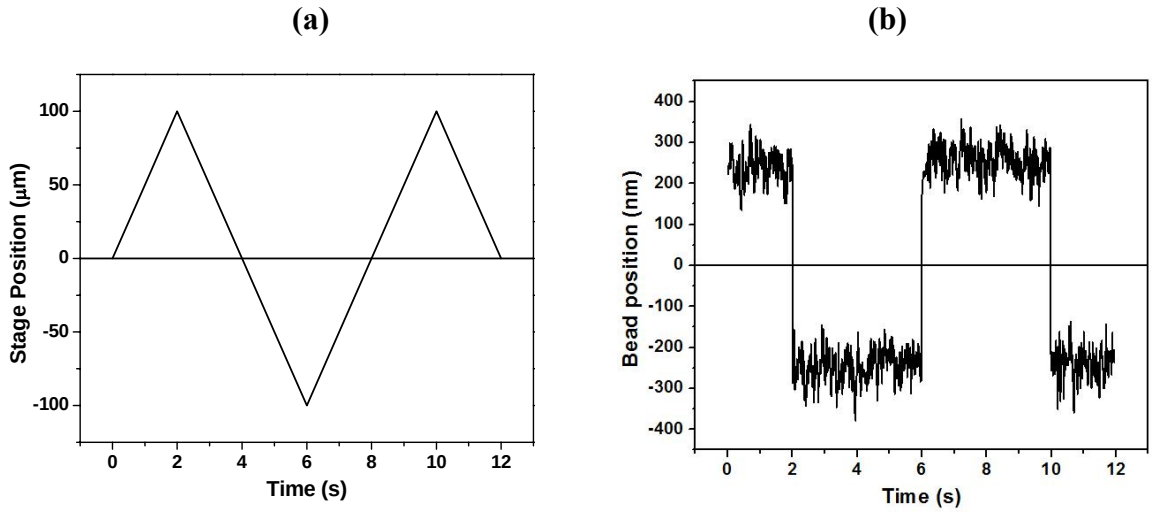

Figure 2.12 (a) Traingular displacement pattern of the Piezo stage. (b) Corresponding measured displacements of a trapped 2 μm polystyrene bead.

Viscous drag forces are produced by periodic movement of the microscope stage while holding the particle in a fixed trap. Commonly a triangle wave of displacement of piezo stage as shown in figure 2.12a, corresponding to a square wave of drag force are used for calibration [121]. The

resultant displacement pattern follows the applied drag force (figure 2.12(b)) and it needs to be ensured that measurements are made within the linear (Hookeian) region of the trap. The method requires a well-calibrated piezo stage to produce the fluid flow profile, a position detection technique with few nm precision, and knowledge of the viscous drag coefficient.

Since the Stokes drag force on spherical particles having a relative velocity of v with respect to the medium is given as,

$$F_d = \beta v \tag{2.12}$$

At equilibrium condition of the trapped bead under a flowing medium we have,

$$F_t = F_d$$

$$\text{or} \quad k_t = \frac{F_d}{x} \tag{2.13}$$

Where x is the mean of the measured displacements.

2.6.2.2 EQUIPARTITION METHOD

A trapped bead is in thermal equilibrium with a much larger system (the surrounding fluid). An important result of statistical mechanics is the equipartition theorem that states that each rotational or translational component of the random thermal motion of the trapped particle has an average kinetic energy of $(1/2)k_bT$, where k_b is the Boltzmann constant. For a harmonic potential well the average potential energy can be described as [121],

$$\langle U(x) \rangle = \frac{1}{2} k_t \langle (x - x_0)^2 \rangle = \frac{1}{2} k_b T \tag{2.14}$$

The brackets denote the time-averaged quantity,

$$\left\langle (x - x_0)^2 \right\rangle = x_{rms}^2 = \lim_{t_n \to \infty} \frac{1}{t_n} \sum_{i=1}^{N} (x_i - \bar{x})^2 . \Delta t \tag{2.15}$$

which is actually the statistical variance of the bead x-coordinate with t_n being the total observation time, Δt being the time interval between observations, and $\bar{x}$ being the sample mean. Thus if we can accurately estimate the statistical variance we can deduce the spring constant, k_t. In figure 2.13(a) time signals are shown for a 2 μm bead acquired at different trap stiffnesses with a sample frequency of 120 Hz. Higher trap stiffness results in a stronger confinement of the bead and therefore a smaller variation of the position.

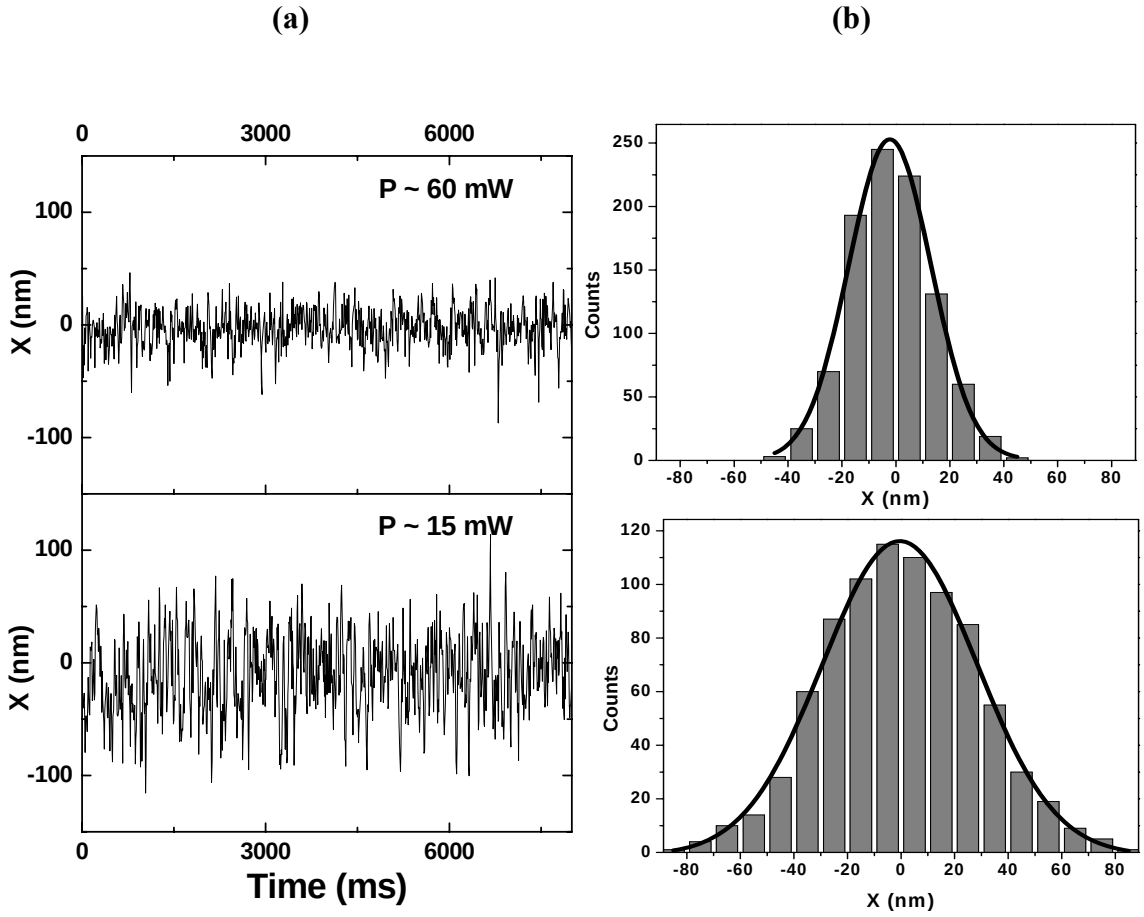

Figure 2.13 (a) Time vs position data for a trapped 2 μm diameter polystyrene (refractive index 1.59) bead at trap powers of 15 mW (lower panel) and 60 mW (upper panel)

respectively. (b) Corresponding position histograms for 2 μm diameter bead at trap power of ~ 15 mW (bottom) and ~ 60 mW (top) yielding stiffness values of ~ 4.09 pN/μm and 16.45 pN/μm respectively.

Another way of determining the trap stiffness based upon the equipartition theorem is fitting a Boltzmann distribution to the position histogram of the bead. The probability density $\rho(x)$ of finding the bead at a certain position can be described by

$$\rho(x) = \frac{1}{Z} e^{-U(x)/k_b T} = \frac{1}{Z} e^{-\frac{1}{2}k_t (x-x_0)^2 / k_b T} = \frac{1}{\sigma\sqrt{2\pi}} e^{-\frac{-(x-x_0)^2}{2\sigma^2}} \qquad (2.16)$$

where Z is the partition function normalizing the probability density function. Actually the Boltzmann distribution can be represented by a Gaussian function that expresses the distribution as a function of statistical parameters given by the latter part of equation 2.16 with σ the standard deviation and σ^2 the variance. Fitting the probability density function, with parameters Z and k_t to a histogram of the position's ensemble gives the trap stiffness k_t (figure 2.13(b)).

2.6.2.3 POWER SPECTRUM METHOD

Another, calibration procedure is to make use of the diffusional Brownian motion of the bead due to the continuous and random bombardment by solvent molecules. Besides an inertial force F_{inert} indicating the resistance of the bead to an acceleration, the bead is subjected to a drag force F_d resulting from the viscous medium around it, a force F_t resulting from the optical trap and the so-called (thermal) Langevin force F_{rand} that represents the random Brownian forces originating from the thermal activity of the surrounding medium, a random Gaussian process. The governing equation of motion is

$$F_{inert} + F_d + F_t = F_{rand}(t)$$

or

$$m\ddot{x} + \beta\dot{x} + k_t x = F_{rand}(t) \qquad (2.17)$$

with m the mass of the bead and β the hydrodynamic drag coefficient. This equation can be simplified if we consider that a micron-sized trapped bead in water behaves as an extremely overdamped oscillator permitting to neglect F_{inert} since its effect is only just noticed for frequencies above 100 kHz. This condition holds only for low Reynolds numbers and for frequencies below 1 kHz. For higher frequencies hydrodynamic corrections should be taken into account since the fluid's velocity field around the sphere cannot be considered constant anymore and becomes frequency dependent.

Fourier transforming equation 2.17 yields the power spectral density of the position of the bead, where the thermal white-noise force magnitude can be expressed as

$$S_F(f) = 4\beta k_b T \tag{2.18}$$

and therefore the power spectral density reflects the transfer function of the optical tweezers. For such a Brownian harmonic oscillator, where motion takes place at small Reynolds numbers, one can show that the power spectral density of the bead position is [153],

$$S_x(f) = \frac{k_b T}{\beta \pi^2 (f_C^2 + f^2)} \tag{2.19}$$

where k_b is Boltzmann's constant, T is the absolute temperature. The corner-frequency f_c is a function of the trap stiffness k_t and is related as,

$$k_t = 2\pi\beta f_c \tag{2.20}$$

The units of $S_x(f)$ are nm^2/Hz. In figure 2.14 the typical power spectral density for a trapped bead is shown. At low frequencies the power spectrum is approximately constant, given by

$$f << f_C \Rightarrow S_x(0) \approx \frac{k_b T}{\beta \pi^2 f_C^2} = \frac{4\beta k_b T}{k_t^2} \tag{2.21}$$

Note that the thermal white-noise force magnitude is reflected by $S_F(f) = 4\beta k_b T$ and $S_x(0)$ thus

reflects the confinement of the bead, dependent on the trap stiffness. For frequencies $f >> f_c$ the power spectrum drops off like $1/f^2$, indicating free diffusion. Integrating the power spectral density of the whole frequency range the position variance is obtained.

The trap stiffness can be deduced by fitting the Lorentzian function given by equation 2.19 to the measured power spectral density. Introducing Einstein's equation $D = k_bT/\beta$, which relates the diffusion constant D (m^2/s) to the Boltzmann energy and the drag coefficient, the fit parameters are f_c and D.

An advantage of the method is that it does not require any means of precisely moving a bead to calibrate the optical trap. However, the calibration obtained by this method is valid only for small displacements, for which a linear approximation to the position signal is valid. In

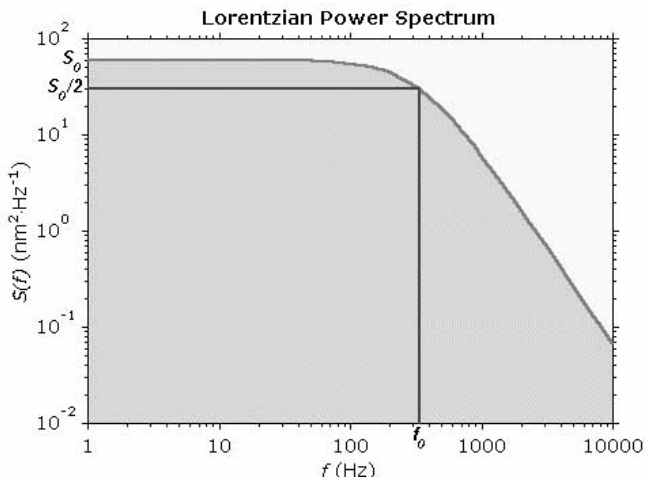

Figure 2.14 Typical power spectrum of a trapped bead.

addition, the system detection bandwidth must be adequate to record accurately the complete

$$x_{rms}^2 = \int S_x(f)df \tag{2.22}$$

power spectrum without distortion, particularly in the high frequency regime. Typically a

bandwidth of a few kHz is sufficient to correctly estimate the corner frequency f_C, necessitating use of either quadrant photodiodes or high speed CCD cameras.

2.7 SUMMARY

The design considerations for building an optical trapping set-up, guidelines for selection of different modules and the set-ups developed have been detailed. Methods used to generate special trap beams and the calibration of the optical trapping set-ups have also been discussed.

CHAPTER 3

TRAPPING OF MICRON SIZED OBJECTS AT A LIQUID-AIR INTERFACE

In this chapter the results of our studies on the use of long working distance objective lens for trapping objects at air-liquid interface are presented. The observed trapping of objects in an annular region around the laser beam is shown to be caused by simultaneous action of liquid thermocapillary forces along with optical forces. Using the available theoretical models of the thermocapillary effect estimates were made for the diameter of the annular trapping region as a function of the laser power. These were found to be in good agreement with the experimental observations.

3.1. INTRODUCTION

In optical tweezers one needs to use a high NA objective so that the gradient forces are able to overcome the axial scattering force and thus ensure stable three-dimensional trapping. The limited working distance for these objective lenses, however, makes it difficult to manipulate objects close to a free liquid surface. We have therefore investigated the possibility of using a trap beam focused by a low NA objective lens for this purpose. The basic idea was that since the gradient forces would be weak, the object immersed in the liquid will be pushed along the direction of the beam and distort the liquid surface. The resulting surface tension forces may help balance the scattering force and thus lead to a stable trapping of the object. The results presented in this chapter would show that although the approach does succeed in trapping objects

at liquid interface, the mechanisms involved in the trapping are more involved. The thermocapillary effect caused by trap beam absorption induced spatial variation of the liquid surface tension leads to trapping of objects in an annular region about the trap beam. The experimental results, their analysis and possible applications of this technique are discussed.

3.2 EXPERIMENTAL SET UP

The set up used for the experiments is similar to that shown in figure 2.10 in chapter 2. For the experiments described in this chapter we used the 1064 nm output from a cw, Nd:YAG laser coupled to the 25X, NA 0.5 microscope objective lens. An open film of sample consisting of polystyrene microspheres suspended in water was placed on a cover slip mounted on the XY translation stage just above the 25X, NA 0.5 objective lens. The objective height was adjusted to make the focal point coincident with the liquid surface. The trapped objects were imaged using a combination of a 40X microscope objective and a CCD camera. An IR cut-off filter was used to suppress the laser beam from reaching the CCD. The 40X objective, IR cut-off filter and the CCD camera were mounted on a 3-axis translation stage to scan the whole volume of liquid sample.

3.3 OBSERVATIONS

For a 2 μm polystyrene sphere the threshold power for trapping was found to be ~ 15 mW. In figure 3.1 we show the trapping of a single 2 μm polystyrene microsphere at the water-air interface with a trap laser beam (power ~ 20 mW) focused at the liquid surface using the 25 X objective. Interestingly, although sometimes the objects did get trapped at the location of the focused trap beam (seen as the bright spot in the figure), it was seen that the stable trapping

occurred only in an annular trapping region about the trap beam axis. This is evident from the images of the trapped microsphere shown in figure 3.1, where the microsphere is seen to be

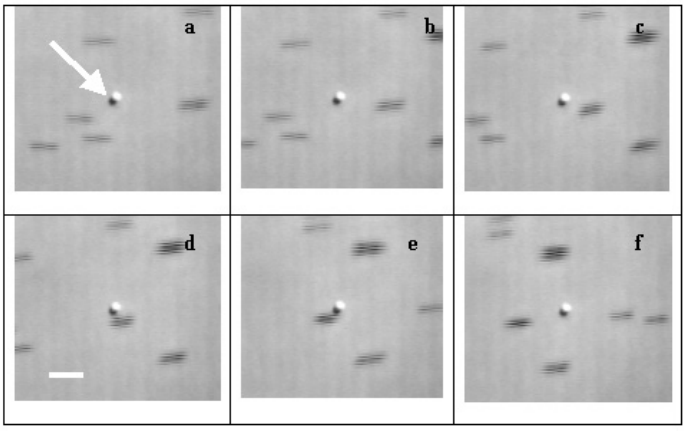

Figure 3.1 Trapping of a single 2 μm polystyrene microsphere. The trapped microsphere is indicated by the white arrow and the bright spot corresponds to the trap beam. The moving microspheres appear blurred. Scale bar, 10 μm.

trapped at a peripheral point of the central bright spot that corresponds to the position of the trap beam. To further investigate this aspect we pushed a trapped microsphere by subjecting it to a flow of liquid (speed ~ 20 μm/s) directed from the top end of the image to the bottom end (figure 3.2). The microsphere that was trapped at the top end of the annulus was seen to move in the annular trap region and finally got trapped near the diametrically opposite end of its initial trap position.

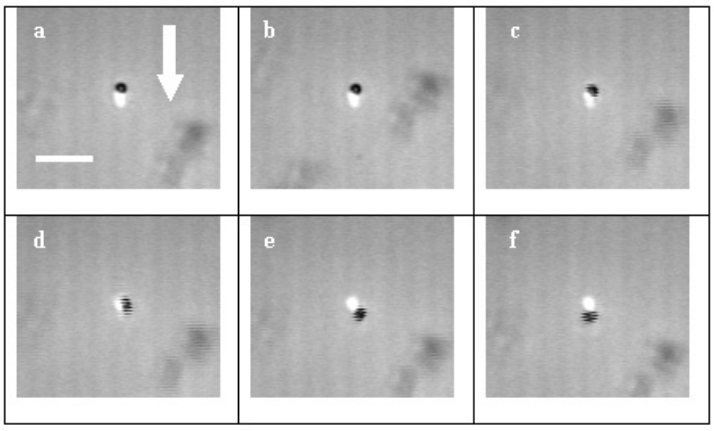

Figure 3.2 Effect of viscous drag from flowing fluid on a trapped polystyrene microsphere. The bright spot corresponds to the trap beam. The direction of the fluid flow is from top of the frame to its bottom as shown by white arrow. (a)-(h) The trapped microsphere moved in the annular trap region before it got stably trapped at a point diametrically opposite to its initial trap position on the annulus. Scale bar, 10 μm.

For a given trap beam power a gradual accumulation of microspheres in the annular trapping geometry was observed with time, leading to the formation of a closed chain like structure. The formation of such a structure at a trap beam power of ~ 40 mW is shown in (figure 3.3 (a)-(f)). It is important to note that with an increase in trap beam power, an increase

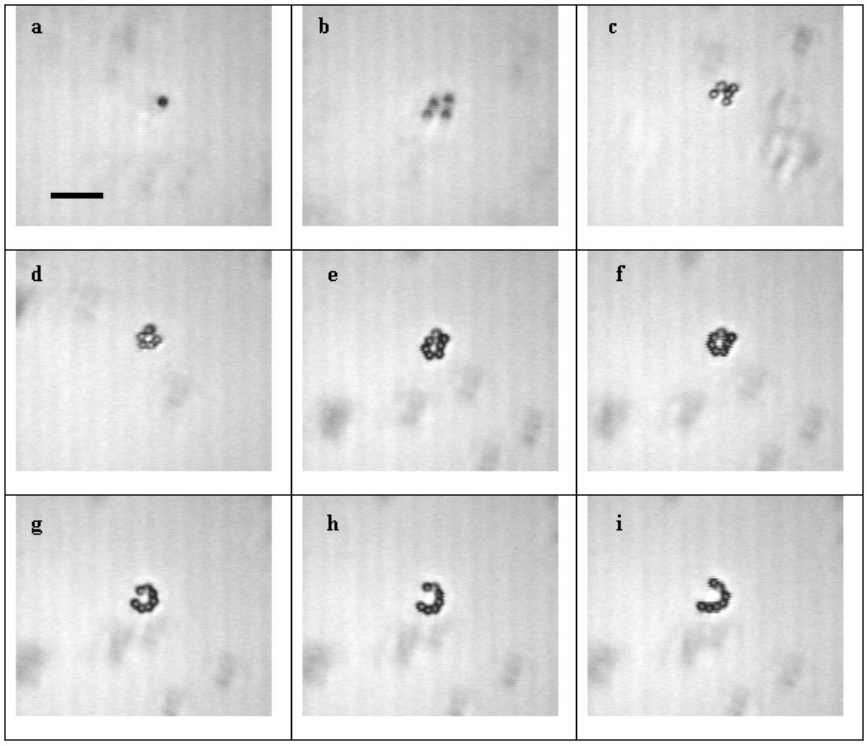

Figure 3.3 Trapping of multiple polystyrene microspheres inside the annular trap region due to thermocapillary action at the water-air interface. (a)-(f) shows the accumulation of microspheres driven from bottom of the liquid film by axial scattering force of the trap beam. As can be seen the trapped microspheres are at a different plane (at the water-air interface) than the other microspheres (appearing blurred) immersed in the bulk liquid medium. (g)-(i) shows the effect of increased laser power on the annular structure. Since

the diameter of the annulus increase the closed chain of microspheres gets disrupted. Scale bar, 10 μm.

in the diameter of the annular trap region was also observed. Therefore, for the closed chain like structure of seven microspheres shown in figure 3.3(g-i), the chain breaks when the power was increased to 50 mW because the number of the trapped microspheres was not sufficient to close the chain.

The accumulation of microspheres in the annular trap region occurred faster when the trap power was increased. The results of an experiment carried out at the trap laser beam power of ~ 60 mW, where the particles were injected into the water film from the top right corner, are shown in figure 3.4. A gradual build up of a cluster of polystyrene microspheres was observed to occur preferentially at one or two points on the annular trap region. It is interesting to note that the cluster could grow to a certain maximum size, beyond which the microspheres in the neighbourhood of the trap showed a periodic motion, initially these were observed to be driven closer to the cluster and thereafter got driven away from it.

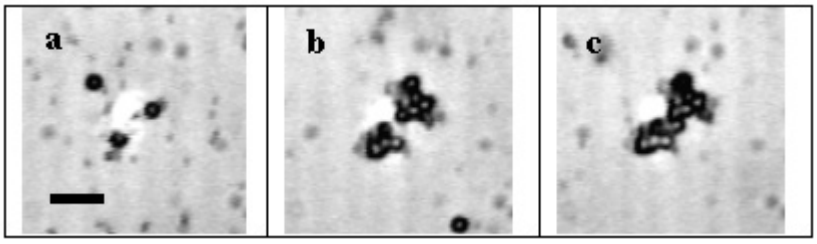

Figure 3.4 Trapping of cluster of 2 μm diameter polystyrene microspheres at increased trap beam power (~60 mW). The laser beam appears as bright spot. Gradual accumulation of microspheres at the trapping region can be seen. Scale bar, 10μm.

The approach could also be used to trap human erythrocytes. In figure 3.5(a) we show trapping of a single human erythrocyte cell in side-on orientation at the trap beam power of 20

mW. A gradual formation of a large cluster around the single trapped erythrocyte cell with increasing trap beam power (~ 60 mW) can be seen in figure 3.5(b-f).

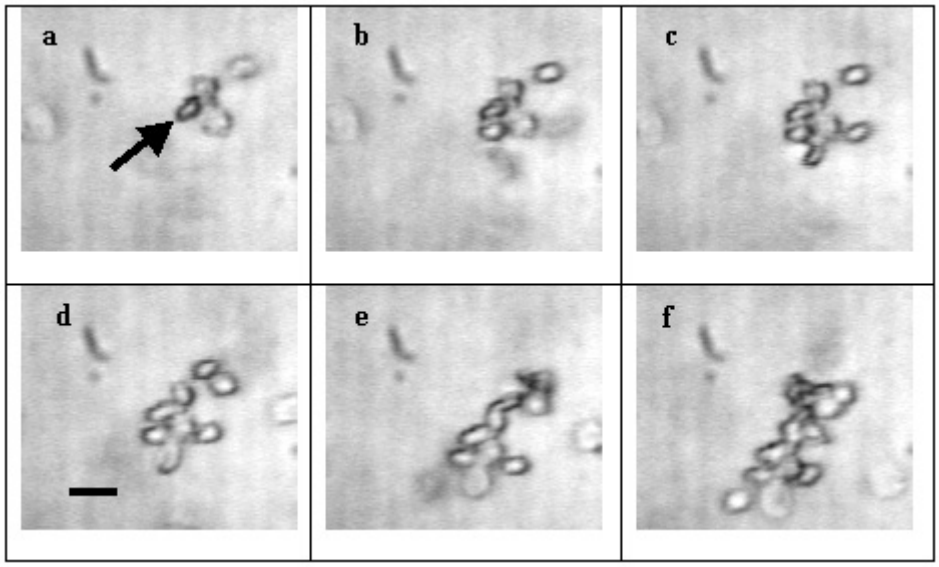

Figure 3.5 Trapping of human erythrocytes at the trap beam power of ~ 60mW. (a) A single trapped erythrocyte cell. (b)-(f) Gradual trapping of a large number of erythrocyte cells. Scale bar, 10 μm.

3.4 DISCUSSIONS

When a microscopic particle is pressed against the free liquid surface by a weakly focused laser beam, it will deform the surface resulting in the onset of surface tension forces which may balance the axial scattering force much like these balance the weight of an insect sitting on a water surface. If this were the only mechanism responsible for the observed trapping of particles at the liquid-air interface the particles would get trapped at the centre of the trap beam. The results presented earlier show that this is not the case suggesting that additional processes are involved in the trapping of objects in an annular region about the beam axis.

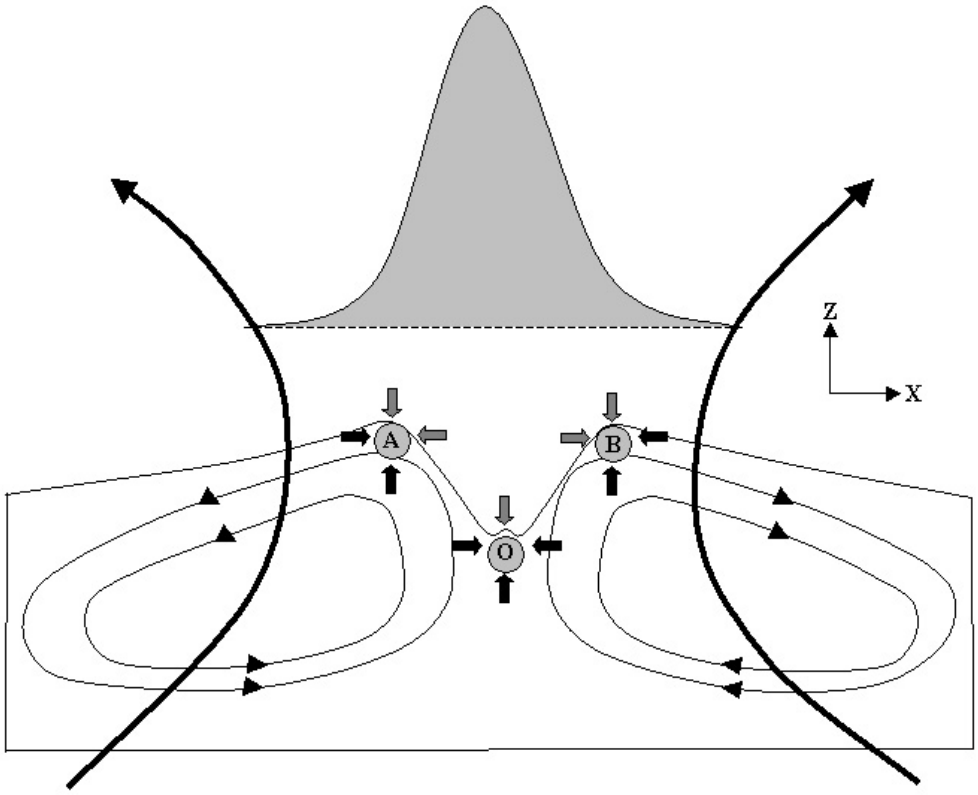

Figure 3.6 Trapping of microspheres near liquid surface. A 1064 nm laser beam coming from the bottom is focused on the liquid surface. The local heating at the liquid surface by the laser beam cause a surface tension variation in the surface and lead to thermocapillary pit formation. The microspheres can be trapped at the periphery of this thermocapillary pit by combined action of optical forces and surface tension forces as shown. The black arrows shown are for optical forces and the gray arrows shown are for liquid surface tension forces. Due to change of optical momentum of a laser beam at the interface bulging of the liquid surface occurs towards the low refractive index region as shown at point O. At this position also unstable trapping of the microsphere is possible as shown.

It is known that the absorption of 1064 nm laser light in water would result in a steady state temperature rise of ~ 1.45 °C/100 mW in the focal volume of the trap beam [107]. Further, due to the Gaussian intensity distribution of the beam an axi-symmetric temperature distribution will be created at the liquid surface with the maximum of the temperature at the beam axis. As

the surface tension of a liquid is usually a decreasing function of temperature, the temperature distribution would result in an axi-symmetric surface tension distribution with minimum at the central hot point. Since a liquid with a high surface tension pulls more strongly on the surrounding liquid than one with a low surface tension, the presence of a gradient in surface tension causes the liquid to flow away from regions of low surface tension leading to surface currents that are referred to as Marangoni surface currents. These and the concomitant internal gravity waves lead to further deformation of the surface profile of the liquid interface and the depletion of the fluid in the central region results in the formation of a pit [154]. For this situation, shown in figure 3.6 a microsphere suspended inside the liquid medium at position A, will be acted upon by optical forces (gradient as well as scattering forces, shown as dark arrows) and surface tension forces (shown as faded arrows). A careful examination of the forces on the object shows that the surface tension force acting in –Z direction can balance the scattering force (+ Z direction), on the object. Similarly the radial gradient force of the beam (acting along the negative x-axis at A) can balance the surface tension component along positive x-axis. Thus, due to these counter-acting forces, the microsphere can get trapped at point A. The gravitational force will also be along the –z-axis and thus add to the surface tension force. Since this force is expected to be negligible, it is not shown in figure 7. Due to the cylindrical symmetry of the laser beam profile and the resulting surface deformation, stable trapping would occur in an annular region about the laser beam axis, unlike at the beam focus as in the case of optical tweezers.

The diameter of the thermocapillary pit at the liquid surface (the distance between A and B) that would determine the approximate size of the observed annular trapping region can be determined

using the following expression for the profile of the thermocapillary pit worked out by Da Costa *et al* [155],

$$y/y_0 = [1 + bf(\beta,\gamma)]^{1/2} \tag{3.1}$$

where, $$f(\beta,\gamma) = \int_{\beta^2/1+\gamma}^{\beta^2} \frac{d\theta}{\theta e^{\theta}},\ b = \frac{3}{4\pi}\frac{cP}{\rho g k y_0^3}, \gamma = t/t_0, t_0 = \alpha^2/4\kappa, \beta = x/a$$

Here, y is the depth of the pit at a radial distance x from the beam axis, y_0 is the thickness of the liquid film, P is the absorbed laser power, c the thermal coefficient of surface tension, ρ the density of liquid, g is gravitational acceleration, k the thermal conductivity of the liquid, α the surface tension of liquid, κ the thermal diffusivity, and a is the radius of the optical beam.

In our experiments the thickness of the water film (y_0) was measured to be ~ 400 μm by measuring its vertical cross-section with a microscope objective mounted on a vertical stage. For the laser irradiation geometry under consideration the thermal time constant ($\tau_h = d^2/\kappa$, where d is the diameter of the trap beam) is expected to be hundreds of μs. Therefore, on time scale of ms or longer a steady state temperature distribution in water medium can be assumed. Taking the steady state temperature rise in aqueous medium when irradiated by a focused 1064 nm laser beam to be ~ 1.45 °C/100 mW [107], and putting the values for other parameters of water in equation 3.1, for a trap beam power of 40 mW, the estimate for the diameter of the themocapillary pit at the liquid surface (i.e distance AB in figure 3.6) comes out to be ~ 9 μm. This is in very good agreement with the measured diameter of the annulus ~ 8 μm at the same trap beam power (figure 3.3). Further the maximum depth of the pit (i.e y at x=0) was estimated to be ~ 48 μm.

It should be noted that the radiation pressure of the trap beam would also lead to a bulging of the liquid surface at the position O [156]. The resulting surface tension forces may also lead to trapping of microobjects at the position O. The position O however is an unstable equilibrium trapping position. This follows because any small displacement of the microsphere from this position will cause it to be driven along the liquid surface, by the strong axial scattering force of the trap beam until it reaches point A or B or other equivalent positions in the annular trap region.

An estimate for the bulge in the liquid surface at point O due to radiation pressure can be made by using the following expression worked out by Mitani *et al* [156],

$$\xi(r) = \frac{w^2 P_0}{4} \int_0^\infty \frac{k J_0(kr) \exp(-w^2 k^2 / 8)}{\gamma k^2 + \Delta\rho g} dk \tag{3.2}$$

Where, r is the radial coordinate, w is the width of the laser beam, k is the wave number in the first medium and J_0 is the zeroth order Bessel function, γ is the interfacial tension, $\Delta\rho = |\rho_1 - \rho_2|$ is the density difference between the mediums and P_0 is given by,

$$P_0 = \frac{2I_0}{c\pi w^2}(n_2 - n_1)\left(1 - \frac{n_2 - n_1}{n_2 + n_1}\right) \tag{3.3}$$

Here, c is velocity of light, I_0 is the total light intensity, n_1 and n_2 are the refractive index of the first and the second medium respectively.

For the beam size of ~ 4 μm and power ~ 40 mW, taking the surface tension value for water as ~7.29×10^{-2} N/m, the maximum height of the bulged liquid surface at point O was estimated to be ~ 5 nm. It is therefore apparent that the thermocapillary action is the main source for the distortion of liquid air interface.

The above analysis is able to explain the experimental results presented in figures 3.1 - 3.5. The observation of the annular trap region about the trap beam (figures 3.1 – 3.3) is consistent with the distortion of liquid-air interface expected when thermocapillary effects are incorporated. As discussed earlier, the unstable trapping observed in the high intensity region can be attributed to the radiation pressure induced small bulging of the liquid surface occurs at position O in figure 3.6. The dependence of the thermocapillary pit on trap beam power (equation 3.1) also explains the increase in the diameter of the annular region with increasing trap beam power observed in figure 3.3(g-i). Further, while at lower trap beam power convective currents will be weak and therefore only those particles that diffuse into the trap beam volume get trapped. At higher beam power the presence of strong convective currents due to thermocapillary effect are responsible for the rapid formation of large particle clusters like that observed in figure 3.4. To verify the presence of these convective currents we carried out some experiments using water micro droplets (refractive index ~ 1.33) in paraffin (refractive index ~1.42). The water droplets were observed to initially move towards the trap beam because of the convective currents inside the liquid film and then moved away due to repulsion by regions of higher intensity as would be expected for particles with lower refractive index than the medium in which these are suspended. The microsphere cluster was seen to grow only up to a certain maximum size. This we believe happens because beyond this size the radial gradient force from the trap beam is not sufficient for transverse confinement of the trapped particles (figure 3.4). The observed preferential accumulation of a large number of trapped particles at some locations of the annular trap region may be due to perturbation caused to the thermocapillary pit by the initially trapped particles. Such perturbations in the form of small changes in the surface profile superimposed over the thermocapillarity induced deformation are likely to act as favorable

trapping points for the incoming particles. The observed periodic motion of the microspheres may arise due to the convective current build up into the liquid film due to the interplay of Marangoni surface waves and gravity. Previous studies [157] of such convective currents indicate the presence of large horizontal velocity component compared to the vertical component due to the smaller dimension of the liquid film in the vertical direction. The trajectories of the moving microspheres observed in our experiments is consistent with this fact.

For an annular trapping geometry it is expected that if the medium is moved relative to the trap beam the trapped particle should move to the diametrically opposite point on the annulus along the direction of movement. This is because if the force exerted by the moving liquid on the trapped particle has a tangential component with respect to the annular trap region the particle will move around the annular trap and eventually get trapped at the point where the tangential component vanishes. Referring to figure 3.6, if the specimen stage is moved in the - x-direction, the tangential force component would vanishes at points A and B. If the initial position of the trapped particle is at point B, and it is slightly displaced from there by convection current, it will experience a tangential force due to the moving liquid and thus get driven away from point B along the annular trap region. Finally the particle reaches at point A, where the tangential flow components of the moving liquid vanishes. It should be noted that the particle can stay at A indefinitely, because for any slight displacement from there, the tangential force due to liquid flow acts towards A. This observation is consistent with the results shown in figure 3.2. It is pertinent to note here that a movement of the medium with respect to the trap beam may lead to a change in the temperature gradient and thus cause some distortion in the shape of the pit. However, since the movements effected are slow (the speed for the movement of stage was ~ 20

μm/s implying a traversal time of ~ 200 ms through the laser focal spot) compared to the thermal time constant (~ hundreds of μs), these distortions are expected to be small.

It is also pertinent to note here that although thermoporetic force would also push the particles out of the beam focus (due to its elevated temperature compared to surrounding) these are much smaller compared to both, the optical trapping forces for transparent objects [19] and the surface tension forces and thus cannot account for the observed annular arrangement of trapped microsphere around the trap beam. Further, with thermophoretic forces the object can never be trapped even in an unstable manner on the beam axis.

The thermocapillarity assisted trapping at a liquid-air interface may prove useful for studying interaction of objects close to liquid-air interface [158, 159]. It may be particularly attractive for manipulation of biological objects since the objects are trapped away from the axis of the trap beam where due to lower intensity the concern about optical damage would be minimum. The presence of surface waves driven convection current in such a trap may serve as a constant supply of micro-objects into the trapping region thereby making this configuration particularly suitable for studies relating to colloidal cluster formations.

3.5 SUMMARY

We have demonstrated an approach for the trapping of micron size objects at liquid-air interface, which is difficult to achieve by conventional optical tweezers employing high numerical aperture microscope objectives. It is shown that laser induced thermocapillary effects are responsible for the observed trapping of objects in an annular region about the trap beam. The large trapping region (linear dimensions of ~ ten μm) available with this approach makes it suitable for trapping of large clusters of micro-objects at liquid-air interface.

CHAPTER 4

OPTICAL TRAPPING NEAR A COLLOIDAL CLUSTER FORMED BY A WEAKLY FOCUSED LASER BEAM

The results of our study on the use of weakly focused laser beam for creation of colloidal clusters at a glass-water boundary and trapping of other nearby particles by "optical binding" action are described in this chapter. The theoretical analysis carried out to investigate optical binding effect produced by a simpler to model one-dimensional chain of microspheres is described and comparison of the theoretical predictions with experiments carried out on a one-dimensional chain of microspheres using an elliptic trap beam is presented.

4.1 INTRODUCTION

There is significant interest on the use of optical forces for the organization of micro-objects into arrays [160-163] in a fashion similar to the formation of matter by electronic interactions. Such optical binding forces may result in new ordered states of matter with the possibility for the manipulation and study of systems ranging from small "optical molecules" to extended condensed matter systems. While these reports discussed optical binding of objects in a plane normal to the beam propagation direction, one-dimensional optically bound array of colloidal particles has also been generated along the path of the beam by the use of two counter propagating Gaussian laser beams [164]. More recently Grzegorczyk *et al* [165] have shown

theoretically that an assembly of very small cylindrical objects (i.e. Rayleigh type scatterers) stacked along the beam propagation direction, on illumination, by a plane wave, can generate stable optical trapping sites. Unlike the conventional trapping geometries that make use of optical gradient forces or a balance between optical scattering force and some other external force, the trapping configuration discussed by Grzegorczyk *et al* arises due to field profile generated by scattering of illuminating beam by a collection of particles. There have also been reports, mainly theoretical, exploring the possible use of these optical forces to organize metallic nanoparticles into desired geometries [166].

In this chapter, we report an experimental demonstration of the idea discussed by Grzegorczyk *et al* [165]. Although our trapping configuration differs from that discussed in reference 165, we have observed trapping of polystyrene (PS) microspheres near a cluster of PS microspheres that was trapped using a weakly focused laser beam. We could also demonstrate trapping of a microsphere close to a one-dimensional chain of three polystyrene microspheres that was generated and illuminated by a focused elliptical trap beam. The trapping characteristics observed in this experiment were in reasonable agreement with the calculated scattered intensity pattern from the chain of polystyrene microspheres.

4.2 EXPERIMENTAL METHODS

The set up used for the experiments is similar to that described in figure 2.10 of chapter 2. For the experiments described in this chapter we used a dilute colloidal suspension of PS microspheres and the sample taken in a chamber formed by two glass cover slips separated by plastic spacers. Separation between the two cover slips was maintained to ~ 30 μm. The sample chamber was placed on a XY translation stage just above the 25X objective. A cw, TEM_{00}, 1064 nm, Nd:YAG laser beam was focused into an aqueous suspension of 2 μm diameter PS

microspheres using a 25X, NA 0.5 microscope objective. The laser beam travels into the cell from bottom to top, pushing the spheres toward the upper glass boundary of the cell. The objective height was adjusted to make the focal point near the upper glass boundary. The trapped colloids were imaged using a combination of a 40X microscope objective and a CCD camera. An IR cut-off filter was used to suppress the laser beam from reaching the CCD. The 40X objective, IR cut-off filter and the CCD camera were mounted on a 3-axis translation stage to scan the whole volume of liquid sample.

4.3 RESULTS

In the experimental configuration shown in figure 4.1 a large cluster of microspheres was seen to form due to the combined action of the optical gradient and binding forces [160]. The spheres are pushed by the scattering force to the top of the cell and towards the center of the beam due to the gradient force. Due to these optical forces the microspheres self organize to reach a minimum energy configuration. It takes a few seconds to a few minutes to generate these optical clusters, depending on the concentration of beads in the water solution, on the laser power, and on the laser beam size at the top of the cell. At trap beam power of ~ 40 mW formation of closely packed microsphere clusters of size of up to ~15 μm was observed. Further, when a flow of particles was set into the medium (without disturbing the stability of the trapped cluster), by injecting a small volume of suspension from the direction appearing as top-left corner in the frames, some particles moving closer to the cluster were observed to get trapped. This is shown in figure 4.2(a). Two particles, indicated by arrow, moving with the liquid current can be seen to get trapped in the vicinity of the cluster of microspheres, whereas others keep moving with the

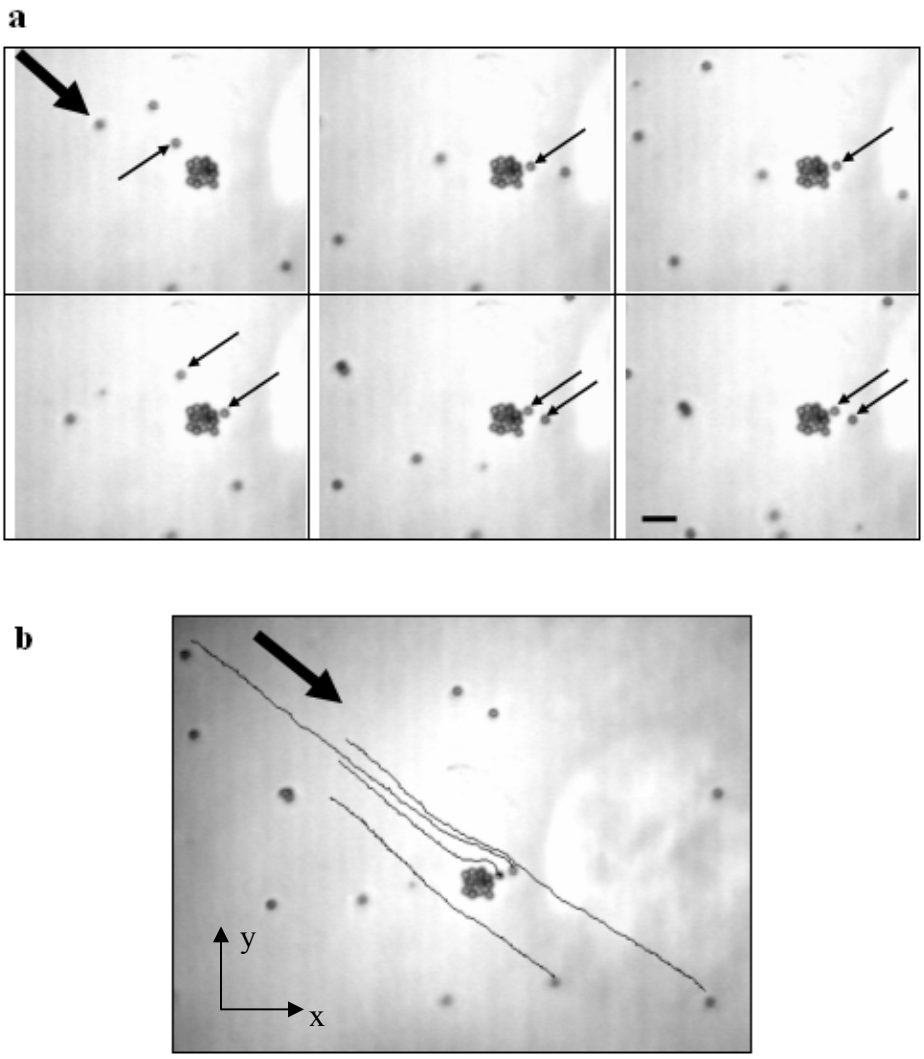

Figure 4.1 Trapping action near a microsphere cluster. a) The particles approaching and getting trapped near the cluster are indicated by arrows. Freely flowing particles can be seen at distances from the cluster. Scale bar, 8 μm. b) Trajectories of particles moving near the cluster under the influence of liquid current were tracked over ~ 6 secs. The particles moving very close to the cluster were observed to become trapped. The flow direction of the medium is indicated by bold arrows in figures 4.1(a) and (b).

flow. In figure 4.2(b) the observed trajectories of microspheres moving nearby the cluster are shown. From the recorded trajectories it is clearly seen that out of the moving microspheres only those moving in close vicinity of the cluster have got deviated from their initial direction of

motion and became trapped. The trajectories were recorded over a time duration of ~ 6 s. The trapping sites could be observed to be located at distances of ~1 or ~ 4 particle diameters from the cluster and in a plane normal to the laser beam axis i.e in the same plane in which the cluster is formed. Using centroid detection technique the position spectrum of the trapped sphere was

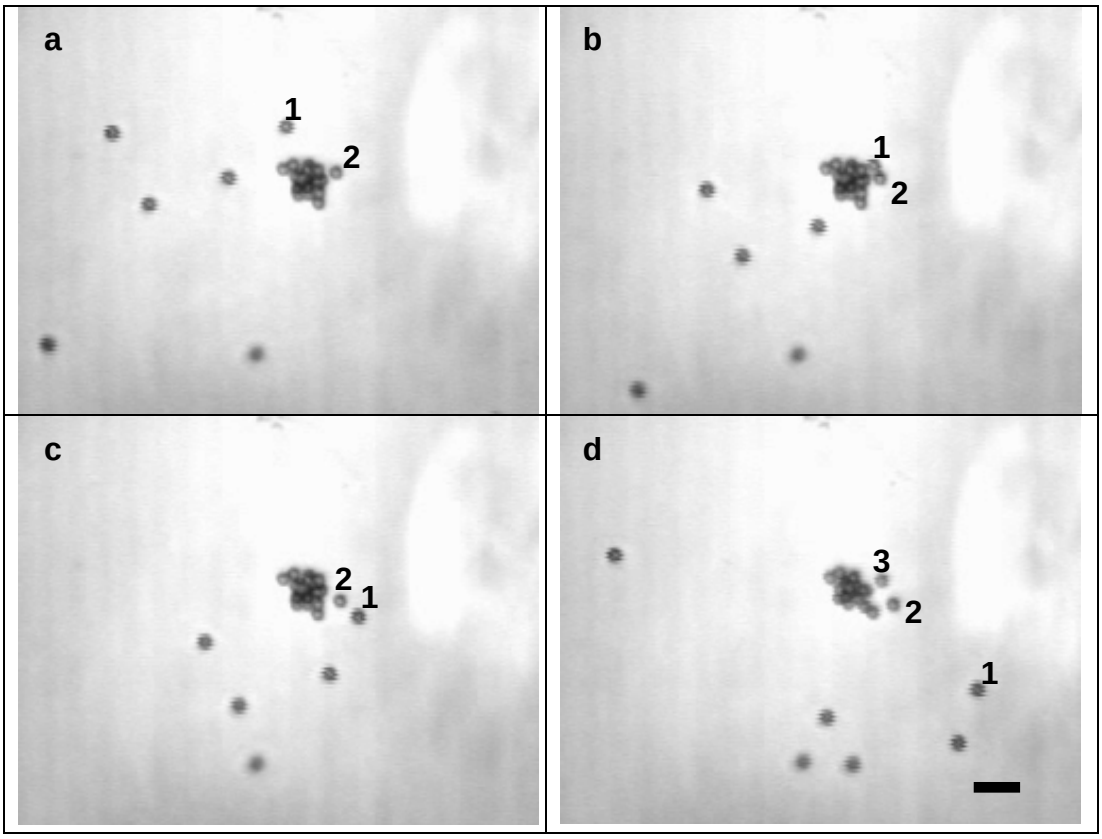

Figure 4.2 Image frames showing that a moving microsphere (marked as 1) knocking out a trapped sphere (marked as 2) out of its initial trapping position (the position in frames (a-b)). Sphere 2 therefore gets trapped at a new position as can be seen in frames (c-d). A new sphere (marked as 3) occupies the trapping site initially occupied by sphere 2. Scale bar, 6 μm.

determined at a sampling rate of 25 Hz. The measured position spectrum was used to estimate the trapping stiffness using equipartition method. For the microsphere trapped closest to the colloidal cluster, stiffness values of 0.187 pN/μm and 0.115 pN/μm were estimated in the x

direction and y direction respectively. The corresponding corner frequencies of the power spectrum of a 2 μm diameter particle were ~ 1-2 Hz. The sampling rate of 25 Hz was therefore suficient to get good estimate for the trap stiffness. We further estimated the drag force applied on the trapped sphere by the flowing medium. By noting the positions of a freely flowing sphere at known time intervals the x and y components of medium velocity were measured to be ~ 6 μm/sec and ~ 5μm/sec respectively. The drag forces on a 2 μm sphere were calculated using Stokes law (F_{drag}= - $6\pi\eta rv$, where η is the dynamic viscosity of the medium and r is the sphere radius) to be ~ 0.095 pN and ~0.079 pN in x and y directions respectively. The estimates for the trap stiffness and drag forces confirm the experimental observation that the trapping action was strong enough to prevent dislodging of the particles out of the trapping sites by the flowing medium. It is worthwhile to note here that the peak trapping force occurs at a distance of approximately the particle radius from the trap centre and is higher than the value estimated from the Hook's law. This is because the trap force profile for a spherical particle has an increasing slope until peaking at a displacement approximately equal to the radius of the bead [167]. For the 2 μm diameter bead the peak trapping force should therefore be significantly higher than ~ 0.187 pN and ~ 0.115 pN along x and y directions respectively.

We carried out several experiments to confirm that such binding action was not due to some experimental artifacts like non-specific binding to surface, polymer 'hair' sticking on the microspheres etc. The reproducibility of the binding action was ensured by noting that on several occasions a microsphere previously trapped at a nearby trapping site around the cluster could be dislodged by collisional impact from another moving microsphere and a new microsphere occupied the trapping site by itself (figure 4.2). These clearly indicate the observed trapping action at specific locations nearby the cluster was reproducible.

To further confirm that trapping indeed occurs at specific location relative to the trapped cluster we rotated the trapped cluster by introducing slight ellipticity (ellipticity ratio is ~ 1:2) in the trapping beam with help of a rectangular aperture (2 mm x 6 mm). With such elliptic beam the trapped microspheres cluster arranged itself in a preferred orientation with respect to the beam and when we rotated the beam by rotating the rectangular aperture the external sphere trapped by the scattered light from the cluster also followed the rotation. This conclusively shows that the observed trapping is indeed by scattered light from the microsphere cluster and not by any non-specific interactions. The results have been shown in figure 4.3(a-b).

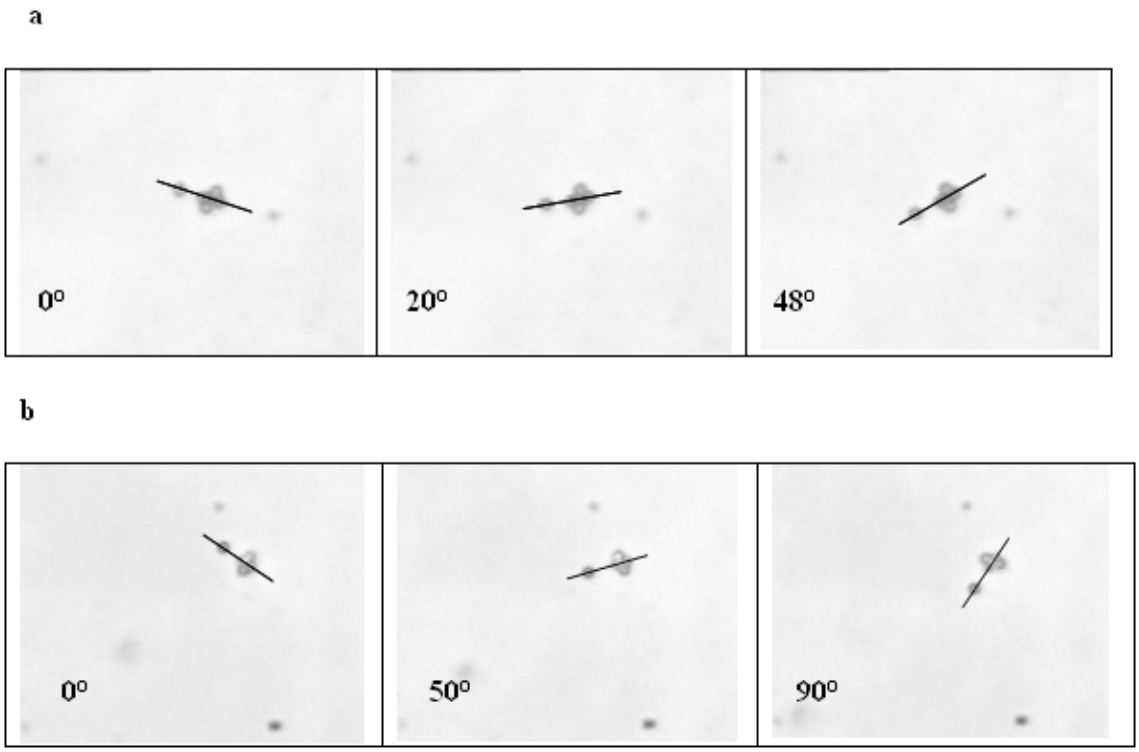

Figure 4.3 (a –b) Rotation of the trapped external microsphere in synchronism with the rotating trapped cluster. Interval between successive frames is ~ 15 sec.

Since modeling the coherently scattered optical fields from a random multiparticle cluster is not straightforward we carried out experiments using a simple one dimensional chain of polystyrene microspheres. To create this chain we used an elliptical trapping beam. This was

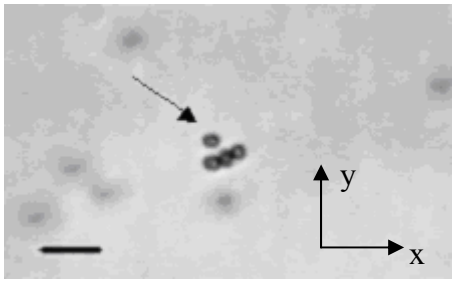

(a)

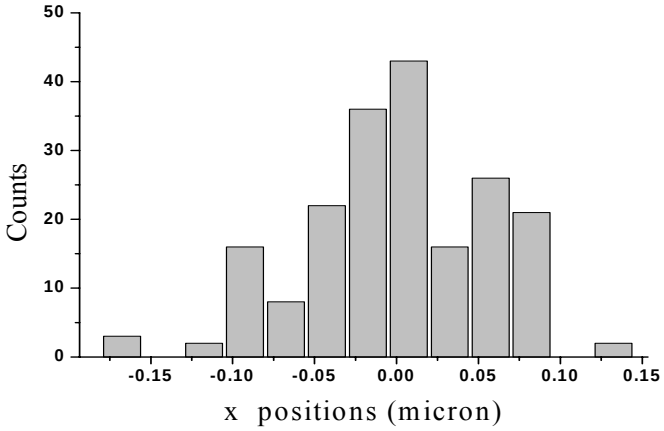

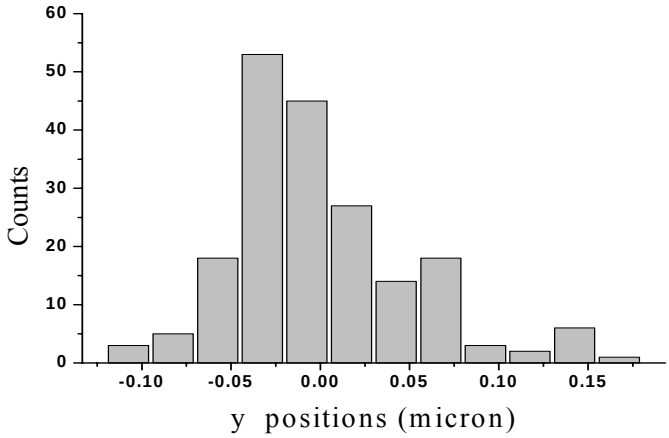

(b)

Figure 4.4 (a) Trapping action near a linear array of three particles. The trapped particle near the microsphere chain is indicated by arrow. Scale bar, 8 μm. (b) Position histogram of the trapped particle. The positions were recorded over 200 frames taken at 40 ms intervals.

generated using the zeroth order diffraction pattern from a rectangular aperture (~1 mm x ~6.5 mm) placed in the path of the laser beam. The higher orders, which may cause ambiguous effects, were removed by the finite back aperture of the microscope objective. Trapping of microspheres around this array at trap beam power of ~ 40 mW was investigated. In figure 4.4(a) we have shown the trapping of a microsphere near such an array of three microspheres. The microsphere was found to get trapped in the plane of the array at a distance of ~ 3 μm from the central microsphere. In the figure 4.4(b) the histograms for the positions of the trapped particle are shown. The observed slightly asymmetric shape of the histograms is due to the fact that the position histograms were recorded in presence of the fluid flow and also the trapping field pattern is not identical with that of a focused Gaussian beam but is an interference pattern produced as a result of scattered optical field from the microspheres. From the measured histogram the stiffness of the trapped particle was estimated to be ~ 1.3 pN/μm and 1.66 pN/μm in the x direction and y direction respectively.

4.4 DISCUSSIONS

The observation of the nearby (at distances of few μm from the cluster periphery) trapping sites outside the closely packed cluster suggests presence of optical binding forces arising because of interference between scattered light components from constituent microspheres of the

cluster. The intensity maxima occur due to interference among the scattering light fields from the constituent microspheres result in formation of local trapping sites.

In order to quantitate these results we experimentally investigated trapping of microsphere around a 1-D arrangement of three microspheres and compared the results with the calculated distribution of the light scattered from this array of microspheres. Assuming that the microspheres act as independent Mie scatterer, the scattered field from each of them can be expressed as [52],

$$\begin{bmatrix} E_i^s \\ E_r^s \end{bmatrix} = \frac{e^{-ikr+ikz}}{ikr} \begin{bmatrix} S_2(\theta) & 0 \\ 0 & S_1(\theta) \end{bmatrix} \begin{bmatrix} E_i^i \\ E_r^i \end{bmatrix} \tag{4.1}$$

Where the scattering functions $S_1(\theta)$ and $S_2(\theta)$ are given as

$$S_1(\theta) = \sum_{n=1}^{\infty} \frac{2n+1}{n(n+1)} [a_n \pi_n(\cos\theta) + b_n \tau_n(\cos\theta)]$$

$$S_2(\theta) = \sum_{n=1}^{\infty} \frac{2n+1}{n(n+1)} [b_n \pi_n(\cos\theta) + a_n \tau_n(\cos\theta)] \tag{4.2}$$

the functions π_n and τ_n are defined as,

$$\pi_n(\cos\theta) = \frac{1}{\sin\theta} P_n^1(\cos\theta)$$

$$\tau_n(\cos\theta) = \frac{d}{d\theta} P_n^1(\cos\theta) \tag{4.3}$$

Where P_n^1 are associated Legendre polynomials. Also

$$a_n = \frac{\Psi_n'(m\alpha)\Psi_n(\alpha) - m\Psi_n(m\alpha)\Psi_n'(\alpha)}{\Psi_n'(m\alpha)\xi_n(\alpha) - m\Psi_n(m\alpha)\xi'(\alpha)}$$

$$b_n = \frac{m\Psi_n'(m\alpha)\Psi_n(\alpha) - \Psi_n(m\alpha)\Psi_n'(\alpha)}{m\Psi_n'(m\alpha)\xi_n(\alpha) - \Psi_n(m\alpha)\xi'(\alpha)} \tag{4.4}$$

where $\alpha = ka = 2\pi ma/\lambda$ is the size parameter, m is the index of refraction, a is the particle radius, and Ψ_n and ξ_n are related to spherical Bessel functions.

For the trap beam parameters (power ~ 40 mW, focal plane size 1μm x 4μm) the total scattered power by a 2 μm diameter sphere can be estimated as,

$$P_{scat} = P_{in}.\ \sigma_{scat} \tag{4.5}$$

Where scattering cross-section σ_{scat} is given as,

$$\sigma_{sca} = Q_s.\pi r^2 \tag{4.6}$$

Q_s is the scattering efficiency can be estimated from equations 4.1 to 4.4 as 3.16 for polystyrene microspheres (refractive index ~ 1.59) with radius r as 1 μm. Out of the total scattered power only the fraction radiated into the solid angle subtended by the trapped sphere to the scattering sphere will contribute to the formation of interference maximum responsible for creating the trapping site. It should be noted that considering the close proximity of the trapped sphere to the scattering spheres the subtended solid angle is significant i.e ~ 0.35 sr for the trapped sphere onto the central scattering sphere. Considering the relevant solid angles and the angular distribution of the scattering pattern the interference pattern along the line joining the trapped external sphere and the central scattering sphere could be computed and shown in figure 4.5. The intensity distribution shows a periodic variation, resulting from the interference of the scattered field components from the three microspheres, with an intensity maximum at a distance of ~ 3 μm from the central microsphere of the array. This is in agreement with the observed trapping location as shown in figure 4.4(a). It should be noted that the two adjacent local maxima were estimated to be situated at 3 μm and 3.5 μm respectively. Among this the strongest one is located

at 3 μm at a distance equal to the average observed distance of the trapped microsphere. The difference of 0.5 μm between the two maxima is small compared to the particle diameter of 2 μm. In such a situation hopping between the two maxima is not likely to take place. One may

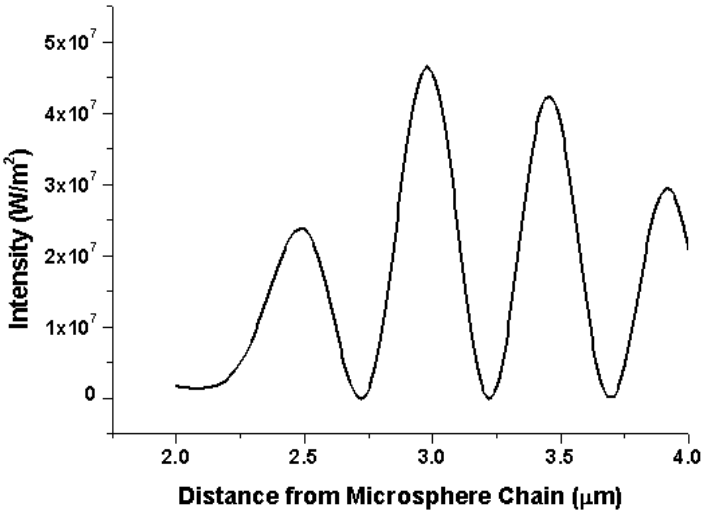

Figure 4.5 Calculated intensity pattern along the line joining the middle sphere in the 1-D array and the trapped sphere. The strongest peak is seen at a separation of 3 μm.

expect a larger positional fluctuation in the direction connecting the two maxima. This was indeed the case. The mean square position fluctuation in direction connecting the two maxima was measured to be ~ 4200 nm^2 whereas the value in a direction normal to that is ~2000 nm^2. Though the microsphere was expected to get trapped on the symmetry axis i.e. line perpendicularly bisecting the linear array structure, the observed small deviation of the trapping point from symmetry axis is believed to be due to the variation in size (~ 3% as per manufacturer's specifications) of the constituent spheres and small irregularities present in the intensity distribution along the line trap profile. It is also pertinent to note form figure 4.5 that the maximum intensity in the scattered field pattern is ~ 47 $\mu W/\mu m^2$. Therefore, the experimentally measured trapping stiffness of ~ 1.3-1.66 pN/μm for an intensity of ~ 47 $\mu W/\mu m^2$ appears

reasonable as in conventional optical tweezers trapping stiffness of ~ tens of pN/μm is obtained for a trap intensity of ~ mW/ μm^2 .

4.5 SUMMARY

We have shown that the scattered optical field from a trapped chain of microspheres can lead to trapping of nearby microscopic objects. Theoretically computed scattered field distribution from a one dimensional chain of polystyrene microspheres could successfully predict the experimentally observed trapping site. Such trapping mechanism using optical binding action may lead to newer approaches for building up self organized small systems and may even lead to sorting and guiding of microscopic bodies [168].

CHAPTER 5

LONG DISTANCE AXIAL TRAPPING WITH LAGUERRE-GAUSSIAN BEAMS

In this chapter I present the results of our study showing that the axial spread of the focal volume of a tightly focused beam propagating through a glass-water interface is much reduced for Laguerre-Gaussian (*LG*) modes as compared to the TEM_{00} mode. Therefore, the use of *LG* beam helps achieving a significant improvement in the axial trapping range of optical tweezers. The use of *LG* modes to manipulate biological cells from the bottom layer of the medium to the top surface layer was also demonstrated. The exposure of the cells to a higher oxygen concentration at the surface layer was used for estimation of the intra-membrane oxygen diffusion rate.

5.1. INTRODUCTION

Optical tweezers require tight focusing of laser light through a high NA microscope objective lens to produce the strong gradient forces necessary to overcome axial scattering forces and thus achieve stable three-dimensional trapping. The short working distance associated with high NA (NA>1) limits the axial trapping range to a typical value of ~ 200 μm. Further, because the particles to be trapped are often suspended in an aqueous medium the trap beam suffers significant spherical aberration at the glass-water interface leading to an increased axial spread of the focal volume with increasing distances from the substrate. The resulting reduction in the power density at focus leads to a reduction in the gradient forces [169-171] and consequently a limited axial trapping range which is significantly shorter (often under 100 μm) than the

available working distance of the objective lens. Longer axial trapping range is however required for carrying out experiments on objects at free liquid surface or for minimizing the influence of substrate while studying sensitive processes like nucleation of crystals. Trapping of objects at liquid air interface has been achieved using longer working distance, low NA objective lenses by exploiting some additional forces like surface tension to balance the axial scattering force (as discussed in chapter 3 and in references 172 and 173). However, such approaches lack the versatility and simplicity of conventional optical tweezers. Deformable mirrors [169] have been used to change the wavefront curvature of the trapping laser beam and thus compensate for the spherical aberrations occurring at glass-water interface. However, this could help improve the trap efficiency in axial direction only for small trapping depth (< few tens μm). Changing the microscope tube length can change the divergence of the trapping laser beam at the entrance aperture of the objective lens and causes an aberrative effect opposite to that caused by the glass-water interface. Therefore, a change in the microscope tube length has also been used to compensate for the spherical aberration caused at the interface and increase the axial trapping distance [170]. However, this procedure is also a bit cumbersome and difficult to implement on commercial microscopes having the tube lens fitted inside the microscope frame.

It is known that *LG* modes can lead to improved axial trapping stiffness [174-176] since for these modes the axial rays that generate axial scattering force are not present. We show that the *LG* modes owing to a narrower range of cone angles also have a reduced axial spread of the focal volume due to spherical aberration at the glass-water interface. Thus the use of *LG* beam has help achieve significant improvement in the axial trapping range compared to the use of TEM_{00} mode. We present in this paper the results of our simulation of the axial trapping ranges for different trap laser modes and the experimental verification of the same. We also describe the

use of the large axial trapping range achieved using LG_{01} mode to transport a human colon adenocarcinoma (Colo-205) cell from the bottom layer of the medium to the top surface layer, exposing it to a higher atmospheric oxygen concentration and report measurements on the diffusion of oxygen in the plasma membrane.

5.2. THEORY

A simple ray optics description shown in figure 5.1(a) can help understand how *LG* modes suffer a lower degree of spherical aberration at the glass-water interface. Since the *LG* mode traverses the glass-water interface with a narrower angular range of rays vis a vis the TEM_{00} mode, the spherical aberration gets reduced for the *LG* mode. For a quantitative estimation of the spread in focal volume due to spherical aberration at the glass-water interface we have used the electromagnetic theory treatment developed in references 177-178 for the propagation of a tightly focused laser beam through an optical system consisting of two media separated by a plane interface

The diffracted field of *LG* mode, at the point p (r_p,θ_p,φ_p) can be expressed as the function of conic angle θ as

$$E(p) = \int_0^{\alpha}\int_0^{2\pi} \Psi_{m,l}(\theta)\sqrt{\cos\theta}\, P(\theta\ ,\phi)\exp[ik_0(r_p\kappa + \psi_d)]\exp(im\phi)\sin\theta\ d\theta\ d\phi \tag{5.1}$$

Where, the origin of the coordinate system is assumed at the Gaussian focus in the absence of the aberration caused by the refractive index interface and

$$\Psi_{m,l}(\theta) = A_0 \exp\left[-\gamma^2\frac{\sin^2\theta}{\sin^2\alpha}\right]\left(\sqrt{2}\gamma\frac{\sin\theta}{\sin\alpha}\right)^{|m|} L_l^{|m|}\left[2\gamma^2\frac{\sin^2\theta}{\sin^2\alpha}\right] \tag{5.2}$$

and,
$$\gamma = \frac{a}{w_0} \tag{5.3}$$

a being the microscope objective aperture radius and α is the largest conic angle determined by the numerical aperture of the objective lens. A_0 is the amplitude, w_0 is the beam radius at waist and $L_l^m(x)$ are the Laguerre polynomials, here l is the radial mode number and m is called the azimuthal index, with $l = 0$ and $m = 0$ denoting a zeroth order Gaussian mode (TEM_{00}). k_0 is the free space wavenumber of the optical beam and $P(\theta,\varphi)$ and ψ_d represents the polarization distribution and spherical aberration effect respectively [178].

Oil immersion objectives are commonly used for optical trapping since the larger numerical aperture for these helps produce the strong gradient forces necessary to overcome axial scattering forces. However, the typical working distances of immersion objective lenses are up to ~200 μm. Further due to a finite thickness of the immersion medium the effective working distance of such lenses are even less. In order to demonstrate long distance (>200 μm) axial trapping we have used a non-immersion objective (Zeiss Acroplan 60X, NA 0.8) that has a working distance of ~ 300 μm. The non-immersion objective lens was also found to be particularly suitable for demonstrating the usefulness of the *LG* trap mode for manipulation of cells at free liquid surface (typical thickness of liquid film was observed to be ~ 200 μm). The choice of *NA* ~0.8 was made because it can produce sufficient optical field gradient to trap microscopic objects [179]. In our experiments with TEM_{00} mode we overfilled (fill factor, $w_0/a \sim 1.5$) the objective entrance aperture to ensure good trapping efficiency. For *LG* modes with azimuthal index m the maximum intensity occurs at a radial distance [174],

$$r_{\max} = w_0 \sqrt{\frac{m}{2}} \tag{5.4}$$

Therefore, to avoid significant loss of power due to annular nature of the *LG* modes we keep the Gaussian beam radius (w_0) smaller than that of the objective entrance aperture (fill factor $w_0/a \sim 0.65$).

Figure 5.1(b) and 5.1(c) show the grayscale images depicting the transverse and axial intensity profiles (I_f) respectively around the focus with increasing height (d) of the beam focus from the substrate for (i) TEM_{00} and (ii) LG_{01} modes. The origin was taken as coincident with the focal point predicted from geometrical optics and z- axis is along the laser beam axis. The intensity values are normalized with respect to the maximum value and represented in gray shades. The shortest trapping distance was considered as $d \sim 15$ μm. The intensity profiles show a decrease in the peak intensity at the focal plane with d due to an increase of focal volume that results because of an increase in the spherical aberration with increasing d. Note that because of spherical aberration the peak intensity positions along the beam axis also get displaced from the geometric axis predictions ($z=0$). In figure 5.1(d) we plot the fall in peak intensity ($I_{f,max}$) with d for different laser modes. Taking the distance over which the focal intensity falls to 50% of its value at $d \sim 15$ μm as the axial trapping range the corresponding ranges were estimated to be ~100 μm for TEM_{00} mode and ~ 215 μm *for* LG_{01}, ~ 150 μm for LG_{02} and ~ 135 μm for LG_{03} mode. The estimated trapping distance found to be the maximum for first order *LG* mode whereas from the point of view of the reduced angular spread for higher order *LG* modes one should have expected it to be larger for higher order *LG* modes. This may be due to the fact that although the range in cone angles becomes smaller with increasing order of the *LG* modes the average cone angles also increase. The latter should lead to an increase in spherical aberrations and may account for the estimated reduction in axial trapping range for $m = 2$ and 3 modes.

While for work with silica microspheres we used trap beam at 532 nm, for experiments with cells 1064 nm trapping wavelength was used. This was done because significant damage to cells was observed when using 532 nm trap beam due to the strong absorption by cells at 532 nm. For work with silica microspheres the use of the 532 nm was more convenient because the

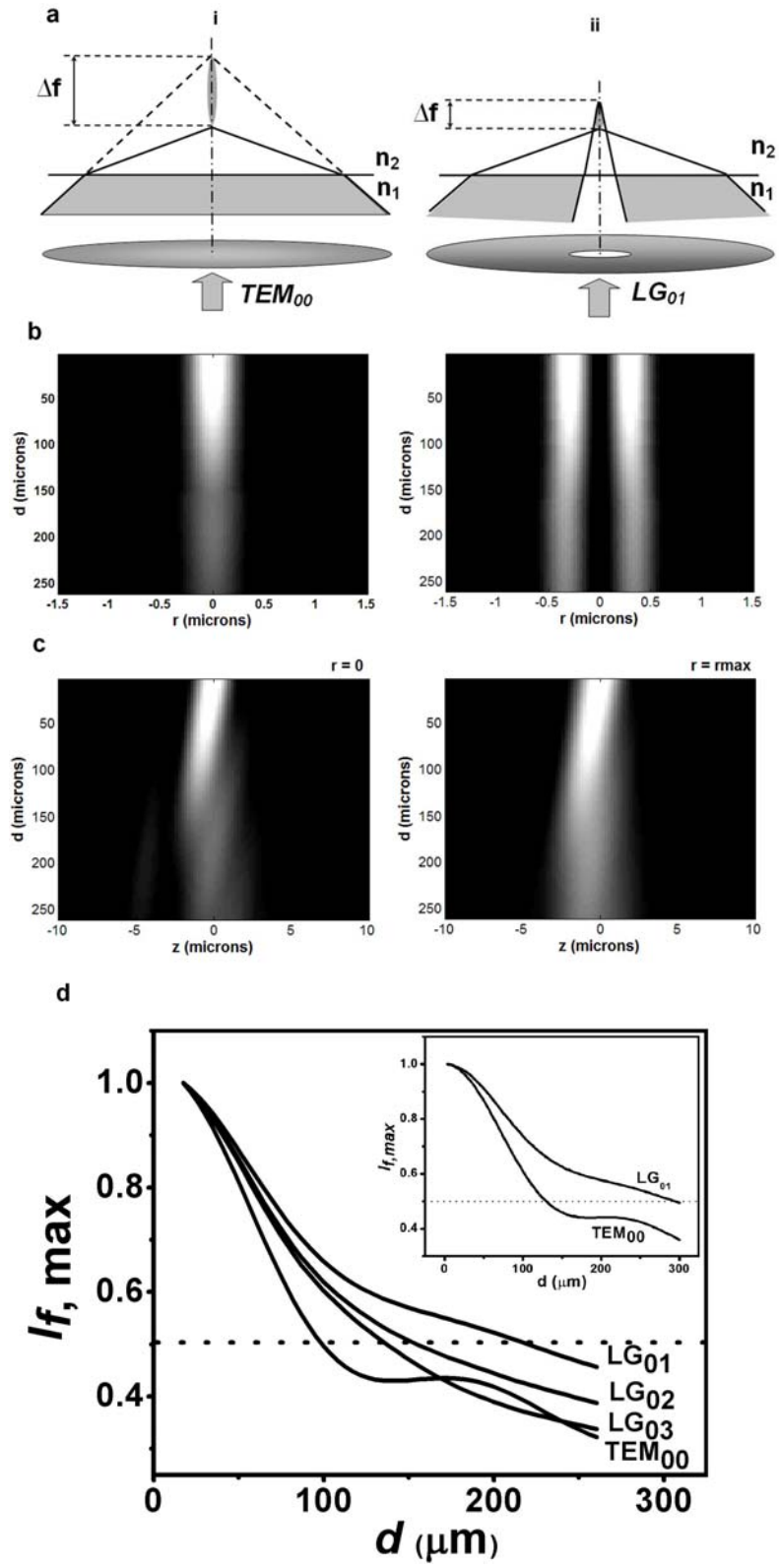

Figure 5.1 (a) Geometric optics representation of the refraction of a light beam focused through a refractive index interface with $n_2 < n_1$. (b) The geayscale images showing

transverse focal profiles as a function of trapping distances for (i) TEM_{00} mode and (ii) LG_{01} mode. (c) The axial focal spread as a function of trapping distances for (i) TEM_{00} mode and (ii) LG_{01} mode. (d) The variation of peak intensity of the trap beam with trapping distance for different laser modes. All data shown are for laser wavelength of 532 nm. Inset in 1(d) shows the peak intensity of the trap beam with trapping distance for TEM_{00} and LG_{01} mode at laser wavelength 1064 nm.

beam being visible made it easier to ensure that the fill factor for trapping beam at objective entrance pupil was same for all the orders of *LG* beams. With a change in laser wavelength the axial trapping range is expected to vary as degree of aberration is wavelength dependent, theoretical analysis was performed at 1064 nm trapping wavelength for TEM_{00} and LG_{01} modes. The analysis shows an increase in trapping range for all the laser modes with 1064 nm trapping wavelength compared to 532 nm (figure 5.1(d), inset).

5.3 MATERIALS AND METHODS

The experimental arrangement for trapping with *LG* beams is similar to that shown in figure 2.9 of chapter 2. The trapping laser sources used in the experiments were both the fundamental mode Nd:YVO_4 laser emitting at 1064 nm (Compass 1064-4000, Coherent Inc) and the frequency doubled Nd:YVO_4 laser emitting at 532 nm (Verdi-5, Coherent Inc). The linearly polarized cw Gaussian beam from the laser source was phase modulated by a spatial light modulator (SLM, LCR-2500, Holoeye) to generate different orders of *LG* modes. The diffracted first order was directed onto the microscope objective lens (Zeiss Acroplan 63X, NA 0.8) to form the optical trap. The sample cells were mounted upon a piezo-controlled x-y-z translation stage (P-517.3CL, Physik Instruments) that can be moved with a step resolution of ~ 1nm. A three lens zoom assembly was used to adjust the size of different laser modes and thus optimize

their coupling into the entrance aperture of the objective. The polarization ellipticity of the trap laser beam was controlled using a polarizer and quarter wave plate combination so that only left circularly polarized state being used due to its usefulness for producing most symmetric intensity distribution and complete disappearance of axial intensity at the focus in case of first order *LG* mode [177]. The brightfield/fluorescence images were observed with a monochrome CCD camera (DC350F, Leica Microsystems).

Silica microspheres (of diameters ~2, 3 and 5 μm,) were used to evaluate the performance of different laser modes (TEM_{00} and *LG modes (m=1,2,3)* at 532 nm) for trapping over varying axial distance. The microspheres were suspended in water in a sample chamber made of two cover slips sticked together with spacers of ~ 450 μm in between them.

The large axial trapping range achieved using LG_{01} mode was used to transport a human colon adenocarcinoma (Colo-205) cell from the bottom layer of the medium to the top surface layer exposing it to a higher oxygen concentration. The diffusion of oxygen in the plasma membrane was investigated using quenching of a membrane tagged fluorophore (6-lauroyl,1-2-dimethylamino naphthalene (laurdan)). Fluorescence measurements of laurdan were done using excitation light at 340-360 nm and emission light was collected above 400 nm. Notably the emission maximum of laurdan can shift from 440 nm to 490 nm depending on whether the lipids are in a gel-phase or in a liquid-crystalline phase. The unquenched lifetimes in both the cases are nearly identical and therefore an average value of ~ 5 ns was considered in our studies [180].

Human colon adenocarcinoma (Colo-205) cell line, was purchased from National Centre for Cell sciences (NCCS), Pune, India. It was grown in monolayer in RPMI medium supplemented with 10% FBS, penicillin (50 units/ml) and streptomycin (50 units/ml) at 37^{o} C in

a humidified incubator with 5% CO_2 atmosphere. Medium used for growth of cells was buffered with 2.2 g/lit sodium bicarbonate and 20 mM HEPES. Cells were incubated with laurdan (30 μg/ml) diluted in culture medium with continuous stirring in rotary vessel for 30 minutes. It is pertinent to note here that the uptake of laurdan (30 μg/ml) by the colo cells was estimated by monitoring the time lapsed fluorescence intensity from the cells. Measurements were carried out on at least twenty cells taken fresh from the incubated population at different incubation times separated with a time interval of five minutes. After incubation the cells were washed with phosphate buffer saline (PBS). Experiments were carried out on open coverslips. For trapping the colo cells LG_{01} mode generated from a laser operating at 1064 nm wavelength was used, as trapping the cells with 532 nm wavelength was observed to severely damage the cells. The laser power used for trapping colo cells was ~ 10 mW before the 63X objective. Fluorescence images were recorded with the CCD camera with an acquisition time of ~100 ms. When the cells were trapped at the bottom of the fluid layer where the quenching of laurdan fluorescence by dissolved oxygen is expected to be negligible due to the low concentration of oxygen no significant change in the 340-360 nm excited fluorescence (measured in sequential measurements with 100 ms exposure time) from laurdan was observed for time period of up to 20 s after which some reduction was observed suggesting some photobleaching beyond this point. At the air interface due to significant oxygen quenching fluorescence intensity was observed to be decayed within 3-4 s. Because for making comparison between fluorescence intensities recorded from colo cells trapped at bottom and top layer of the sample volume, the cells were exposed to 340-360 nm excitation light for only 100 ms, photobleaching effect was not expected to be significant.

The measured fluorescence intensity of the fluorophore in the absence of oxygen (F_0) can be related to F_{eq}, the corresponding intensity after equilibration with an ambient medium having oxygen solubility of C_{eq}, following Stern-Volmer type of relation [181, 182],

$$\frac{F_0}{F_{eq}} = 1 + k\tau_0 C_{eq} \tag{5.5}$$

Where, τ_0 represents the unquenched fluorescence lifetime. C_{eq} at the surface layer was estimated using Henry's law i.e $C_{eq}=S.p_{eq}$, where p_{eq} is the external partial pressure of oxygen, and S is the Henry's law constant of the gas solubility (~ 2.68 x 10^{-7} mol.cm^{-3}). Since oxygen is a lipophillic substance, its concentration in the plasma membrane is expected to be higher than in the aqueous medium by ~ 4.4 times [181] leading to a value of C_{eq} ~ 1.18 x 10^{-6} mol.cm^{-3} in plasma membrane. To minimize the oxygen quenching effect inside the medium small amount of sodium dithionite was added.

The rate coefficient k, is related to the diffusivity of the quencher. Making the assumption that every collision between singlet fluorophore state and oxygen is effective in quenching [181], k is related to the diffusion constant by the Einstein-Smoluchowski expression,

$$k=4\pi\sigma N_A D \tag{5.6}$$

where N_A is Avogadro's number, σ is the sum of the molecular radii of oxygen and the fluorophore, and D is the diffusion coefficient of oxygen alone, a reasonable assumption on the basis that the diffusion coefficient of oxygen is much larger than that for the fluorophore. The interaction radius, σ, was taken as ~ 1x10^{-7} cm [182].

5.4 RESULTS & DISCUSSIONS

The silica microspheres were trapped at a height of ~ 15 μm from bottom surface. The trapping power was adjusted to be such that particles are just ejected out of the trap when the stage is moved in vertically upward direction with a velocity greater than 4 μm/s. The choice of upward motion was guided by the fact that in an inverted optical tweezers, the trap is the weakest in that direction due to the opposing action of light scattering and gradient forces [56]. Since at a distance of ≥ 15 μm from the glass surface the increase in medium viscosity due to surface effects is < 5%, drag force can be expressed as $F_{drag} = 3\pi\eta dv$ (η medium viscosity, v relative velocity and d particle diameter). A relative speed of 4μm/s would correspond to drag force of 0.0754 pN, 0.113 pN and 0.188 pN for 2, 3 and 5 μm particles respectively. For TEM_{00} laser mode the trapping powers required to hold the 2, 3 and 5 μm particles were 1.5 mW, 3.8 mW and 5.6 mW. The powers were measured at the entrance aperture of the objective. These power levels were kept unchanged when using *LG* modes to ensure an even comparison of trapping range. It may be noted here that unlike drag forces the trap powers are not linearly proportionate with the particle diameters [183].

To estimate the axial trapping range we moved the objective lens vertically in steps of 20 μm starting from d ~ 15 μm and at each point we checked for the trapping strength by subjecting the trapped sphere to a vertical drag of about half of that value used at d ~ 15 μm by moving the stage at a speed of 2 μm /s over 10 μm distance. The height at which the particle just escapes from the trap was taken as an estimate of the axial trapping range for the trapping laser mode.

The measured trapping ranges for 2, 3 and 5 μm silica spheres with TEM_{00} and *LG* modes *(m=1,2,3)* are shown in figure 5.2(a). For each mode of the trap beam and particle size the measurements were made for five particles. Consistent with theoretical estimates, for all particle

sizes the trapping range is seen to be the maximum for LG_{01} mode. While for 2 μm spheres, the trapping ranges with LG_{02} and LG_{03} modes were observed to be shorter than with TEM_{00} mode. For sphere sizes of 3 μm and 5 μm, the axial trapping ranges with all *LG* modes were observed to be larger than that with TEM_{00} mode. This appears to be due to the fact that with increasing *m* values the size of the bright annulas in *LG* modes increases and thus a smaller fraction of the light field interact with the trapped 2 μm sphere [174].

For an open film of sample (typical thickness of the liquid film was ~ 200 μm) with the use of LG_{01} mode trap beam we could trap particles near the bottom glass surface and move it upto the free air interface. Figure 5.2 (b) shows manipulation of a 3 μm silica sphere from bottom layer of the medium up to the free surface. When we move the sphere up to the air interface the sphere gets pushed against the free water surface and therefore gets displaced downward and seen as an out-of-focus image. It is pertinent to note here the no signature of thermocapillary effect was observed due to the use of an order of magnitude smaller laser power than that required for any significant thermocapillary action [172].

The ability of *LG* trapping mode to manipulate objects at air-liquid interface leads to the possibility that response of biological objects to the environment near the free surface can be studied. For example, with *LG* trap beam we can hold a cell deep inside the medium having minimum concentration of dissolved oxygen and thereafter lift the trapped cell upto the top layer near the air interface for exposure to a higher oxygen concentration. By tagging the cell with suitable membrane probe, the difference in the extent of oxygen mediated fluorescence quenching between the two cases can be used to estimate the oxygen diffusion rate in the membrane. It is pertinent to note here that with ~10 mW of trapping laser power we noted that

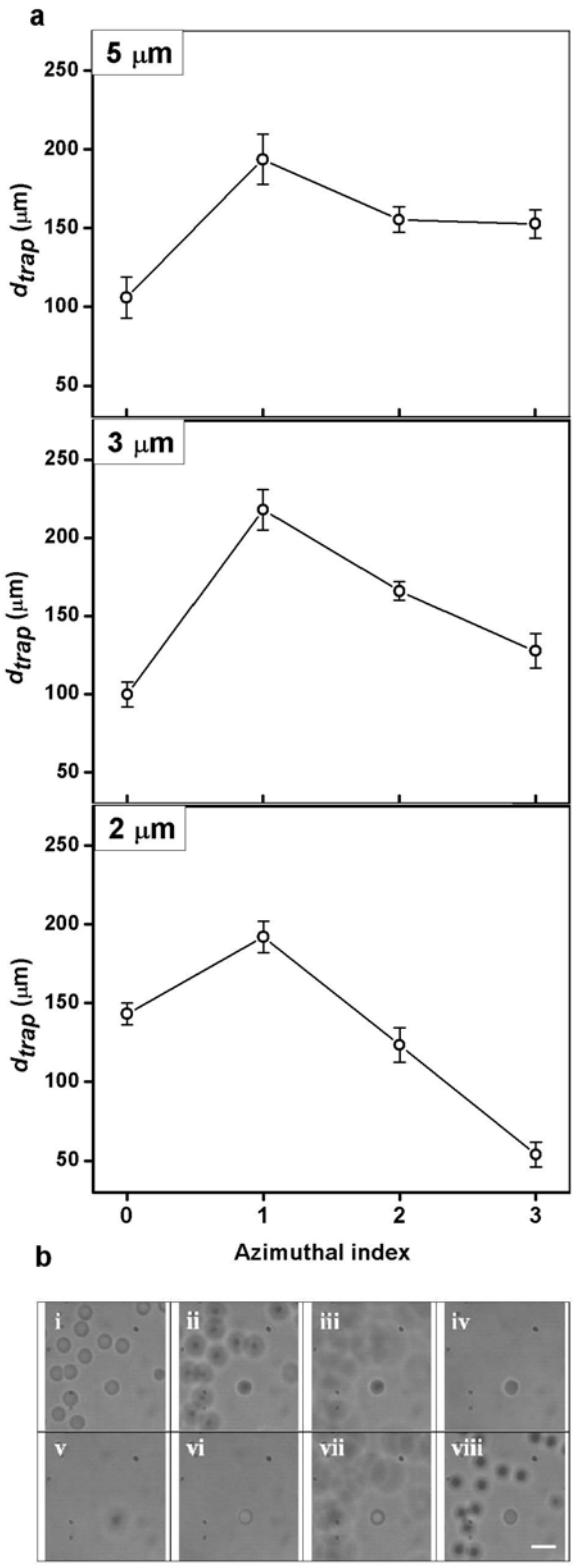
a
5 μm
3 μm
2 μm
d_{trap} (μm)
250
200
150
100
50
0
1
2
3
Azimuthal index
b
i
ii
iii
iv
v
vi
vii
viii

Figure 5.2 (a) Maximum trapping depth observed for different size of silica microspheres using TEM_{00} and LG modes (b) Manipulation of a 3 μm silica sphere from bottom of the medium upto the top free surface and back using LG_{01} mode: (i) The silica sphere was trapped at the bottom layer identifiable by other untrapped spheres. (ii)-(iv) The trapped sphere being lifted from the bottom layer towards the top free surface. The untrapped spheres can be seen to be out of focus. (v) The sphere is trapped at the free top layer. As the trap focus is lifted above the top free surface the sphere can be seen to be pushed down by surface tension force. (vi-viii) The trapped sphere is manipulated back towards the bottom of the medium. Thickness of open sample film ~ 200 μm. Scale bar for 5.2b, 5 μm.

colo cells could be moved over an average height of ~ 240 μm as measured over five cells using LG_{01} trap beam whereas with TEM_{00} mode the cells can be taken to a mean height of ~ 145 μm (Figure 5.3a). Considering the typical thickness of an open sample film ~ 200 μm, use of LG_{01} trapping mode was considered to be more appropriate for trapping the cells at free liquid surface.

In Figure 5.3 b(i) and (ii) we show the brightfield image and laurdan fluorescence intensity image of a trapped colo cell respectively. Figure 5.3c shows the time lapsed data for dye uptake by the cells at 30 μg/ml concentration. Over a total observation time of 40 minutes the fluorescence intensity was observed to increase up to 25 minutes and then leveled off. Therefore, for all our experiments an incubation time of 30 minutes was used. Sodium dithionite was added into the cells suspension to deoxygenate the cell membranes and to minimize the dissolved oxygen concentration in the medium. Therefore, the fluorescence intensity observed for the cells trapped near the bottom layer were taken as unquenched fluorescence intensity (F_0). Also we observed that for the cells trapped deep inside the medium the fluorescence intensity remained stable with time indicating absence of oxygen quenching. When we move the trapped

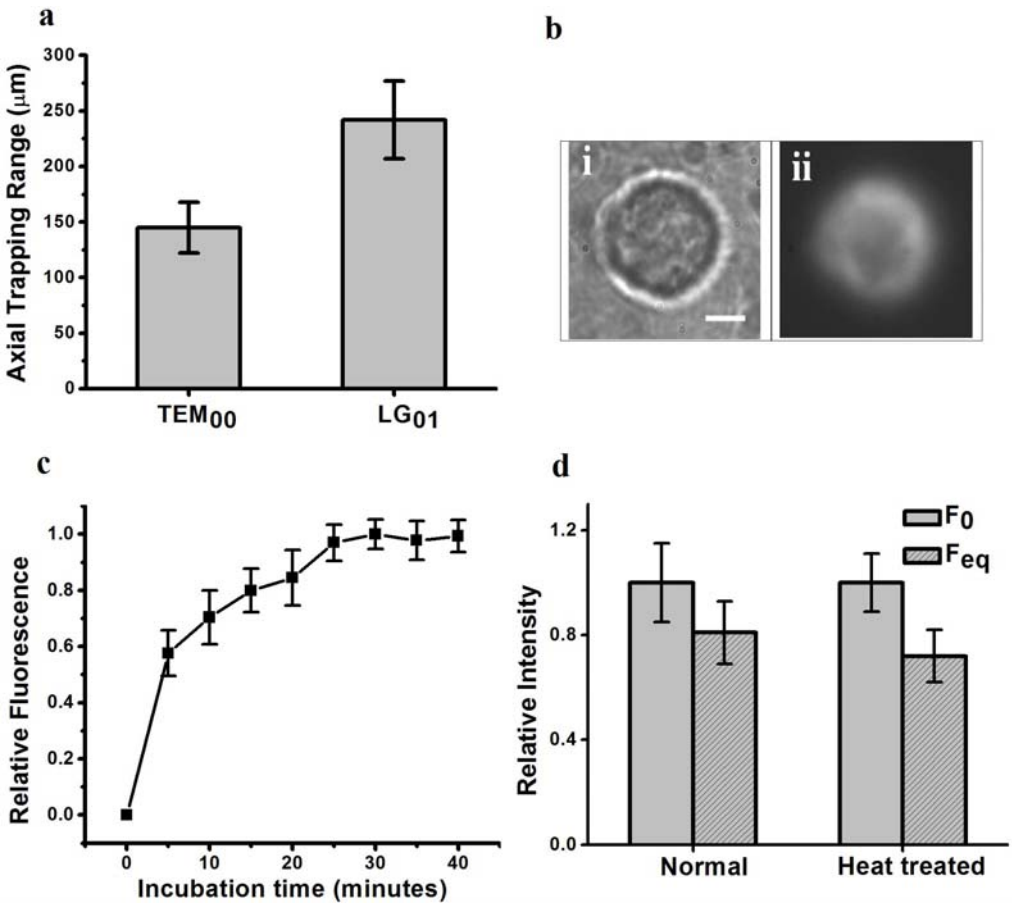

Figure 5.3 (a) The axial trapping range observed for colo cells with TEM_{00} and LG_{01} modes. The data shown are the mean over five cells. (b) Brightfield (i) and fluorescence image (ii) of a trapped colo cell. (c) The fluorescence equilibration profile of the colo cells when incubated with 30 μg/ml laurdan. The observed fluorescence seen to reach a steady state after an incubation period of ~ 25 minutes. (d) Observed mean relative fluorescence intensities of cells when trapped at the bottom (F_0) and at the top surface (F_{eq}). The data for cells although kept at room temperature (25 ºC) and cells heat treated for ~1 hr at an elevated temperature of ~ 55 ºC are shown. Scale bar for 5.3b, 5 μm.

cells onto the free surface we could observe a reduction in fluorescence intensity (F_{eq}). Also the decay of fluorescence intensity with time confirmed the role of oxygen quenching. The relative fluorescence intensity for the cells at the air-liquid interface with respect to the cells trapped deep

inside the medium is shown in figure 5.3(d). The data shown is the mean value taken over ten cells. The mean F_0/F_{eq} ratio was ~ 1.23 yielding an oxygen diffusion rate of ~ 5.2 x10^{-5} $cm^2.s^{-1}$. The value is in reasonable agreement with the value for biological membranes [181]. It is also known that membrane fluidizers like a heat treatment [184] can increase the membrane permeability of the cells and therefore can effect a higher intra-membrane oxygen diffusion rate [185]. The measured values for F_0 and F_{eq} for cells heat treated for ~ 1 hour at a temperature of 55 °C are shown in figure 5.3d. As expected the value of F_{eq} is reduced compared with normal cells indicating an increase in oxygen diffusion rate inside the membrane of heat treated cells. The mean F_0/F_{eq} ratio for the heat treated cells was ~ 1.38 yielding an oxygen diffusion rate of ~ 8.5 x10^{-5} $cm^2.s^{-1}$.

5.5 SUMMARY

Use of *LG* mode trap minimizes the effect of spherical aberration at glass-liquid interface and facilitates trapping of objects at a larger (~ 200 μm) axial distance. The large axial trapping range achieved using LG_{01} mode could be used to transport a human colon adenocarcinoma (Colo-205) cell from the bottom layer of the medium to the top surface layer exposing it to a higher oxygen concentration. Measurements on the diffusion of oxygen in the plasma membrane could be made by monitoring the oxygen induced quenching of fluorescence from cells tagged with membrane probe laurdan.

CHAPTER 6

OPTICAL TRAPPING OF SPERMATOZOA USING LAGUERRE-GAUSSIAN LASER MODES

Results of a study on the use of *LG* modes for optical trapping of spermatozoa are presented in this chapter. The results show that for a given trap beam power the first order *LG* mode (LG_{01}) leads to lower photo damage to the cells without compromising the trapping efficiency.

6.1. INTRODUCTION

Optical tweezers are being used for measurements on the motility of spermatozoa [186-188], and for *in-vitro* fertilization by facilitating selective transport of individual spermatozoon to oocytes [189, 190]. To minimize possible damage to the cells due to exposure to the high light intensity (~hundreds of $MW.cm^{-2}$) at the trap focus, lasers in near infra red region (wavelength ~ 1 μm), where the absorption of the cellular components is minimal, are used. However, even at 1064 nm, negative effects of laser exposure on spermatozoa have been reported [106], which originate presumably from the non-linear light absorption [191]. Studies on the use of *LG* laser modes for trapping of microscopic objects, have shown that compared to the TEM_{00} mode LG_{01} mode leads to an improved axial [174] and transverse [30] trapping efficiency due to the fact that optical trapping force is primarily contributed by the off-axis large conic angle rays. The use of *LG* laser beam may therefore allow efficient trapping of the motile spermatozoa while the absence of strong axial intensity and redistribution of power into the doughnut like region may

help minimize the possible photo damage. We have therefore investigated the use of *LG* modes for manipulation of spermatozoa. The results obtained confirm that as compared to TEM_{00} Gaussian mode the use of LG_{01} mode leads to significantly lower photo damage for similar trapping efficiency.

6.2. MATERIALS AND METHODS:

The optical tweezers set-up is similar to that described in figure 2.9 of chapter 2. The set-up consists of a frequency doubled Nd:YVO_4 laser emitting at 532 nm (Verdi-5, Coherent Inc). It is pertinent to note here that the major motivation for the work described in this chapter is to investigate the relative efficacy of the use of *LG* modes and TEM_{00} Gaussian mode for the trapping of spermatozoa. We therefore chose 532 nm as the trap wavelength, since significant photodamage expected at this wavelength would facilitate a comparative evaluation of photo-damage caused by different trap beam profiles. The linearly polarized cw Gaussian beam from the laser was phase modulated by a spatial light modulator (SLM, LCR-2500, Holoeye) to generate different orders (azimuthal indices) of *LG* modes. The diffracted first order was directed onto a high numerical aperture (NA) microscope objective lens (Zeiss Plan-Neofluor 100X, 1.3) to form the optical trap. The three lens zoom assembly was used to size the different orders of laser beams to fill ~80% of the objective entrance aperture. A left circularly polarized state was chosen for the trap laser beam using a polarizer and quarter wave plate combination placed after the SLM. The brightfield images and DPH fluorescence was observed with a monochrome CCD camera (DC350F, Leica) and color images of acridine orange stained cells were observed using a color CCD camera (Watec Inc).

Goat testes were collected from local abattoir. Spermatozoa were collected from the cauda epididymis by retrograde flushing into the pre warmed (~37 °C) media (1 mg of bovine

serum albumin (BSA) per 1 mL of Biggers, Whittens, and Whittingham (BWW) medium [188]). The above suspension was filtered through nylon mesh filter and thereafter centrifuged (at 2000 rpm for 10 minutes). Finally, the spermatozoa were re-suspended in BWW. The sample and buffer medium used for the experiments were then kept at 37 °C. The average size of the paddle shaped head of a goat spermatozoon estimated from bright field microscope images was ~ 8 μm x 3.5 μm x 1.7 μm (length x width x thickness). For vital staining of spermatozoa, propidium iodide (PI) was used. A stock solution of 0.5 mg PI per ml of water was prepared and stored frozen at –20 °C in the dark. The stock solution was added at the time of experiments into the spermatozoa samples so that the final concentration was 5 μg/ml. The suspension was incubated for 5 min at room temperature (~25º C). Laser exposure induced DNA damage to the spermatozoa was monitored using acridine orange (AO) staining. AO exhibits green and red fluorescence depending on whether it intercalates into double-stranded nucleic acids (DNA) or single-stranded nucleic acids (damaged DNA and RNA) respectively. For staining the spermatozoa with AO, the sperm chromatin structure assay method [192, 193] was used.

In order to assess the two photon effects that can be caused by the LG_{01} and TEM_{00} trapping beams a fluorescent probe (Diphenylhexatriene (DPH)) was used. DPH suspension (~ 4 mM) was prepared by dissolving it in dimethyl sulphoxide (DMSO). Since DPH has minimum absorption above 400 nm, direct single photon excitation of the probe molecules from the 532 nm laser beam is unlikely. It has its strongest absorption bands in the region 300-400 nm and has weak absorption in the spectral region ~ 240-270 nm [194]. The fluorescence emission could be observed using long pass filter having transmission above 400 nm.

6.3. THEORY

It is knwon that for an optical system consisting of two media separated by a plane interface the diffracted field of *LG* mode, at the point *p* (r_p,θ_p,φ_p) can be expressed as the function of conic angle θ as discussed in section 5.2 of chapter 5,

$$E(p)=\int_0^{\alpha}\int_0^{2\pi}\Psi_{m,l}(\theta)\sqrt{\cos\theta}P(\theta,\phi)\exp[ik_0(r_p\kappa+\psi_d)]\exp(im\phi)\sin\theta d\theta d\phi \tag{6.1}$$

The intensity distributions of TEM_{00} and higher order *LG* modes computed using equation 6.1 are shown in figure 6.1. It is pertinent to note that only left circularly polarized (LCP) state is considered for $P(\theta,\varphi)$, as the LCP state produces most symmetric intensity distribution and complete disappearance of axial intensity at the focus in case of LG_{01} mode [178]. For identical power the peak intensities at focus for the LG_{01} beam is ~ 40% of that produced by a TEM_{00} beam (figure 6.1).

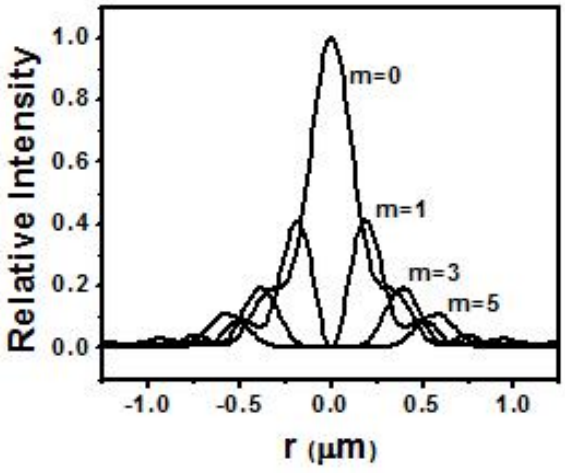

Figure 6.1. The intensity profiles of different laser modes.

The fluorescence yield resulted from two photon absorption can be expressed as,

$$\phi_{FL,2-ph} = Q\sigma_{2-ph}\left(\frac{I}{\hbar\omega}\right)^2 N \tag{6.4}$$

Where, $\sigma_{2\text{-}ph}$ is the mean molecular two photon absorption cross-section, $\hbar\omega$ is the photon energy and Q is the quantum yield for the dye and N is the number of fluorophore molecule present in the excitation volume. Therefore the ratio between total fluorescence yield with TEM_{00} and LG_{01} modes can be given as,

$$\frac{\left(\phi_{FL,2-ph}\right)_{TEM_{00}}}{\left(\phi_{FL,2-ph}\right)_{LG_{01}}} = \frac{\int_x\int_y I^2_{TEM_{00}}(x,y)dxdy}{\int_x\int_y I^2_{LG_{01}}(x,y)dxdy} \tag{6.5}$$

6.4 RESULTS & DISCUSSIONS

To estimate the efficiency of different laser modes to capture spermatozoa, video data were recorded for about one hour and during that period speeds of the moving spermatozoa that could be captured by the different trapping laser modes were estimated. In our study only spermatozoa that are having fairly straight trajectories were considered. Therefore, the difference between curvilinear velocity (VCL) and straight line velocity (VSL) could be minimized for the

cells analyzed in our study. The VSL of a moving spermatozoon could be estimated by noting its initial and final positions. A spermatozoon of interest was observed for ~ 1-2 seconds before

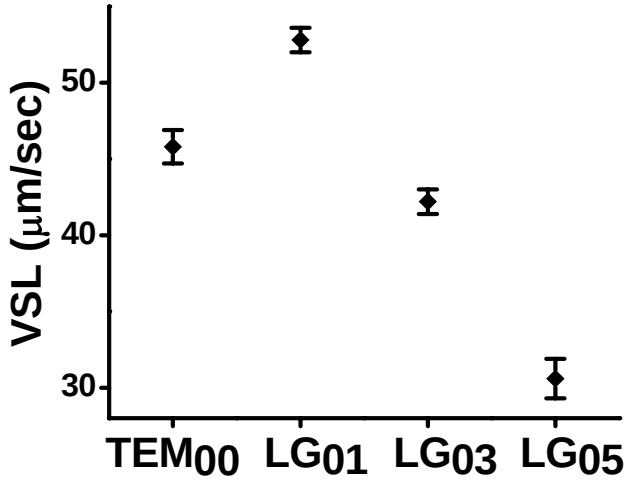

Figure 6.2 Mean VSL of spermatozoa that could be just trapped by different laser modes having identical trapping power of ~ 140 mW at the specimen plane. The data presented are the mean ± standard deviation. The difference in the distribution of data was found to be statistically significant, $p < 0.05$ (one way ANOVA, please see table C1 of appendix C).

trapping. Nearly 50 cells were studied with each type of trap. From these measurements we estimated for each mode the maximum VSL of the spermatozoa that could just be trapped. For this we selected five cells with highest VSL from the ~50 cells on which measurement was made. The mean and standard deviation of these are plotted in figure 6.2. From figure 6.2 it can be seen that as compared to TEM_{00} beam LG_{01} beam can trap spermatozoa swimming at a higher speed. However, the 3rd and 5th order *LG* beams fared worse than the TEM_{00} beam. The observation is consistent with earlier reports that while using LG_{01} mode the transverse trapping

efficiency increases, higher order *LG* modes lead to a reduction in transverse trapping efficiency [174]. The difference in the VSL of spermatozoa that could be trapped using different laser modes was found to be statistically significant with a p value of < 0.05.

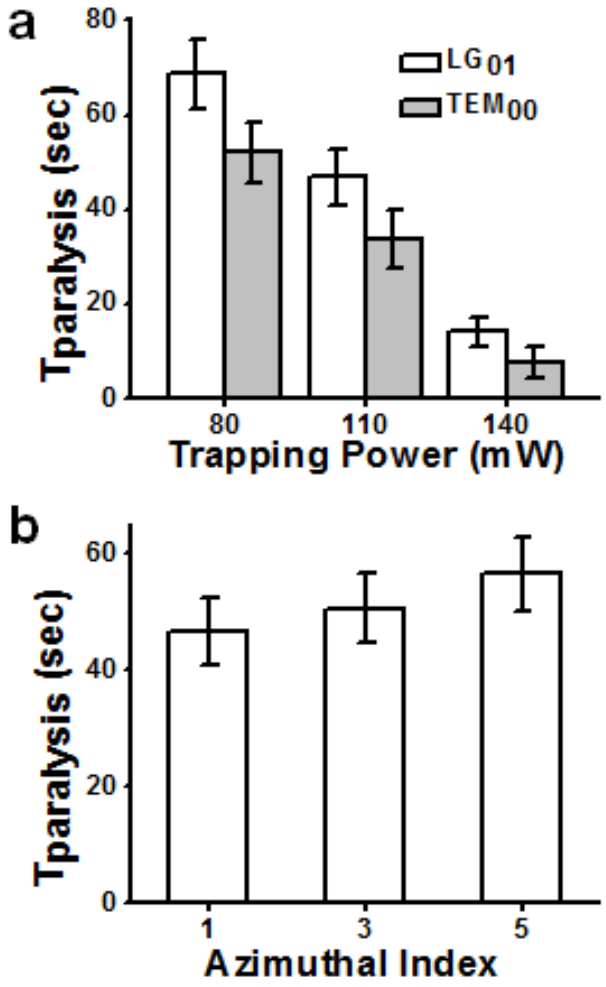

Figure 6.3 (a) $T_{paralysis}$ of the trapped spermatozoa under TEM_{00} and LG_{01} mode. (b) $T_{paralysis}$ of the trapped spermatozoa under LG_{01}, LG_{03} and LG_{05} modes each having trapping power ~ 110 mW. The data presented are the mean ± standard deviation. All distributions were found to be statistically significantly different, $p < 0.05$ (please see table C2 of appendix C and table D1 of appendix D).

When trapped, the motile spermatozoa show strong flagellar and head motion though their position could be held constant by the trap. With increasing trapping duration the flagellar

and head motion tends to die out and eventually ceased indicating a paralyzed cell. The time duration for the onset of paralysis of the cells when held continuously under optical trap can be used as an indicator for the detrimental effect of the trap. To measure the photodamage effect, the motions of the trapped cells were recorded at video rate and the time interval ($T_{paralysis}$) between the capture of the cell and the complete disappearance of any movement was noted. In figure 6.3(a) the data for TEM_{00} mode and LG_{01} mode are shown for three trap beam power levels. A total of ~ 120 cells were studied for the analysis.

The measured $T_{paralysis}$ shows that cells could remain motile over a longer time as the order (azimuthal index) of *LG* mode is increased (figure 6.3(b)). The viability of the trapped cells when they turned non-motile was further checked with PI staining. Strong PI fluorescence could be observed for most of the cells within 1-2 minutes after the cell turns non-motile.

We used AO staining to monitor possible DNA damage in spermatozoa under the trap. The stained cells were irradiated with ~ 1 mW of TEM_{00} and LG_{01} laser profiles and evolution of AO fluorescence, when excited with 450-490 nm excitation, was monitored using a color CCD camera. The temporal evolution of the AO fluorescence with increasing exposure duration for the TEM_{00} and LG_{01} modes is shown in figure 6.4. From the CCD image data (24 bit per pixel, 8 bits for each of the red, green and blue channels) the intensities of the green (500-600 nm) and red channel (600-700 nm) (that shows whether AO intercalates into double-stranded DNA or single-stranded DNA/RNA) were estimated. From figure 6.4(a) it can be seen that for low exposure times (< 15 secs) the red-to-green ratio is small for both the trap beams showing very little DNA double strand breaks. However, with increasing exposure duration the increase in the intensity ratio occurs more quickly for the TEM_{00} mode as compared to LG_{01} mode. Further,

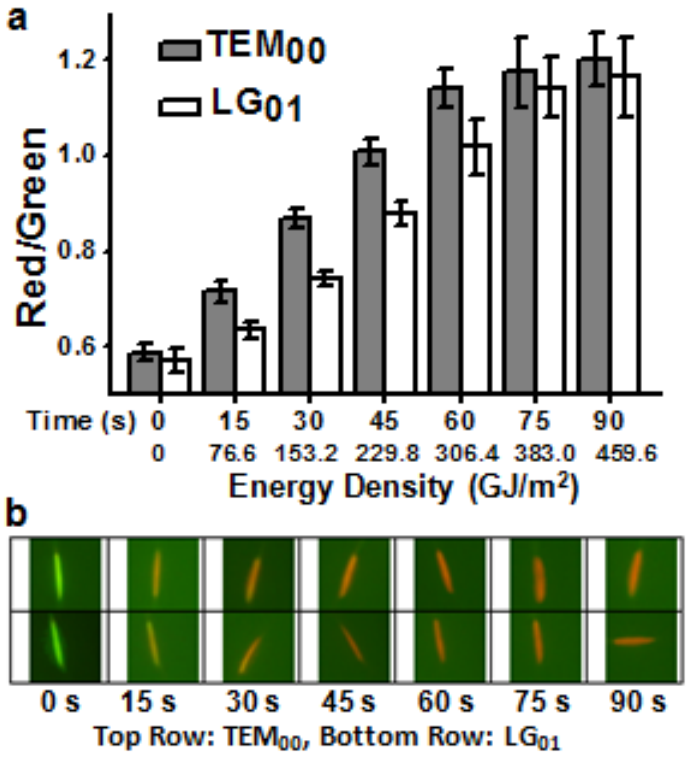

Figure 6.4 Time evolution of fluorescence spectra from AO stained spermatozoa in terms of (a) intensity ratios for red and green channels. The data are averaged over ~ ten cells and presented as mean ± standard deviation. The corresponding light dosages are also shown along the time axis. The intensity ratios are statistically significantly different with $p < 0.05$ (student's t-test, plase see table D2 of appendix D). (b) Time lapse images of AO stained spermatozoan.

while for the TEM_{00} mode the intensity ratio was seen to saturate at ~R:G=1.2 within 60 s, for LG_{01} mode the saturation occurred at ~75 s. These results suggest that the DNA damage rate is faster with TEM_{00} mode and implies an increased level of risk to the genetic purity of the spermatozoa. It is important to note here that although the absorption band for AO ranges from 450-500 nm [195] it has small but nonzero absorption (~5% of the peak value of ~ 50000 $M^{-1}.cm^{-1}$ at ~ 490 nm [196]) at the laser wavelength. Considering AO concentration of ~ 15 μM used in the samples, the temperature increase at focus resulting from direct absorption of laser

light by AO was estimated following the method given in reference 197. The estimated temperature rise is ~ 0.004º C, which is small to cause any significant DNA damage.

It is known that due to very high power density present at the trap beam focus, significant two photon absorption from the cw trap beam can take place [191, 198, 199] leading to possible damage to cell DNA having its absorption peak ~260 nm. Therefore, the observed lower degree of DNA damage with *LG* modes may be attributed to the fact that peak intensity present in an optical vortex profile is significantly lower than that of a TEM_{00} Gaussian beam and this can account for the observation that cells remain motile for a longer period of time with the increasing order of *LG* modes.

The relative values of the two photon absorption induced fluorescence yield under exposure of TEM_{00} and LG_{01} beams can be estimated from equation 6.5. In order to verify these estimates we measured the two photon fluorescence yield for DPH when excited with TEM_{00} and LG_{01} modes. The yield with LG_{01} profile was measured to be about 52% of that with TEM_{00} profile which is in good agreement with the estimate of 56%. Since the probe has a very weak absorption band above 400 nm, direct excitation of the probe molecules from the laser beam due to single photon process is unlikely. Notably similar observation of reduced two-photon fluorescence from trapped dye doped polystyrene beads was obtained by Jeffries *et al* [200] with *LG* modes at 1064 nm wavelength. But with small (diameter 100 nm- 1 μm) dye doped trapped beads the ratio of total two photon excited fluorescence observed for *LG* modes and TEM_{00} mode were much smaller (~ 10%) than observed in our studies (~ 50%). The difference is likely resulted from the incomplete overlap of the annular intensity pattern of *LG* modes with smaller trapped beads.

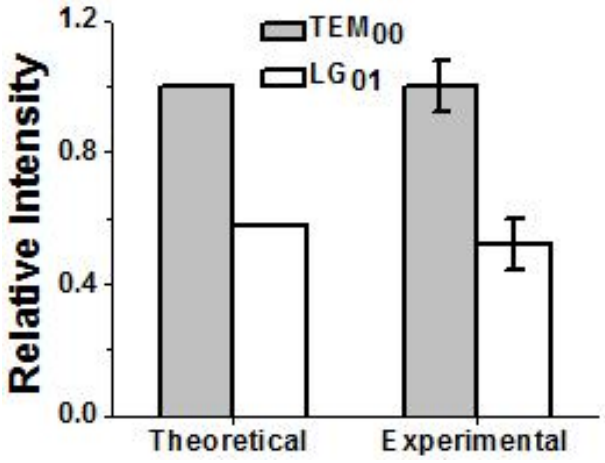

Figure 6.5 The estimated and observed DPH fluorescence when excited by the TEM_{00} mode and LG_{01} mode. The error bars indicate standard deviation of data from the mean value. The values are normalized with respect to the total fluorescence intensity estimated/observed with TEM_{00} mode.

Although the detailed mechanisms of cell damage due to light irradiation are not fully understood photochemical and photothermal effects are believed to be responsible. In ultraviolet region light absorption by nucleic acids and proteins can result in photodamage. In the visible region generation of reactive oxygen species (ROS) and free radicals produced subsequent to photoexcitation of cellular components may damage the lipid membrane, proteins and nucleic acids through oxidative reactions [201]. In particular cytochromes can absorb strongly near 532 nm laser wavelength [202]. Even in the near infrared wavelengths where cellular components do not have significant absorption, photo induced damage has been observed. While for near infrared wavelengths below 800 nm multiphoton absorption has been shown to contribute to photodamage [203, 105], the origin of photo damage for longer wavelengths is still poorly understood. Studies performed on spermatozoa using both cw and pulsed trap beam at 1064 nm showed much pronounced damage with short pulses for the same average power suggesting that transient heating at the trap focus or photochemical effects resulting from multiphoton absorption

may be responsible [106]. With cw trap beam the rise in temperature should be much smaller (~1ºC per 100 mw of trap power [106, 107]). Therefore, damage was much reduced, but for 300 mW cw power noticeable damage was present for exposure durations exceeding 2 minutes [106]. Comet assay technique, that has higher sensitivity, has revealed significant level of DNA damage to cells even when trapped for few tens of seconds using~ 120 mW of cw laser power at 1064 nm [204], the origin of which is not fully understood. Studies carried out on ROS generation in cells exposed to pulsed and cw 1064 nm trap beam has also provided qualitatively similar results [205]. While significant ROS generation in trapped cells took place with pulsed 1064 nm trap beam, with cw trap beam detectable ROS generation occurred at longer exposure times.

6.5 SUMMARY

To conclude, the use of optical vortex for manipulation of spermatozoa offers significant advantages in terms of reduced photo damage to the cells without compromising the trapping efficiency with LG_{01} mode. It is pertinent to note that in the present study we could use trapping power of up to ~ 140 mW which was primarily limited by the diffraction efficiency and damage threshold of the SLM used for the generation of the *LG* modes. This power level is capable of manipulating spermatozoa having modest swimming speed (~ 50 μm/s). For cells with higher motilty a trapping power of ~ 500 mW or more may become necessary. This can be achieved by use of diffractive optical elements offering high diffraction efficiency [206] or methods suitable for direct generation of high power vortex modes in laser cavity [207].

CHAPTER 7

OPTICAL ORIENTATION AND ROTATION OF TRAPPED RED BLOOD CELLS WITH LAGUERRE-GAUSSIAN MODES

The use of *LG* modes for controlled orientation and rotation of optically trapped red blood cells (RBCs) has been described in this chapter. For *LG* modes with increasing topological charge the resulting increase in size of the intensity annulas led to trapping of the cells at larger tilt angle with respect to the beam axis and thus provided additional control on the stable orientation of the cells under trap. Further, the RBCs could also be driven as micro-rotors by a transfer of orbital angular momentum from the *LG* trapping beam having large topological charge or by rotating the profile of *LG* mode having fractional topological charge.

7.1. INTRODUCTION

Recently, there has been considerable interest in Raman spectroscopic studies on optically trapped red blood cells (RBCs). This has been motivated by the fact that optical tweezers can immobilize cells in a physiological buffer medium, away from substrate, and thus help avoiding the adverse effects associated with immobilization of cell on the substrate and the contribution of the substrate to the measured spectra of the cell [45]. Because of these advantages, Raman

tweezers [45] have been successfully used to carry out several rather interesting experiments like, for example, oxy/deoxy transition in a trapped RBC on application of mechanical stress as would happen in the *in vivo* conditions [49]. Polarized Raman spectroscopic measurements have also been reported and these have provided evidence of increased hemoglobin (Hb) ordering as the RBC is stretched with optical tweezers [208]. Indeed it is believed from quite a long time that intracellular Hb is not randomly distributed, as in free liquid, but exists in a semicrystalline state which is believed to play an important role in intracellular oxygen diffusion [209]. However, to obtain a complete picture of Hb packing, Raman measurement at different polarization configurations including polarization of the Raman excitation beam parallel and normal to the plane of the cell are required. Because the RBC when optically trapped, orients with its plane parallel to the trap beam [210, 211], in order to carry out these measurements, techniques need to be developed for controlling the orientation of optically trapped RBC in the vertical plane, that is the plane containing the trap beam axis.

There exist several optical tweezers based techniques for orientation and rotation of trapped objects [28-30, 212-217]. Linearly polarized trap beams [212, 213] or trap beams having elliptical intensity distribution [28-30] have been used for orientation of objects, but these can only orient the object in a plane transverse to the laser beam axis. For orientation of trapped object in the vertical plane, one approach is to use two or more closely separated optical traps to hold different parts of the same object. By changing the relative position of these traps the trapped object can be oriented in three dimensions [214, 215]. Other approaches used to orient a trapped object in three dimension are the use of a combination of two trap beams, one having a circular intensity profile and the other with elliptic intensity profile, [216] or application of a tangential light forces at the periphery of the trapped object using a pulsed laser beam [217]. All

these methods require two or more trap beams leading to some complexity in their implementation. In this paper we show that a more convenient approach for orientation of trapped RBC is the use of *LG* trap beam. Since the *LG* modes have an annular intensity profile, size of which increases with the azimuthal index or topological charge of the mode, the desired control over the orientation of the trapped RBC in the vertical plane could be achieved with a change in the topological charge of the trapping beam. We also show that another advantage with the use of *LG* trap beam is that it can transfer its orbital angular momentum to the cell leading to a rotational torque on the cell, which is proportional to the topological charge of the *LG* beam. Our studies show that at trap beam power of ~ 15 mW, a topological charge of 15 or more provides enough torque to the cell to cause it to rotate in the isotonic buffer medium. Further, we find that *LG* mode with non-integer topological charge ($l = 0.5$), which possesses a semi circular transverse intensity profile, could also be used for rotating the cells in the trapping plane by rotating the beam pattern. The advantages offered by these approaches over other methods for causing rotation of RBCs [29-30, 218-221] are also discussed.

7.2 MATERIALS AND METHODS

The experimental set-up is similar to the one described in figure 2.9 of chapter 2. It consists of a 1064 nm laser source (Compass 1064-4000, Coherent Inc). For the generation of *LG* beams the phase profile of the light incident on the SLM was suitably modified using computer generated holograms imprinted on the SLM. The diffracted first order was selected using an iris and directed through mirrors onto the entrance pupil of a water immersion objective lens (Olympus Plan Apochromat 60X, NA 1.2) to form the optical trap. For all the experiments described here a left circularly polarized *LG* modes were chosen using a polarizer (P) and quarter wave plate

(QWP) combination placed after the SLM. The images and videos of the trapped cells were recorded using a CCD camera (Watec Inc).

Blood (1 ml) was collected by venipuncture from healthy volunteers in glass tubes containing EDTA (5.4mg/3ml) as an anticoagulant. RBCs were separated from these anticoagulated blood samples by centrifugation at 600 g for 3 minutes and suspended in phosphate buffer saline (PBS). For experiments appropriate dilutions of the cells in PBS solution was used. In isotonic buffer the shape of the RBCs is that of a biconcave disks (flattened and depressed in the center to result in a dumbbell-shaped cross section) with a diameter of ~7 μm and a thickness of ~1.5 μm [211].

The radius of the annulas of the *LG* beams is given as [174]

$$r_{\max} = w_0 \sqrt{l/2} \tag{7.1}$$

where w_0 is the Gaussian beam radius. The *LG* modes with $l \neq 0$, carry an orbital angular momentum of $l\hbar$ per photon.

A rotating trapped cell experiences a rotational viscous drag which can be estimated from the following equation [219],

$$T_D = C_D \rho \omega^2 R^5 / 4 \tag{7.2}$$

For disk shaped cells, the drag coefficient can be expressed as $C_D \approx 24/Re$ [222]. For our case, the Reynolds number is expected to be << 1 as the rotational frequency is only fraction of Hz, and can be expressed as $Re \approx \rho \omega R^2 \eta$. Where ρ is the density of the medium, η is the viscosity coefficient on the medium, ω is the rotational speed and R is the average radius of the disk

shaped RBC. For a given trap beam power, the maximum rotational speed of a rotating cell will be determined from the balancing action between the light induced torque and the fluid drag.

7.3 RESULTS & DISCUSSIONS

For the zeroth order *LG* mode (which is identical to TEM_{00}) the cell orients with its plane along the direction of the trapped beam (vertical orientation), since this maximizes the overlap of the cell volume with the region of highest light field. As the size of the bright annulus increases with mode order, maximum overlap between the cell volume and the trapping field is expected for cell orientation away from the vertical direction. Figure 7.1 shows the change in the orientation of a trapped RBC with changes in the topological charge of the *LG* modes. For l =10 the cell can be seen to be oriented in the horizontal plane that is the trapping plane as this maximizes the overlap of the cell volume with the region of highest light field. For the 1064 nm trap beam the diameter of the bright annulas was estimated to be ~ 0.8 μm for l = 1 and ~ 2.6 μm for l =10.

For effecting a change in the orientation of the cell, the optical torque arising due to a change in the mode index of the *LG* trap beam, should exceed the Brownian forces. An estimate for the resulting optical torque can be obtained by finding the maximum frequency of the change in the mode index from l = 0 to 10, up to which the trapped cells could get oriented. It was observed that at a trapping power of ~ 15 mW, if the mode index is changed at a rate faster than 150 ms between the consecutive modes, the trapped RBC fails to orient. This implies that a time of 1.5 s was required for rotating the cell by 90° from the vertical to horizontal orientation, indicating the maximum rotational speed of ~10 rpm. From equation 7.2 we estimate the corresponding rotational torque, T_D ~ 0.17 pN μm. The value is two orders of magnitude higher than the random thermal torque (~ k_BT) which at room temperature equals ~ 10^{-3} pN.μm and therefore ensures stable orientation of the trapped cells by *LG* trap beam against Brownian forces.

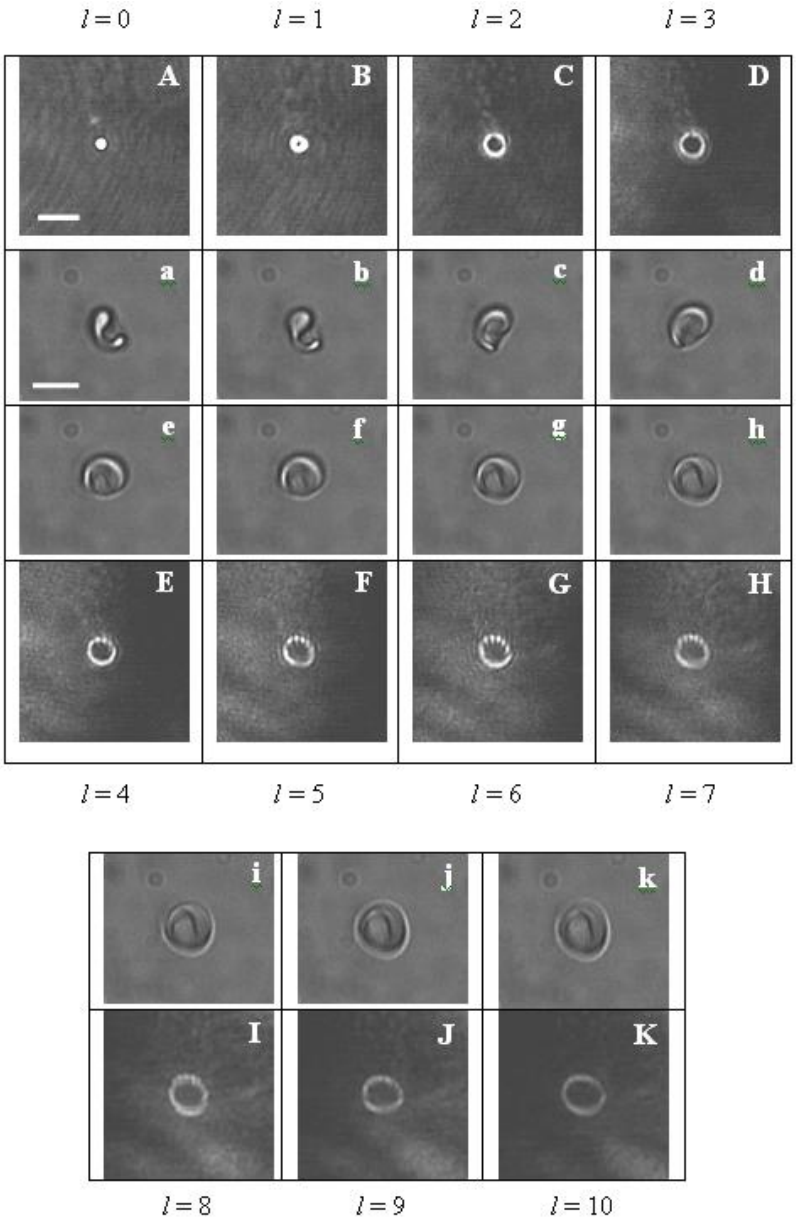

Figure 7.1 Image frames showing the *LG* mode patterns from topological charge 0 to 10 (A-K) and the corresponding orientation of a trapped RBC (a-k) respectively. The time interval between consecutive holograms was ~ 0.5 s. Scale bar, 2.5 μm (A-K) and 6 μm (a-k).

We also observed that the torque exerted by *LG* trapping beam with high topological charges ($|l|$~ 15 or more) could drive RBCs as natural micro-rotors. For $|l|$ ~ 15 the trapped cells

get aligned over the bright annulas of the *LG* trap due to larger circumference of the annulas. Under such condition the cells while being contained within the annular ring of light, orbits the beam axis in a direction determined by the handedness of the helical phase fronts. This is believed to be due to the transfer of light orbital angular momentum to the trapped cells by the

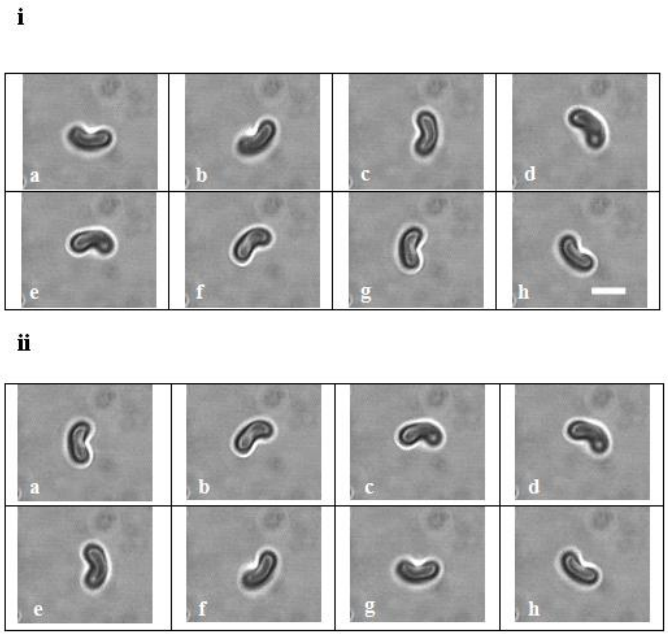

Figure 7.2. Image frames showing the rotation of a trapped RBC via transfer of light orbital angular momentum when trapped under $|l|$=15 mode. The reversal of the rotational sense as the topological charge of the *LG* trapping mode was switched from (i) l =15 to (ii) l = -15. The frames (a-h) show images of the rotating cells, where in each frame the cell is observed to be rotated by an angle of 45º over the previous frame. The time separation between the frames is ~ 625 ms. Scale bar, 5 μm. The rotational speed of the cell was ~ 12 rpm at ~15 mW of trap power.

scattering of the trap beam having helical wavefront [24, 223]. Figure 7.2(i) shows the rotation of an RBC when trapped under l = 15 mode. The observed rotational frequency was ~ 12 rpm at ~ 15 mW of trapping power and it can be increased using higher trap beam power. To check whether the observed rotation is caused by the transferred light orbital angular momentum from

the trap beam to the cell we changed the helicity of the trap beam. Figure 7.2(ii) shows the corresponding rotation of an RBC when trapped under l = -15 mode. The sense of rotation was observed to get reversed that is from counter-clockwise to clockwise direction as the charge of the *LG* mode was made negative. This allows for a means to change the sense of rotation of a micro-rotor system by simply changing the helicity of the trapping beam. Such control over rotational sense is not possible with techniques utilizing specially fabricated micro-structures [224, 225] or RBCs suspended in hypertonic buffers [218, 219]. A control on the sense of rotation can facilitate bi-directional operation for micro-machine components like micro-motors or valves.

It is pertinent to note here that shape anisotropy or birefringence properties of cellular objects could also be exploited for rotation of cells. When inside a hypertonic buffer the RBC's shape becomes asymmetric and can experience rotational torque from the trapping light beam and rotate much like a windmill [218, 219]. Further, as when trapped using linearly or circularly polarized light, birefringent particles get oriented or rotated respectively by transfer of light spin from the trap beam, the birefringence properties of some cellular components like chloroplasts etc have been also exploited to achieve optical rotation [212, 213]. Since with *LG* trapping modes, the scattering of helical light wavefronts by the trapped cell cause it to rotate, this method is independent of shape anisotropy or birefringence properties of the cell and is more generally applicable to any cell type. We could observe similar transfer of light angular momentum to a leucocyte cell when trapped using l = 15 trapping beam. It is also pertinent to note here that when a linearly polarized trap beam is used, due to its shape anisotropy, the vertically oriented RBC gets aligned with its symmetry axis perpendicular to the electric vector of the trapping beam [219, 220]. Rotation of the trapped RBC can be effected by rotation of the plane of

polarization of the trapping beam by use of a half wave plate, much like what has been demonstrated for micro-disks [31]. To avoid any alignment torque produced by a linearly polarized light beam on trapped cells, we used left circularly polarized $|l| = 15$ trapping beam. With 15 mW of circularly polarized *LG* ($l = \pm 15$) trap beam we did not observe the cells to spin about their symmetry axis. These results are at variance to the report from Dharmadhikari *et al* [220, 221] and consistent with results expected from nonbirefrigent flat disks [31, 226].

We also observed that rotational drive could be effected onto the trapped RBCs with employment of *LG* trapping mode having fractional topological charge. The transverse profiles of fractional *LG* modes are circularly asymmetric and can trap the cells in a preferred orientation. A *LG* beam with fractional topological charge is distinguished from an integer-order beam in terms of the intensity pattern, which possesses a radial opening (low-intensity gap) in the annular intensity ring encompassing the dark core [227, 228]. Therefore, rotation of the trapping profile makes the trapped cell to rotate. We used *LG* mode with fractional charge $l = 0.5$, that have a nearly semi-circular intensity pattern. Trapped cells orients in the vertical plane with their longer dimension overlapping with that of the trap profile. The *LG* profile could therefore be rotated by rotation of the generating holographic pattern through SLM. Figure 7.3 shows the rotation of a trapped RBC using $l = 0.5$ mode. Twenty four consecutive holograms were used to generate the rotating $l = 0.5$ patterns where each pattern is rotated by 15º with respect to the preceding pattern. The rotational speed of the trapped cell could be controlled by changing the time intervals between the holograms displayed on the SLM. At ~15 mW of trapping power a rotational speed of up to ~ 18 rpm could be achieved. The rotational frequency can be further increased by increasing the trapping power and also by increasing the step size suitably. The rotational torque corresponding to the maximum speed of 18 rpm could be estimated using equation 2 as ~ 0.3 pN

μm. Compared to the use of a rotating elliptically profiled trap beam generated using either a first order Hermite Gaussian mode [30] or a cylindrical lens [28] or a rotating aperture [29] the present method avoids insertion of a rotating optical element into the trap beam path and thus the associated alignment problems.

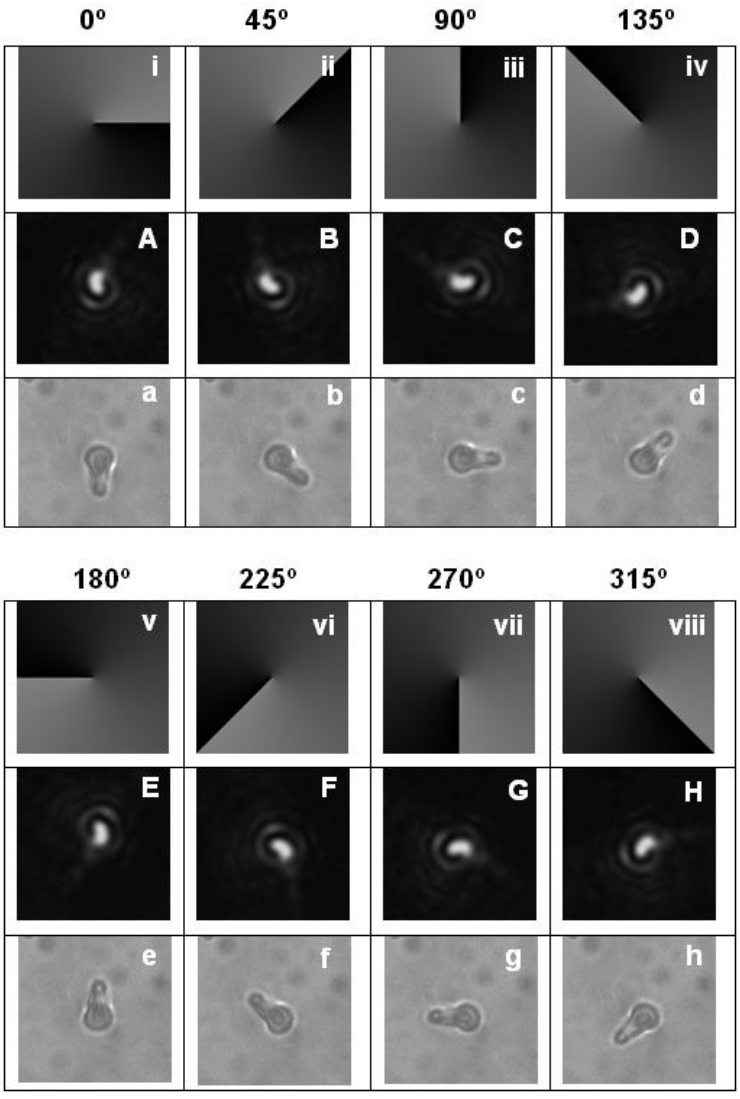

Figure 7.3 (i-viii) The computer generated phase holograms encoded in grayscale (256 levels) images. Phase retardation of zero is encoded in black. Gray value 128 represents phase retardation value π. The angles of rotation of the holograms with respect to the first frame are indicated above the corresponding image frames. (A-H) The l = 0.5 trapping profiles rotated following the generating hologram patterns. As phase in undefined at the

dislocation line the light intensity can be seen to be zero near that region producing an approximate semi-circular profile. (a-h) Image frames showing the rotation of an RBC trapped along the longer dimension of the trap profile. The rotational speed of the cell was ~ 15 rpm.

7.4 SUMMARY

We have shown that *LG* trap beams provide a convenient method for controlled three dimensional orientations of optically trapped RBC. With *LG* modes having increasing topological charge, the increasing size of the intensity annulas led to trapping of the cells at larger tilt angle with respect to the beam axis and this could be used for controlled orientation of the cell. Such a control on orientation of RBC may help in carrying out polarized Raman spectroscopic measurements on trapped RBCs at all possible polarization configurations. Further, the RBCs could also be driven as micro-rotors by a transfer of orbital angular momentum from the *LG* trapping beam having large topological charge and the method also allows for a control in the sense of rotation by reversing the topological charge of the beam. Rotation of the cells by rotating the profile of *LG* mode having fractional topological charge has been also demonstrated.

CHAPTER 8

DEVELOPMENT AND CHARACTERIZATION OF RAMAN OPTICAL TWEEZERS

Details of a set-up developed to simultaneously trap and record Raman spectra from a single cell, referred to as Raman optical tweezers, are presented in this chapter. The basic concepts of Raman scattering and the spectral processing routines used are also discussed. Finally the results of the experiments carried out to study possible photo-induced changes in RBCs as a function of the duration of laser exposure in Raman optical tweezers employing near infrared (785 nm) laser source are described.

8.1 RAMAN SCATTERING

8.1.1 BASIC THEORY

When light is scattered from an atom or molecule, most photons are elastically scattered (Rayleigh scattering) i.e have the same energy as the incident photons. However, a small fraction of the scattered light is scattered with a shift in energy, the difference being accounted by a change in vibrational, rotational or electronic energy of a molecule/atom. This phenomenon of inelastic scattering of light is known as Raman scattering. The Raman scattering was first demonstrated by C.V. Raman in 1928 for a number of different liquids like benzene, pentane, ether etc. Only about 1 in 10^7 photons is Raman scattered and the scattered photon can be at a higher or lower energy than the incident photon [229]. If it is at a lower energy than the incident

photon then it is known as Stokes Raman scattering, and if at a higher energy than the incident photon, then it is known as anti-Stokes Raman scattering (figure 8.1). The importance of Raman scattering for spectroscopic studies comes from the fact that Raman shifts represent characteristic of a given molecule and can act as its fingerprint.

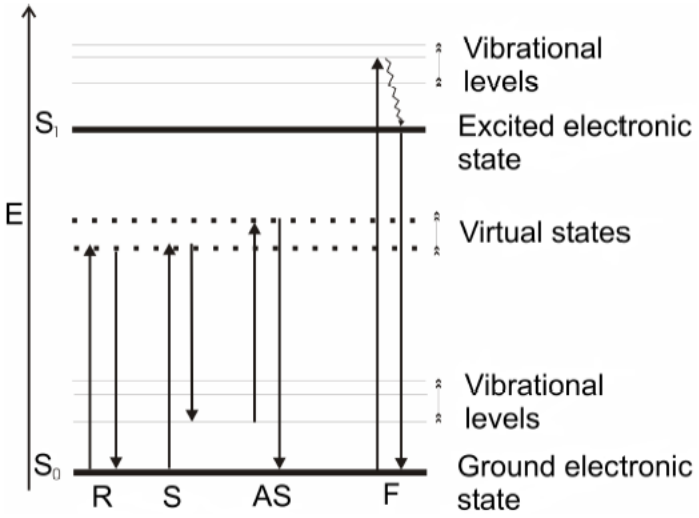

Figure 8.1 Jablonski Diagram depicting Rayleigh scattering(R), Stokes (S) and Anti-Stokes (AS) Raman scattering and Fluorescence (F).

In NIR Raman spectroscopy, the excitation energy is far below the first excited electronic state and it can be assumed that while interacting with the molecule the incident electromagnetic wave perturbs the electron cloud around the nuclei to form a short-lived state known as "virtual" state (figure 8.1). If the molecule returns back to its original ground state after being excited to one of the virtual states, Rayleigh scattering results. In Stokes Raman scattering the molecule, after being excited from the ground electronic state to one of the virtual states, returns to one of the excited state of the ground electronic state. In Anti-Stokes Raman scattering the molecule is already present in one of the excited states of the ground electronic state and after being excited to one of the virtual states, it relaxes back to a lower ground state as shown in figure 8.1.

The classical theory for Raman scattering [229] considers the modulation of the incident electric field by vibrating molecule and gives details on the processes of Rayleigh and Raman scattering. According to the classical picture as the electromagnetic wave interacts with a molecule, the electron cloud gets perturbed periodically by the electric field of the incident wave. This results in induced dipole moment (P) acting as a source of electromagnetic radiation, thereby resulting in scattered light.

The induced dipole moment *P* is proportional to the polarizability α of the molecule and the incident electric field intensity $E\ (=E_0\ Cos(\omega_i t))$. Considering the corresponding molecular vibration to be denoted as

$$q = q_0\ cos(\omega_{vib} t) \tag{8.1}$$

The induced dipole moment (taking into account only small amplitude vibration) can be expressed as,

$$P = \alpha_0 E_0 \cos(\omega_i t) + \frac{1}{2}\left(\frac{\partial \alpha}{\partial q}\right)_0 q_0 E_0 \cos\{(\omega_i + \omega_{vib})t\} + \frac{1}{2}\left(\frac{\partial \alpha}{\partial q}\right)_0 q_0 E_0 \cos\{(\omega_i - \omega_{vib})t\} \tag{8.2}$$

Equation 8.2 describes the processes that occur during Raman scattering. *Term* 1 describes the situation where the scattered photon is of the same frequency as the incident photon i.e. it describes Rayleigh scattering. *Term* 2 describes the anti-Stokes Raman scattering resulting in the generation of a photon of higher frequency (higher energy) than the incident photon. *Term* 3 describes the Stokes Raman scattering where a photon of a lower frequency (lower energy) is generated than the incident photon.

It is also clear from equation 8.2 that if the derivative $\left(\frac{\partial \alpha}{\partial q}\right)_0$ equals zero, so do the terms 2 and 3 and there will be no Raman scattering. This gives the selection rule for Raman-active vibration,

which implies that a molecular vibration will be Raman-active only if the intra-molecular motions involved in that vibration occur with a change in polarizability [230]. This is usually presented in terms of polarizability ellipsoid, for which let us consider the example of CO_2 molecule. Considering that electrons are more polarizable (a larger α) along the chemical bond than in the direction perpendicular to it if we plot α from the center of gravity in all directions, we end up with a three-dimensional surface. Conventionally, $1/\alpha$ is plotted rather than α itself and is called the polarizability ellipsoid. Figure 8.2 shows the changes in the polarizability ellipsoid during the vibrations of the CO_2 molecule.

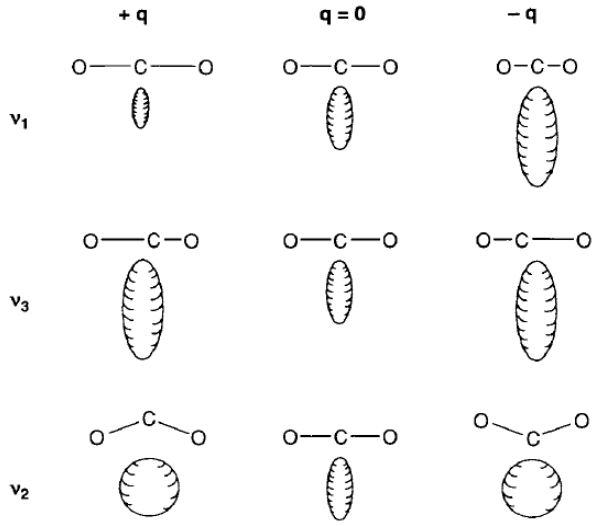

Figure 8.2 Change in polarizability ellipsoid during vibration of CO_2 molecule (reprinted by permission from Elsevier [230]).

In terms of the polarizability ellipsoid, the vibration is Raman-active if the size, shape or orientation changes during the vibration. In the v_1 vibration, as the size of the ellipsoid is changing during a complete motion its polarizability is also changing and it is therefore Raman-active. Although the size of the ellipsoid is changing during the v_2 and v_3 vibration, the ellipsoids at two extreme displacements ($+q$ and $-q$) are exactly the same in these cases. Thus, considering a small displacement around the origin these vibrations are not Raman-active (the Raman

activity is determined by $\left(\frac{\partial \alpha}{\partial q}\right)_0 \neq 0$). The difference between the ν_1 and ν_3 is further depicted in figure 8.3, where it can be seen that $\left(\frac{\partial \alpha}{\partial q}\right)_0$ value given by the slope of the curve at q=0 is positive for v_1 but zero for v_3.

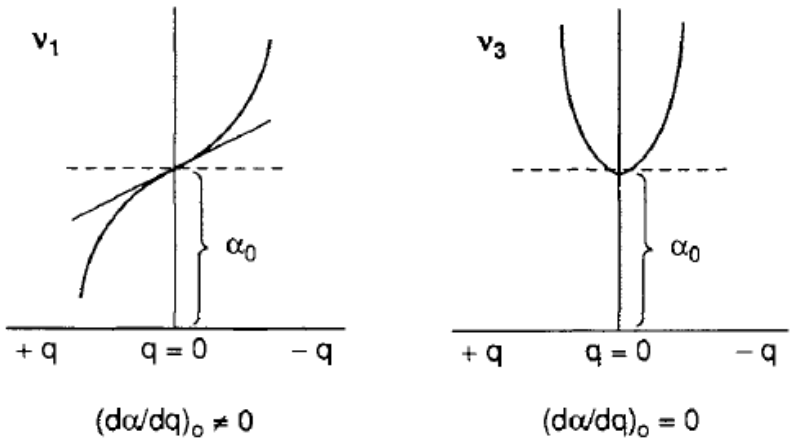

Figure 8.3 Difference between v_1 and v_3 vibration in CO_2 molecule (reprinted by permission from Elsevier [230]).

Though classical theory explains successfully the origin of Raman bands it could not account for the fact that the Stokes scattering is observed to be much stronger than anti-Stokes scattering. The classical theory predicts equal intensities for both Stokes and anti-Stokes scattering.

The quantum-mechanical theory of Raman scattering [229] solves this problem. In the quantum picture, the molecular vibrations are quantized. The scattering process is viewed as the creation and annihilation of vibrational excitations by photons. At room temperature the ground state will be more populated and hence Stokes scattering is in general more likely to be observed than anti-Stokes scattering. The ratio of anti-Stokes to Stokes is given by the Boltzmann distribution and can be expressed as below,

$$\frac{N_u}{N_l} = \frac{g_u}{g_l} e^{\left\{-\frac{E_u - E_l}{kT}\right\}} \tag{8.3}$$

where N_u is the number of molecules in the excited vibrational state (E_u) of the ground energy level, N_l is the number of molecules in the lower vibrational state (E_l) of the ground energy level, g's are the degeneracy of the energy levels, k is the Boltzmann's constant (1.3807×10^{-23}JK^{-1}), and T is the temperature in Kelvin.

8.1.2. RAMAN MICROSPECTROSCOPY: BIOCHEMICAL ANALYSIS AT SINGLE CELL LEVEL

By collecting Raman spectra from a very small volume the identification of species present in that volume can be performed. By using Raman microspectroscopy [229], space-resolved Raman spectra of microscopic regions of samples could be measured. Since the objective lenses of microscopes focus the laser beam down to ~ μm in diameter, the resulting photon flux is much higher than used in conventional Raman setups. This has the added benefit of enhanced fluorescence quenching. However, the high photon flux can also cause sample degradation. Raman microscopy for biological and medical specimens generally uses near-infrared (NIR) lasers since in this spectral range absorption is low and thus reduces the risk of damaging the specimen compared to the use of lower wavelength lasers. NIR Raman signal level is however low (owing to the ω^{-4} dependence of Raman scattering intensity), and most detectors require very long collection times. Therefore, for motile biological systems it becomes necessary to immobilize objects under investigation prior to recording of Raman spectra. Adding confocal detection to micro-Raman system results in a higher spatial resolution typically hundreds of nm in lateral and ~μm in depth profiling.

8.2. RAMAN OPTICAL TWEEZERS

8.2.1. WHY RAMAN OPTICAL TWEEZERS?

By combining Raman spectroscopy with a confocal optical microscope (micro-Raman spectroscopy), one can achieve chemical characterization on a scale of femtolitre volumes within the sample to be probed. But this technique can only be applied when the sample to be analyzed is immobilized because Raman signal being extremely weak, acquisition of spectra from a biological system usually takes long time (~ tens of seconds to few minutes). However, many living cells (blood cells, for instance) and aerosol particles need to be in a liquid or gaseous environment for their normal functionality. Brownian motion and motility (for some living cells) as well as fluxes in the surrounding medium prohibit the direct use of the micro- Raman technique without combining it with an immobilization method. One can apply standard physical or chemical methods for living cell immobilization on planar surfaces. However, in many cases this may induce undesirable perturbations in living cells/bacteria. Chemical immobilization can change the chemical microenvironment of the living cell and may results in undesired experimental artifacts. Surface effects become more important as the size of the micro-object decreases, so it is crucial to protect the surface of object to be studied from any changes caused by the measurement procedures. A very elegant approach for immobilization of micro-sized objects in suspension is to trap them using optical tweezers. The tight focus required by both micro-Raman spectroscopy and the optical trap makes combining the two techniques very attractive. This combination of Raman spectroscopy with optical tweezers is known as Raman optical tweezers [45]. It can provide biochemical characterization of single cell and even of intra-cellular regions by employing a single laser beam to simultaneously trap and excite Raman spectra of optical trapped object. Notably Raman tweezers permit acquisition of Raman spectra

of biological cells/bacteria in their natural environment i.e in suspension and thereby avoids any perturbation resulting form chemical/physical immobilization methods. Though the power required at the specimen plane is only few mW for trapping to occur, due to tight focusing of the laser beam the resultant intensity is very high (~ $MWcm^{-2}$). At such high intensity, uv/visible radiation, having considerably high absorption coefficient in biological objects, are potentially harmful. Therefore, near infrared (NIR) lasers are particularly attractive for Raman optical tweezers applications. Further NIR Raman spectroscopy has its inherent advantages of much reduced fluorescence background as compared to the use of uv/visible excitation sources. Therefore, NIR Raman tweezers, although is a recently developed technique, are already being used for applications ranging in many different branches of biophotonics [45]. Also the manipulation capability of optical tweezers adds to this by allowing observation of real-time response of cells/bacteria to stress factors affected by moving the trapped object through changing environmental conditions [231].

8.2.2 RAMAN OPTICAL TWEEZERS SET UP

A Raman tweezers system comprises of a standard optical microscope, an excitation/trapping laser, a spectrometer, and a suitably sensitive detector (such as a thermoelectrically/liquid nitrogen cooled charge-coupled device (CCD)/photomultiplier tube (PMT)). Choice of all components of the optical system should be made carefully as any Raman active component in the optical path can contribute significantly to the unwanted background Raman signal. As immersion oil used with oil-immersion objective lenses produce strong background, water-immersion objectives are sometimes preferred over oil-immersion objectives. But the available NA with water immersion objectives is usually lower than oil immersion lenses and therefore results in lower resolution. The use of quartz cover-slips can also decrease background

fluorescence signals compared to glass cover-slips often used in microscopy laboratories. Employment of a confocal aperture excludes much of the unwanted signal from the glass cover slip, suspension medium and immersion liquid used with objective lens to yield an optimum Raman spectra.

Spectrometer and the detection system is the most expensive part of the Raman tweezers set-up. Since Raman signals are very weak, to minimize the dark noise which may override the useful signal, it is required to use cooled CCD detectors. Usually every 6°C lowering of the temperature reduces the dark noise to approximately half of its value at the higher temperature. Often the CCD array used for detection of Raman signal is cooled down to near −80 ◦C for acquiring spectra from biological objects typically requiring acquisition time of tens of seconds to few minutes [45]. Also the quantum efficiency of the detector should be high in order to utilize most of the Raman scattered photons reaching the detector. The grating used in the spectrometer system should also be chosen appropriately so that maximum diffraction efficiency is obtained for the major Raman bands.

Filters are indispensable for Raman spectroscopy. A notch filter or an edge filter before a spectrometer is the most effective way to reduce the Rayleigh light from the sample and optical elements along the light path, permitting detection of the much weaker Raman lines coming from sample. The notch filter can also be used for coupling of the trapping/ excitation laser beam onto the microscope objective [45].

Till now several schemes have been suggested (figure 8.4) for Raman tweezers. The simplest technique uses one microscope objective and one optical beam that at the same time traps a microparticle and excites its Raman spectra (figure 8.4 (a)). The alignment of the system is comparatively easy and sample illumination is readily achieved. But as the same beam is used

for trapping as well as Raman excitation, the flexibility of the set-up is very limited. For example, it is not possible to record resonance Raman spectra with this set-up as required power level for achieving trapping action using a uv/visible laser often destroy the biological sample. But due to its simplicity this configuration has been widely exploited for NIR Raman spectroscopy till date.

Using two separate beams for trapping and Raman excitation with a single objective has the advantage that the wavelength and the power of the trapping beam and the Raman excitation beam can be adjusted independently to optimize the functionality (figure 8.4(b)). A combination of two laser beams, of different wavelengths, in the same microscope provides better sensitivity to a Raman tweezers set-up and helps to avoid incurring damage to the biological sample while doing resonance Raman spectroscopy by using a NIR trapping beam and a low power visible/uv excitation beam.

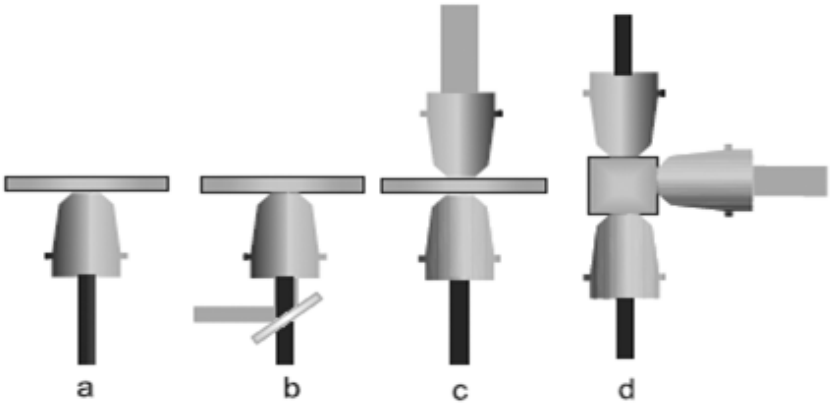

Figure 8.4 Four main configurations of Raman tweezers that are distinct by the coupling geometry of the trapping beam(s) (black) and Raman excitation beam (grey) (reprinted by permission from *Journal of Optics A* [45]).

The most versatile Raman Tweezers systems use two separate beams for trapping and Raman excitation, and each of the beams is focused on the particle by a separate objective

(figure 8.4(c)). When the excitation laser and the trapping laser enter the sample through two different microscope objectives, alignment of the system is difficult and also the sample illumination by the white light source cannot be obtained readily. But this configuration allows one to use low NA objective lens to excite the trapped object and thereby taking advantage of high transmission of these lenses compared to high NA objective lenses required when trapping needs to be done using the same objective lens.

Two counter-propagating optical beams can create a stable optical trap even with objectives with relatively small numerical apertures, because in this case the scattering force of one beam is balanced by the scattering force exerted by the second beam. Raman scattering is excited by a third beam focused on the trapped particle through a separate objective, which also collects Raman spectra (figure 8.4(d)). Recently, this variant of Raman tweezers was realized [232]. The dual-beam trap was created by two optical fibers and, due to their divergent light fields, offers the ability to hold and move large cellular objects with reduced prospects of photodamage. Another significant advantage of this configuration is that two counter propagating trapping beam can also be employed for optical stretching [43] of soft biological cells like erythrocytes and real-time biochemical response of the cells to an applied mechanical stress can be studied.

A schematic of the experimental set-up used for the studies presented in this thesis is shown in figure 8.5(a). The 785 nm cw beam from a Ti:Sapphire laser (Mira 900, Coherent Inc), pumped by a 532 nm diode pumped solid state laser (Verdi-5, Coherent Inc), was used for both trapping the cells and exciting the Raman spectra. The use of near infrared laser beam for trapping/excitation reduces the absorption-induced degradation of the RBCs and also helps

minimizing fluorescence background. The laser beam was filtered to obtain a smooth profile (figures 8.5 (b) and (c)) and then introduced into a home-built inverted microscope equipped

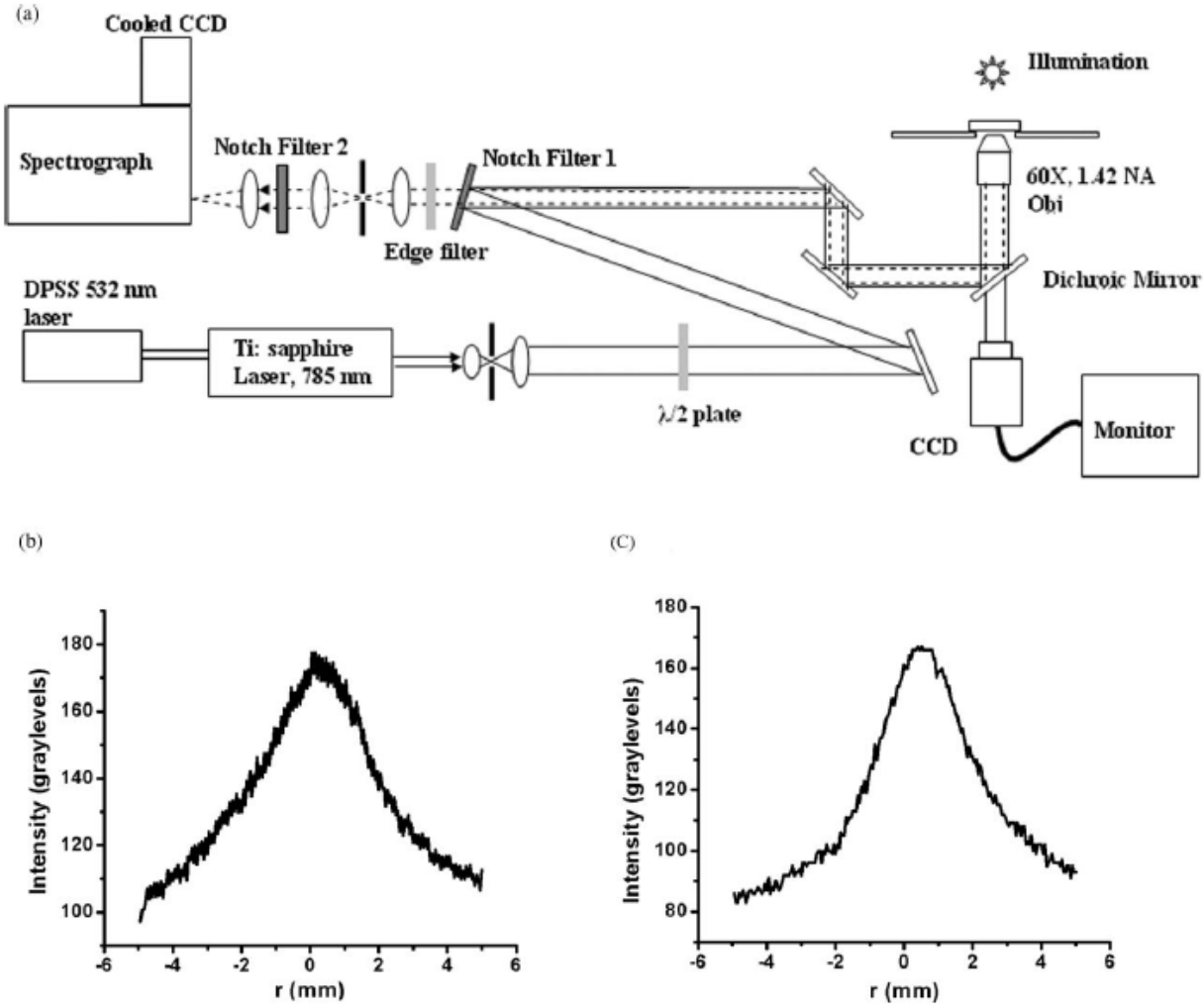

Figure 8.5 (a) Raman optical tweezers set-up. The solid line shows the trapping/excitation beam, whereas the dotted line indicates the Raman signal. For removing high-frequency noise from the laser beam profile, a spatial filter assembly consisting of a pair of convex lenses having 50- and 300-mm focal length and a 50-µm diameter pinhole placed at the focal point of the first lens was used. (b) Original beam profile and (c) the beam profile after spatial filtering, as measured using a monochrome CCD camera.

with a high NA objective lens (Olympus 60X, NA 1.42), forming an optical trap. For trapping and acquisition of Raman spectra laser power can be increased upto ~30 mW, at the specimen plane. The laser spot size at the focus was ~ 1 μm. A holographic notch filter (Notch filter 1), was used to reflect the 785-nm trapping/excitation beam, which was incident on it at an angle of ~12º. The Raman signal back scattered from the trapped RBC was collimated by the objective lens and passed back along the same optical pathway. The notch filter 1 transmits the Raman signals above 800 nm, which are then passed through a 100-μm confocal pinhole to reject most of the off-focus Rayleigh scattered light. It was thereafter passed through another notch filter (Notch filter 2) that further removes the Rayleigh scattered laser light. The beam was then focused onto the entrance slit of an imaging spectrograph (Shamrock SR-303i, Andor Corp). The spectrograph was equipped with either a 600 lines/mm grating or a 1200 lines/mm grating blazed at an wavelength of 900 nm and incorporates a back-illuminated CCD (iDus 401-BRDD, Andor Cop) camera thermoelectrically cooled down to -80º C. To allow observation of the trapped RBC a green-filtered halogen illumination source and a video CCD camera system were used. Calibration of the spectrometer was performed using toluene (Spectroscopic grade, Aldrich) and the assignment of the peaks was made from standard spectra. The spectral resolution of our Raman system is about 6 cm^{-1} with 600 lines/mm grating and the Raman spectra can be recorded in the range from ~500 to ~2100 cm^{-1}. With 1200 lines/mm grating the resolution is ~ 4 cm^{-1} and spectra could be recorded in the range 950-1600 cm^{-1}.

8.2.3 PROCESSING OF RAMAN SPECTRA

Raman spectra are marred by the presence of various noises and strong background. Noise is generated from a variety of sources such as cosmic rays, variations in the intensity of the light source and dark current in the detector system. Different noise removing filters can be employed

to improve the signal-to-noise ratio of the acquired spectra. Backgrounds in Raman spectra are common and arise from either luminescence processes (e.g fluorescence, phosphorescence), non laser induced emissive processes (e.g room light, black body radiation etc) or Raman scattering from other than analyte (e.g substrate, medium, optics etc). These backgrounds mostly have much broader structure in contrast to the useful Raman bands and can be separated on that basis. But it should be noted that spectra improvement techniques are just a way to improve the way the signal looks. Nothing can replace a good collection technique at the first step. The most frequently used preprocessing techniques employed for the better visualization of Raman spectra are described in the following sections.

8.2.3.1 DE-NOISING OF RAMAN SPECTRA

It consists of two sequential stages; the first one is to removes the spikes (cosmic rays) in the spectra, the second stage is a smoothing filter designed to get rid of random fluctuations associated with the excitation source and dark noise.

8.2.3.1.1 COSMIC RAY REMOVAL

CCD detectors are susceptible to the effects of cosmic rays that pass through them during an exposure. The cosmic rays add charge to one or more pixels depending on the direction of travel of the ray. The end result is a spike or peak in the spectrum that does not correspond to a Raman emission. Cosmic filtering involves comparing two successive spectra collected under identical conditions on a pixel-by pixel basis [233]. If the difference in the counts for a given pixel exceeds the expected shot and the readout noise variance for the weaker of the two counts, then greater count is replaced with the lesser count. This approach is very effective at removing cosmic-induced artifacts without degrading the resolution of the Raman spectrum. However, it

does require that the Raman emission from the sample be stable for the time it takes for two successive exposures. If the Raman emission is changing rapidly or the background varies with time, this approach may not be suitable. In that case, a smoothing filter with its inherent resolution reduction may be the only option.

8.2.3.1.2 SPECTRAL SMOOTHENING

The signal-to-noise (S/N) ratio in Raman spectra can be improved by applying smoothing routines. The Savitsky-Golay (SG) smoothing method [234] is considered to be the most versatile and uses a selectable nonlinear function on each side of the central point. Each point in the smoothed spectrum is a weighted average of adjacent points in the original spectrum. An equal number of data points on each side of a target data point are included, making an odd number of total points in the average. The degree of the polynomial and the (odd) number of data points to be included in the smoothing routine can be selected appropriately. It is important to choose a proper degree of polynomial, and also the number of averaging points, so that the original data is not over-smoothed and the positions of Raman peaks are not changed.

Other smoothing technique used widely is the moving point average method [234], which simply replaces each data value with the average of neighboring values. To avoid shifting the data, it is best to average the same number of values before and after where the average is being calculated. Although this technique gives better signal to noise ratio than SG smoothing, it tends to flatten the peaks even more.

8.2.3.2 BACKGROUND REMOVAL

As discussed earlier in Raman tweezers background can be much suppressed by trapping the particle at a separation from the cover glass surface so that collection of background signal

originating from the cover glass and immersion oil is reduced. There can also be stray signals due to the optics of the setup. These backgrounds can be minimized by background subtraction technique. First the signal is obtained from the particle in the trap. Now, keeping the conditions same, the particle is removed from the trap and the signal is obtained. These two signals are subtracted to give the background subtracted signal [233]. It is important to note here that subtraction of background though useful for observing small Raman features on top of a large background but leads to error considering the noise present in the spectra that can not be reproduced for sample and the blank. It is therefore more appropriate to first de-noise both the signal and blank spectra before applying any background subtraction technique.

Although subtraction of spectrum recorded from blank from the spectrum recorded from the subject can largely reduce the background, for increasing the efficiency of this method various approaches have been taken. One major effort was the use of two separate laser beams with different wavelengths [235]. In this technique, first the particle is trapped using a 785 nm beam and its Raman spectrum is recorded. Then another 1064 nm laser is switched on and used to remove the particle from the 785 nm laser beam waist in order to take the background under the exactly same experimental condition.

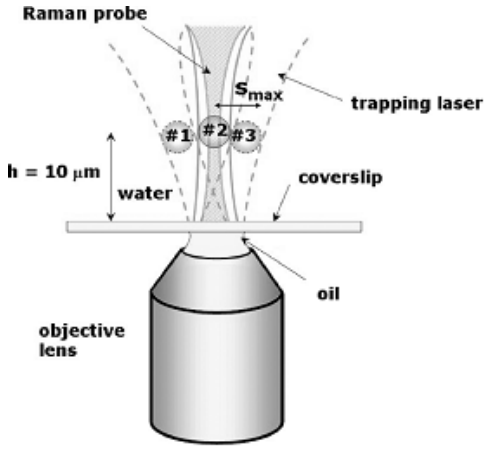

Figure 8.6 Schematic of the setup for background removal using lock-in amplifier (reprinted by permission from *Applied Physics Letters* [236]).

Rusciano *et al* introduced an experimental method which allows the acquisition of the Raman spectrum of a trapped object not requiring any background subtraction procedure [236]. This method is based on the periodical modulation of the trap position, obtained by means of a galvo-mirror. A sketch of this method is shown in figure 8.6. The trapped particle periodically crosses a second laser, used as Raman probe, whose position is fixed in space. The Raman signal coming from the sample is analyzed by using a lock-in amplifier. When the voltage applied to the galvo-mirror is zero, the Raman probe and the trapping beam are completely overlapped (position 2 in figure 8.6) and the Raman signal reaches its maximum. As far as the bead goes away from the Raman probe, the intensity of the Raman signal decreases, vanishing definitively when the bead is not illuminated by the Raman exciting beam (positions 1 and 3 in figure 8.6). During each oscillation period of the trap position, the bead goes through the Raman probe for two times so that the Raman signal is modulated at a frequency twice that of the glavo-mirror. This signal can be selectively detected using a lock-in amplifier.

Though much of the background in Raman tweezers can be suppressed using the above techniques, background originating due to luminescence processes from the sample remain in the acquired spectra. To remove this, derivative filters can be employed that make use of low-frequency nature of the background spectra. Point differences and Savitzky-Golay (SG) derivative techniques are the two most commonly used approaches [233]. Point difference is done by simply subtracting each spectral point from its adjacent points (before and after). SG derivative makes use of polynomial function to fit number of points around each spectral point and then determine the derivative at each point from the function used for that point. Each time a derivative is performed on a spectrum, the offset is removed and subsequently higher order shapes get simplified: linear trends become offset; quadratic becomes linear and so forth.

Unfortunately with each subsequent derivative, noise (consisting of high frequency components) is also amplified unless the procedure used, incorporates some filtering mechanism (the use of polynomial in SG process serves this purpose).

To overcome the above limitations other methods like shifted excitation, Fourier filtering and polynomial fitting are becoming increasingly popular in recent times. Shifted excitation makes use of a tunable laser source to record the Raman spectra at two or more excitation wavelength slightly shifted from each other. Since the resulting fluorescence spectra remains unaffected by the small shifting of excitation laser wavelength but Raman spectra get shifted accordingly, comparison of the acquired spectra can extract the Raman signal from the fluorescence background. Though it is a very promising method for suppressing fluorescence backgrounds, it involves both hardware modifications and additional spectral processing. Fourier transform filtering is one of the most accurate methods for fluorescence rejection, but it depends on direct human intervention to manually specify the upper and lower limits in the frequency domain. Not only is this time consuming, but the limits also differ from case to case. Thus, for biomedical applications, the most popular fluorescence removal technique has proven to be polynomial fitting because of its simplicity and convenience. Fluorescence can be mathematically modeled as a polynomial function, the order of which is selected to effectively remove the fluorescence baseline signal while at the same time minimizing the subtraction of the desired Raman scattering peaks. Based on empirical experience, commonly fifth-order polynomials provide the best fluorescence approximations for biomedical applications. Instead of somewhat arbitrary approach for choosing orders and fitting ranges, Lieber and Mahadevan-Jansen proposed a modified multi-polynomial fitting method that substantially improved the fluorescence background removal in Raman spectra processing [237]. This is an iterative

polynomial algorithm in which the spectral values for the raw spectrum are compared to the polynomial model at each wavenumber. For each successive round of polynomial fitting the lower values for

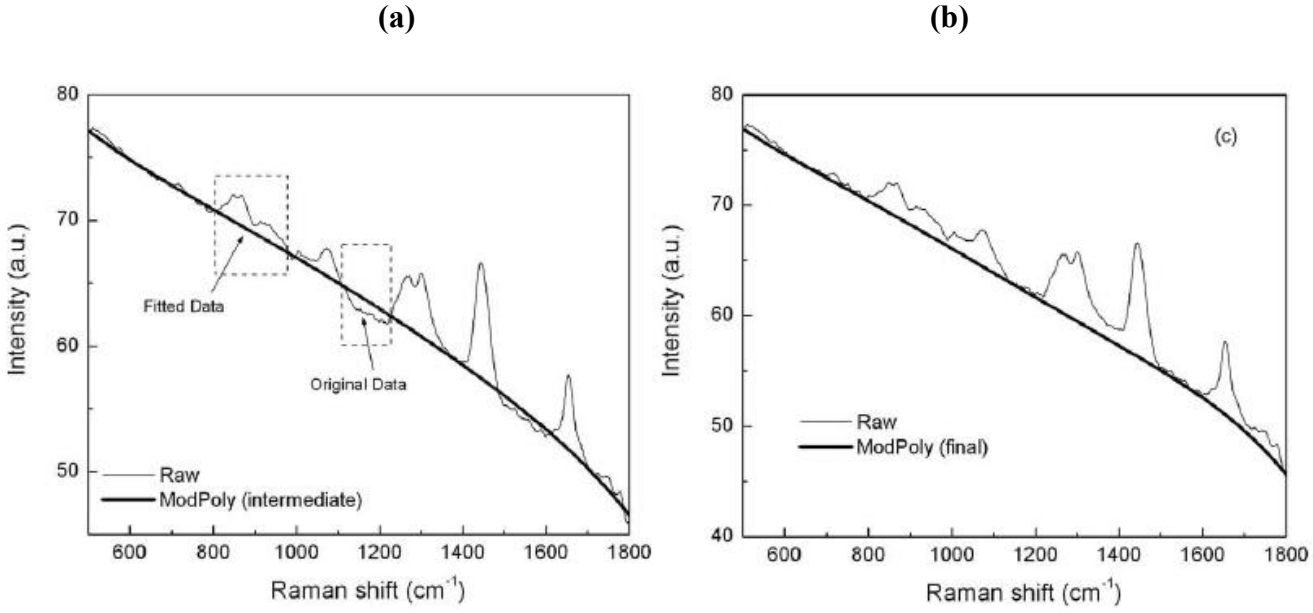

Figure 8.7 Selection of values during iterative polynomial fitting (reprinted by permission from *Applied Spectroscopy* [238]).

each wavenumber are selected and then concatenated to construct a modified spectrum, which is then in turn re-fitted. An example of an intermediate step during the iterative polynomial fitting is shown in figure 8.7 (a). The right-hand box shows where the original signal is lower than the fitted function and therefore the original data are used, while the left-hand box shows where the original data are greater than the fitted function and thus the fitted data is incorporated into the input for the next round of polynomial fitting. The result after the final iteration in the iterative polynomial fitting method is shown in figure 8.7 (b). However, there are still a number of limitations for iterative fitting method of fluorescence removal: (1) noise that is greater than the fitted function is incorrectly treated as Raman signal and is therefore replaced by the fitted function in the next round of polynomial fitting; (2) similar to single polynomial fitting, iterative

polynomial fitting can introduce artificial peaks where the original data in peak-free regions are slightly higher than the curvatures of the polynomial curve and thus are incorrectly replaced by the fitted ones; (3) the contribution of some major large peaks in the polynomial fitting is significant, which may bias the fitting results; and (4) it takes from 20 to 500 iterations to compute the polynomial as compared to a single polynomial fitting, which could be fairly long for real-time spectroscopy.

8.2.4 IMPROVEMENT OVER MICRO-RAMAN SPECTROSCOPY

Compared to Raman spectroscopic method applied to bulk sample, micro-Raman technique suffers from the drawback that the number of micro-objects contributing to the observed Raman spectra is very small (may even be single) leading to a much weaker Raman signal which can get masked by the background. As most of the background in micro-Raman spectroscopy comes from the glass slide used for fixing the sample, employing optical tweezers for trapping the cell away from the coverslip surface reduces the background.

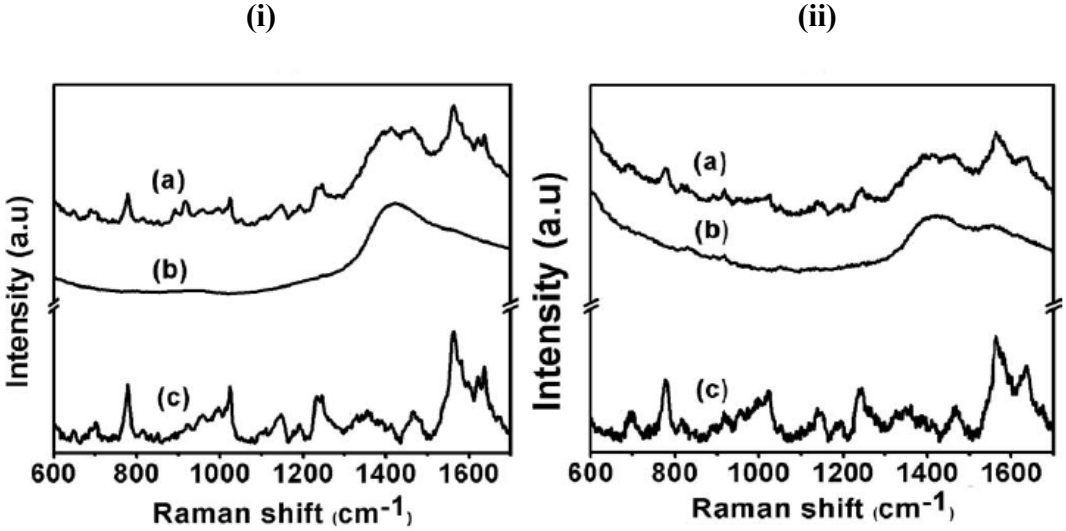

Figure 8.8 (i)(a) Raman spectrum of RBC optically trapped ~ 15 μm above the glass substrate, (b) is the background and (c) the background subtracted Raman spectrum. (ii) (a) Raman spectrum of RBC adhered to the glass substrate, (b) is the background without

RBC, and (c) is the background subtracted Raman spectrum. The data shown are the mean of spectra collected from 5 cells in each case. The acquisition time with each single cell was ~ 30 s with ~ 2 mW excitation.

In figure 8.8 (i) we show the Raman spectra, recorded between 600 and 1700 cm^{-1}, from a red blood cell (RBC) held under optical trap ~ 15 μm above the substrate. The excitation laser power and the acquisition time were ~ 2 mW and ~ 30 s respectively. Curve (a) is the spectra recorded when the RBC was in the trap, (b) is the background with RBC removed from the trap region, and curve (c) is the back ground subtracted Raman spectrum, suitably magnified for viewing. In figure 2A(ii) we show the corresponding spectra from a RBC adhering on the glass substrate. An improvement of ~ 3 dB can be seen in the signal-to-noise ratio (SNR) of Raman spectra recorded from the optically trapped cell.

8.3 CHARACTERIZATION OF RAMAN OPTICAL TWEEZERS FOR RECORDING SPECTRA FROM RED BLOOD CELLS

Raman optical tweezers are being extensively used for studying RBCs since Raman spectroscopy is a powerful technique to monitor the oxygen carrying capacity of RBCs as the binding or the dissociation of oxygen from heme leads to significant conformational changes of hemoglobin (Hb) that can be sensitively monitored by this technique. Since recording of Raman spectra from cells involves trapping of the cells over long duration with light power level of few $MW.cm^{-2}$, the possibility of photo induced damage to the trapped cells needs to be carefully examined. We have therefore studied photo-induced changes in RBCs as a function of the duration of laser exposure in Raman optical tweezers employing NIR (785 nm) laser source. Recording of time lapsed Raman spectra from a trapped RBC show spectral changes that were attributed to the cell degradation.

8.3.1 BACKGROUND

Previous studies on Raman spectroscopy of RBCs utilizing Ar:Kr ion [239,240], He-Ne [241] and NIR [242] lasers to excite Raman spectra have shown significant photoinduced damage for long exposure time. With a power of ~ 0.75 mW (irradiance at the sample ~ 80 $kW.cm^{-2}$) at Ar:Kr ion laser lines (488 nm, 514 nm and 568.2 nm) used to excite Raman spectra, significant changes in the Raman spectra acquired from RBC trapped using 830 nm laser beam were observed as a function of time [239]. These changes were attributed to the formation of methemoglobin (met-Hb) due to photo-induced irreversible binding of oxygen to the heme groups. However, it should be noted that in the studies carried out by Ramser *et al* [239] the resonant absorption of the laser wavelengths by met-Hb led to high fluorescence background, which may obscure observation of small changes that may be crucial for understanding the role of other possible pathways of photo induced damages. Micro-Raman studies carried out by Wood *et al* using He-Ne laser beam (632.8 nm, irradiance ~113 $kW.cm^{-2}$) also showed significant changes in the spectra as a function of the exposure time [241]. The observation that these changes were similar to that observed in Raman spectra of RBC acquired at elevated temperature led them to suggest that the laser exposure induced changes may be arising due to Hb aggregate formation resulting from photoinduced protein denaturation. Though in the study carried out by Ramser *et al* no photo damage was observed in cells trapped for duration of up to 10 min by NIR trapping laser light (830 nm, irradiance ~ 13 $MW.cm^{-2}$) [239], in the study carried out by Wood *et al* using 785 nm excitation, significant damage above 18 mW (irradiance ~ 1 $MW.cm^{-2}$) for exposure duration ~ 200 s [242] was observed. In this study the RBCs were

fixed onto the glass substrate using poly-L-lysine which may also lead to unwanted surface induced effects and may also hinder observation of early stage of photo damage.

We have therefore studied photo-induced changes in RBCs as a function of the duration of laser exposure in Raman optical tweezers employing NIR (785 nm) laser source. The use of Raman optical tweezers helped in acquisition of good quality spectra by manipulating the trapped cell away from the surface, thereby minimizing unwanted background originating mostly from the substrate and immersion medium. Further fluorescence coming from the trapped RBC itself, which may suppresses the small spectral alterations present at early stages of photodamage, was minimized by using NIR excitation. The changes observed in the Raman spectra and bright field images as a function of exposure time suggest initiation of aggregation of Hb in the trapped RBC at a much lower exposure value than reported previously. The spectral changes suggest simultaneous occurrence of protein denaturation and hemichrome formation. The possible involvement of non-linear light absorption effect in the observed photo induced changes in the cells is also discussed.

8.3.2 MATERIALS AND METHODS

For trapping and acquisition of Raman spectra we used laser power varying from 3 mW to 9 mW, measured at the specimen plane. The laser spot size at the focus was ~ 0.5 μm and the RBCs were trapped ~ 15 μm above the bottom cover plate of the sample holder. We recorded spectra without a cell in the trap and then subtracted this background spectra from the Raman spectra acquired from the trapped RBC in order to remove the background arising from the buffer, substrate and objective immersion oil.

The absorption spectra of met-Hb, hemichrome and oxy-hemoglobin (oxy-Hb) were monitored over ~400 to 900 nm using a Cintra 20 (GBC, Australia) UV-visible spectrometer. The measurement parameters were set to 1 mm slit width, 500 nm/min scan speed and data were recorded at ~1 nm intervals. About 2 ml of samples were placed in a quartz cuvette while another quartz cuvette filled with 1.5 mM phosphate buffer served as background.

Blood (1 ml) was collected by venipuncture from healthy volunteers in glass tubes containing EDTA (5.4mg/3ml) as an anticoagulant. RBCs were separated from these anticoagulated blood samples by centrifugation at 3000 rpm for 3 minutes. The separated RBCs were then washed with phosphate buffer saline (PBS) and suspended in 1.5 mM phosphate buffer containing 290 mM sucrose. This buffer maintains the osmolarity of the suspending media and inhibits the adherence of cells to glass surface [243]. Appropriate dilutions of the cells in buffer solution were then used for experiments. For experiments with RBC containing met-Hb the washed RBCs were resuspended in 0.1% sodium nitrate solution and the suspension was allow to stand for ~1 hour at room temperature [241]. The cells were thereafter washed in PBS and resuspended in the same buffer. Oxy-Hb solution was prepared following method describe in reference 244. For preparation of hemichrome solution method described in reference 245 was used. The formation of met-Hb and hemichrome was confirmed from UV-visible spectroscopy showing marker band at ~ 635 nm and ~537 nm for met-Hb and hemichrome respectively [245].

8.3.3 RESULTS AND DISCUSSIONS

For studying the effect of laser exposure on RBC held in Raman optical tweezers, first we acquired consecutive time lapsed Raman spectra in the wavenumber region of 525-1700 cm^{-1} with an acquisition time of 30 s for each spectra over a total time period of 3 minutes. The results

are shown in figure 8.9. The trapping/excitation power used was ~ 7 mW and for exposure time of few tens of seconds significant changes could be seen for the Raman bands at 1244 cm^{-1}, 1366

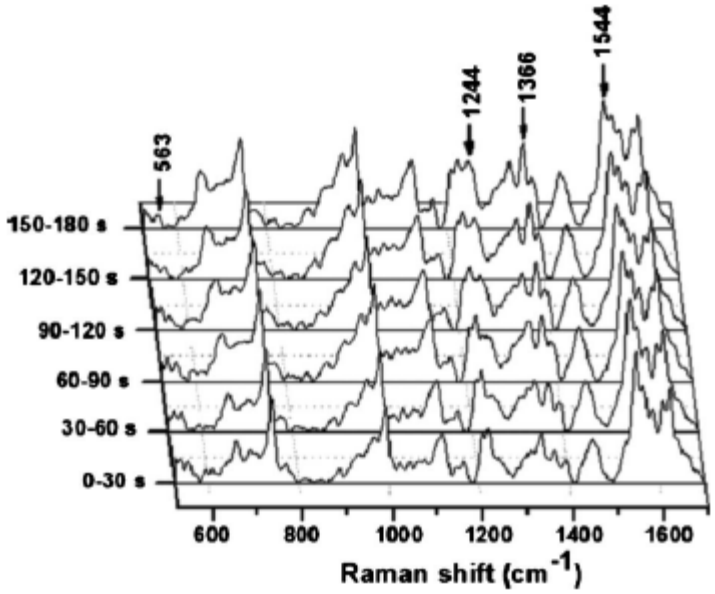

Figure 8.9 Temporal evolution of Raman spectra observed from trapped RBCs with trapping/excitation laser power of ~7 mW, recorded over a 525- to 1700-cm^{-1} region using a 600-lines/mm grating. The spectra shown are the mean of three cells. Iterative polynomial fitting was applied to the baseline to remove the background. The Raman bands showing temporal change in intensity are indicated.

cm^{-1} and 1544 cm^{-1} alongwith a small decrease in intensity of the band at 563 cm^{-1} and a gradual increase in signal to noise ratio (SNR). As the spectral region above 1000 cm^{-1} undergoes most significant changes we investigated this region in detail. Further, for improved statistical validation, spectra were recorded from blood samples collected from five healthy volunteers. For each blood sample at least seven RBCs were studied. In figure 8.10 (a) we show the Raman spectra acquired at time intervals 0-5 s and 175-180 s and recorded with ~5 mW laser power, from seven RBCs in the blood sample of a healthy donor. Significant time dependent changes can be seen in all the spectra. Notably when we apply no baseline fitting to the acquired spectra there was also a significant difference in the baseline offset between the

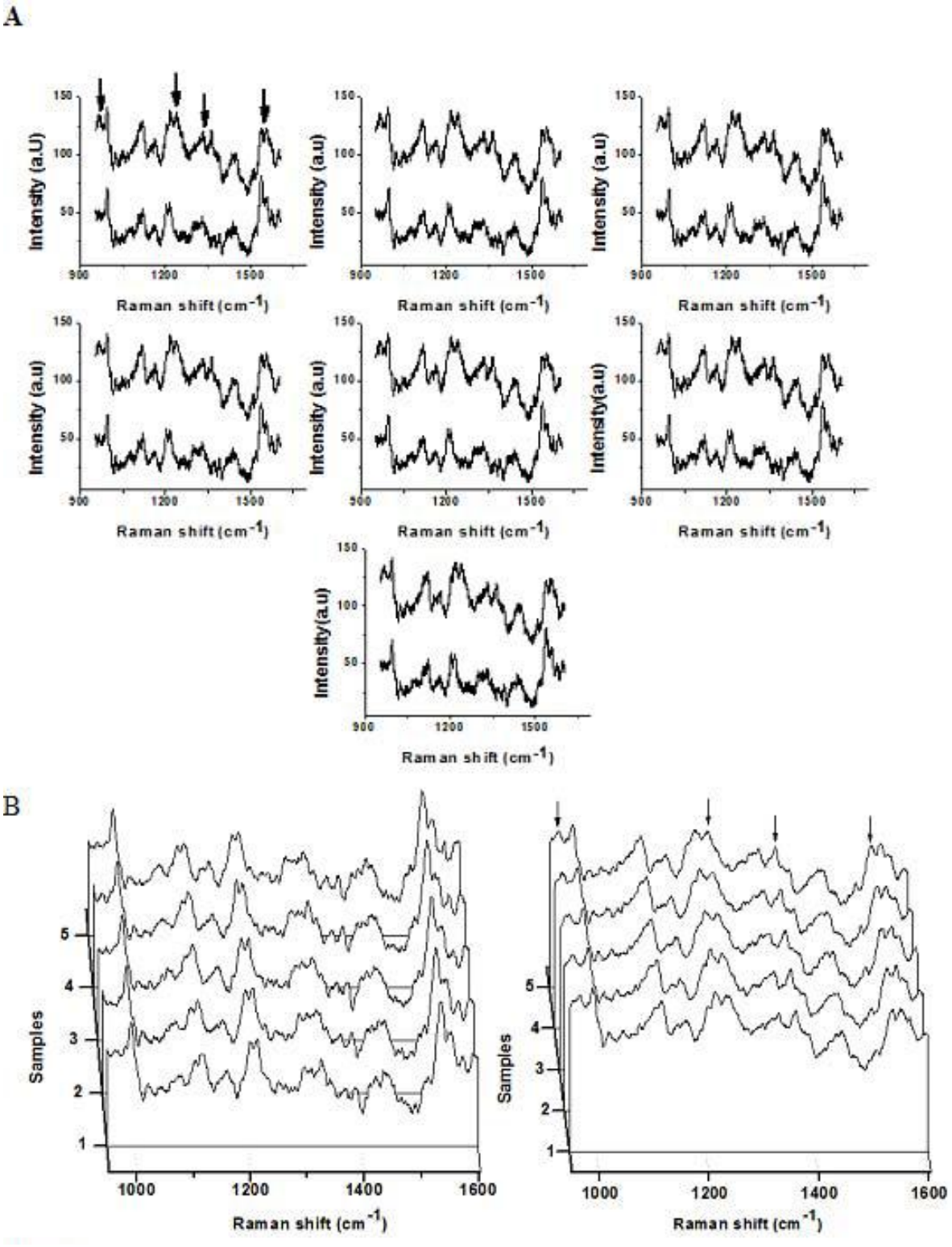

Figure 8.10 (A) Raman spectra acquired from trapped RBCs at 5 mW of trapping power. In each graph the bottom spectra are acquired at 0 to 5 s and top spectra are acquired at

175 to 180 s. The large baseline shift can be seen for spectra collected at the 175-180 s interval. Further, several Raman peaks indicated by arrows located at 975, 1244, 1366, and 1544 -cm^{-1} suffer significant change in intensity due to prolonged laser exposure. (B) Mean Raman spectra from five blood samples at 0 to 5 s (left) and 175 to 180 s (right). From each sample, spectra were acquired from seven cells. The changes are indicated by arrows. All spectra were acquired with a 1200-lines/mm grating.

spectra collected at 0-5 s and 175-180 s. In figure 8.10 (b) mean spectra from five samples are also shown. The spectral changes with time were noted to be similar for RBCs collected from all the five blood samples.

To observe the effect of laser power on the time evolution of the spectra, the spectra were recorded at laser powers of ~5 mW, ~7 mW and ~9 mW. Figure 8.11 shows the temporal evolution of the mean Raman spectra (recorded between 950 and 1600 cm^{-1}) from trapped RBCs, at room temperature (~ 25° C). For clarity, spectra collected only over seven time intervals are shown as representative of the observed time lapse changes. The spectra collected at increasing exposure time show substantial baseline shift with time.

From figure 8.11 it can be seen that with increased exposure duration the Raman spectra show change in many Raman bands. Notably most of the significant Raman bands observable in RBC spectra are contributed by intracellular hemoglobin as the cytoplasmic proteome in red blood cells is composed of 98% hemoglobin and therefore while acquiring Raman spectra of RBCs the signature of Hb supersedes all other proteins. The assignments (Table 8.1) for some important Raman bands follow from the work by Wood *et al* [242]. Band assignments have been considered for only oxygenated Hb as the cells were kept at equilibrium with atmospheric oxygen.

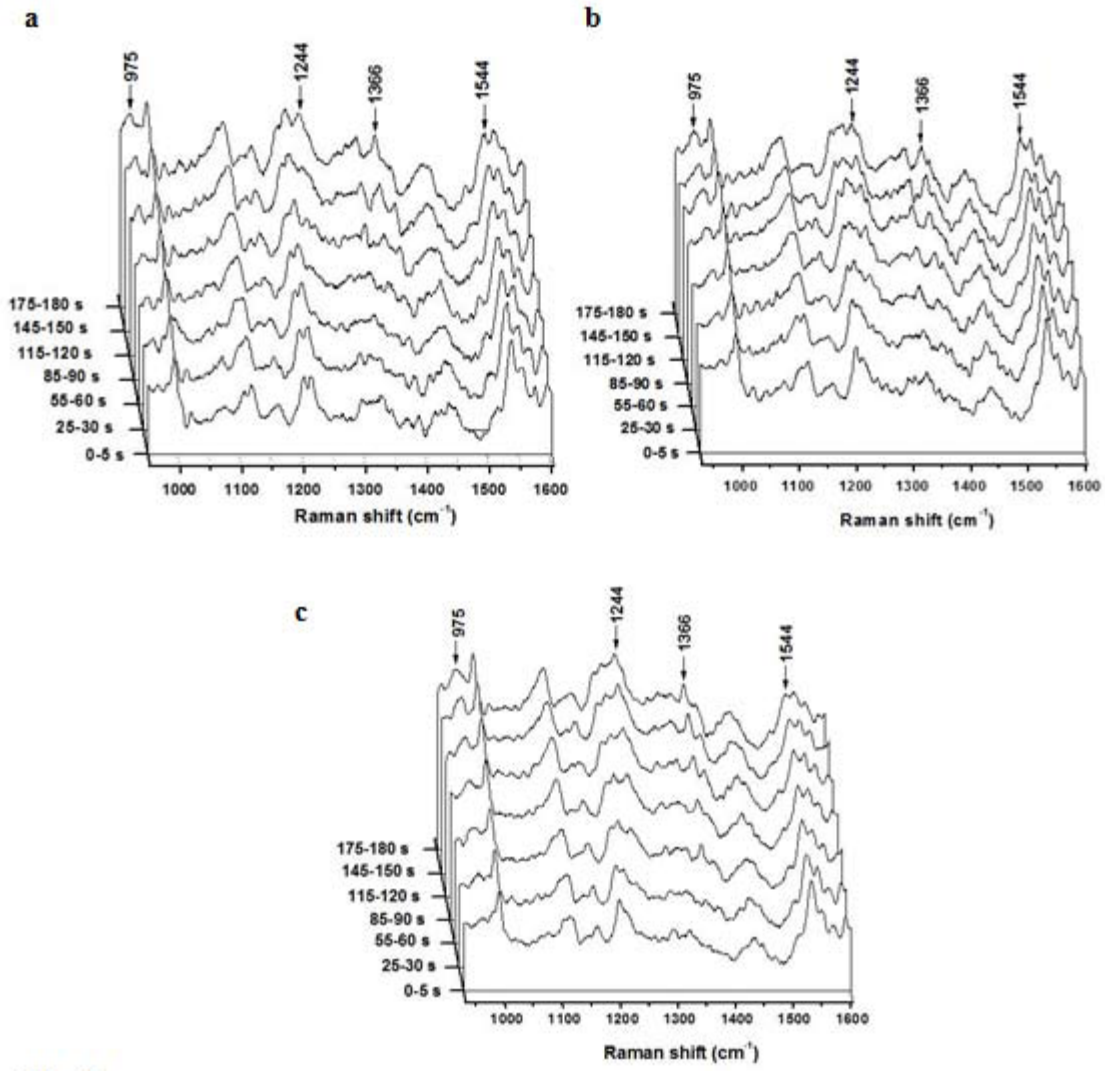

Figure 8.11 Time evolution of Raman spectra observed from trapped RBCs with trapping/excitation laser power of (a) 5, (b) 7, and (c) 9 mW. The corresponding irradiance at the specimen is (a) 2.55, (b) 3.57, and (c) 4.58 MWcm^{-2}. The Raman bands showing temporal change in intensity are indicated.

The bands in the region between 1500-1700 cm^{-1} are known to serve as spin state markers. The normal mode at 1544 cm^{-1} primarily consists of C_β-C_β bond stretching and is sensitive to photo-oxidation of heme. The 1366 cm^{-1} band assigned to local co-ordinate ν_4 involve pyrrole half ring

stretching vibration and are known as oxidation state marker. The band at 1244 cm^{-1} is associated with *C-H* in plane vibrations of methine hydrogen in porphyrin macrocycle [246, 247, 248]. The 563 cm^{-1} band comes from *Fe-O_2* stretching and is indicative of oxygenation state of the central iron atom.

Table 8.1. Assignment and spectral position (cm^{-1}) of the Hb Raman bands undergoing significant temporal intensity change as shown in figure 8.11. For comparison bands observed by Wood *et al* [242] for oxygenated Hb are also shown.

Band Assignment	**Local co-ordinates**	**Band Position(cm^{-1})**	**Band position (cm^{-1}) [242]**
ν_{11}	$\nu(C_\beta C_\beta)$	1544	1547
ν_4	$\nu(\text{pyr half-ring})_{sym}$	1366	1371
ν_{42}	$\delta(C_mH)$	1244	1248
ν_{46}	$\delta(\text{pyr deform})_{asym}$ and/or $\gamma\ (C_bH_2)_{sym}$	975	974
$\nu(Fe\text{-}O_2)$	$\nu(Fe\text{-}O_2)$	563	567

The observation of enhanced intensities of the 975 cm^{-1}, 1244 cm^{-1} and 1366 cm^{-1} Raman bands is consistent with the previous report by Wood *et al* [241]. Since similar spectral changes were observed during thermal denaturation of Hb, they attributed these changes to the aggregation of heme moieties as a consequence of photo-induced denaturation of Hb. Further, the peak at 1544 cm^{-1} is resonantly enhanced with laser wavelength of 785 nm and decrease in intensity of this peak can be ascribed to conversion of oxy-Hb to met-Hb, in which oxygen is irreversibly bound to heme, as indicated in previous studies [239, 249]. It is pertinent to note here that high spin met-Hb is less stable than hemicrome, a low-spin component in which the sixth coordination site of the iron is occupied by the imidazole group of the distal histidine, and can be spontaneously converted to the later [250, 251]. Additionally, any possible denaturation

of intracellular Hb due to light damage action also helps the formation of hemichrome as disruption of globin structure facilitates the coordination of the imidazole group of the distal histadine with the iron atom [250]. Therefore, we recorded met-Hb and hemichrome Raman spectra to correlate with the observed photo induced changes. The spin marker bands in the spectral region ~1500-1600 cm^{-1} for met-RBC and hemichrome are shown in figure 8.12 (a) and (b). The spectra shown in figure 8.12 (a)-(b) were acquired with an excitation/trapping power of ~ 3 mW to ensure no photo induced changes in the spectra. The spectral changes noted for met-Hb and hemichrome when compared with photo induced changes shown in figure 8.12 (c), indicate predominant formation of hemichrome in the damaged cells. A reduction in 563 cm^{-1} peak, as seen from spectra in figure 8.9, is also indicative of the above fact [250]. Therefore photo induced degradation of Hb inside optically trapped RBCs may be an interplay of photo-induced denaturation of Hb as well as photooxidation effected hemichrome formation.

As the photo-damage observed for RBCs due to laser exposure can be largely attributed to Hb denaturation phenomena, similar as observed for heat treated RBCs [241] it is important to investigate the possible role that the elevated temperature at the trap focus might play. The steady state temperature rise in optical trap has been estimated by Ramser *et al* to be less than one Kelvin, considering water as the prime absorber of laser power [239]. However, it is important to note that as RBCs contain very high concentration of Hb (~ 5 mM) [252] and the absorption coefficient of Hb at near infrared region is much higher than that of water, light absorption by intracellular Hb cannot be neglected for reasonable estimation of temperature increase. The temperature increase at the focus can be given as [197],

$$\Delta T = P\left(b\left[\ln\left(\frac{2\pi R}{\lambda}\right) - 1 \right] + db\left[\frac{\ln\left((2\pi r_p/\lambda)^2 + 1\right)}{2} \right] \right) \tag{8.4}$$

Where P is the trapping laser power, R is the distance of the focus from the cover glass surface, λ is the laser wavelength, r_p is the effective radius of the red blood cells. The coefficient b is defined as,

$$b \equiv \frac{\alpha}{2\pi K} \tag{8.5}$$

Where α is the absorption coefficient and K is the thermal conductivity of water. db is the differential change of b for the RBCs with respect to water.

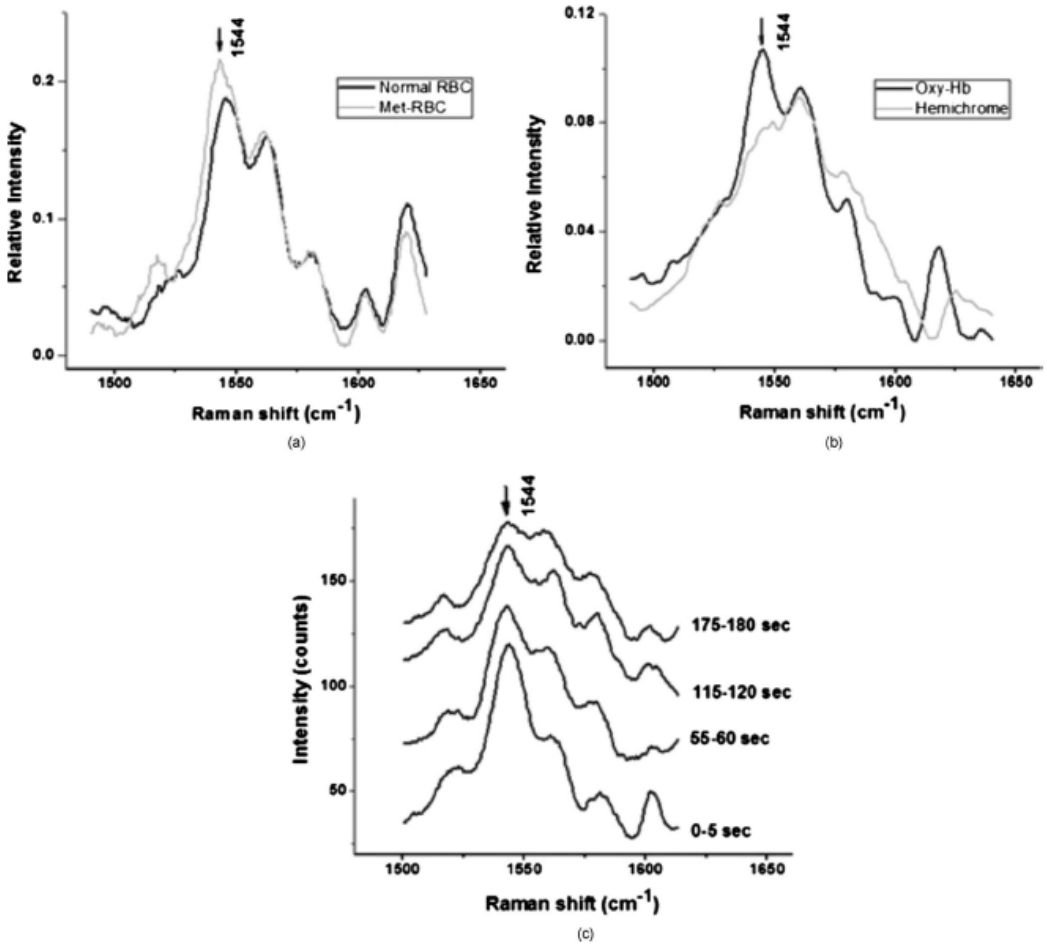

Figure 8.12 (a) Raman spectra of RBC containing oxy-Hb and met-Hb. (b) Raman spectra from oxy-Hb solution and hemichrome solution. The spectra were recorded at an excitation/trapping power of ~3 mW over a recording time of ~30 s. Spectra shown are

the mean from five acquisitions. (c) The time-lapse spectra from photodamaged RBCs at an excitation/trapping power of ~9 mW. The 1544 cm^{-1} Raman peak is indicated by arrow.

Taking the values as α_{water} ~3m^{-1} [253], K_{water} ~ 0.6 W/mK [197], α_{Hb} ~ 370 m^{-1} [254], K_{Hb} ~ 0.45W/mK [255] and the mean radius for the RBCs as ~ 3 μm, the temperature rise at the focus for laser power of 5 mW to 9 mW, was estimated to be between 2 ºK to 3.7 ºK. As the experiments were performed at room temperature (~ 25 ºC), the elevated temperature at the focus was < 29º C, not sufficient for causing heat denaturation to the cells.

The Raman spectra also show a marked increase in baseline and a gradually increasing intensity for all the Raman bands with laser exposure time. Wood *et al* had also observed same effect and ascribed it to excitonic interaction mechanism between the metalloporphyrins resulting in migration of energy throughout the aggregated heme network [241]. However, intrinsic fluorescence coming from photo generated hemichrome [256] may also contribute to the baseline enhancement. Therefore we investigated the time evolution of the bright field images of the cell. Figure 8.13 shows time separated images of a trapped cell at ~ 9 mW of laser power. It is pertinent to note here that RBCs were suspended in isotonic buffer so that they maintained their natural bi-concave shape. Though the equilibrium orientation of the bi-concave RBC under

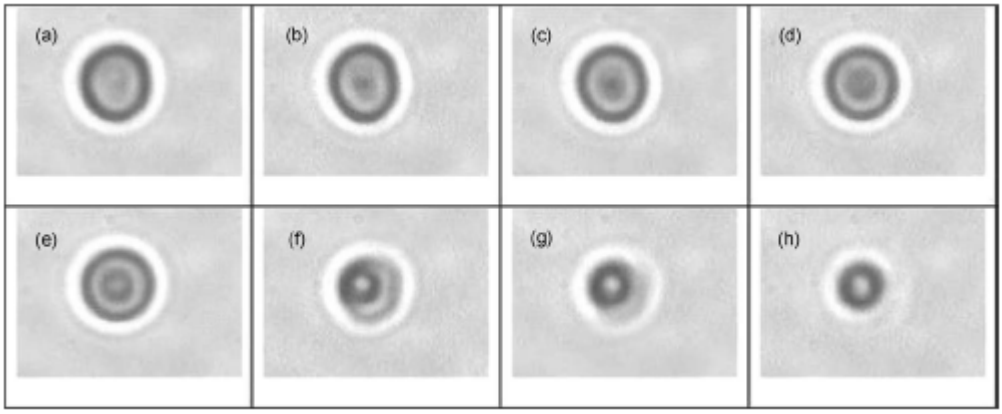

Figure 8.13 Images of a trapped RBC with ~9 mW of laser power showing changing appearance of the cell, due to condensation of the cell mass at the trap focus, with duration of laser exposure of (a) 22, (b) 25, (c) 28, (d) 31, (e) 33, (f) 33.6, (g) 33.9, and (h) 36 s.

optical trap is side-on type [210, 211, 219], we observed that for small trapping power (< 10 mW) used in our studies the cells can be captured by optical forces but they do not turnover. This is possibly caused by the small gradient force resulted in our case which is unable to generate sufficient torsional moment required to turnover the cells [257].

As can be seen from bright field images of the trapped cell in figure 8.13, that the change in density of the cytoplasmic mass starts at the centre and gradually the entire cell get affected and majority of the cell mass gets densely packed at the trap focus. A plausible explanation for this observation is that in optically trapped RBC the precipitated heme, resulting from protein denaturation and photo-oxidation, gets attracted towards the trap focus and this may lead to the formation of heme aggregate at the trap focus. We also checked the effect of relaxation on the cells when they were released from the trap after 36 seconds. Monitoring the cell for ~ 10 minutes showed no sign of regaining its normal physiology and therefore it could be concluded that the laser induced effects were not reversible.

In figure 8.14 the time evolution of the intensity of Raman bands at 975 cm^{-1}, 1244 cm^{-1}, 1366 cm^{-1} and 1544 cm^{-1}, relative to the baseline have been shown. As the peak intensities are influenced significantly by adjacent Raman bands, to estimate the actual intensities of the Raman peaks Lorentzian fitting was performed that can effectively minimize the error contributed by overlapping regions of adjacent bands. Also the temporal change in baseline offset of the spectra and mean Raman signal amplitude are shown. The mean Raman signal amplitudes were

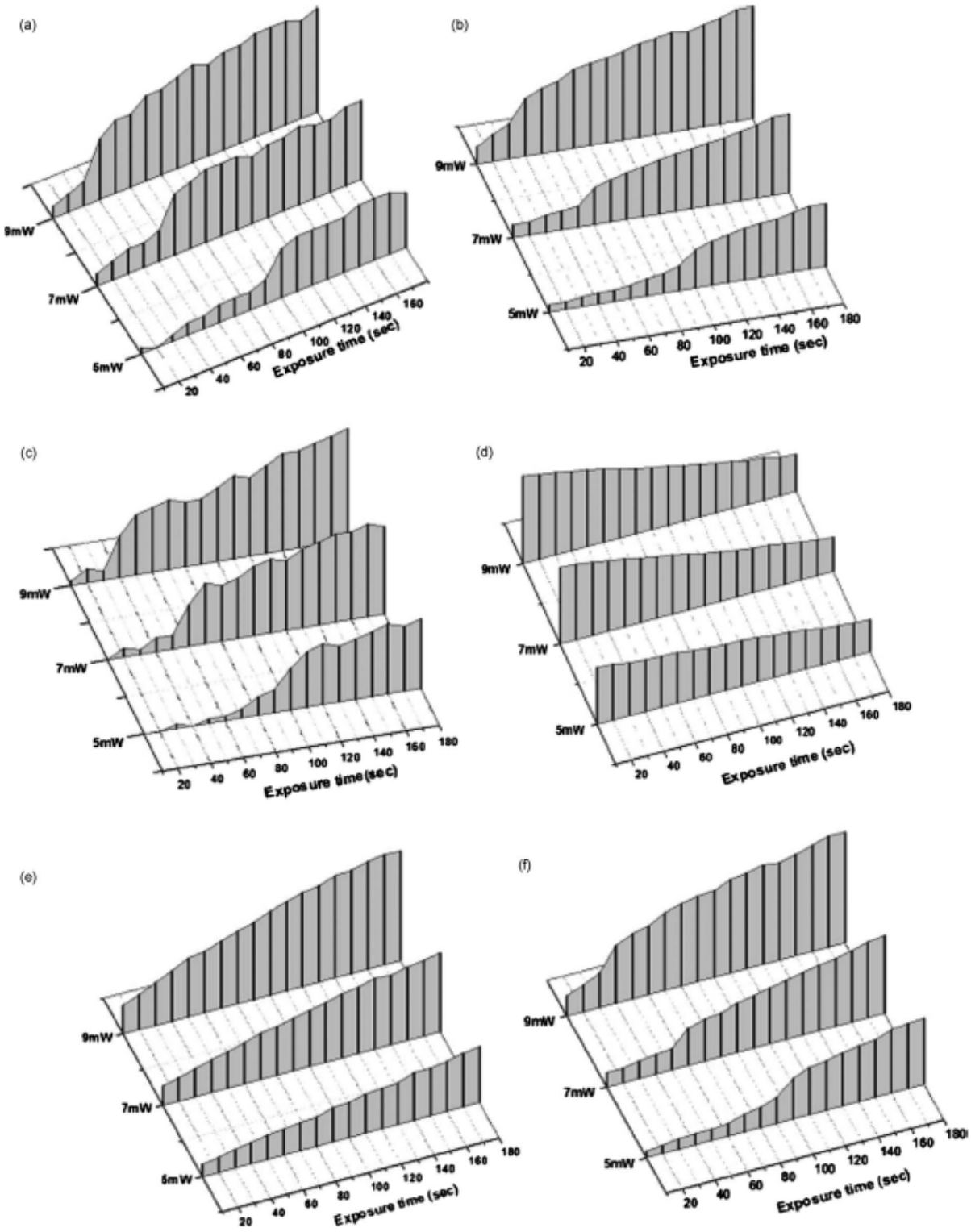

Figure 8.14 Temporal variation of relative intensity of Raman bands at (a) 975, (b) 1244, (c) 1366, and (d) 1544 cm^{-1}. The temporal variation of baseline shift (e) in the acquired spectra and (f) the mean Raman signal amplitude are also shown.

estimated over other Raman peaks (996 cm^{-1} (ν_{45}), 1170 cm^{-1} (ν_{30}), 1210 cm^{-1} ($\nu_5 + \nu_{18}$), 1434 cm^{-1} (ν_{28}), 1551 cm^{-1} (ν_{11})) that do not show significant temporal variation. It can be seen that for peaks at 975 cm^{-1}, 1244 cm^{-1} and 1366 cm^{-1}, initially the intensity increases slowly until at a particular point of time is reached where a steep increase in intensity could be noted. The time interval at which the steep increase in intensity could be seen are 90-100 s, 50-60 s and 30-40 s for excitation power of ~ 5 mW, ~ 7 mW and ~ 9 mW respectively. These similar time variation patterns of these Raman bands can be understood considering their primary association with photo induced denaturation of Hb inside RBC. The rapid intensity variation of the Raman bands associated with photo-denaturation at specific time interval is also in quantitative agreement with the microscopy data presented in figure 8.13 which shows that the rate of dense packing of erythrocyte cell mass rises sharply at ~33-34 s at trapping power of ~ 9 mW. Since inside the RBC, Hb is present in very high concentration [241], initiation of aggregation by the photo-induced effect may lead to intracellular concentration of Hb beyond the critical supersturation ratio and thus induces rapid polymerization nucleation. Notably the change in mean Raman signal amplitude (figure 8.14(f)) also follows the heme aggregation pattern. As both elastically and inelastically (Raman scattering) scattered light are expected to be proportional to the number density of the scatterers, therefore, we believe that an aggregated cell mass at the laser focus is the main cause for the observed increase in Rayleigh scattered and Raman scattered light with increasing exposure time.

The decrease in intensity of the Raman band at 1544 cm^{-1} (figure 8.14(d)) follows a linear relationship with exposure time. Intensity of this peak is inversely related to the extent of photo induced hemichrome formation and therefore suggests increased level of hemichrome with

prolonged laser exposure. The hemichrome is known to give strong intrinsic fluorescence that may result in enhanced background in the spectra [256]. We noted a similar linear variation for the baseline offsets present in the acquired spectra (figure 8.14(e)).

As discussed earlier, based on the 785 nm excited micro-Raman spectra of RBC Wood *et al* estimated a safe upper limit to be ~ 18 mW [242]. However, results presented in figure 8.11 show that significant photo-induced damage can occur at much lower trap power level (~ 5 mW) for acquisition time of ~ 100s. It should be noted that in contrast to Raman optical tweezers, where cells are optically held in suspension, the cells were fixed on aluminum coated Petri dish by poly-L-lysine [242], which could often result in unwanted surface induced effects and may also lead to an enhanced background in the acquired spectra, that may mask the small changes that are clearly identifiable in our data.

It is pertinent to note that optical tweezers are increasingly being used for manipulation of different cell types and for manipulation of highly motile cells, like sperms, employment of hundreds of mW of laser power is often necessary. In such studies it has been shown that cells can be trapped with hundreds of mW of 1064 nm laser power over several minutes without causing significant photodamage [258]. The observation of severe photdamage suffered by the RBCs when irradiated with few mW of 785 nm laser wavelength possibly results from the fact that RBCs have significantly higher light absorption due to high concentration of intracellular Hb. The molar absorption of oxy-Hb (predominant form of Hb present in the cells studied in our experiments) is ~ 0.1 $mm^{-1}.mM^{-1}$, orders of magnitude higher than water (major cellular constituent of the sperm cells) absorption (0.005 $mm^{-1}.mM^{-1}$) in this spectral region [253, 254]. Therefore, while trapping of sperm cells with hundreds of mW near infrared laser power for minutes produces minimum damage, trapping of RBCs using 785 nm laser is resulting

significant damage to the cells. The choice of 785 nm laser beam for Raman optical tweezers is driven by several facts as that at even longer wavelengths the Raman scattering efficiency (vary as $\sim \lambda^{-4}$) is extremely low. This is also aided by the availability of efficient CCD based detectors at this spectral region. For RBCs using wavelength ~785 nm also offers the advantage of resonance enhancement of the Raman spectra [242]. Therefore use of 780-850 nm as the excitation wavelength has become a standard for studying Raman spectra of RBCs [47, 49, 242].

We would also like to note that for short exposure durations the recorded Raman spectra suggested normal functionalities of the cells and the observed morphology of the cells in microscope appears to be normal. Significant photodamage was only observed for longer exposure times (> 30 s @ 9 mW to >90 s @ 5 mW). Since for longer trapping duration the photo damage resulting to the cells is also consistent over samples collected from different donors, presence of any pre-damage in the samples is unlikely.

In figure 8.15 we plot the accumulated light dosage (denoted as $D_{critical}$) required to observe rapid enhancement of Raman bands associated to photo-induced aggregation process. The value of $D_{critical}$ estimated for each laser power considering trap spot size is ~ 0.5 μm for diffraction limited focusing and the resultant irradiance was ~ 2.55 MW. cm^{-2}, ~3.57 $MW.cm^{-2}$ and ~ 4.58 $MW.cm^{-2}$ for trapping power of ~ 5 mW, ~ 7 mW and ~ 9 mW respectively. The time period for accumulation of light dosage was estimated from figure 8.14. It can be seen from figure 8.15 that, reduced light dosages are required at higher trapping power for initiation of rapid photo-aggregation of Hb. This loss of linear reciprocity between laser power and duration of exposure suggests that non-linear processes may also contributing to the photo-degradation of Hb. Such non-linear absorption is known to take place due to very high light intensity present at

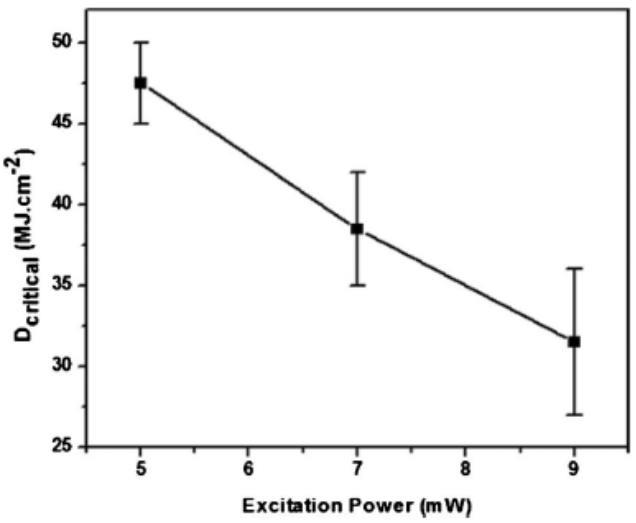

Figure 8.15 Accumulated light dosage on RBC at the time of rapid intensity enhancement of Raman bands at 975, 1244, and 1366 cm^{-1}.

the trap focus even while employing cw NIR sources [198, 199, 259], whereas hemoglobin is known to have very high two photon absorptivity in NIR region (780-880 nm) with a substantial value of ~35 GM at 785 nm [260]. Considering the molecular two photon absorption rate can be expressed as,

$$\phi_{2-ph} = \sigma_{2-ph}\left(\frac{P}{\hbar\omega A}\right)^2 N \tag{8.6}$$

Where, $\sigma_{2\text{-}ph}$ is the two photon absorption cross-section for Hb (~ 35 x 10^{-50} cm^4.s.photon^{-1}.molecule^{-1}), P is the laser power, $h\omega$ is the photon energy and A is the focal area. The quantity $(P/h\omega A)$ represents the photon flux density at focus and could be estimated as ~ 10^{25} photon.cm^{-2}.s^{-1} for trapping/excitation power of ~ 5 mW @ 785 nm. N , the number of Hb molecules present in laser excitation volume, can be estimated considering the mean cellular hemoglobin concentration is ~ 30-35 g/dl and laser excitation volume is limited by the laser spot size and thickness of the bi-concave RBC (~ 2 μm), as ~10^6. Therefore a two photon absorption rate ($\Phi_{2\text{-}ph}$) of ~ 4 x10^7 photons.s^{-1} is predicted, which is a modest value.

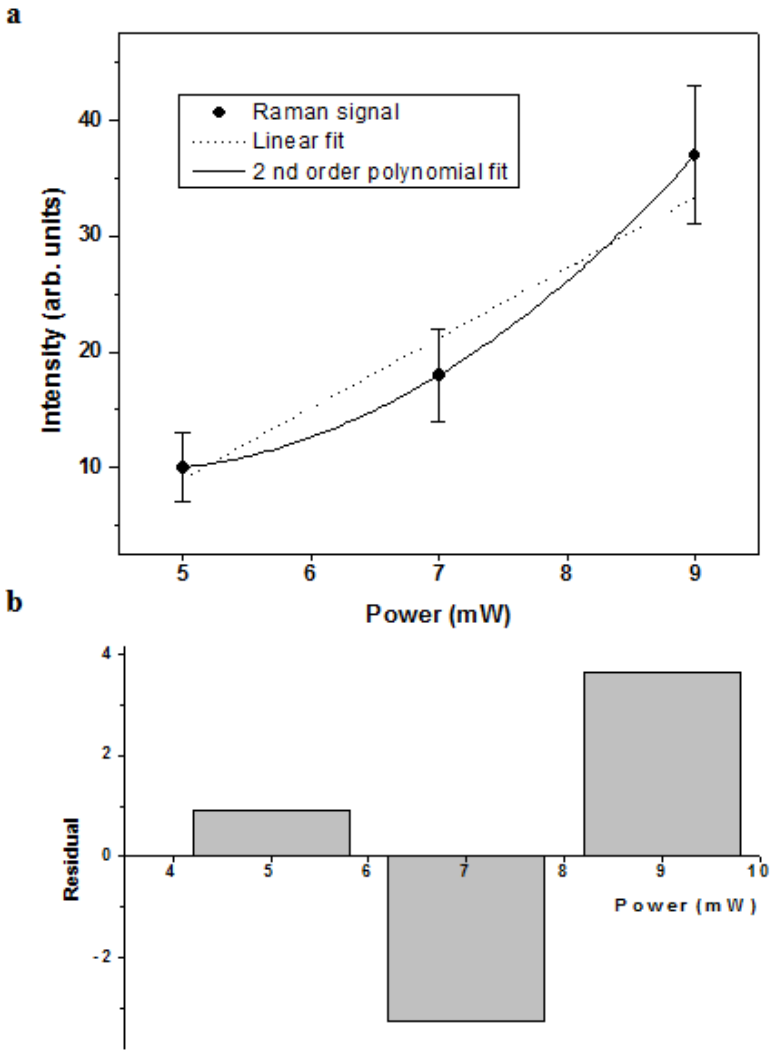

Figure 8.16 (a) Change in mean Raman signal amplitude recorded at 25- to 30-s intervals with varying laser power. The solid line shows a second-order polynomial fit and the dashed line shows a linear fit to the data. (b) Residuals for linear fit. Large residual values indicate minimal linear correlation between data.

In figure 8.16 the mean Raman signal amplitude recorded from trapped RBC at 25-30 s interval is plotted as a function of laser power. The time interval was chosen so that it is at an early point of time before initiation of any rapid aggregation of intracellular mass (see figure 8.13). From the linear fit and second order polynomial fit applied to the data, it can be clearly seen that variation of intensity is non-linearly dependent on the excitation laser power. This

suggests that as the use of higher laser power leads to higher power density at the beam focus, therefore, an increased two photon absorption induced effect may result which possibly caused enhanced photodamage to the intracellular Hb.

8.4 SUMMARY

Development of a Raman optical tweezers set-up and the use of spectral processing routines for extraction of weak Raman signal have been described. Since recording of Raman spectra from cells involves trapping of the cells over long duration with light power level of few $MW.cm^{-2}$, the possibility of photo induced damage to the trapped RBCs was critically examined. The changes observed in the Raman spectra and bright field images as a function of exposure time suggest initiation of aggregation of hemoglobin in the trapped RBC at a much lower exposure value than reported previously.

CHAPTER 9

STUDIES ON ERYTHROCYTES IN MALARIA INFECTED BLOOD SAMPLE WITH RAMAN OPTICAL TWEEZERS

The results of Raman spectroscopic studies performed on optically trapped red blood cells (RBCs) from blood samples of healthy volunteers (h-RBCs) and from patients suffering from *P. vivax* infection (m-RBCs) are presented in this chapter. A significant fraction (~30%) of m-RBCs produced Raman spectra with altered characteristics relative to h-RBCs. The observed spectral changes suggest a reduced oxygen-affinity or right shifting of the oxygen-dissociation curve for the intracellular hemoglobin in this fraction of m-RBCs with respect to its normal functional state.

9.1. INTRODUCTION

Malaria is often associated with the development of severe anemic condition in patients which causes more than half of the mortality resulting from the disease [261]. The pathogenesis of malarial anemia is complex and not well understood. Since the destruction of the parasitized red blood cells (p-RBCs) can only account for less than 10% of the overall red blood cell loss in malaria patients [262, 263], the accelerated destruction of the non-parasitized RBCs (np-RBCs)

is believed to be the primary cause behind development of severe anemic condition in patients. The reduced deformability of np-RBCs [42, 44, 210, 218-220, 226, 264, 265], which may lead to failure in passing through splenic clearance or phagocytosis by spleen cells due to biochemical changes induced by parasite metabolites [262] are some of the factors that could trigger early removal of np-RBCs in malaria patients. Apart from the accelerated destruction of np-RBCs other factors like dyserythropoiesis or ineffective erythropoiesis, reduced haemoglobin-oxygen affinity or disturbed metabolic pathways in RBCs may also contribute to the development of malarial anemia and the associated hypoxia condition. Further studies on np- RBCs are therefore required to get answers to these questions.

Spectroscopic techniques and in particular Raman scattering has been found to be useful for investigating RBCs in malaria infected blood samples. For example the use of confocal Raman spectroscopy could shed new lights on the electronic structure of hemozoin, a by-product of hemoglobin (Hb) catabolization by the malaria parasite and also an important target site for anti-malarial drugs [266, 267]. Significant differences in Raman spectra have been reported for p-RBC and np-RBC in continuous in-vitro culture [268, 269]. Therefore, Raman spectroscopy may help in understanding the altered properties of RBCs in malaria patients (m-RBCs). Raman optical tweezers [45, 46] are particularly appropriate for probing subtle changes in m-RBCs as acquisition of Raman spectrum from RBC optically trapped in buffer media helps avoid perturbations arising due to the immobilisation of the cells on substrate. [240, 270].

In this chapter I provide the results on Raman spectroscopy study of m-RBCs collected from patients suffering from *P. vivax* infection, using Raman optical tweezers. The results show

marked differences in the Raman spectra of a significant fraction (~30%) of m-RBCs relative to their normal counterpart (h-RBC). These changes are consistent with the possibility that the m-RBCs were incompletely oxygenated, even when they were kept in ambient oxygen, i.e. an excess of oxygen.

9.2 MATERIALS AND METHODS:

The experimental set-up used is similar to that described in chapter 8. For experiments with RBCs we used a laser power of ~2 mW, at the specimen plane. The RBCs were trapped ~ 15 μm above the bottom cover plate of the sample holder. To remove the presence of the background from the RBC spectra the background was acquired without a cell in the optical trap. This was subtracted from the original spectra to produce the Raman spectra of the trapped RBC. Further removal of background could be obtained using Lieber and Mahadevan-Jansen (LMJ) iterative polynomial fitting method [237] for better visualization of spectra. It is pertinent to note that for all the analysis presented in the paper Raman spectra in the region 600-1700 cm^{-1} is used and an identical cropping window of 550-1750 cm^{-1} was used while applying the polynomial baseline fitting. This is so done to ensure that nature of the fitted polynomials have minimal variation from spectra to spectra so that the position of zero is closely matched for all the spectra. As will be discussed in next section the spectral changes observed in our study connects with the oxy/deoxy conformational changes of heme from a planar to a non-planar form. Therefore, to quantitatively compare the related spectral changes we normalized the spectra with respect to the phenylalanine band (1001 cm^{-1}). The choice of phenylalanine band for the normalization was made because previous studies on the changes observed in Raman spectra of RBCs arising due to oxy-deoxy transitions [241, 242, 246, 248] suggest that the changes in the Raman spectra are

primarily in the bands arising due to heme as it undergoes significant conformational changes during the process. It is also pertinent to note here that the changes in the membrane of the malaria affected RBCs [42, 44, 262, 271] can also lead to changes in the intensity of the phenylalanine band. However, previous studies suggest that the contribution of membrane proteins to the Raman bands of RBCs is minimum compared to the contribution from intracellular hemoglobin [241, 242, 246, 248]. In view of this it appears a reasonable assumption that the intensity of phenylalanine band can be used as a normalizer. All the measurements of the peak intensities of the Raman bands were carried out on the normalized spectra.

Blood (1 ml) was collected by venipuncture from healthy volunteers and malaria patients and RBC samples were prepared using the methods described in section 8.3.2 of chapter 8. The cell sample was kept in open on a laminar flow table (which was earlier sterilized using UV radiation and chemical cleaning of the working surface) for about an hour period before recording their Raman spectra. Appropriate dilutions of the cells in buffer solution were then used for experiments.

Raman spectra were recorded from blood samples collected from five healthy donors and five patients suffering from *P. vivax* infection. For the malaria samples investigated, the number of parasitized cells (p-RBC), as confirmed from acridine orange staining was ~ 1-2% of all the cells (m-RBCs), and therefore, all the RBCs studied from malaria infected samples were treated as non-parasitized (np-RBC) type. While for each blood sample collected from healthy donors Raman spectra were recorded from ~ 15 RBCs, for blood samples collected from malaria patients, Raman spectra were recorded from at least 50 cells in each sample. This was done to account for the much larger cell-to-cell spectral variations in the spectra of RBCs from blood samples of malaria patients.

9.3 RESULTS & DISCUSSIONS

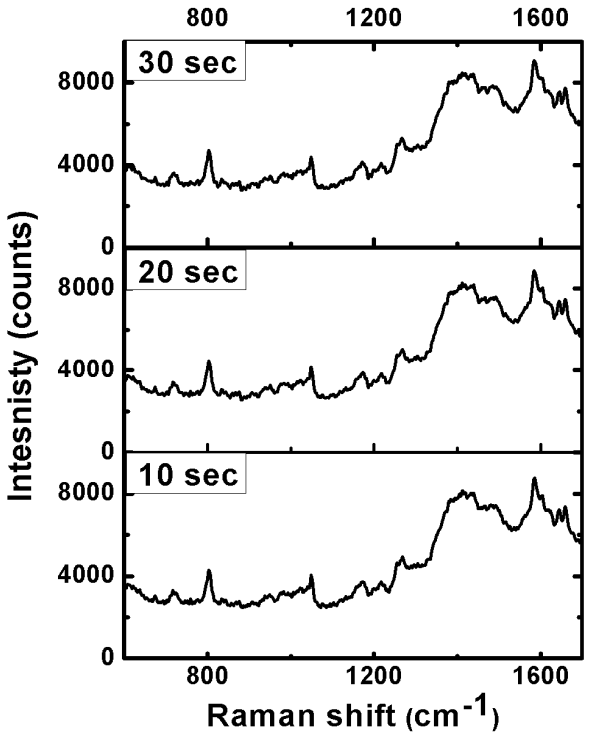

Figure 9.1 Time lapsed Raman spectra of trapped h-RBCs along with the background. Acquisition time for each spectra was 10 s with ~2 mW excitation. The presented spectra are the mean of the spectra from five h-RBCs.

There are several reports [239, 241, 242] on photoinduced changes in the Raman spectra of RBC. We choose a laser power level of ~ 2mW over a time duration of 30 s that is lower than the safe limit of exposure as discussed in section 8.3 of chapter 8. To further ensure authentic Raman spectra that is not influenced by photoinduced alterations we carried out time lapse measurements on the Raman spectra of RBCs at ~ 2 mW power levels. The recorded time lapsed Raman spectra at 2 mW of trap beam power over 30 s period are shown in figure 9.1. The time lapsed Raman spectra of trapped RBCs over a period of 30 s and with trapping power of ~ 2 mW revealed no changes in the spectra or the background level, indicating absence of any

photoinduced changes of the cells. This result is consistent with our estimate of the < 1º C rise in temperature of the cell for laser power of ~2 mW based on the work of Peterman *et al* [197]. We also confirmed that for 2 mW laser power no changes were observed even for hundreds of seconds of exposure. Therefore, for all the experiments reported in the manuscript

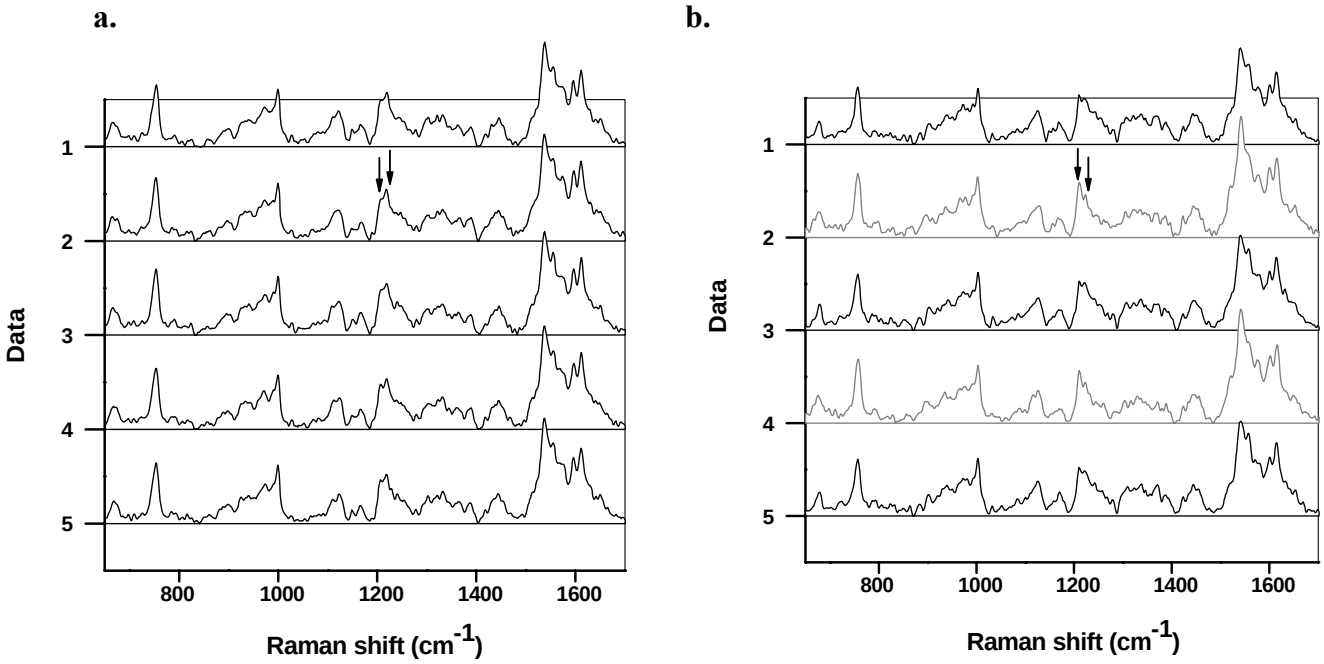

Figure 9.2 Representative Raman spectra as collected from (a) h-RBCs and (b) m-RBCs. Each spectrum was acquired over 30 s with ~ 2 mW of excitation at 785 nm. All the spectra were smoothened using Savitzky-Golay filter for removal of noise. The spectra from h-RBCs show nearly uniform spectral characteristics. However, the Raman spectra from a significant fraction of m-RBCs have characteristics different (shown as faded line) from that of the h-RBCs. The most noticeable changes in methine deformation bands at 1210 cm^{-1} and 1223 cm^{-1} are indicated by arrows.

the laser power used was 2 mW and the exposure duration was kept limited to 30 s. It is also pertinent to note that cells held under the optical trap can undergo some positional fluctuations which was estimated to be < 50 nm (< 1% of cell diameter) for the trap conditions used in our studies. Since RBCs are fairly homogeneous structure these small fluctuations in the cell position

are not expected to contribute to significant changes in the Raman spectra. However, the use of low trap beam power results in poor SNR of spectra recorded from individual cells. To address this aspect we collected spectra from about hundred of cells and used the mean spectrum of each class of cells (h-RBCs or m-RBCs) that had much improved SNR for analysis.

To show the inter class variability of the Raman spectra of h-RBCs and m-RBCs we show representative Raman spectra collected from five individual h-RBCs and m-RBCs in figures 9.2a and 9.2b respectively. The spectra of h-RBCs are similar and display fairly uniform peak distribution and intensities from one cell to another. However for m-RBCs large variability was observed. While the spectrum of the ~ 70 % of the m-RBCs was similar to that for h-RBCs, ~ 30% of m-RBCs show a decrease in intensity of the low spin (oxygenated-Hb) marker Raman band at 1223 cm^{-1} along with a concomitant increase in the high spin (deoxygenated-Hb) marker band at 1210 cm^{-1} present in methine C-H deformation region. We designate the m-RBCs with Raman spectra similar to h-RBCs as non-modified m-RBCs (nm-m-RBCs) and the other as modified m-RBCs (m-m-RBCs). The mean spectrum for h-RBCs, n-m-RBCs and m-m-RBCs averaged over all the spectra collected from five healthy donors and five malaria patients is shown in figures 9.3A(a), (b) and (c) respectively. One can see the significant improvement in SNR ~ 34 dB as compared to SNR ~ 22 dB for individual cell spectra.

It is worthwhile to note that though the blood samples collected from P. vivax infected patients were having ~ 1-2% parasitized or infected cells (the level of parasitemia considered to be significant as per World Health Organization guidelines [272, 273]), it is well known that apart from the fraction of red cells invaded by the parasites a large fraction of non-parasitized

A.

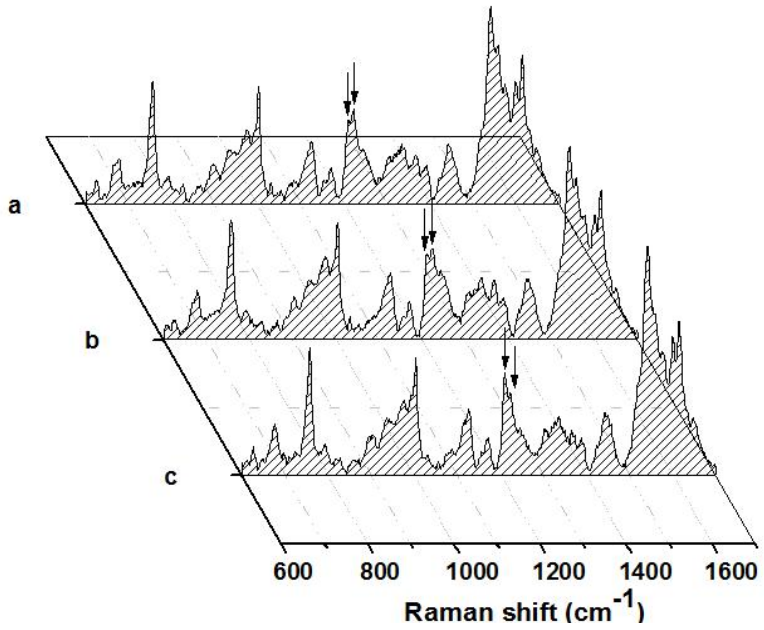

B.

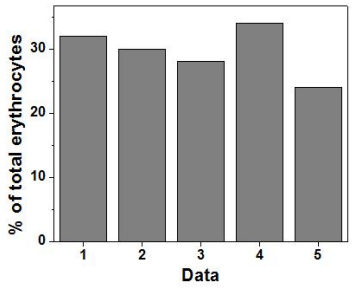

Figure 9.3 A. Mean Raman spectra of (a) h-RBCs, (b) nm-m-RBCs and (c) m-m-RBCs. Spectra were recorded from 15 cells from each healthy donors and nearly 50 cells from each malaria patients. B. Percentage of m-m-RBCs from each malaria patients.

cells may also have altered characteristics in malaria patients. Such changes may be directly induced by exo-antigens/chemicals released by the parasites [274-276] or dyserythropoiesis resulted from the infection [277, 278]. With the SNR available in the present study significant changes in the Raman spectra were observed in ~ 30% of the red blood cells of the blood samples from malaria infected patients studied in the present experiment.

Apart from the prominent changes observed for methine hydrogen deformation doublet at 1210 cm^{-1} and 1223 cm^{-1}, the spectra from m-m-RBCs show changes in Raman bands at 1366 cm^{-1}/1356 cm^{-1} (ν_4) and the spin marker bands in the region 1500-1700 cm^{-1}. In Table 1 we show

the assignment of these Raman bands based on the work of Abe *et al* [279] and Wood *et al* [242].

Table 9.1 Assignment and spectral position (cm^{-1}) of the Hb Raman bands showing significant changes between h-RBC and m-m-RBC. For comparison bands observed by Wood *et al* [242] are also shown (complete list of assignment of bands in the recorded Raman spectra has been provided in appendix E).

Band Assignment	**Local co-ordinates**	**Hb band Position(cm^{-1}) in m-m-RBC**	**Hb Band position (cm^{-1}) in h-RBC**	**Deoxy-Hb band position (cm^{-1}) [242]**	**Oxy-Hb band position (cm^{-1}) [242]**
$\nu_5+\nu_{18}$	$\delta(C_mH)$	1210	1210	1213	1212
ν_{13} or ν_{42}	$\delta(C_mH)$	1223	1223	1223	1226
ν_{42}	$\delta(C_mH)$	1245	1245	1248	1248
ν_4	$\nu(\text{pyr half-ring})_{sym}$	1356/1366	1366	1356	1371
ν_{11}	$\nu(C_\beta C_\beta)$	1546	1546	1548	1547
ν_{10}	$\nu(C_\alpha C_m)_{asym}$	1633	1636	Absent	1639

In figure 9.4 we show a scatter plot of the intensities of the Raman bands at 1210 cm^{-1} and 1223 cm^{-1}, 1356 cm^{-1} and 1366 cm^{-1}, 1546 cm^{-1} and 1636 cm^{-1} for h-RBCs and m-m-RBCs. Column A shows the intensities of these bands in the mean Raman spectrum obtained from m-m-RBCs and h-RBCs. In the column B the normalized intensities of the Raman bands for all h-RBCs and m-m-RBCs studied are presented to show inter and intra class scatter in data. Notably, the numbers presented in the scatter plots are the peak intensities of the relevant Raman bands. Since the Raman bands at 1210 cm^{-1},1223 cm^{-1} and 1356 cm^{-1}, 1366 cm^{-1} in figures 9.4 a & b respectively have well separated peaks the peak intensities of these bands measured directly from

the spectra were used in the related scatter plots. However, the eight spin marker Raman bands in the region 1500 cm^{-1} to 1700 cm^{-1} are closely spaced and strongly overlapped. The peak position of these bands cannot be determined directly from the spectra. In this case multiple peak fitting was applied. The previous reports by Wood *et al* [242, 248] show that the Raman spectrum of RBCs is dominated by intracellular Hb and that Hb Raman spectrum in the range 1500-1700 cm^{-1} has eight bands that can be denoted as ν_{38}, ν_{11}, ν_{19}, ν_{37}, $\nu(C{=}C)_{vinyl}$, $\nu(C{=}C)_{vinyl}$, ν_{10} and Amide I [242, 248]. Eight Lorentzian peaks allowed to vary independently in terms of intensity, width and position were used to obtain the best fit profile to the experimental data. It can be seen that the fitted profile approximates quite well with the observed data. Therefore, the peak intensities of the fitted Lorentzian profiles were used in the related scatter plot.

The ratio between the Raman bands at 1210 cm^{-1} and 1223 cm^{-1} in the mean spectrum from m-m-RBCs were observed to have an average value of ~ 1:0.8, different from the value of 1:1.1 observed in the mean spectrum from h-RBCs (figure 9.4(a)). The intensities of the Raman bands for each h-RBCs and m-m-RBCs are shown in column B. The relative intensities of the Raman bands can be clearly seen to be well distinguishable for the h-RBCs and m-m-RBCs. Further for mean Raman spectra from m-m-RBCs, we also observed partial shifting of the Raman band at ~ 1366 cm^{-1} to 1356 cm^{-1} in comparison to h-RBCs mean spectra (figure 9.4(b)). The intensities of 1356 cm^{-1} and 1366 cm^{-1} Raman bands for each h-RBCs and m-m-RBCs are shown in column B. For spin marker bands in the 1500-1700 cm^{-1} region, major changes can be seen for the 1546 cm^{-1} peak (ν_{11}) and 1636/1633 cm^{-1} peak (ν_{10}) and therefore intensity for these peaks for each h-RBCs and m-m-RBCs are shown in column B. While intensity of the peak at 1546 cm^{-1} is found to be enhanced in case of m-m-RBCs with respect to that for h-RBCs, the opposite can be seen for the Raman band at 1636 cm^{-1}. The 1636 cm^{-1} band for h-RBCs also

found to be shifted to 1633 cm^{-1} in the spectra from m-m-RBCs. However, this shift is below the resolution of the set-up (6 cm^{-1}) and thus not significant. The differences in intensity ratios for the Raman bands between h-RBCs and m-m-RBCs were found to be significant to a *p* value of <0.05 for all cases (a-c) (details are provided in table D3 of appendix D).

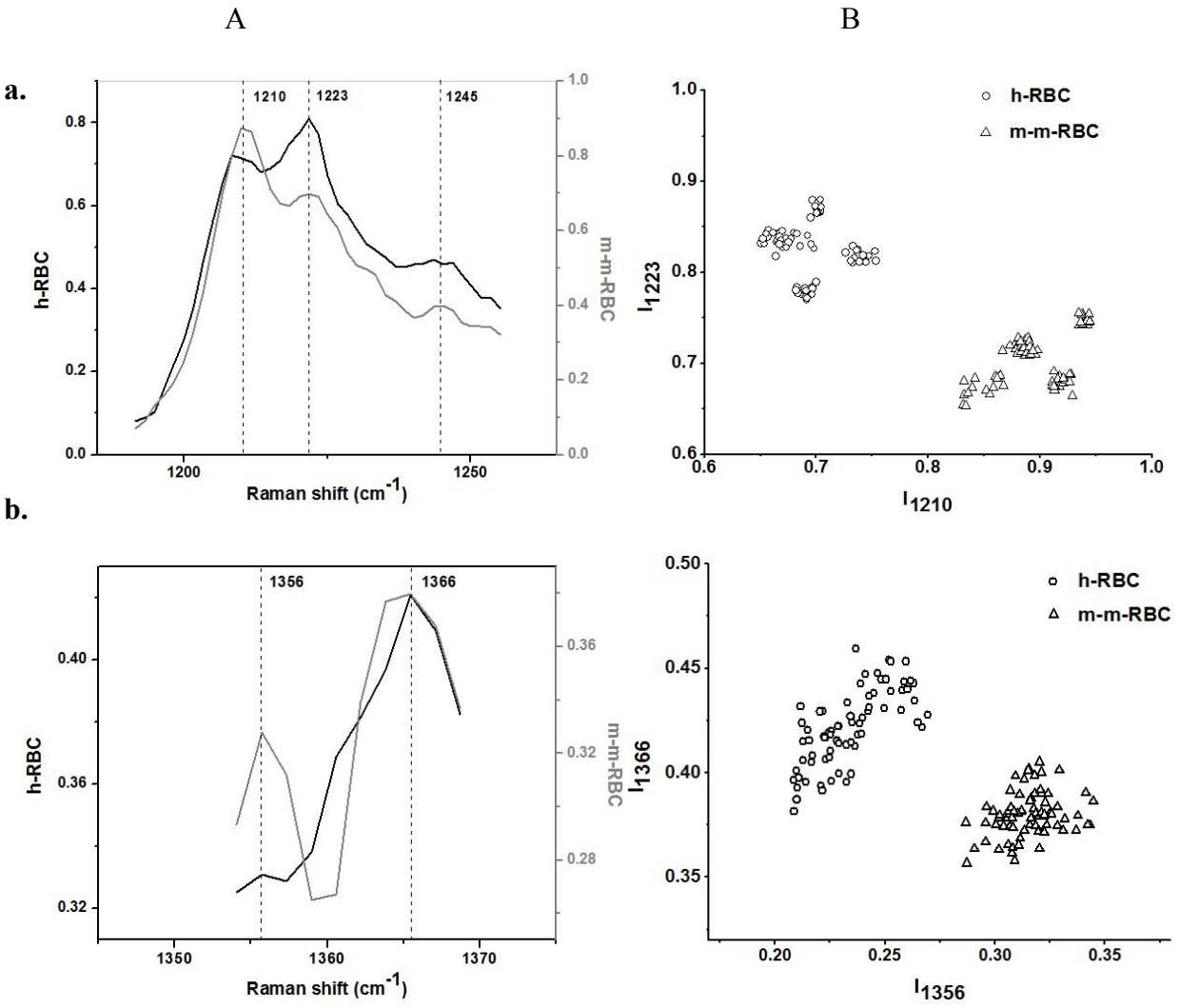

c.

h-RBC

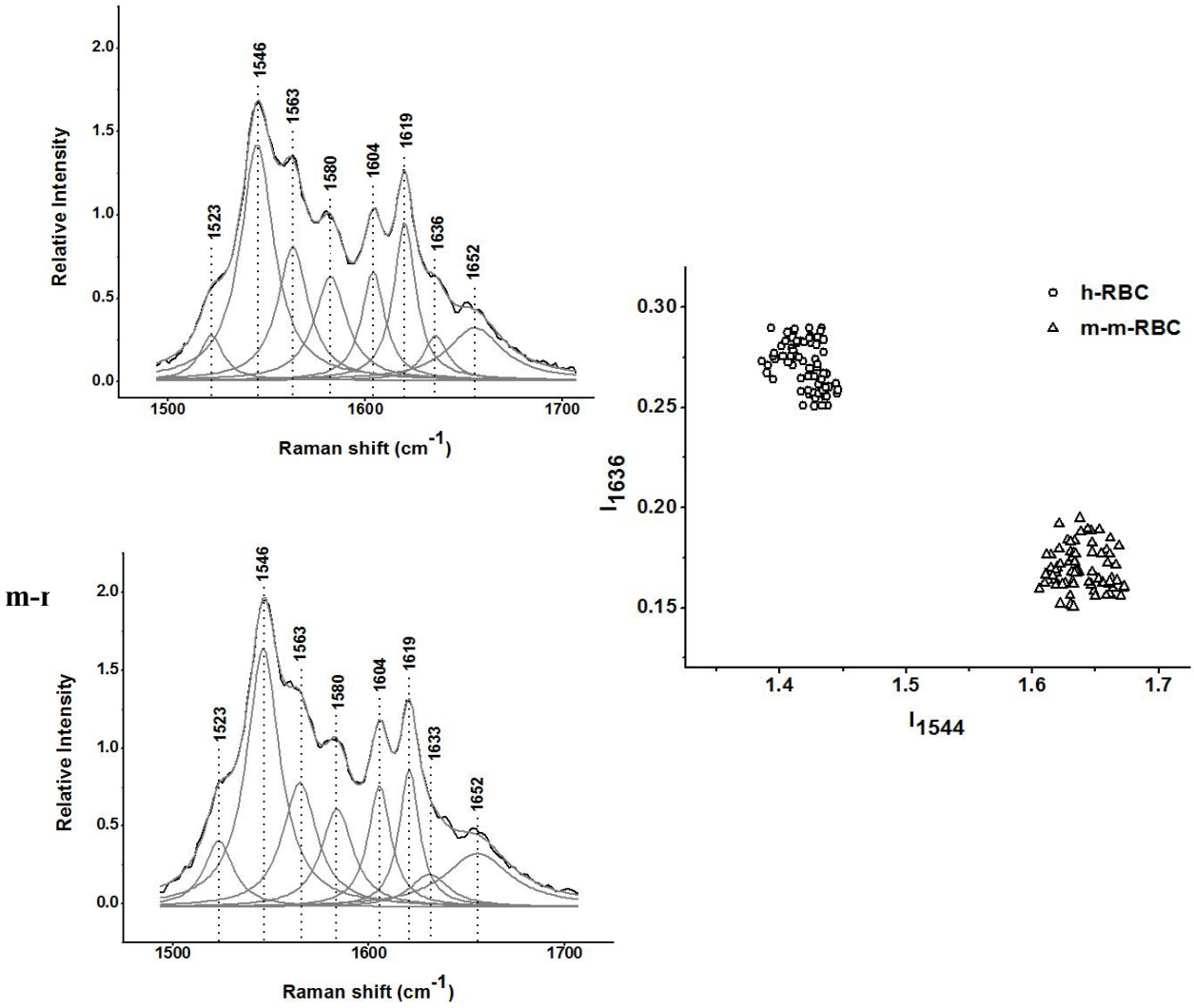

Figure 9.4 Raman bands showing significant intensity differences in the spectra recorded from m-m-RBCs over that recorded from h-RBCs. **A.** (a)-(b) Relative intensity of bands in the mean Raman spectra of h-RBCs (dark line) and the mean spectra for m-m-RBCs (faded line). (c) The mean Raman spectra (dark line) for ~1500-1700 cm^{-1} region and the fitted peaks for m-m-RBCs and h-RBCs are shown. **B.** Scatter plot showing the relative intensities of the Raman bands for all the h-RBCs and m-m-RBCs studied. It can be seen that the Raman band intensities for h-RBCs and m-m-RBCs are well separated.

The available Raman data of model porphyrin compounds [247, 279] suggests that the above mentioned changes can be attributed to changes in the oxygenation status of the intra-erythrocytic Hb. The most striking change in the spectra recorded from m-m-RBCs is the change in the ratio of the intensities of the 1210 cm^{-1} and 1223 cm^{-1}peaks. While Salmaso *et al* [280] have assigned the 1223 cm^{-1} band to ν_{13} and the band at 1210 cm^{-1} to $\nu_5+\nu_8$, the 1223 cm^{-1} has also been assigned to ν_{42} [247]. These modes are associated with C-H in plane vibrations of methine hydrogen. Proximity to the protein sub units influences the deformation angle and consequently a change in intensities between the planar oxygenated (oxy-Hb) and non-planar deoxygenated (deoxy-Hb) Hb structure. It is known that the doublet located at 1245 cm^{-1} and 1223 cm^{-1} in the spectra of low spin heme (oxy-Hb) get shifted to 1223 cm^{-1} and 1210 cm^{-1} in the spectra of high spin heme (deoxy-Hb) [242, 246]. Studies carried out on RBCs subjected to periodic oxygenation and de-oxygenation cycles have also revealed significant enhancement of the intensity of the 1210 cm^{-1} band for deoxy-Hb [242]. Therefore, observed elevated intensity at 1210 cm^{-1} for m-m-RBCs over h-RBCs suggests a complete or partly deoxygenated state of a significant fraction (~30%) of the m-RBCs in *P. vivax* infected blood sample.

It is pertinent to note that the RBCs used in our experiments were collected by venipuncture and will therefore be initially in deoxygenated state. However, for normal functional state of Hb these should almost completely get transformed into oxygenated condition upon exposure to atmospheric oxygen [248]. The Raman signatures of m-m-RBCs, on the other hand, suggest that significant number of red cells from blood samples of malaria infected patients were only partially oxygenated or remained deoxygenated even after exposure to atmospheric oxygen. This could be further verified by studying the relative intensities of the bands at 1366 cm^{-1} and 1356 cm^{-1}. The bands appearing between 1366 cm^{-1} (oxy-Hb) and 1356

cm^{-1} (deoxy-Hb) assigned to local co-ordinate ν_4 [246, 280, 281], involve pyrrole half ring stretching vibration and are known as oxidation state marker. The oxygen molecule upon binding to deoxy-Hb withdraws an electron from the ferrous (Fe(II)) ion leaving the metal in a low spin ferric (Fe(III)) state in oxy-Hb and resulting in an increase in vibrational wavenumber of ν_4 mode [246, 248]. We observed partial suppression of the band at 1366 cm^{-1} for m-m-RBCs and a corresponding enhancement of the band at 1356 cm^{-1}, suggesting a partially de-oxygenated state of the cells.

The bands in the region between 1500-1700 cm^{-1} are known to serve as spin state marker. The normal mode at 1546 cm^{-1} (ν_{11}) primarily consists of C_β-C_β bond stretching, which is strongly influenced by the conformational transitions and hence show significant change in intensity between the planar oxy-Hb and non-planar deoxy-Hb structure and is known to be the most intense band in the deoxygenated form [242, 282]. In our study we also observed significant enhancement in intensity at this band for m-m-RBCs. We also observed a partial suppression of the ν_{10} band (1636 cm^{-1}) for m-m-RBCs, which is also suggestive of the presence of partially oxygenated Hb inside the cells [242].

To summarize, the observed changes in the Raman bands in m-m-RBCs suggest a reduction of Hb-oxygen affinity which are consistent with the results of a previous study on *P. berghei* infected mice [283]. It is known that metabolic acidosis, a common complication of malaria, can cause a lowering of blood pH (down to ~ 7.2 to 7.0) in malaria patients [262, 284]. This can affect the oxygen affinity of Hb via Bohr effect. However, in our study RBCs collected from malaria patients and healthy persons were suspended in identical phosphate buffer solution (pH ~ 7.4) and stabilized for ~ 1 hour before recording the Raman spectra. Therefore, pH change induced shift of oxygen dissociation curve cannot account for the observed spectral changes.

Other potential cause that can effect an altered Hb-oxygen affinity is the intracellular concentration of 2,3-Diphosphoglycerate (2,3-DPG), an important metabolite in RBCs, involved in the stabilization of the deoxy-form of Hb. Also dyserythropoiesis or ineffective erythropoiesis has been reported in adults with *P. vivax* malaria which correlated well with the severity of the anemic condition [277]. Such dyserythropoeisis may often consist of megaloblastosis [278, 285], which has been known to be associated with increased level of 2,3-DPG and consequent decrease of Hb-oxygen affinity [286].

9.4 SUMMARY

Employment of Raman optical tweezers facilitated means for single cell level evaluation of oxygenation state of the RBCs from malaria patients. The Raman spectroscopic studies carried out on optically trapped red blood cells collected from blood samples of healthy volunteers (h-RBCs) and from patients suffering from *P. vivax* infection (m-RBCs) reveal that a significant fraction of m-RBCs produced Raman spectra with altered characteristics relative to h-RBCs. The observed spectral changes suggest a reduced oxygen-affinity or right shifting of the oxygen-dissociation curve for the intracellular haemoglobin with respect to its normal functional state. Recently *P. vivax* malaria has been reported to cause severe anemic condition and acute respiratory distress syndrome in patients which may result in hospital stay and even mortality [287, 288]. Raman spectroscopic study of m-RBCs in blood sample of *P. vivax* infected patients may provide a useful mean for estimation of complication that may result from altered oxygen loading capability of RBCs in malaria patients.

CHAPTER 10

CONCLUSIONS AND FUTURE STUDIES

In this chapter we present a summary of the major accomplishments and outline of some of the future investigations that may evolve from the work presented in this thesis.

Studies carried out as part of this thesis have shown possible ways to overcome the limited axial trapping range of laser tweezers. One of the approaches investigated for this purpose was the use of long working distance objective lens to push the object immersed in the liquid along the direction of the beam and distort the free liquid surface so that the resulting surface tension forces may help balance the scattering force and thus lead to a stable trapping of the object. Using this approach although the particles could be trapped, the trapping position was observed to be not at the centre of the trap beam but in an annular region around it because of trap beam induced thermocapillary effect. It is worthwhile noting here that although the approach does not offer a single trapping point for microscopic particles, the trapping of objects away from the beam axis potentially offers an important advantage of reduced light damage when trapping biological cells. During this study we also observed that for increased focal spot size of the trap beam compared to diffraction limited spot, as obtained with a low NA objective lens, multiple particles could be trapped against a glass boundary and the light field scattered from these particles could also lead to a new trapping mechanism for the nearby isolated particles. Theoretical simulations also confirmed that the observed trapping actually results from the optical binding action, as was predicted earlier theoretically. We have also shown that use of

Laguerre-Gaussian (*LG*) beams provides a more general approach for enhancing the axial trapping range in optical tweezers. One important reason for limited axial range of TEM_{00} beam is due to spherical aberration at glass-water interface that results in increase in the focal volume of the trap beam at larger depth inside the liquid medium. Since the *LG* beam consists of a reduced angular spread of light intensity, it suffers less from the spherical aberration effect at glass-water interface and thus leads to an increase in trapping range. A trapping range of > 200 μm was achieved and could be used for transporting cells from bulk medium to the air interface and monitoring the changes in oxygen diffusion rate in plasma membrane. The technique is interesting since it may have potential application for single cell level study of the effect of environmental parameters (like for example pH of the medium) on cell membrane diffusivity by optically manipulating the cell through different microfluidic chambers filled with media of different properties. It is also worthwhile noting here that more recently there have been several efforts on formation of structured light field patterns having axial intensity modulation, by the interference of a number of suitably phase engineered beams. Such axial modulation in intensity may provide another useful means for generating strong axial gradient force without the need for using a high NA objective lens. Some studies in this direction have already been carried out by us but have not been described in this thesis.

Our studies on the use of *LG* beam for micromanipulation applications led to several other interesting results. Due to its annular light profile, LG_{01} beam is known to have better trapping efficiency as confirmed with spherical particles. Further, *LG* modes have lower peak intensities compared to the usual Gaussian mode for identical beam power. We realized that these properties of *LG* beams can offer important advantage for manipulating biological cells by

reducing the level of photodamage. Since nowadays spermatozoa are being routinely manipulated by laser tweezers for assessing quality of sperm samples and assisting the in vitro fertilization method, we chose spermatozoa as the model biological cells. The results of our studies revealed two important advantages: firstly, LG_{01} mode offers better trapping efficiency than TEM_{00} mode for highly motile spermatozoa and second, the light damage on the cells is significantly reduced with *LG* beams. The reason for reduced light damage on the cells is believed to be due to lowered degree of nonlinear absorption of trapping light and experiments performed with acridine orange stained cells supported this conjecture. Considering high level of concern over the genetic purity of spermatozoa the results should motivate evaluation of the special laser beams for manipulating the cells.

Another very interesting application of *LG* trapping beams that came out of these studies was its use for orientation and rotation of trapped red blood cells (RBCs). It was observed that since the size of the intensity annulas of *LG* modes increases with the topological charge the cells get trapped at larger tilt angle with respect to the beam axis and thus provided additional control on the orientation of the cells under trap. Further, the RBCs could also be driven as micro-rotors by a transfer of orbital angular momentum from the *LG* trapping beam having large topological charge or by rotating the profile of *LG* mode having fractional topological charge. The technique for controlling the orientation of the trapped RBC may find useful applications while studying polarized Raman spectra of the cells. Since the approach is simple, as only a change in the azimuthal orders of the *LG* beams is required, the integration of the technique with Raman spectroscopy is expected to be straightforward.

Another important aspect of this thesis work was the development of a set-up that integrates Raman spectroscopy with optical trapping (Raman optical tweezers), and its application for studying RBCs. Our study to check for photoinduced effects on the Raman spectra of RBC showed that in contrast to earlier reports based on micro-Raman technique, photoinduced changes occur at a much lower light exposure level. This observation was made possible because of the improvement of signal quality in the Raman optical tweezers set-up compared to micro-Raman technique. Having established the exposure parameters where light induced effects are negligible in the recorded Raman spectra, we studied RBCs from *P. vivax* infected patients to understand the changes suffered by the cells during malaria infection. The results indicated reduction in oxygen carrying capacity of significant fraction (~ 30%) of non-parasitized RBCs in blood samples from malaria patients. This observation may help devise better diagnosis for malaria since the present diagnosis that is based on identification of the parasitized cells is hampered by the rather small fraction of these and should also be helpful in better understanding the hypoxia condition in malaria patients.

It is worthwhile noting here that in the recorded spectra from RBCs majority of the bands occurred from intracellular hemoglobin since hemoglobin is present in very high concentration in RBCs and undergoes a near resonant excitation when using 785 nm laser light [242]. But it is quite well known that membranes of non-parasitized RBCs in malaria patients undergo significant changes due to exo-antigens released by the parasites [261]. Therefore, to investigate the changes occurring at the membrane of the cells surface enhanced Raman spectroscopy technique may be particularly useful. The other major species of malaria parasite beside *P. vivax* is the *P. falciperum* and the species is believed to responsible for cerebral malaria, acute renal

failure and severe anemia leading to serious complications in the patients. Therefore, Raman spectroscopic studies need to be carried out over *P. falciperum* infected patients to see the nature and degree of alterations in the oxygen carrying capacity of the RBCs.

In the studies presented in this thesis, the Raman optical tweezers set-up made use of a cw Ti: Sapphire laser emitting at 785 nm. Although use of near IR wavelength for exciting the Raman spectra greatly reduces the background fluorescence from the sample, for resonant enhancement of a family of molecules or a specific type of bonds, use of multiple laser sources at properly chosen excitation wavelengths will be useful for future studies on RBCs and other cell types. Also polarized Raman spectroscopic study is particularly attractive for studying the hemoglobin ordering in RBCs and the related changes under diseased conditions. Therefore, the technique making use of varying azimuthal index of *LG* beams to control the orientation of the trapped RBC will need to be incorporated into the Raman optical tweezers set-up to facilitate acquisition of polarized Raman spectra from RBCs.

It would also be interesting to integrate holographic optical trapping technique with Raman optical tweezers so that spatially resolved Raman spectra can be recorded from trapped cells. For this a laser source emitting at 1064 nm wavelength has to be phase modulated using a spatial light modulator to create array of traps to hold the cell under investigations at multiple points and thereby scanning the trapped cells over the Raman excitation beam to create a Raman image of the cell. The system will be particularly useful for investigating intracellular distribution of different cellular components and to understand the effect of external stimuli on the cell.

References

1. A. Ashkin, J. M. Dziedzic, J. E. Bjorkholm, and S. Chu, "Observation of a single beam gradient force optical trap for dielectric particles," *Opt. Lett.* **11**, 288-290 (1986).

2. A. Ashkin, "Optical trapping and manipulation of neutral particles using lasers," *Proc. Nat. Acad. Sci. USA* **94**, 4853-4860 (1997).

3. S. Chu, "Laser manipulation of atoms and particles," *Science* **253**, 861-866 (1991).

4. D.G. Grier, "Optical tweezers in colloid and interface science," *Curr. Opn. Coll. Interface Sc.* **2,** 264-270 (1997).

5. M. P. Sheetz ed, (1998) *Laser Tweezers in Cell Biology, Methods in Cell Biology,* Vol. 55, Academic Press, New York.

6. K. O. Greulich, (1999). *Micromanipulation by light in biology and medicine: the laser microbeam and optical tweezers*. Birkhäuser Verlag, Basel.

7. S. C. Kuo, and M. P. Sheetz, "Optical tweezers in cell biology" *Trends. Cell Biol.* **2**,116-118 (1992).

8. D. Allaway, N. A. Schofiel, and P. S. Poole, "Optical traps: shedding light on biological processes," *Biotech. Lett.* **22**, 887-892 (2000).

9. P. T. Korda, G. C. Spalding, and D. G. Grier, "Evolution of a colloidal critical state in an optical pinning potential landscape," *Phy. Rev. B* **66**, 024504 (2002).

10. C. Bustamante, S. B. Smith, J. Liphardt, and D. Smith, "Single-molecule studies of DNA mechanics," *Curr. Opin. Struct. Biol.* **10,** 279-285 (2000).

11. M. L. Bennink, O. D. Scharer, R. Kanaar, K. Sakata-Sogawa, J. M. Schins, J. S. Kanger, B. G. de Grooth, and J. Greve, "Single-Molecule Manipulation of Double-Stranded DNA Using Optical Tweezers: Interaction Studies of DNA with RecA and YOYO-1," *Cytometry* **36**, 200-208 (1999).

12. K. C. Neuman, and A. Nagy, "Single-molecule force spectroscopy: optical tweezers, magnetic tweezers and atomic force microscopy," *Nature Methods.* **5,** 491-505 (2008).

13. S. M. Block, L. S. B. Goldstein, and B. J. Schnapp, "Bead movement by single kinesin molecules studied with optical tweezers," *Nature* **348**, 348-352 (1990).

14. S. C. Kuo, and M. P. Sheetz, "Force of single kinesin molecules measured with optical tweezers," *Science* **260**, 232-234 (1993).

15. A. D. Mehta, M. Rief, J. A. Spudich, D. A. Smith, and R. M. Simmons, "Single-molecule biomechanics with optical methods," *Science* **283**, 1689-1695 (1999).

16. J. Dai and M. P. Sheetz, Cell Membrane Mechanics. In: M.P. Sheetz (ed.), *Laser Tweezers in Cell Biology*, Academic Press, 1998, pp 157-171.

17. A. Kusumi, Y. Sako, T. Fujiwara, and M. Tomishige, Application of Laser Tweezers to Studies of the Fences and Tethers of the Membrane Skeleton that Regulate the Movements of Plasma Membrane Proteins. In: M. P. Sheetz (ed.), *Laser Tweezers in Cell Biology, Academic Press*, 1998, pp 174-194.

18. S. Henon, G. Lenormand, A. Richert, and F. Gallet, "A new determination of the Shear modulus of the human erythrocyte membrane using optical tweezers," *Biophys. J.* **76**, 1145-1151 (1999).

19. A. Ashkin, "Acceleration and trapping of particles by radiation pressure," *Phys. Rev. Lett.* **24**, 156-159 (1970).

20. A. Ashkin, and J. M. Dziedzic, "Optical levitation by radiation pressure," *Appl. Phys. Lett.* **19**, 283-285 (1971).

21. A. Ashkin, and J. M. Dziedzic, "Observation of Radiation-Pressure Trapping of Particles by Alternating Light Beams," *Phys. Rev. Lett*. **54**, 1245–1248 (1985).

22. M. E. J. Friese, T. A. Nieminen, N. R. Heckenberg, and H. Rubinsztein-Dunlop, "Optical alignment and spinning of laser-trapped microscopic particles," *Nature* **394**, 348-350 (1998).

23. H. He, M. E. J. Friese, N. R. Heckenberg, and H. Rubinsztein-Dunlop, "Direct observation of transfer of angular momentum to absorptive particles from a laser beam with phase singularity," *Phys. Rev. Lett.* **75**, 826-829 (1995).

24. A. T. O'Neil, I. MacVicar, L. Allen, and M. J. Padgett, "Intrinsic and Extrinsic Nature of the Orbital Angular Momentum of a Light Beam," *Phys. Rev. Lett.* **88**, 053601 (2002).

25. W. Huang, B. Anvari, J. H. Torres, R. G. LeBaron, and K. A. Athanasiou, "Temporal effects of cell adhesion on mechanical characteristics of the single chondrocyte," *J. Orthopaed. Res.* **21**, 88–95 (2003).

26. N. Askenasy, and D. L. Farkas, "Optical imaging of PKH labeled hematopoietic cells in recipient bone marrow in vivo," *Stem Cells* **20**, 501–513 (2002).

27. B. Maier, M. Koomey, and M. P. Sheetz, "A force dependent switch reverses type IV pilus retraction," *Proc. Natl. Acad. Sci. USA* **101**, 10961–10966 (2004).

28. R. Dasgupta, S. K. Mohanty, and P. K. Gupta, "Controlled rotation of biological microscopic objects using optical line tweezers," *Biotechnol. Lett.* **25**, 1625-1628 (2003).

29. A. T. O'Neil, and M. J. Padgett, "Rotational control within optical tweezers by use of a rotating aperture," *Opt. Lett.* **27**, 743-745 (2002).

30. S. Sato, M. Ishigure, and H. Inaba, "Optical trapping and rotational manipulation of microscopic particles and biological cells using higher order mode Nd: YAG laser beams," *Electron. Lett.* **27**, 1831-1832 (1991).

31. P. Galajda, and P. Ormos, "Complex micromachines produced and driven by light" *Appl. Phys. Lett.* **78**, 249-251 (2001).

32. R. Dasgupta, and P. K. Gupta, "Rotation of transparent, non-birefringent object by transfer of spin angular momentum of light," *Opt. Lett.* **30**, 394-396 (2005).

33. L. Paterson, M. P. MacDonald, J. Arit, W. Sibbett, P. E. Bryant, and K. Dholakia, "Controlled rotation of optically trapped microscopic particles," *Science* **292,** 912-914 (2001).

34. M. P. MacDonald, L. Paterson, K. Volke-Sepulveda, J. Arit, W. Sibbett, and K. Dholakia, "Creation and manipulation of three-dimensional optically trapped structures," *Science* **296**, 1101- 1103 (2002).

35. S. K. Mohanty, and P. K. Gupta, "Transport of microscopic objects using asymmetric transverse optical gradient force," *Appl. Phys. B* **81**, 159 – 162 (2005).

36. H. Little, C. T. A. Brown, V. Garces-Chavez, W. Sibbett, and K. Dholakia, **"**Optical guiding of microscopic particles in femtosecond and continuous wave Bessel light beams," *Opt. Exp.* **12**, 2560-2565 (2004).

37. P. Fischer, A. E. Carruthers, K. Volke-Sepulveda, E. M. Wright, C. T. A. Brown, W. Sibbett, and K. Dholakia, **"**Enhanced optical guiding of colloidal particles using a supercontinuum light source," *Opt. Exp.* **14**, 5792-5802 (2006).

38. S. Ahlawat, R. S. Verma, R. Dasgupta, and P. K. Gupta, "Long distance optical guiding of colloidal particles using holographic axilens," *Appl. Opt.* **50**, 1933-1940 (2011).

39. C.T. Lim, M. Dao, S. Suresh, C. H. Sow, and K. T. Chew, "Large deformation of living cells using laser traps," *Acta Materialia.* **52**, 1837-1845 (2004).

40. G. Lenormand, S. Hénon, A. Richert, J. Siméon, and F. Gallet, "Direct Measurement of the Area Expansion and Shear Moduli of the Human Red Blood Cell Membrane Skeleton," *Biophys. J.* **81**, 43-56 (2001).

41. S. Hénon, G. Lenormand, A. Richert and F. Gallet, "A New Determination of the Shear Modulus of the Human Erythrocyte Membrane Using Optical Tweezers," *Biophys. J.* **76**, 1145-1151 (1999).

42. S. Suresh, J. Spatz, J. P. Mills, A. Micoulet, M. Dao, C. T. Lim, M. Beil, and T. Seufferlein, "Connections between single-cell biomechanics and human disease states: gastrointestinal cancer and malaria," *Acta Biomaterialia* **1**, 15-30 (2005).

43. J. Guck, R. Ananthakrishnan, H. Mahmood, T. J. Moon, C. C. Cunningham and J. Käs, "The Optical Stretcher: A Novel Laser Tool to Micromanipulate Cells," *Biophys. J.* **81**, 767-784 (2001).

44. S. K. Mohanty, A. Uppal, and P. K. Gupta, "Optofluidic stretching of RBCs using single optical tweezers," *J. Biophoton.* **1**, 522-525 (2008).

45. D. V. Petrov, "Raman spectroscopy of optically trapped particles," *J. Opt. A: Pure Appl. Opt.* **9**, S139-S156 (2007).

46. A. Min, L. Jun-Xian, H. Shu-Shi, W. Gui-Wen, C. Xiu-Li, C. Zhi-Cheng, and Y. Hui-Lu, "Application and Progress of Raman Tweezers in Single Cells," *Chin. J. Anal. Chem.* **37**, 758-763 (2009).

47. C. Xie, M. A. Dinno, and Y. Q. Li, "Near-infrared Raman spectroscopy of single optically trapped biological cells," *Opt Lett* **27**, 249-251 (2002).

48. C. Xie, Y. Li, W. Tang, and R. J. Newton, "Study of dynamical process of heat denaturation in optically trapped single microorganisms by near-infrared Raman spectroscopy," *J. Appl. Phys.* **94**, 6138-6142 (2003).

49. S. Rao, S. Bálint, B. Cossins, V. Guallar, and D. Petrov, "Raman Study of Mechanically Induced Oxygenation State Transition of Red Blood Cells Using Optical Tweezers," *Biophys. J.*, **96**, 209-216 (2009).

50. C. Xie, C. Goodman, M. A. Dinno, and Y. Li, "Real-time Raman spectroscopy of optically trapped living cells and organelles," *Opt. Exp.* **12**, 6208-6214 (2004).

51. C. F. Bohren and D. R. Huffman, (1983). *Absorption and scattering of light by small partciles*. John Wiley & Sons, USA.

52. H. C. van de Hulst, (1999). *Light Scattering by small partciles*. Dover, New York.

53. K. F. Ren, G. Gréha, and G. Gouesbet, “Radiation pressure forces exerted on a particle arbitrarily located in a Gaussian beam by using the generalized Lorenz-Mie theory, and associated resonance effects,” *Opt. Comm.* **108**, 343-354 (1994).

54. G. Gouesbet, B. Maheu, and G. Gréhan, “Light scattering from a sphere arbitrarily located in a Gaussian beam, using a Bromwich formulation,” *J. Opt. Soc. Am. A* **5**, 1427-1443 (1988).

55. Y. K. Nahmias, and D. J. Odde, “Analysis of radiation forces in laser trapping and laser-guided direct writing applications,” *IEEE J. Quant. Electron.* **38**, 131-141 (2002).

56. A. Ashkin, “Forces of a single-beam gradient laser trap on a dielectric sphere in the ray optics regime,” *Biophys. J.* **61**, 569-582 (1992).

57. G. Roosen, “Optical levitation of spheres,” *Can. J. Phys*. **57**, 1260-1279 (1979).

58. H. Furukawa, and I. Yamaguchi, “Optical trapping of metallic particles by fixed Gaussian beams,” *Opt. Lett.* **23**, 216-218 (1998).

59. K. Svoboda, and S. M. Block, “Biological applications of optical forces,” *Ann. Rev. Biophys. Biomol. Struct.* **23**, 147-285 (1994).

60. Y. Harada, and T. Asakura, “Radiation forces on a dielectric sphere in the Rayleigh scattering regime,” *Opt. Comm.* **124**, 529-541 (1996).

61. http://research.stowers-institute.org/microscopy/external/Technology/NLO/index.htm. Online access date 12.12.2011.

62. H. He, N. R. Heckenberg, and H. Rubinsztein-Dunlop, ‘‘Optical particle trapping with higher-order doughnut beams produced using high-efficiency computer generated holograms,’’ *J. Mod. Opt*. **42**, 217–223 (1995).

63. K. T. Gahagan, and G. A. Swartzlander, Jr., "Optical vortex trapping of particles," *Opt. Lett.* **21**, 827-829 (1996).

64. K. T. Gahagan, and G. A. Swartzlander, Jr., "Trapping of low-index microparticles in an optical vortex," *J. Opt. Soc. Am B* **15**, 524-534 (1998).

65. J. Courtial, K. Dholakia, D. A. Robertson, L. Allen, and M. J. Padgett, "Measurement of the Rotational Frequency Shift Imparted to a Rotating Light Beam Possessing Orbital Angular Momentum," *Phys. Rev. Lett.* **80**, 3217-3219 (1998).

66. D. Cojoc, V. Garbin, E. Ferrari, L. Businaro, F. Romanato, and E. D. Fabrizio, "Laser trapping and micro-manipulation using optical vortices," *Microelec. Eng.* **78**, 125–131 (2005).

67. N. Matsumoto, T. Ando, T. Inoue, Y. Ohtake, N. Fukuchi, and T. Hara, "Generation of high-quality higher-order Laguerre–Gaussian beams using liquid-crystal-on-silicon spatial light modulators," *J. Opt. Soc. Am. A* **25**, 1642-1651 (2008).

68. M. W. Beijersbergen, L. Allen, H. Vanderveen, and J. P. Woerdman, "Astigmatic Laser Mode Converters and Transfer of Orbital Angular-Momentum," *Opt. Comm*. **96**, 123-132 (1993).

69. M. W. Beijersbergen, R. P. C. Coerwinkel, M. Kristensen, and J. P. Woerdman, "Helical-Wave- Front Laser-Beams Produced with a Spiral Phase plate," *Opt. Comm.* **112**, 321-327 (1994).

70. R. Oron, S. Blit, N. Davidson, A. A. Friesem, Z. Bomzon, and E. Hasman, "The formation of laser beams with pure azimuthal or radial polarization," *Appl. Phys. Lett.* **77**, 3322-3324. (2000).

71. R. Oron, N. Davidson, A. A. Friesem, and F. Hasman, "Efficient formation of pure helical laser beams," *Opt. Comm.* **182,** 205-208 (2000).

72. M. A. Clifford, J. Arlt, J. Courtial, and K. Dholakia, "High-order Laguerre-Gaussian laser modes for studies of cold atoms," *Opt. Comm.* **156,** 300-306 (1998).

73. E. R. Dufresne, G. C. Spalding, M. T. Dearing, S. A. Sheets, and D. G. Grier, "Computer generated holographic optical tweezer arrays*," Rev. Sc. Inst.* **72**, 1810-1816 (2001).

74. P. C. Mogensen, and J. Gluckstad, "Dynamic array generation and pattern formation for optical tweezers" *Opt. Comm.* **175**, 75-81 (2000).

75. N. R. Heckenberg, R. McDuff, C. P. Smith, H. Rubinsztein-Dunlop, and M. J. Wegener, "Laser beams with phase singularities," *Opt. Quant. Electron.* **24**, S951- S962 (1992).

76. http://departments.colgate.edu/physics/research/optics/oamgp/gp.htm. online access date 13.12.2011.

77. J. A. Davis, D. M. Cottrell, J. Campos, M. J. Yzuel, and I. Moreno, "Encoding amplitude information onto phase-only filters," *Appl. Opt.* **38**, 5004-5013 (1999).

78. M. Reicherter, T. Haist, E. U. Wagemann, and H. J. Tiziani, "Optical particle trapping with computer-generated holograms written on a liquid-crystal display," *Opt. Lett.* **24**, 608-610 (1999).

79. J. E. Curtis, B. A. Koss, and D. G. Grier, "Dynamic holographic optical tweezers," *Opt. Comm.* **207**, 169-175 (2002).

80. S. Chu, J. E. Bjorkholm, A. Ashkin, and A. Cable, "Experimental Observation of Optically Trapped Atoms," *Phys. Rev. Lett.* **57**, 314–317 (1986).

81. K. Hirano, Y. Baba, Y. Matsuzawa, and A. Mizuno, "Manipulation of single coiled DNA molecules by laser clustering of microparticles," *Appl. Phys. Lett.* **80**, 515-517 (2002).

82. Y. Nishimura, O. Misumi, S. Matsunga, T. Higashiyama, A. Yokota, T. Kuroiwa, "The active digestion of uniparental chloroplast DNA in a single zygote of Chlamydomonas reinhardtii is revealed by using the optical tweezers," *Proc. Natl. Acad. Sci. USA* **96**,12577-12582 (1999).

83. A. D. Mehta, K. A. Pullen, and J. A. Spudich, "Single molecule biochemistry using optical tweezers," *FEBS Lett.* **430**, 23-27 (1998).

84. C. Veigel, J. E. Molloy, S. Schmitz, and J. Kendrick-Jone, "Load-dependent kinetics of force production by smooth muscle myosin measured with optical tweezers," *Nature Cell. Biol.* **5**, 980-986 (2003).

85. S. M. Block, L. S. B. Goldstein, B. J. Schnapp, "Bead movement by single kinesin molecules studied with optical tweezers," *Nature* **348**, 348-352 (1990).

86. Y. Tadir, W. H. Wright, and O. Vafa, "Micromanipulation of sperm by laser generated trap," *Fertil. Steril.* **52**, 870-873 (1989).

87. Y. Tadir, W. H. Wright, O. Vafa, T. Ord, R. H. Asch, and M. W. Berns, "Force generated by human sperm correlated to velocity and determined using a laser generated optical trap," *Fertil. Steril.* **53**, 944-947 (1990).

88. S. B. Smith, Y. Cui, and C. Bustamante, "Overstretching B-DNA: The Elastic Responseof Individual Double-Stranded and Single-Stranded DNA Molecules," *Science* **271**, 795-799 (1996).

89. M. W. Berns, Y. Tadir, H. Liang, and B. Tromberg, 1998. Laser scissors and tweezers. In: Sheetz MP, editor. *Laser Tweezers in Cell Biology, Methods in Cell Biology*, Vol. 55. New York: Academic Press, pp. 71-98.

90. H. Liang, W. H. Wright, S. Cheng, W. He and M. W. Berns, "Micromanipulation of chromosomes in PTK2 cells using laser microsurgery (optical scalpel) in combination with laser-induced optical force (optical tweezers)," *Exp. Cell. Res*. **204**, 110-120 (1993).

91. A. I. Bishop, T. A. Nieminen, N. R. Heckenberg, and H. Rubinsztein-Dunlop, "Optical Microrheology Using Rotating Laser-Trapped Particles," *Phys. Rev. Lett.* **92**, 198104 (2004).

92. J. Leach, G. Sinclair, P. Jordan, J. Courtial, M. Padgett, J. Cooper, and Z. Laczik, "3D manipulation of particles into crystal structures using holographic optical tweezers," *Opt. Exp.* **12**, 220-226 (2004).

93. G. Sinclair, P. Jordan, J. Courtial, M. Padgett, J. Cooper, and Z. Laczik, "Assembly of 3-dimensional structures using programmable holographic optical tweezers," *Opt. Exp.* **12,** 5475-5480 (2004).

94. K. Ladavac, K. Kasza, and D. G. Grier, "Sorting microscopic objects with periodic potential landscapes: Optical fractionation," *Phys. Rev. E* **70**, 010901 (2004).

95. M. P. MacDonald, G. C. Spalding, and K. Dholakia, "Microfluidic sorting in an optical lattice," *Nature* **426**, 421-424 (2003).

96. L. Paterson, E. Papagiakoumou, G. Milne, V. Garcés-Chávez, S. A. Tatarkova, W. Sibbett, F. J. Gunn-Moore, P. E. Bryant, A. C. Riches, and K. Dholakia, "Light-induced cell separation in a tailored optical landscape," *Appl. Phys. Lett.* **87**, 123901 (2005).

97. G. Milne, K. Dholakia, D. McGloin, K. Volke-Sepulveda, and P. Zemánek, "Transverse particle dynamics in a Bessel beam," *Opt. Exp.* **15,** 13972-13987 (2007).

98. T Čižmár, M Šiler, M Šerý, P Zemánek, V.Garcés-Chávez, and K. Dholakia, "Optical sorting and detection of submicrometer objects in a motional standing wave" *Phys. Rev. B* **74**, 035105 (2006).

99. P. Jákl, T. Čižmár, M. Šerý, and P. Zemánek, "Static optical sorting in a laser interference field," *Appl. Phys. Lett.* **92**, 161110 (2008).

100. A. Jesacher, S. Furhapter, C. Maurer, ¨S. Bernet, and M. Ritsch-Marte, "Holographic optical tweezers for object manipulations at an air-liquid surface," *Opt. Exp.* **14**, 6342-6352 (2006).

101. D. G. Grier, "Optical tweezers in colloid and interface science," *Curr. Opin. Coll. Int. Sc.* **2**, 264-270 (1997).

102. G. M. Wang, E. M. Sevick, E. Mittag, D. J. Searles, and D. J. Evans, "Experimental Demonstration of Violations of the Second Law of Thermodynamics for Small Systems and Short Time Scales," *Phys. Rev. Lett.* **89**, 050601 (2002).

103. K. Svoboda, and S. M. Block, "Optical trapping of metallic Rayleigh particles," *Opt. Lett.* **19**, 930-932 (1994).

104. S. Tan, H. A. Lopez, C. W. Cai, and Y. Zhang, "Optical Trapping of Single-Walled Carbon Nanotubes," *Nano Letters* **4**, 1415–1419 (2004).

105. K. C. Neuman, E. H. Chadd, G. F. Liou, K. Bergman, and S. M. Block, "Characterization of Photodamage to Escherichia coli in Optical traps", *Biophys. J.* **77**, 2856-2863 (1999).

106. Y Liu, G J Sonek, M W Berns, and B J Tromberg. "Physiological monitoring of optically trapped cells: assessing the effects of confinement by 1064-nm laser tweezers using microfluorometry". *Biophys. J.* **71**, 2158–21 (1996).

107. Y. Lui, D. K. Cheng, G. J. Soneck, M. W. Berns, C. F. Chapman, and B. J. Tromberg, "Evidence of localized cell heating induced by infrared optical tweezers" *Biophys. J.* **68**, 2137 (1995).

108. K. König, H. Liang, M. W. Berns, and B. J. Tromberg, "Cell damage in near-infrared multimode optical traps as a result of multiphoton absorption", *Opt Lett.* **21**, 1090-1092 (1996).

109. S. K. Mohanty, M. Sharma, and P. K. Gupta, "Generation of ROS in cells on exposure to CW and pulsed near-infrared laser tweezers" *Photochem. Photobiol. Sc.*, **5**, 134-139 (2006).

110. D. C. Appleyard, K. Y. Vandermeulen, H. Lee, and M. J. Lang, "Optical trapping for undergraduates," *Am. J. Phys.* **75**, 5-14 (2007).

111. D. N. Moothoo, J. Arlt, R. S. Conroy, F. Akerboom, A. Voit, and K. Dholakia, "Beth's experiment using optical tweezers," *Am. J. Phys.* **69**, 271-276 (2001).

112. W. Grange, S. Husale, H. Güntherodt, and M. Hegner, "Optical tweezers system measuring the change in light momentum flux," *Rev. Sci. Instrum.* **73**, 2308-2316 (2002).

113. A. Rohrbach, and E. H. K. Stelzer, "Trapping Forces, Force Constants, and Potential Depths for Dielectric Spheres in the Presence of Spherical Aberrations," *Appl. Opt.* **41**, 2494-2507 (2002).

114. E. Fällman, and O.Axner, "Influence of a Glass-Water Interface on the On-Axis Trapping of Micrometer-Sized Spherical Objects by Optical Tweezers," *Appl. Opt*. **42**, 3915-3926 (2003).

115. http://micro.magnet.fsu.edu/primer/anatomy/numaperture.html. Online access date December 15, 2011.

116. N. B. Viana, M. S. Rocha, O. N. Mesquita, A. Mazolli, and P. A. Maia Neto, "Characterization of objective transmittance for optical tweezers," *Appl. Opt.* **45**, 4263-4269 (2006).

117. H. Misawa, M. Koshioka, K. Sasaki, N. Kitamura, and H. Masuhara, “Three-dimensional optical trapping and laser ablation of a single polymer latex particle in water,” *J. Appl. Phys.* **70**, 3829-3835 (1991).

118. J. T. Finer, R. M. Simmons, and J. A. Spudic, “Single myosin molecule mechanics: piconewton forces and nanometre steps,” *Nature* **368**, 113-119 (1994).

119. R. M. Simmons, J. T. Finer, S. Chu, and J. A. Spudich, “Quantitative Measurements of Force and Displacement Using an Optical Trap,” *Biophys. J.* **70**, 1813-1822 (1996).

120. M. J. Kendrick, D. H. McIntyre, and O. Ostroverkhova,"Wavelength dependence of optical tweezer trapping forces on dye-doped polystyrene microspheres," *J. Opt. Soc. Am. B* **26**, 2189-2198 (2009).

121. M. Capitanio, G. Romano, R. Ballerini, M. Giuntini, F. S. Pavonea, D. Dunlap, and L. Finzi, “Calibration of optical tweezers with differential interference contrast signals,” *Rev. Sci. Instrum.* **73**, 1687-1696 (2002).

122. K. Svoboda, C. F. Schmidt, B. J. Schnapp, and S. M. Block, “Direct observation of kinesin stepping by optical trapping interferometry,” *Nature* **365**, 721-727 (1993).

123. M. W. Allersma, F. Gittes, M. J. deCastro, R. J. Stewart, and C. F. Schmidt, “Two-Dimensional Tracking of ncd Motility by Back Focal Plane Interferometry,” *Biophys. J.* **74**, 1074–1085 (1998).

124. S. F. Tolic-Norrelykke, E. Schaeffer, J. Howard, F. S. Pavone, F. Juelicher, and H. Flyvbjerg, “Calibration of optical tweezers with positional detection in the back-focal-plane,” *Rev. Sci. Instrum*. **77**, 103101 (2006).

125. F. Gittes, and C. F. Schmidt, "Interference model for back-focal-plane displacement detection in optical tweezers," *Opt. Lett.* **23**, 7-9 (1998).

126. J. Gelles, B. J. Schnupp, and M. P. Sheetz, "Tracking kinesin-driven movements with nanometre-scale precision," *Nature* **331,** 450-453 (1988).

127. M. K. Cheezum, W. F. Walker, and W. H. Guilford, "Quantitative Comparison of Algorithms for Tracking Single Fluorescent Particles," *Biophys. J.* **81**, 2378 – 2388 (2001).

128. R. E. Thompson, D. R. Larson, and W. W. Webb, "Precise Nanometer Localization Analysis for Individual Fluorescent Probes," *Biophys. J.* **82**, 2775 – 2783 (2002).

129. J. C. Crocker, and D. G. Grier, "Methods of Digital Video Microscopy for Colloidal Studies," *J. Colloid Interface Sci.* **179**, 298-310 (1996).

130. W. P. Wong, and K. Halvorsen, "The effect of integration time on fluctuation measurements: calibrating an optical trap in the presence of motion blur," *Opt. Exp* **14**, 12517-12531 (2006).

131. A. van der Horst, and N.R. Forde, "Power spectral analysis for optical trap stiffness calibration from high-speed camera position detection with limited bandwidth," *Opt. Exp.* **18**, 7670-7677 (2010).

132. L. P. Ghislain, and W. W. Webb, "Scanning-force microscope based on an optical trap," *Opt. Lett.* **18**, 1678-1680 (1993).

133. I. M. Peters, B. G. de Grooth, J. M. Schins, C.G. Figdor, and J. Greve, "Three dimensional single-particle tracking with nanometer resolution," *Rev Sci. Instrum.* **69**, 2762-2766 (1998).

134. E. Florin, J. K. H. Hörber, and E. H. K. Stelzer, "High-resolution axial and lateral position sensing using two-photon excitation of fluorophores by a continuous-wave Nd:YAG laser," *Appl. Phys. Lett.* **69**, 446-448 (1996).

135. A. R. Clapp, A. G. Ruta, and R. B. Dickinson, "Three-dimensional optical trapping and evanescent wave light scattering for direct measurement of long range forces between a colloidal particle and a surface," *Rev Sci. Instrum.* **70**, 2627-2636 (1999).

136. K. Sasaki, M. Tsukima, and H. Masuhara, "Three-dimensional potential analysis of radiation pressure exerted on a single microparticle," *Appl. Phys. Lett.* **71**, 37-39 (1997).

137. J. K. Dreyer, K. Berg-Sørensen, and L. Oddershede, "Improved axial position detection in optical tweezers measurements," *Appl. Opt*. **43**, 1991-1995 (2004).

138. P. C. Ashok, R. Dasgupta, and P. K. Gupta," Measurement of Axial Position Spectrum of Trapped Microspheres using Image Correlation Technique," *National laser symposium*,17-20 December, 2007, M.S. University of Baroda, Vadodara, India.

139. J. H. Bao, Y. M. Li, L. R. Lou, and Z. Wang, "Measurement of the axial displacement with information entropy," *J. Opt. A: Pure Appl. Opt*. **7**, 76–81 (2005).

140. T. Gigras, R. Dasgupta, and P. K. Gupta, "Axial Displacement Measurement Of A Trapped Object using Principal Components Analysis," *Photonics-2008, International conference on fiber optics and photonics*, New Delhi, India, 13- 17 December, 2008.

141. K. C. Neuman, and S. M. Block, "Optical trapping", *Rev. Sci. Instrum.* **75**, 2787-2809 (2004).

142. S. J. Koch, and M. D. Wang, "Dynamic Force Spectroscopy of Protein-DNA Interactions by Unzipping DNA," *Phys. Rev. Lett.* **91**, 028103 (2003).

143. T. T. Perkins, R. V. Dalal, P. G. Mitsis, and S. M. Block, "Sequence-Dependent Pausing of Single Lambda Exonuclease Molecules," *Science* **301**, 1914-1918 (2003).

144. J. Man Kim, B. S. Choi, S. Kim, J. M. Kim, H. I. Bjelkhagen, and N. J. Phillips, "Holographic optical elements recorded in silver halide sensitized gelatin emulsions. Part I. Transmission holographic optical elements," *Appl. Opt*. **40**, 622-632 (2001).

145. C.Neipp, A. M´arquez, I. Pascual, and A. Bel´endez, "Thick phase holographic gratings recorded on BB-640 and PFG-01 silver halide materials," *J. Opt. A: Pure Appl. Opt.* **5,** S183–S188 (2003).

146. D. M. Walba, "Ferroelectric Liquid Crystals," *Adv. Synth. React. Sol.* **1**, 173-235 (1991).

147. J. Reményi, P. Várhegyi, L. Domján, P. Koppa, and E. Lõrincz, "Amplitude, Phase, and Hybrid Ternary Modulation Modes of a Twisted-Nematic Liquid-Crystal Display at ~400 nm," *Appl. Opt.* **42**, 3428-3434 (2003).

148. M. Yamauchi, "Jones-matrix models for twisted-nematic liquid-crystal devices," *Appl. Opt.* **44**, 4484-4493 (2005).

149. http://www.ece.nmsu.edu/~migiles/publications/lctvapps.html. online access date December 16, 2011.

150. R. S. Verma, M. K. Swami, S. S. Manhas, and P. K. Gupta, "Mueller matrix-based optimization of reflective type twisted nematic liquid crystal SLM at oblique incidences," *Opt. Comm.* **283**, 2580-2587 (2010).

151. F. Merenda, G. Boer, J. Rohner, G. Delacretaz, and R. Salath´, "Escape trajectories of single-beam optically trapped micro-particles in a transverse fluid flow," *Opt. Exp.* **14**, 1685-1699 (2006).

152. W. H. Wright, G. J. Sonek, and M. W. Berns, "Parametric study of the forces on microspheres held by optical tweezers," *Appl. Opt.* **33**, 1735-1748 (1994).

153. A. Buosciolo, G. Pesce, and A. Sasso, "New calibration method for position detector for simultaneous measurements of force constants and local viscosity in optical tweezers," *Opt. Comm.* **230**, 357–368 (2004).

154. J. Calatroni, and G. Da Costa, "Interferometric determination of the surface profile of a liquid heated by a laser beam," *Opt. Comm.* **42**, 5-9 (1982).

155. G. Da Costa, and J. Calatroni, "Transient deformations of liquid surfaces by laser-induced thermocapillarity," *Appl. Opt.* **18**, 233-235 (1979).

156. S. Mitani, and K. Sakai, "Measurement of ultralow surface tension with a laser interface manipulation technique," *Phys. Rev. E* **66**, 031604 (2002).

157. G. Da Costa, "Optical visualization of the velocity distribution in a laser induced thermocapillary liquid flow," *Appl. Opt.* **32**, 2143-2151 (1993).

158. A. J. Hurd, and D. W. Schaefer, "Diffusion-limited aggregation in two dimensions," *Phys. Rev. Lett.* **54**, 1043-1046 (1985).

159. J. Stankiewicz, M. A. Cabrerizo Vílchez, and R. H. Alvarez, "Two dimensional aggregation of polystyrene latex particles," *Phys. Rev. E* **47**, 2663-2668 (1993).

160. M. M. Burns, J. M. Fournier, and J. A. Golovchenko, "Optical Binding," *Phys. Rev. Lett.* **63,** 1233-1236 (1989).

161. M. M. Burns, J. M. Fournier, and J. A. Golovchenko, "Optical matter: Crystallization and binding in intense optical fields," *Science* **249**, 749-754 (1990).

162. S. K. Mohanty, J. T. Andrews, and P. K. Gupta, "Optical binding between dielectric particles," *Opt. Exp*. **12,** 2749-2756 (2004).

163. F. Depasse, and J. M. Vigoureux, "Optical binding force between two Rayleigh particles," *J. Phys. D: Appl. Phys.* **27**, 914–919 (1993).

164. S. Tatarkova, A. E. Carruthers, and K. Dholakia, "One dimensional optical bound arrays of microscopic particles," *Phys. Rev. Lett.* **89**, 283901-1-4 (2002).

165. T. M. Grzegorczyk, B. A. Kemp, and J. A. Kong, "Stable optical trapping based on optical binding forces," *Phys. Rev. Lett.* **96,** 113903-1-4 (2006).

166. A. S. Zelenina, R. Quidant, and M. Nieto-Vesperinas, "Enhanced optical forces between coupled resonant metal nanoparticles," *Opt. Lett.* **32**, 1156-58 (2007).

167. L. Ling, F. Zhou, L. Huang, and Z. Y. Lia, "Optical forces on arbitrary shaped particles in optical tweezers," J. Appl. Phys. **108**, 073110 (2010).

168. T. M. Grzegorczyk, B. A. Kemp, and J. A. Kong, "Passive guiding and sorting of small particles with optical binding forces," *Opt. Lett.* **31**, 3378-3380 (2006).

169. T. Ota, T. Sugiura, S. Kawata, M. J. Booth, M. A. A. Neil, R. Juškaitis, and T. Wilson, "Enhancement of Laser Trapping Force by Spherical Aberration Correction Using a Deformable Mirror," *Jpn. J. Appl. Phys*. **42**, L701-L703 (2003).

170. S. N. S. Reihani, M. A. Charsooghi, H. R. Khalesifard, and R. Golestanian, ''Efficient in-depth trapping with an oil-immersion objective lens," *Opt. Lett.* **31**, 766-768 (2006).

171. S. N. S. Reihani, and L. B. Oddershede, "Optimizing immersion media refractive index improves optical trapping by compensating spherical aberrations," *Opt. Lett.* **32**, 1998-2000 (2007).

172. R. Dasgupta, S. Ahlawat, and P. K. Gupta, "Trapping of micron-sized objects at a liquid–air interface." *J. Opt. A: Pure Appl. Opt.* **9,** S189-195 (2007).

173. A. Jesacher, S. Fürhapter, C. Maurer, S. Bernet, and M. Ritsch-Marte, "Holographic optical tweezers for object manipulations at an air-liquid surface," *Opt. Exp.* **14**, 6342-6352 (2006).

174. A. T. Oneil, and M. J. Padgett, "Axial and lateral trapping efficiency of Laguerre-Gaussian modes in inverted optical tweezers," *Opt Comm.* **193**, 45-50 (2001).

175. M. E. J. Friese, H. Rubinsztein-Dunlop, N. R. Heckenberg, and E. W. Dearden, "Determination of the force constant of a single-beam gradient trap by measurement of backscattered light," *Appl Opt.* **35**, 7112-7116 (1996).

176. N. B. Simpson, D. McGloin, K. Dholakia, L. Allen, M. J. Padgett, "Optical tweezers with increased axial trapping efficiency," *J. Mod. Opt.* **45**, 1943-1949 (1998).

177. P. Török, and P. R. T. Munro, "The use of Gauss-Laguerre vector beams in STED microscopy," *Opt Exp* **12**, 3605-3617 (2004).

178. S. Deng, L. Liu1, Y. Cheng, R. Li, and Z. Xu. "Investigation of the influence of the aberration induced by a plane interface on STED microscopy," *Opt Exp* **17**, 1714-1725 (2009).

179. M. T. Wei, and A. Chiou, "Three-dimensional tracking of Brownian motion of a particle trapped in optical tweezers with a pair of orthogonal tracking beams and the determination of the associated optical force constants," *Opt Exp.* **13**, 5798-5806 (2005).

180. "Laurdan Generalized Polarization: from cuvette to microscope". http://www.formatex.org/microscopy3/pdf/pp1007-1014.pdf. online access date May 3, 2010.

181. S. Fischokoff, and J.M. Vanderkooi, "Oxygen Diffusion in Biological and Artificial Membranes Determined by the Fluorochrome Pyrene," *J. Gen. Physiol.* **65**, 663-676 (1975).

182. T. Parasassi, and E Gratton, "Packing of phospholipid vesicles studied by oxygen quenching of Laurdan fluorescence," *J. Fluorescence.* **2**, 167-174 (1992).

183. R. M. Simmons, J. T. Finer, S. Chu, J. A. Spudich, P. Török, and P.R.T. Munro, "Quantitative Measurements of Force and Displacement Using an Optical Trap," *Biophys. J.* **70**, 1813-1822 (1996).

184. H. Schneckenburger, M. Wagner, M. Kretzschmar, W. S. L. Strauss, and R. Sailer, "Laser-assisted fluorescence microscopy for measuring cell membrane dynamics," *Photochem. Photobiol. Sci.* **3**, 817-822 (2004).

185. J. R. Dynlacht, and M. H. Fox, “Heat induced changes in membrane fluidity of Chinese Hamster Ovary cells measured by flow cytometry,” *Radiotaion Res.* **130**, 48-54 (1992).

186. J. M. Nascimento, E. L. Botvinick, L. Z Shi, B. Durrant, and M. W. Berns, “Analysis of sperm motility using optical tweezers,” *J. Biomed. Opt.* **11**, 044001 (2006).

187. B. Shao, L. Z. Shi, J. M. Nascimento, E. L. Botvinick, M. Ozkan, M. W. Berns, and S.C. Esener “High-throughput sorting and analysis of human sperm with a ring-shaped laser trap,” *Biomed. Microdevices.* **9**, 361–369 (2007).

188. J. M. Nascimento, L. Z. Shi, S. Meyers, P. Gagneux, N. M. Loskutoff, E. L Botvinick, and M. W. Berns, “The use of optical tweezers to study sperm competition and motility in primates,” *J. R. Soc. Interface* **5**, 297 – 302 (2008).

189. Y. Tadir, W. H. Wright, O. Vafa, L. H. Liaw, R. Asch, and M. W. Berns “Micromanipulation of gametes using laser microbeams,” *Hum. Reprod.* **6**, 1011-6 (1991).

190. B. Schopper, M. Ludwig, J. Edenfeld, S. Al-Hasani, and K Diedrich. “Possible applications of lasers in assisted reproductive technologies,” *Hum. Reprod.* **14**, 186–193 (1999).

191. K. Konig, Y. Tadir, P. Patrizio, M. W. Bems, and B. J. Tromberg, “Effects of ultraviolet exposure and near infrared laser tweezers on human spermatozoa,” *Hum. Reprod.* **11**, 2162–2164 (1996).

192. C. Paul, J. E. Povey, N. J. Lawrence, J. Selfridge, D.W. Melton, and P. T. K. Saunders. “Deletion of Genes Implicated in Protecting the Integrity of Male Germ Cells Has

Differential Effects on the Incidence of DNA Breaks and Germ Cell Loss." *PLoS One* **10**, e989 (2007);

193. D. P. Evenson, L. K. Jost, D. Marshall, M. J. Zinaman, E. Clegg, K. Purvis, P. de Angelis, and O. P. Claussen, "Utility of the sperm chromatin structure assay as a diagnostic and prognostic tool in the human fertility clinic," *Human Reprod.* **14**, 1039-1049 (1999).

194. 1,6-Diphenylhexatriene. Online access date 25 th May, 2010, from Web site: http://omlc.ogi.edu/spectra/PhotochemCAD/html/diphenylhexatriene.html

195. Z. Darzynkiewicz, "Differential staining of DNA and RNA in intact cells and isolated cell nuclei with acridine orange," *Methods Cell Bio.* **33**, 285-298 (1990).

196. N. Kure, T. Sano, S. Harada, and T. Yasunaga, "Kinetics of interactions between DNA and Acridine Orange," *Bull. Chem. Soc. Jpn.* **61**, 643-653 (1988).

197. E. J. G. Peterman, F. Gittes, and C. F. Schmidt, "Laser-Induced Heating in Optical Traps," *Biophys. J.* **84**, 1308-1316 (2003).

198. Y. Liu, G. J. Sonek, M. W. Berns, K. Konig and B. J. Tromberg, "Two-photon fluorescence excitation in continuous-wave infrared optical tweezers," *Opt. Lett.* **20**, 2246-48 (1995).

199. K. König, H. Liang, M. W. Berns, and B. J. Tromberg, "Cell damage in near-infrared multimode optical traps as a result of multiphoton absorption", *Opt. Lett.* **21**, 1090-1092 (1996).

200. G. D. M. Jeffries, J. S. Edgar, Y. Zhao, J. P. Shelby, C. Fong, and D. T. Chiu, "Using Polarization Shaped Optical Vortex Traps for Single-Cell Nanosurgery," *Nano Lett* **7**, 415-420 (2007).

201. P. Hinterdorfer, and A. van Oijen, *Handbook of single molecule biophysics*, p-71, (Springer, New York, 2009)

202. D. Rickwood, M. T. Wilson and V.M. Darley-Usmar "Quantitation and characteristics of intact mitochondria," in *Mitochondria –A Practical Approach* V.M. Darley-Usmar, D. Rickwood and M. T. Wilson Eds, pp.1-16, (IRC Press, Oxford, Washington (1987).

203. H. Liang, K. T. Vu, P. Krishnan, T. C. Trang, D. Shin, S. Kimel, and M. W. Berns, "Wavelength dependence of cell cloning efficiency after optical trapping," *Biophys. J* **70**, 1529-1533 (1996).

204. S. K. Mohanty, A. Rapp, S. Monajembashi, P. K. Gupta, and K. O. Greulich, "Comet assay measurements of DNA damage in cells by laser microbeams and trapping beams with wavelengths spanning a range of 308 nm to 1064 nm," *Rad. Res.* **157**, 378-385 (2002)

205. S. K. Mohanty, M. Sharma, and P. K. Gupta, "Generation of ROS in cells on exposure to CW and pulsed near-infrared laser tweezers" *Photochem. Photobiol. Sc.* **5**, 134-139 (2006).

206. K. Sueda, G. Miyaji, N. Miyanaga, and M. Nakatsuka. "Laguerre-Gaussian beam generated with a multilevel spiral phase plate for high intensity laser pulses," *Opt. Exp.* **12**, 3548-3553 (2004).

207. J. F. Bisson, Y. Senatsky, and K. I. Ueda, "Generation of Laguerre-Gaussian modes in Nd:YAG laser using diffractive optical pumping," *Laser Phys. Lett.* **2**, 327–333 (2005).

208. S. Rao, Š. Bálint, L. del Carmen Frias, and D. Petrov, "Polarization Raman study of protein ordering by controllable RBC deformation," *J. Raman Spec.* **40**, 1257-1261 (2009).

209. M. F. Perutz, "Submicroscopic Structure of the Red Cell," *Nature* **161**, 204-205 (1948).

210. K. Mohanty, S. Mohanty, S. Monajembashi, and K.O. Greulich, "Orientation of erythrocytes in optical trap revealed by confocal fluorescence microscopy," *J. Biomed. Opt.* **12**, 060606-1-3 (2007).

211. S. C. Grover, R. C. Gauthier, and A. G. Skirtach, "Analysis of the behaviour of erythrocytes in an optical trapping system," *Opt. Exp.* **7**, 533-539 (2000).

212. S. Bayoudh, T. A. Nieminen, N. R. Heckenberg, and H. Rubinsztein-Dunlop, "Orientation of biological cells using plane-polarized Gaussian beam optical tweezers," *J. Mod. Opt.* **50**, 1581–1590 (2003).

213. G. Garab, P. Galajda, I. Pomozi. L. Finzi, T Praznovszky, P. Ormos, and H. Amerongen, "Alignment of biological microparticles by a polarized laser beam*," Eur. Biophys. J.* **34**, 335–343 (2005).

214. V. Bingelyte, J. Leach, J. Courtial, and M. J. Padgett, "Optically controlled three-dimensional rotation of microscopic objects," *Appl. Phys. Lett.* **82**, 829-831 (2003).

215. "BioRyx 200 Applications," http://www.arryx.xom/PDFdocs/BiorryxApplications.pdf. online acess date December 20, 2011.

216. S. K. Mohanty, R. Dasgupta, and P. K. Gupta, “Three-dimensional orientation of microscopic objects using combined elliptical and point optical tweezers,” *Appl. Phys. B* **81**, 1063-1066 (2005).

217. S. K. Mohanty, and P. K. Gupta, “Laser-assisted three-dimensional rotation of microscopic objects,” *Rev. Sci. Inst.* **75**, 2320-2322 (2004).

218. S. K. Mohanty, A. Uppal, and P. K. Gupta, “Self-rotation of red blood cells in optical tweezers: prospects for high throughput malaria diagnosis,” *Biotechnol. Lett.* **26**, 971-974 (2004).

219. S. K. Mohanty, K. S. Mohanty, and P. K. Gupta, “Dynamics of Interaction of RBC with optical tweezers,” *Opt. Exp.* **13**, 4745-4751 (2005).

220. J. A. Dharmadhikari, S. Roy, A. K. Dharmadhikari, S. Sharma, and D. Mathur, "Naturally occurring, optically driven, cellular rotor," *Appl. Phys. Lett.* **85**, 6048-6050 (2004).

221. J. A. Dharmadhikari, S. Roy, A. K. Dharmadhikari, S. Sharma, and D. Mathur, “Torque-generating malaria-infected red blood cells in an optical trap,” *Opt. Exp.* **12**, 1179-1184 (2004).

222. H. Rouse, *Elementary Mechanics of Fluids, Ch. VIII* (Wiley Eastern Pvt. Ltd, 1970).

223. V. Garcés-Chávez, K. Volke-Sepulveda, S. Chávez-Cerda, W. Sibbett, and K. Dholakia, “Transfer of orbital angular momentum to an optically trapped low-index particle,” *Phys. Rev. A* **66**, 063402-8 (2002).

224. H. Ukita, and M. Kanehira, "A Shuttlecock Optical Rotator—Its Design, Fabrication and Evaluation for a Microfluidic Mixer," *IEEE J. Quantum Electn.* **8**, 111-117 (2002).

225. S. Maruo, and H. Inoue, "Optically driven viscous micropump using a rotating microdisk," *Appl. Phys. Lett.* **91**, 084101-3 (2007).

226. M. Khan, S. K. Mohanty, and A. K. Sood, "Optically-driven red blood cell rotor in linearly polarized laser tweezers," *Pramana* **65**, 777-786 (2005).

227. J. Leach, E. Yao, and M. J. Padgett, "Observation of the vortex structure of a non-integer vortex beam," *New J. Phys.* **6**, 71 (2004).

228. S. H. Tao, X-C. Yuan, and J. Lin, "Fractional optical vortex beam induced rotation of particles," *Opt Exp.* **13**, 7726-7731 (2005).

229. E. Smith, and G. Dent, *Modern Raman spectroscopy-A practical approach* (John Wiley & Sons, 2005).

230. J. R. Ferraro, K. Nakamoto, and C. W. Brown, *Introductory Raman Spectroscopy* (Elsevier, 2003).

231. K. Ramser, J. Enger, M. Goksör, D. Hanstorp, K. Logg, and M. Käll, "A microfluidic system enabling Raman measurements of the oxygenation cycle in single optically trapped red blood cells," *Lab Chip* **5**, 431-436 (2005).

232. P. R. T. Jess, V. Garces-Chavez, D. Smith, M. Mazilu, L. Paterson, A .Riches, C. S. Herrington, W. Sibbett, and K. Dholakia, "Dual beam fibre trap for Raman microspectrocopy of single cells," *Opt. Exp.* **14**, 5779 – 5791 (2006).

233. I. R. Lewis, and H. G. M. Edwards, *Handbook of Raman Spectroscopy* (Marcel Dekker, 2001).

234. R. L. McCreeey, *Raman Spectroscopy for Chemical Analysis* (Wiley-IEEE, 2000).

235. C. M. Creely, G. P. Singh, and D. Petrov, "Dual wavelength optical tweezers for confocal Raman spectroscopy", *Opt. Comm.* **245**, 465-470 (2005).

236. G. Rusciano, A. C. De Luca, G. Pesce, and A. Sasso, "Phase sensitive detection in Raman tweezers," *Appl. Phys. Lett.* **89**, 261116 (2006).

237. C. A. Lieber, and A. Mahadevan-Jansen, "Automated Method for Subtraction of Fluorescence from Biological Raman Spectra," *App. Spec.* **57**, 1363-1367 (2003).

238. J. Zhao, H. Lui, D. I. Mclean, and H. Zeng, "Automated Autofluorescence Background Subtraction Algorithm for Biomedical Raman Spectroscopy," *Appl. Spec.* **61**, 1225-1232 (2007).

239. K. Ramser, K. Logg. M. Goksor, J. Enger, M. Kall, and D. Hanstorp, "Resonance Raman spectroscopy of optically trapped functional erythrocytes," *J. Biomed. Opt.* **9**, 593-600 (2004).

240. K. Ramser, C. Fant, and M. Kall, "Importance of substrate and photo-induced effects in Raman spectroscopy of single functional erythrocytes," *J. Biomed. Opt.* **8**, 173-178 (2003).

241. B. R. Wood, L. Hammer, L Davis, and D. McNaughton, "Raman microspectroscopy and imaging provides insights into heme aggregation and denaturation within human erythrocytes," *J. Biomed. Opt.* **10**, 014005 (2005).

242. B. R. Wood, P. Caspers, G. J. Puppels, S. Pandiancherri, and D. McNaughton, "Resonance Raman spectroscopy of red blood cells using near infrared excitation", *Anal. Bioanal. Chem.* **387**, 1691-1703 (2007).

243. A. Trommler, D. Gingell, and H.Wolf, "Red blood cells experience electrostatic repulsion but make molecular adhesions with glass," *Biophys. J.* **48**, 835-841 (1985).

244. A Rossi-Fanelli, E. Antonini, and A. Caputo, "Studies on the Relations between Molecular and Functional Properties of Hemoglobin," *J. Biol. Chem.* **236**, 391-396 (1961).

245. A. K. Sau, D. Currell, S. Mazumdar, and S. Mitra, "Interaction of sodium dodecyl sulfate with human native and cross-linked hemoglobins: a transient kinetic study", *Biophys. Chem.* **98**, 267-273 (2002).

246. B. R. Wood, B. Tait, and D. McNaughton, "Micro-Raman characterization of the R to T state transition of haemoglobin within a single living erythrocyte", *Biochem. Biophys. Acta* **1539**, 58-70 (2001).

247. S. Hu, K. M. Smith, and T. G. Spiro, "Assignment of protoheme resonance Raman spectrum by heme labeling in myoglobin," *J. Am Chem. Soc.* **118**, 12638-12646 (1996).

248. B. R. Wood and D. McNaughton, "Raman excitation wavelength investigation of single red blood cells in vivo," *J. Raman Spec.* **33**, 517-523 (2002).

249. A. C. De Luca, G. Rusciano, R. Ciancia, V. Martinelli, G. Pesce, B. Rotoli, L. Selvaggi, and A. Sasso, "Spectroscopical and mechanical characterization of normal and thalassemic red blood cells by Raman Tweezers," *Opt. Exp*. **16**, 7943-7957 (2008).

250. M. Asghari-Khiavi, A. Mechler, K. R. Bambery, D. McNaughton, and B. R.Wood, "A resonance Raman spectroscopic investigation into the effects of fixation and dehydration on heme environment of hemoglobin," *J. Raman Spec.* **40**, 1668–1674 (2009).

251. M. Asghari-Khiavi, B. R. Wood, A. Mechler, K. R. Bambery, D. W. Buckingham, B. M. Cookec, and D. McNaughton, "Correlation of atomic force microscopy and Raman micro-spectroscopy to study the effects of ex vivo treatment procedures on human red blood cells," *Analyst* **135**, 525–530 (2010).

252. L. R. Moore, H. Fujioka, P. S. Williams, J. J. Chalmers, B. Grimberg, P. A. Zimmerman, and M. Zborowski. "Hemoglobin degradation in malaria-infected erythrocytes determined from live cell magnetophoresis," *FASEB J.* **20**, 747-749 (2006).

253. R. C. Smith, and K.S. Baker. "Optical Properties of the Clearest Natural Waters (200-800 nm)," *Appl. Opt*. **20**, 177-184 (1981).

254. Optical absorption of haemoglobin by Scott Prahl, Oregon Medical Laser Center. Online access date 5 th February, 2010, from http://www.imt.liu.se/edu/courses/TBMT36/artiklar/4_Tissue_prop/hemoglobin_spectra.pdf

255. V. M. Nahirnyak, S. Wang Yoon, and C. K. Holland. "Acousto-mechanical and thermal properties of clotted blood," *J. Acoust. Soc. Am.* **119**, 3766-3772 (2007).

256. S. C. M Agustinho, M. H. Tinto, J. R. Perussi, M. Tabak and H. Imasato, "Fluorescence Studies of Extracellular Hemoglobin of Glossoscolex paulistus in Met Form Obtained from Sephadex Gel Filtration - A natural deconvolution of circular dichroism curves of proteins", *Comp. Biochem. Physiol. A: Physiol.* **118**, 171-18 (1997).

257. M. Zhou, H. Yang, J.Di, and E. Zhao, "Manipulation on human red blood cells with femtosecond optical tweezers," *Chin Opt Lett.* **6**, 919-921 (2008).

258. J. M. Nascimento, E. L. Botvinick, L. Z Shi, B. Durrant, and M. W. Berns, "Analysis of sperm motility using optical tweezers," *J. Biomed. Opt.* **11**, 044001 (2006).

259. S. W. Hell, M. Booth, .S. Wilms, C. M. Schnetter, A.K. Kirsch, D. J. Arndt-Jovin, and T. M. Jovin, "Two-photon near- and far-field fluorescence microscopy with continuous-wave excitation," *Opt. Lett.* **23**, 1238-1240 (1998).

260. G. O. Clay, C. B. Schaffer, and D. Kleinfeld, "Large two-photon absorptivity of hemoglobin in the infrared range of 780–880 nm," *J. Chem. Phys.* **126**, 025102 (2007).

261. S. Rogerson, "What is the relationship between haptoglobin, malaria, and anaemia," *PLoS. Med.* **3**, 0593-0594 (2006).

262. I. W. Sherman, *Malaria: Parasite Biology, Pathogenesis and Protection* (Am Soc Microbiol, USA, 1998).

263. R. N. Price, J. A. Simpson, F. Nosten, C. Luxemburger, L. Hkirjaroen, F. Kuile, T. Chongsuphajaisiddhi, and N. J. White, "Factors contributing to anemia after uncomplicated falciparum malaria," *Am. J. Trop. Med. Hyg*. **65**, 614-622 (2001).

264. K. Bambardekar, A. K. Dharmadhikari, J. A. Dharmadhikari, D. Mathur, and S. Sharma, "Measuring erythrocyte deformability with fluorescence, fluid forces, and optical trapping," *J. Biomed. Opt.* **13**, 064021 (2008).

265. V. Saraogi, P. Padmapriya, A. Paul, U. S. Tatu, and V. Natarajan, "Change in spectrum of Brownian fluctuations of optically trapped red blood cells due to malarial infection," *J. Biomed. Opt.* **15**, 037003 (2010).

266. C. Brémard, J. J. Girerd, P. Kowalewski, J. C. Merlin, and S. Moreau, "Spectroscopic Investigations of Malaria Pigment," *Appl. Spec.* **47**, 1837-1842 (1993).

267. B. R. Wood, S. J. Langford, B. M. Cooke, J. Lim, F. K. Glenister, M. Duriska, J. K. Unthank, and D. McNaughton, "Resonance Raman Spectroscopy Reveals New Insight into the Electronic Structure of β-Hematin and Malaria Pigment," *J. Am. Chem. Soc.* **126**, 9233-9239 (2004).

268. C. W. Ong, Z. X. Shen, K. K. H. Ang, U.A.K Kara, and S. H. Tang, "Raman Microspectroscopy of Normal Erythrocytes and Plasmodium berghei-Infected Erythrocytes," *Appl. Spec.* **56**, 1126-1131 (2002).

269. B. R Wood, J. L. Steven, B. M Cooke, F. K Glenister, J. Lim, and D. McNaughton, "Raman imaging of hemozoin within the food vacuole of Plasmodium falciparum trophozoites," *FEBS Lett.* **554**, 247-252 (2003).

270. 2008 Undergraduate Summer Research Program in Modern Optics and Optical Materials: Detection of nanosize biological threats. Online acess on 14 December, 2009, from University of Arkansas Web site: http://www.uark.edu/depts/physics/reu05/proj-4.html;

271. Y. K. Park, M. Diez-Silva, G. Popescu, G. Lykotrafitis, W. Choi, M. S. Feld, and S. Suresh, "Refractive index maps and membrane dynamics of human red blood cells parasitized by Plasmodium falciparum," *Proc. Nat. Acad. Sc.* **105**, 13730-13735 (2008).

272. Determination of Parasitemia. Online access on 8 August, 2010, from http://www.med-chem.com/procedures/DetofPara.pdf

273. H. Löffler, J. Rastetter, and T. Haferlach, *Atlas of clinical hematology*, pp-401 (Springer, USA, 2005).

274. K. M. Naumanna, G. L. Jonesb, A. Saulb, and R. Smith, "A Plasmodium falciparum exo-antigen alters erythrocyte membrane deformability," *FEBS Lett.* **292**, 95-97 (1991).

275. A. M. Dondorp, P. A. Kager, J. Vreeken, and N. J. White, "Abnormal Blood Flow and Red Blood Cell Deformability in Severe Malaria," *Parasitol. Today* **16**, 228-232 (2000).

276. F. Nuchsongsin, K. Chotivanich, P. Charunwatthana, O. Fausta, D. Taramelli, N. P. Day, N. J. White, and A. M. Dondorp, "Effects of Malaria Heme Products on Red Blood Cell Deformability," *Am. J. Trop. Med. Hyg.* **77**, 617-622 (2007).

277. S. N. Wickramasinghe, S. Looareesuwan, B. Nagachinta and N. J. White, "Dyserythropoiesis and ineffective erythropoiesis in Plasmodium vivax malaria," *British J. Hematol.* **72**, 91-99 (1989).

278. P. Pradhan, "Malarial anaemia and nitric oxide induced megaloblastic anaemia: a review on the causes of malarial anaemia," *J. Vector Borne Dis.* **46**, 100–108 (2009).

279. M. Abe, T. Kitagawa and Y. Kyogoku, "Resonance Raman spectra of octaethylporphyrinato-Ni(II) and meso-deuterated and 15N substituted derivatives. II. A normal coordinate analysis", *J. Chem. Phys.* **69**, 4526-4534 (1978).

280. B. L. N. Salmaso, G. J. Puppels, P. J. Caspers, R. Floris, R. Wever, and J. Greve, "Resonance Raman Microspectroscopic Characterization of Eosinophil Peroxidase in Human Eosinophilic Granulocytes," *Biophys. J.* **67**, 436-446 (1994).

281. T. Yammoto, and G. Palmer, "The valence and spin state of iron in oxyhemoglobin as inferred from resonance Raman spectroscopy," *J. Biol. Chem*. **248**, 5211-5213 (1973).

282. M. Forster, R E Hester, B. Cartling, and R. Wilbrandt, "Continuous flow-resonance Raman spectroscopy of an intermediate redox state of cytochrome c," *Biophys. J.* **38**, 111-116 (1982).

283. F. Palaceck, M. Palacekova, and D M Aviado, "Pathologic physiology and chemotherapy of Plasmodium berghei: II. Oxyhemoglobin dissociation curve in mice infected with chloroquine-sensitive and resistant strains," *Exp. Parasitol.* **21**, 16-30 (1967).

284. P. Sasi, S. P. Burns, C. Waruiru, M. English, C. L. Hobson, C. G. King, M. Mosobo, J. S. Beech, R. A. Iles, B. J. Boucher, R. D. Cohen, "Metabolic Acidosis and Other Determinants of Hemoglobin-Oxygen Dissociation in Severe Childhood Plasmodium falciparum Malaria," *Am. J. Trop. Med. Hyg.* **77**, 256–260 (2007).

285. S. N. Wickramasinghe, and S. H. Abdalla, "Blood and bone marrow changes in malaria," *Baillièrès Clinical Haematol.* **13**, 277-299 (2000).

286. F. J. Fernandes-Costa, R.Green, and J. D. Torrance, "Increased Erythrocytic Diphosphoglycerate in Megaloblastic Anaemia," *S. Afr. Med. J*. **53**, 709-712 (1978).

287. R. N. Price, E. Tjitra, C. A. Guerra, S. Yeung, N. J. White, and N. M. Anstey, "Vivax Malaria: Neglected and Not Benign," *Am. J. Trop. Med. Hyg.* **77**, 79-87 (2007).

288. A. Aparecida , M. Fernandes, L. José de Moura Carvalho, G. M. Zanini, A. M. R. da Silva Ventura , J. M. de Souza, P. M. Cotias, I. L. Da Silva Filho, and C. T. Daniel Ribeiro, "Similar Cytokine Responses and Degrees of Anemia in Patients with Plasmodium falciparum and Plasmodium vivax Infections in the Brazilian Amazon Region," *Clin. Vaccine. Immunol.* **15**, 650-658 (2008).

APPENDIX A

FORCES ARISING FROM A SINGLE RAY WHEN INCIDENT ON A DIELECTRIC SPHERE

When a ray of power P hits the sphere at an angle θ, it gets partially reflected and transmitted. These result in series of scattered rays of power PR, PT^2, PT^2R, ..., PT^2R^n,.... etc. Referring to figure 1.3 of chapter 1 it is seen that these scattered rays make angles with the incident forward direction of $\pi+2\theta$, α, $\alpha+\beta$,...., $\alpha+n\beta$,... respectively. Since the total force in the Z direction is consists of the net change in momentum per second in the z direction of all the scattered rays, we may write [1]

$$F_Z = \frac{n_1 P}{c} - \left[\frac{n_1 PR}{c} \cos(\pi + 2\theta) + \sum_{n=0}^{\infty} \frac{n_1 P}{c} T^2 R^n \cos(\alpha + n\beta) \right] \tag{A1}$$

Where n_1P/c is the momentum per second in Z direction of the incident ray.

For Y direction the incident momentum is zero and therefore

$$F_Y = 0 - \left[\frac{n_1 PR}{c} \sin(\pi + 2\theta) - \sum_{n=0}^{\infty} \frac{n_1 P}{c} T^2 R^n \sin(\alpha + \beta) \right] \tag{A2}$$

Following reference 1, one can sum over the rays scattered by the sphere by considering the total force in the complex plane, $F_{tot}=F_Z+iF_Y$,

$$F_{tot} = \frac{n_1 P}{c}[1 + R\cos 2\theta] - i\frac{n_1 P}{c} R \sin 2\theta - \frac{n_1 P}{c} T^2 \sum R^n e^{i(\alpha+n\beta)} \tag{A3}$$

The sum over n can be expressed as,

$$F_{tot} = \frac{n_1 P}{c}[1 + R\cos 2\theta] + i\frac{n_1 P}{c} R \sin 2\theta - \frac{n_1 P}{c} T^2 e^{i\alpha} \left[\frac{1}{1 - \mathrm{Re}^{i\beta}} \right] \tag{A4}$$

Substituting $\alpha=2\theta-2r$ *and* $\beta=\pi-2r$ (see figure 1.3) the expressions for F_Z and F_Y can be obtained from equation A4 as real and imaginary parts of $F_{tot.}$.

References:

1. A. Ashkin, "Forces of a single-beam gradient laser trap on a dielectric sphere in the ray optics regime," *Biophys. J.* **61**, 569-582 (1992).

APPENDIX B

CONVERSION EFFCICIENCIES OF COMPUTER GENERATED HOLOGRAMS DISPLAYED ON SPATIAL LIGHT MODULATORS FOR GENERATION OF LAGUERRE GAUSSIAN BEAMS

The measured conversion efficiencies for different orders (l) of Laguerre-Gaussian modes generated from the input TEM_{00} laser beam @ 1064 nm using a spatial light modulator (Model: Pluto, Holoeye Photonics AG) are given in the table below.

Laser Power	**1 W**
SLM 0 th order diffraction efficiency	~ 68.4%
Conversion Efficiencies:	
l=1	65.4%
l=5	65.2%
l=10	64.5%
l=20	63.8%

Table B1. Conversion efficiencies for different orders of *LG* modes.

APPENDIX C

ANOVA (ANALYSIS OF VARIANCE AMONG GROUPS) RESULTS

Table C1. ANOVA for VSL of spermatozoa that could be just trapped by different laser modes

	Mean	Standard Deviation
TEM_{00}	45.8	1.04
LG_{01}	52.8	0.76
LG_{03}	42.2	0.80
LG_{05}	30.4	1.23

Sources of variation	Sum of squares	DF	Mean Squares	F
Between	1318	3	439.5	469.3
Error	14.98	16	0.9360	
Total	1333	19		

Note: $p < 0.05$

Table C2. ANOVA for $T_{paralysis}$ observed for sperm cells trapped under *LG* trap beams with azimuthal indices 1, 3 and 5.

	Mean	Standard Deviation
LG_{01}	46.8	5.76
LG_{03}	50.6	5.94
LG_{05}	56.6	6.40

Sources of variation	Sum of squares	DF	Mean Squares	F
Between	7324	2	3662	100.4
Error	16296	447	36.46	
Total	23620	449		

Note: $p < 0.05$

APPENDIX D

t-TEST RESULTS

The t statistic to test whether the population means of two independent data sets are significantly different can be calculated as,

$$t = \frac{\bar{x}_1 - \bar{x}_2}{\sigma_d} \tag{D1}$$

Where $\bar{x}_1$ and $\bar{x}_2$ are the means of the data sets and σ_d is the variance of the difference between the two means,

$$\sigma_d = \sqrt{\left(\frac{\sigma_1^2}{n_1} + \frac{\sigma_2^2}{n_2}\right)} \tag{D2}$$

Here, σ_1, n_1 and σ_2, n_2 are the standard deviations and the total number of data points for the two data sets respectively.

The degrees of freedom for the data sets are given as n_1+n_2-2.

Table D1. t-Test for $T_{paralysis}$ observed for sperm cells trapped under TEM_{00} and *LG* trap beams

Power: 80 mW

	LG_{01}	TEM_{00}
Mean	68.7	52.0
Standard Deviation	7.41	6.58
Degrees of freedom	95	
t-statistics	11.62	
Critical Value	1.990	
$p < 0.05$?	YES	

Power: 110 mW

	LG_{01}	TEM_{00}
Mean	46.8	33.7
Standard Deviation	5.77	6.21
Degrees of freedom	97	
t-statistics	10.76	
Critical Value	1.990	
$p < 0.05$?	YES	

Power: 140 mW

	LG_{01}	TEM_{00}
Mean	14.2	7.6
Standard Deviation	3.14	3.25
Degrees of freedom	102	
t-statistics	10.59	
Critical Value	1.984	
$p < 0.05$?	YES	

Table D2. t-Test for time evolution data of fluorescence spectra from acridine orange stained spermatozoa in terms of intensity ratios between red and green channels

Time (s)	TEM_{00}		LG_{01}		Degrees of freedom	t-statistics	Critical Value	$p < 0.05$?
	Mean	Std Dev	Mean	Std Dev				
0	0.59	0.018	0.57	0.025	18	2.053	2.101	NO*
15	0.72	0.021	0.64	0.018		9.147		YES
30	0.87	0.022	0.74	0.016		15.112		YES
45	1.01	0.029	0.88	0.025		10.737		YES
60	1.14	0.040	1.02	0.056		5.514		YES
75	1.17	0.076	1.14	0.063		0.961		NO*
90	1.20	0.055	1.17	0.083		0.953		NO*

*Since at time zero no photodamage occurs to the cells the data for LG_{01} and TEM_{00} beams are expected to be similar. Also after 70 s since the ratio levels off for both types of trap beams the data for LG_{01} and TEM_{00} beams are expected to be similar.

D3. t-Test for intensity ratios of Raman bands as observed from RBCs collected from healthy donors (h-RBC) and malaria patients (m-m-RBC).

Ratio	h-RBC		m-m-RBC		Degrees of freedom	t-statistics	Critical Value	$p < 0.05$?
	Mean	Std Dev	Mean	Std Dev				
1223/ 1210	1.20	0.068	0.79	0.029	144	47.608	1.984	YES
1366/ 1356	1.81	0.092	1.21	0.050		48.773		YES
1636/ 1544	5.25	0.256	9.72	0.611		57.925		YES

APPENDIX E

ASSIGNMENT AND SPECTRAL POSITIONS (cm^{-1}) OF THE RED BLOOD CELL RAMAN BANDS

The Raman spectra of an optically trapped red blood cell recorded using 785 nm excitation wavelength at ~2 mW power and 600 lpmm grating spectrometer is shown below.

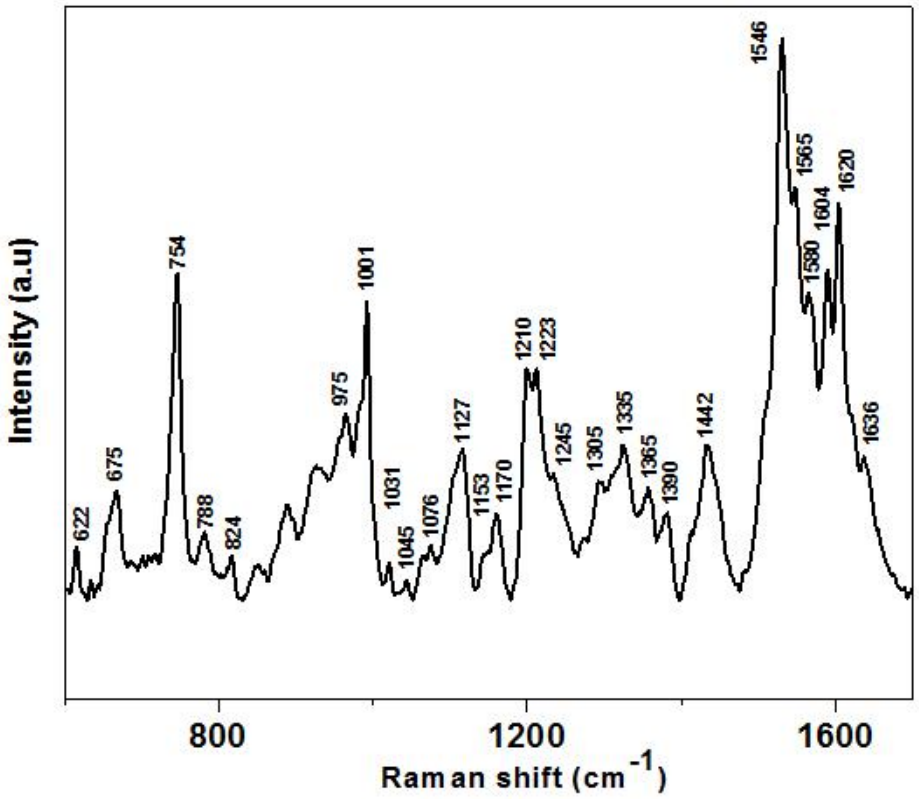

Figure E1. Raman spectra of red blood cell.

The Raman spectra observed from red blood cells are dominated by Raman bands originating from the porphyrin macrocycle and can be assigned to its different vibration modes as detailed by Abe *et al* [1] and Wood *et al* [2]. Table E1 contains the description of different Raman bands observable in the RBC spectra recorded in our set-up. For comparison bands observed by Wood *et al* [2] are shown.

Table E1. Band assignements in RBC Raman spectra.

Band Assignment	Local co-ordinates	Symmetry	Oxy-Hb Band position (cm^{-1})	Oxy-Hb band position (cm^{-1}) [2]
?			622	622
ν_7	δ(pyr deform)$_{sym}$	A_{1g}	675	676
ν_{15}	ν(pyr breathing)	B_{1g}	754	754
ν_6	ν(pyr breathing)	A_{1g}	788	789
γ_{10}	$\gamma(C_mH)$	B_{1u}	824	827
$\gamma(C_aH=)$			975	974
	phenylanaline		1001	1003
$\delta(=C_bH_2)_4$	$\delta(=C_bH_2)_4$		1031	1031
ν(O=O)	ν(O=O)		1045	1047
ν_{30}	ν(pyr half-ring)$_{asym}$	B_{2g}	1076	1074
ν_5	$\nu(C_\beta$-methyl)$_{asym}$	B_{1g}	1127	1127
ν_{44}	ν(pyr half-ring)$_{asym}$	E_u	1153	1156
ν_{30}	ν(pyr half-ring)$_{asym}$	B_{2g}	1170	1174
$\nu_5+\nu_{18}$	$\delta(C_mH)$	$A_{1g}+B_{1g}$	1210	1212
ν_{13} or ν_{42}	$\delta(C_mH)$	B_{1g} or E_u	1223	1226
ν_{42}	$\delta(C_mH)$	E_u	1245	1248
ν_{21}	$\delta(C_mH)$	B_{1g}	1305	1306
ν_{41}	ν(pyr half-ring)$_{sym}$	E_u	1335	1337
ν_4	ν(pyr half-ring)$_{sym}$	A_{1g}	1366	1371

Band Assignment	Local co-ordinates	Symmetry	Oxy-Hb Band position (cm^{-1})	Oxy-Hb band position (cm^{-1}) [2]
ν_{20}	ν(pyr quarter-ring)	A_{2g}	1390	1397
$\delta(CH_2/CH_3)$	$\delta(CH_2/CH_3)$	A_{1g}	1442	1448
ν_{11}	$\nu(C_\beta C_\beta)$	B_{1g}	1546	1547
ν_{19}	$\nu(C_\beta C_\beta)$	B_{1g}	1565	1566
ν_{37}	$\nu(C_\alpha C_m)_{asym}$	E_u	1580	1582
$\nu(C{=}C)_{vinyl}$	$\nu(C_a{=}C_b)$		1604	1604
$\nu(C{=}C)_{vinyl}$	$\nu(C_a{=}C_b)$		1620	1620
ν_{10}	$\nu(C_\alpha C_m)_{asym}$	B_{1g}	1636	1639

References:

1. M Abe, T. Kitagawa, and Y. Kyogoku, "Resonance Raman spectra of octaethylporphyrinato-Ni(II) and meso-deuterated and 15N substituted derivatives. II. A normal coordinate analysis", *J. Chem. Phys.* **69**, 4526-4534 (1978).

2. B. R. Wood, P. Caspers, G. J. Puppels, S. Pandiancherri, and D. McNaughton, "Resonance Raman spectroscopy of red blood cells using near infrared excitation", *Anal. Bioanal. Chem.* **387**, 1691-1703 (2007).